

# UNIVERSITÀ DEGLI STUDI DELLA CALABRIA

DIPARTIMENTI DI CHIMICA E DI FISICA

---

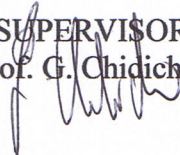
Dottorato di Ricerca in  
“Scienze e Tecnologie delle Mesofasi e Materiali Molecolari”  
(STM<sup>3</sup>)- XXIII° Ciclo

**Ph. D. Thesis**

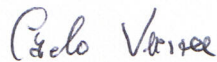
**Study of biomimetic membrane systems  
and their interaction with low power millimeter waves.**

Settore disciplinare: CHIM02

SUPERVISORE  
Prof. G. Chidichimo



COORDINATORE  
Prof. C. Versace



CANDIDATA  
Katia Cosentino



Dicembre 2010

*Alla mia famiglia*

*A zio Ernesto*

*Pondus meum amor meus, eo feror quocumque feror.*

*S. Agostino (Confess. 13, 9, 10)*

*Avevo promesso, se ricordi,  
di dimostrarti che v'è un essere più elevato  
della nostra mente e della nostra ragione.*

*Ecco, è la verità stessa:  
abbracciala, se puoi, e godila.*

*S. Agostino (De lib. arb. 2, 13, 35)*

## TABLE OF CONTENTS

<b>PREFACE</b> . . . . .	v
<b>MOST COMMON ABBREVIATIONS</b> . . . . .	viii
<b>LIST OF FIGURES</b> . . . . .	ix
<b>LIST OF TABLES</b> . . . . .	xiii
<b>CHAPTER 1 – BIOLOGICAL AND MODEL MEMBRANES: STRUCTURE AND PROPERTIES</b> . . . . .	1
1.1 MEMBRANE LIPID COMPOSITION . . . . .	4
1.2 STRUCTURE OF MEMBRANE LIPIDS. . . . .	7
1.2.1 Polar region. . . . .	7
1.2.2 Role of water. . . . .	9
1.2.3 Hydrophobic inner region. . . . .	9
1.3 POLYMORPHISM OF LIPIDS. . . . .	10
1.4 MEMBRANE MODELS AS AN INVESTIGATIVE RESOURCE. . . . .	15
1.5 PHASE TRANSITION IN LIPID MEMBRANE . . . . .	17
1.6 MEMBRANE FLUIDITY . . . . .	21
1.6.1 Headgroups and water dipoles as probes. . . . .	21
1.6.2 Diffusion of lipids in membranes. . . . .	22
1.7 CURVATURE, ELASTIC CONSTANTS AND FLUCTUATIONS . . . . .	23
1.7.1 Elastic constants and curvature. . . . .	23
1.7.2 Membrane fluctuations. . . . .	26
1.8 TEMPERATURE DEPENDENCE OF MEMBRANE PHYSICAL PROPERTIES . . . . .	28
1.9 VESICLE SHAPE . . . . .	29
1.9.1 The ADE model. . . . .	29
1.9.2. Adhesion. . . . .	31
1.9.2.1 Macroscopic model. . . . .	32
1.9.2.2 Mesoscopic model. . . . .	32
1.9.2.3 Adhesion transition. . . . .	32

<b>CHAPTER 2 – INTERACTION BETWEEN MILLIMETER WAVES AND BIOLOGICAL SYSTEMS . . . . .</b>	<b>34</b>
2.1 FUNDAMENTAL ON THE INTERACTION OF MILLIMETER WAVES WITH MATTER . . . . .	36
2.1.1 The macroscopic model. . . . .	36
2.1.2 Reflection and transmission of a wave at the boundary between two media. . . . .	37
2.1.3 Propagation of waves within matter. . . . .	38
2.1.4 Electrical Properties of Biological Materials in MMWs range. . . . .	40
2.1.5 Frequency dielectric response of water. . . . .	42
2.2 BIOPHYSICAL MECHANISM OF INTERACTION . . . . .	44
2.2.1 Thermal vs Non-Thermal Effects. . . . .	44
2.2.2 Hypothesis of the Mechanism. . . . .	46
2.3 BIOLOGICAL EFFECTS OF MILLIMETER WAVES . . . . .	47
2.3.1 Biological membrane is the primary target of MMWs. . . . .	47
<b>CHAPTER 3 – EXPERIMENTAL TECHNIQUES AND DEVICES . . . . .</b>	<b>51</b>
3.1 VESICLE PREPARATIONS . . . . .	52
3.1.1 Large unilamellar vesicle preparation by extrusion technique. . . . .	53
3.1.2 Giant unilamellar vesicle preparation by electroformation. . . . .	54
3.2 ANALYTICAL METHODS . . . . .	55
3.2.1 <sup>2</sup> H Nuclear Magnetic Resonance. . . . .	56
3.2.1.1 NMR of Anisotropic media. . . . .	57
3.2.1.2 Quadrupolar Interaction. . . . .	57
3.2.2 Dynamic Light Scattering. . . . .	60
3.2.2.1 Basic equations. . . . .	61
3.2.3 Fluorescence spectroscopy. . . . .	62
3.2.4 Phase Contrast Microscopy. . . . .	64
3.3 INSTRUMENTS FOR IRRADIATING TREATMENTS. . . . .	65
3.3.1 Wide band (53,57-78,33 GHz) noise source generator. . . . .	65
3.3.2 The IMG-56/76. . . . .	67
<b>CHAPTER 4 – PHASE TRANSITION IN MULTILAMELLAR VESICLES UNDER MMWs: A <sup>2</sup>H NMR STUDY . . . . .</b>	<b>69</b>
4.1 INTRODUCTION . . . . .	70
4.2 MATERIALS AND METHODS . . . . .	71
4.2.1 Materials. . . . .	71
4.2.2 Sample preparation. . . . .	71
4.2.3 <sup>2</sup> H-NMR acquisitions. . . . .	72
4.2.4 Real-time NMR acquisition under exposure. . . . .	72

4.2.5 Dosimetry. . . . .	73
4.3 RESULTS. . . . .	75
4.3.1 MW induced effect on the membrane main phase transition. . . . .	75
4.3.2 Dosimetric study. . . . .	79
4.3.3 Theoretical interpretation. . . . .	80
4.4 DISCUSSION. . . . .	85
4.4.1 Membrane-MW interaction: a microscopic interpretation. . . . .	85
4.5 CONCLUSION . . . . .	88
<b>CHAPTER 5 – PHYSICAL PROPERTIES OF LARGE AND GIANT UNILAMELLAR VESICLES AFFECTED BY MMWS. . . . .</b>	<b>89</b>
5.1 SIZE CHANGES AND PHYSICAL STABILITY OF LUVs UNDER RADIATION EXPOSURE. . . . .	91
5.1.1 Introduction. . . . .	91
5.1.2 Materials and Methods. . . . .	92
5.1.2.1 Sample preparation. . . . .	92
5.1.2.2 DLS acquisitions. . . . .	93
5.1.2.3 Exposure set-up. . . . .	94
5.1.2.4 Dosimetry. . . . .	95
5.1.3 Results. . . . .	95
5.1.4 Discussion. . . . .	97
5.2 CALCEIN PERMEABILITY IN LUVS UNDER RADIATION EXPOSURE . . . . .	99
5.2.1 Introduction. . . . .	99
5.2.2 Materials and Methods. . . . .	102
5.2.2.1 Materials. . . . .	102
5.2.2.2 Sample preparation. . . . .	102
5.2.2.3 Separation of vesicles and free calcein solution. . . . .	102
5.2.2.4 Stewart assay. . . . .	103
5.2.2.5 Calcein-release measurement. . . . .	104
5.2.2.6 Exposure set-up. . . . .	107
5.2.2.7 Dosimetry. . . . .	108
5.2.3 Results. . . . .	109
5.3 WATER OSMOTIC PERMEABILITY IN GUVS UNDER RADIATION EXPOSURE. . . . .	110
5.3.1 Introduction. . . . .	110
5.3.2 Materials and Methods. . . . .	112
5.3.2.1 Materials. . . . .	112
5.3.2.2 Sample preparation. . . . .	112
5.3.2.3 Osmotic vesicle shrinkage. . . . .	113
5.3.2.4 Microscopic equipment. . . . .	113
5.3.2.5 Exposure set-up. . . . .	114
5.3.2.6 Experimental procedure. . . . .	114
5.3.2.7 Dosimetry. . . . .	116

5.3.3 Results. . . . .	116
5.3.3.1 Formation of giant vesicles. . . . .	116
5.3.3.2 Osmotic Effects of Giant DLPC Vesicles. . . . .	119
5.3.3.3 Millimeter wave effects on water osmotic permeability of Giant DLPCVesicles. . . . .	121
5.3.4 Discussion. . . . .	123
5.4 CONCLUSION . . . . .	124
<b>CHAPTER 6 – COOLING RATE EFFECTS ON PHASE SHAPE TRANSITION IN GUVS . . . . .</b>	<b>126</b>
6.1 INTRODUCTION . . . . .	128
6.1.1 Equilibrium and non-equilibrium dynamics in vesicles. . . . .	129
6.1.2 Relaxation times in vesicles. . . . .	129
6.2 MATERIALS AND METHODS . . . . .	133
6.2.1 Materials. . . . .	133
6.2.2 Sample preparation. . . . .	133
6.2.3 Experimental set-up. . . . .	134
6.2.4 Experimental procedure. . . . .	135
6.3 RESULTS. . . . .	136
6.3.1 Phase transition induces rupture of adhered vesicles above a temperature threshold. . . . .	136
6.3.2 Temperature evolution of the adhesion area. . . . .	139
6.3.3 Mechanical and Thermodynamic Coupling. . . . .	144
6.3.4 Relaxation process. . . . .	146
6.4 DISCUSSION. . . . .	149
6.4.1 Cooperative relaxation processes in GUVs. . . . .	149
6.4.2 Role of adhesion in area fluctuations and related relaxation times. . . . .	150
6.4.3 Mechanism of vesicle rupturing. . . . .	152
6.5 CONCLUSION . . . . .	154
<b>CONCLUSION . . . . .</b>	<b>156</b>
<b>BIBLIOGRAPHY . . . . .</b>	<b>160</b>
<b>ACKNOWLEDGMENTS . . . . .</b>	<b>178</b>

## **PREFACE**

Biological membrane, that allows cells to maintain their individuality, plays a crucial role in all biological processes. Despite its complexity, the basic structure of the membrane consist of a phospholipid bilayer and membrane functionality is ultimately determined by its mechanical and electrical properties.

Membrane models are often used in studies concerning biological membranes properties in order to reduce the complexity of the problems. In such way physical, biochemical, and physiological processes can be generally isolated and analyzed individually.

In this work we have used biomimetic membrane systems to study the interaction between low power millimeter waves and biological membranes.

Millimeter waves (MMWs) are microwave radiations in the range 30-300 GHz.

The study of the impact of MMWs radiation on biological systems is interesting for both biomedical applications and health hazard problems. At high power densities, MMWs induce thermal effects linked to water absorption of the radiation. More interesting, they induce a variety of biological effects, that are considered non-thermal at low power densities, and many evidence point to a direct involvement of the phospholipid membranes.

An active role of water molecules, considered to be the main target of the MMW radiations, and other dipolar residues present at the interface with the membrane, has been advanced in order to explain the observed phenomena; nonetheless, no clear evidence have been reported up to now nor the molecular mechanisms involved have been clarified.

The aims of this work are:

- To study the influence of low power MMWs on interfacial properties of lipid membranes;
- To establish the non-thermal nature of the observed effects;
- To better understand the mechanisms of MMW radiation/biological membrane interaction.

In this thesis, further experiments to test the influence of MMWs on the properties of lipid membranes, are illustrated. While the previous studies have mainly focused on the alteration of membrane processes at a cellular level, like ion channels functionality, or



on membrane structural changes, the very original contribution of the experiments presented here, is that we have directly monitored the behavior of water at the membrane polar interface.

With these experiments we elucidate the effects of MMWs on the physical properties of biological membranes and the special role of water in mediating the membrane/radiation interaction.

After an introduction on the structure and properties of biological membranes (Chapter 1) and an overview on the state of art on the interaction between millimetre waves and biological systems (Chapter 2), we will present our results on the effects of MMWs on different biomimetic membrane models.

Initially (Chapter 4), we used multilamellar vesicular systems, characterized by an onion structure, to monitor membrane-bound deuterated water by using  $^2\text{H}$  NMR spectroscopy.

An effect of the radiation on the phase transition properties of the membrane has been observed and a non-thermal nature of the phenomenon has been established. The sensitivity of the investigation technique (described in Chapter 3), has allowed, above all, a microscopic interpretation of MMW-membrane interaction, involving a redistribution of water molecules between different sites in the polar region of phospholipids.

Subsequently (Chapter 5), unilamellar systems, more similar to real biological cells, of different size (different membrane curvature), including large unilamellar vesicles (LUVs) of 100 nm in size, and giant unilamellar vesicles (GUVs) with size between 1 and 100  $\mu\text{m}$ , have been used to study the effects of MMWs on the elastic and chemical-physical properties of the membrane, like molecule diffusion, osmotic properties and physical stability of the vesicles.

The initial step of this work required the preparation and characterization of these biomimetic systems, which I learned during my internship at ETH, Zürich.

LUVs have been used to study the effect of radiation on 1. the physical stability of vesicles, and 2. the membrane permeability to big molecules, like calcein, making use of dynamic light scattering and fluorescence techniques. GUVs, have been used to study the effect of millimeter waves on membrane water permeability by directly monitoring vesicle shape and size distribution under a light microscope.

All these experiments suggest that membrane-MMW interaction involves the absorption of energy by water that may cause a re-organization of water molecules around the phospholipid polar head groups. This can have far-reaching consequences on the membrane properties at the water-lipid interface and, more in general, on active biological systems.

The last part of this thesis (Chapter 6) has been devoted to a thermodynamic and kinetics study on GUVs. The initial idea was to prove MMW effects on the phase shape transition of these systems. Nevertheless, during the standardization procedure, we observed some interesting effects to which we decided to devote our attention.

Fluid-to-gel phase transition of GUVs supported on a ITO glass surface has been induced under different cooling rates. It has been observed that irreversible vesicle breakdown occurred only above a threshold cooling rate value. Calculations of the membrane area relaxation time through measurements of the vesicle adhesion area as a function of the temperature, support the hypothesis that membrane adhesion may play a major role in regulating relaxation processes in biomembranes. This work provides a simple method to have an estimation of relaxation times of cooperative processes at the transition temperature in biological membranes.

## MOST COMMON ABBREVIATIONS

A	Vesicle Area
ADE	Area Difference Elasticity
$C_p$	Heat Capacity
DLPC	1,2-Dilauroyl-sn-Glycero-3-Phosphocholine
DLS	Dynamic Light Scattering
DMPC	1,2-Dimyristoyl-sn-Glycero-3-Phosphocholine
DPPC	Dipalmitoyl-sn-Glycero-3-Phosphocholine
DSPC	1,2-Distearoyl-sn-Glycero-3-Phosphocholine
GUV	Giant Unilamellar Vesicle
LUV	Large Unilamellar Vesicle
MLV	Multi Lamellar Vesicle
MMW	Milli-Meter Wave
MW	Micro-Wave
POPC	1-palmitoyl-2-oleoly-snglycero-3-phosphocholine
QELS	Quasi Elastic Light Scattering
SAR	Specific Absorption Rate
SOPC	1-stearoyl-2-oleoly-snglycero-3-phosphocholine
SUV	Small Unilamellar Vesicle
$T_m$	Main Transition Temperature
V	Vesicle Volume
$\Delta A$	Excess Area
$\Delta H$	Excess Enthalpy
$\tau$	Relaxation Time
$^2\text{H}$ NMR	Deuterium Nuclear Magnetic Resonance

## LIST OF FIGURES

**Figure 1.1** Structure of the double layer of lipid molecules in a biological membrane.

**Figure 1.2** The phospholipid bilayer.

**Figure 1.3** Head group structures of some phospholipids with palmitic fatty acid chains.

**Figure 1.4.** Schematic of a phosphatidylcholine molecule showing the structural notation defining various regions.

**Figure 1.5** The crystal structures of three phospholipids.

**Figure 1.6** The effect of double bond.

**Figure 1.7** Phase diagram showing structure changes with increasing concentration of amphiphilic molecules.

**Figure 1.8** Representation of a hexagonal phase.

**Figure 1.9** Schematic example of a cubic phase.

**Figure 1.10** Representation of a lamellar structure.

**Figure 1.11** Representation of the structures in lamellar phase.

**Figure 1.12** Biological model structures.

**Figure 1.13** Calorimetric melting profile of dimyristoyl phosphatidylcholine (DMPC).

**Figure 1.14** Melting temperature,  $T_m$ , as a function of the chain length.

**Figure 1.15** Phase diagram for the water-dimyristoylphosphatidylcholine (DMPC) system.

**Figure 1.16** Different diffusion process and relative times.

**Figure 1.17** The three possible deformation modes: a) compression-extension mode, b) shear mode, and c) curvature mode.

**Figure 1.18** GUV under light microscope.

**Figure 1.19** Permeability of a lipid vesicles for a fluorescent dye as a function of temperature compared to the melting profile.

**Figure 1.20** a)Phase diagram of possible vesicle shapes in the ADE model. b) Starfish-shaped vesicle.

**Figure 1.21** Schematic phase diagram with free and bound shapes at constant area and volume.

**Figure 2.1** Plane millimeter wave propagating through air that impinges at angle  $\theta$  on a three-layered system.

**Figure 2.2** Relative dielectric constant  $\epsilon'(\nu)$  of a typical tissue as a function of the frequency from 0 up to 300 GHz.

**Figure 2.3** Relative dielectric constant  $\epsilon'(\nu)$ , relative loss factor  $\epsilon''(\nu)$  and dielectric conductivity  $\sigma(\nu)$  (S/m) of water at 303 K as a function of the frequency.

**Figure 2.4** Scanning electron microscopy of K562 cells as they appear before (left) and after MMW irradiation (right).

**Figure 2.5** Scanning electron microscopy of MCF-7 cells as they appear before (left) and after MMW irradiation (right).

**Figure 2.6** Left. Photograph of H1299 cell field expressing lipid bound fGFP at cell membrane (transfected with pEGFP-F vector). Right. Photograph of single fGFP expressing cell in oxonol and PBS before (top) and during (bottom) millimeter wave exposure.

**Figure 3.1** Evolution of Vesicles.

**Figure 3.2** Extrusion technique.

**Figure 3.3** Confocal microscopy image of a 33:67 DLPC:DPPC mixture at 26 °C, showing domain formation.

**Figure 3.4** Inside cover of *ChemBioChem* issue of May 2010, dedicated to preparations and applications of GUVs.

**Figure 3.5** Separation of the peaks as a function of  $\theta$ .

**Figure 3.6** Deuterium spectral pattern.

**Figure 3.7** Diagram showing the various kinds of electronic excitation that may occur in organic molecules.

**Figure 3.8** Cut-away diagram of a modern upright phase contrast microscope.

**Figure 3.9** a) A photograph of the instrument called AMPHIT. b) Section view of the “noise” generator AMPHIT.

**Figure 3.11** Radiating power of AMPHIT as a function of frequency.

**Figure 3.12** The IMG-56/76 generator.

**Figure 4.1** MW exposure set-up for  $^2\text{H}$  NMR measurements in real time. The whole irradiating system is inserted in the NMR magnet.

**Figure 4.2** Model of the scenario for MMWs applicator inserted into a NMR tube with the exposed sample.

**Figure 4.3** DMPC-<sup>2</sup>H<sub>2</sub>O membrane phase transition.

**Figure 4.4** Effects of MW on the P<sub>β</sub>→L<sub>α</sub> transition.

**Figure 4.5** Effects of MW on the L<sub>α</sub>→P<sub>β</sub> transition.

**Figure 4.6** Local electric field amplitude per unit incident power [V/m].

**Figure 4.7** Effect of microwaves on the membrane dynamic behaviour near the transition.

**Figure 5.1** Typical window where dynamic light scattering results for DLPC-LUVs appear.

**Figure 5.2** Exposure set-up for irradiation of DLPC LUV<sub>100</sub> by multiscan IMG 56-76.

**Figure 5.3** Relative increase of the effective vesicle diameter as a function of time for the exposed (red line) and sham (blue line) system.

**Figure 5.4** Relative polydispersity variation as a function of time for the exposed (red line) and sham (blue line) system.

**Figure 5.5** Calcein molecular structure

**Figure 5.6** Permeability coefficient of molecules and ions crossing lipid bilayer.

**Figure 5.7** Separation of free calcein (upper band in the chromatographic column) from loaded POPC LUVs (lower band).

**Figure 5.8** Stewart assay standard curve.

**Figure 5.9** Dilution series of 80 mM calcein solution ending at 156 nM.

**Figure 5.10** Calcein standard curve in 10 mM phosphate buffer.

**Figure 5.11** Fluorescence intensity as a function of calcein concentration.

**Figure 5.12** a) Exposure set-up for irradiation of SOPC LUV<sub>100</sub> by multiscan IMG 56-76. b) Diagram of the experimental set-up.

**Figure 5.13** Percentage of calcein release as a function of time for exposed (red line) and sham (blue line) POPC LUVs (100 nm) systems.

**Figure 5.14** a) Chamber with Pt wires for the electroformation of b) DMPC GUVs.

**Figure 5.15** Diagram of the experimental set-up used for the exposure of GUVs to 52-72 GHz radiations.

**Figure 5.16** Size distribution of giant unilamellar vesicles obtained from EPC/CHOL (70/30 %wt) lipid mixture.

**Figure 5.17** Fatty acid distribution in Egg PC.

**Figure 5.18** Sequence showing the effect of increasing voltage in EPC/CHOL (70/30) lipid mixture.

**Figure 5.19** a) Electroformed DLPC GUVs in pure water; b) same vesicles under osmotic pressure.

**Figure 5.20** a) Size distribution of DLPC GUVs in pure water; b) Vesicle size distribution measured 5 minutes and c) 30 minutes after the addition of a glucose solution 1,25 mM.

**Figure 5.21** Size distribution of DLPC GUVs a) in pure water, b) after 4 hours of vesicle exposure to MMWs; c) 30 minutes after the addition of a glucose solution 1,25 mM.

**Figure 6.1** a) ITO chamber and b) DMPC GUVs formed by the electroformation technique.

**Figure 6.2** Experimental set-up for the study of shape phase transition in DMPC GUVs.

**Figure 6.3** Monitoring of a free tubular vesicle cooling and heating the system at a rate of 0.2 °C/min.

**Figure 6.4** Glass supported DMPC GUVs a) before (26°C) and b) after (18°C) cooling the system through DMPC main phase transition at a rate of 0.2 °C/min.

**Figure 6.5** Glass supported DMPC GUVs going through DMPC main phase transition at a rate of 0.5 °C/min.

**Figure 6.6** Cartoon of a glass supported DMPC GUV in its a) fluid phase and b) gel phase.

**Figure 6.7** The degree of deformation,  $(a/R)$ , at DMPC's  $T_m=22.5$  °C, against vesicle diameter of glass supported DMPC GUVs.

**Figure 6.8** The degree of vesicle deformation  $a/R$  against the increase of temperature for DMPC GUVs adherent to a glass support.

**Figure 6.9** View from the top of DMPC GUVs on a glass support: the vesicle can be approximate to an ellipsoid.

**Figure 6.10** Variation of the adhesion area during fluid-gel transition.

**Figure 6.11** Heat capacity profile of DMPC GUVs during the fluid-gel transition.

**Figure 6.12** Entropy as a function of the enthalpy of a lipid membrane.

**Figure 6.13** Heat capacity and relaxation times of DMPC GUV during the fluid-gel transition.

**Figure 6.14** An hypothesis of mechanism for explaining rupturing of vesicles during the fluid-to-gel transition above a cooling rate of 0.2 °C/min.

## LIST OF TABLES

**Table 1.1** Approximate lipid composition of different cell membranes.

**Table 1.2** Some fatty acids commonly present in membrane lipids.

**Table 1.3** Some typical values for the compression modulus, the shear modulus, and the curvature modulus.

**Table 2.1** Dielectric properties of water and some lower alcohols at 70 GHz and at 20°C.

**Table 4.1** Electromagnetic parameters adopted in numerical simulations.

**Table 4.2** SAR values for different sample layers in case of 1W (average) and 20 $\mu$ W input power.

**Table 4.3** Fitting results of the normalized splitting by Eq. 4.2.

**Table 5.1** Calcein dilution series design including FI results.

**Table 5.2** GUVs obtained from different POPC/CHOL mixtures.

**Table 6.1** Relaxation times,  $\tau$ , found for different lipid models.



# **CHAPTER 1**

**Biological and model membranes:  
structure and properties**

Biological membranes surround cells and organelles, acting as a barrier to the passive transport of matter between the extra- and intra-cellular aqueous environment, and support a wide variety of important metabolic processes, including active transport, the flow of energy, signal transduction and mobility.

According to the “fluid mosaic model” of Singer and Nicolson (1972), the two main components of membranes are lipids and proteins. Depending on the type of membrane, lipids are between 20 and 80% of the total weight, while the remainder are proteins. Minor but functionally important components of membranes, are carbohydrates. In biological membranes, lipid molecules are in contact with water and, thanks to their amphiphilic nature, spontaneously arrange in a double layer structure (bilayer, Figure 1.1) in which proteins are embedded and can freely diffuse.

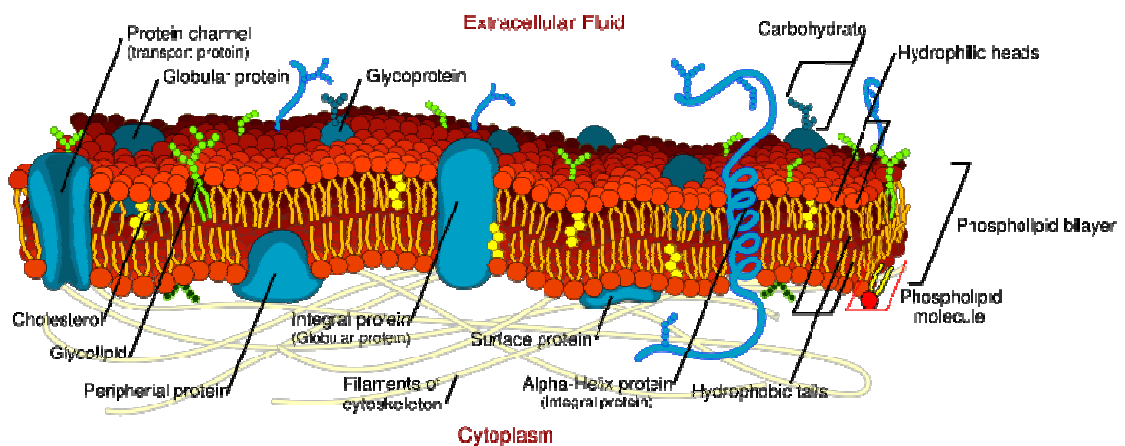


**Figure 1.1** Structure of the double layer of lipid molecules in a biological membrane (from <http://cellbiology.med.unsw.edu.au>)

Thus, in a membrane bilayer, two different parts can be distinguished (Figure 1.2):

- a polar part, which is at the interface with the aqueous environment and includes the polar head (usually containing charged groups), the glycerol backbone (usually present in lipid molecules; see below) and the ester groups of lipid molecules (Figure 1.2a). The molecular details of the membrane surface, like the surface electric charges, are relevant to the membrane recognition by molecules such as enzymes dissolved in the extracellular and intracellular environment;
- a hydrophobic part, which consists of the hydrocarbon chains of lipids. The order and dynamics of the hydrophobic heart determines the membrane permeability to molecules such as drugs and can modulate the function of trans-membrane proteins.

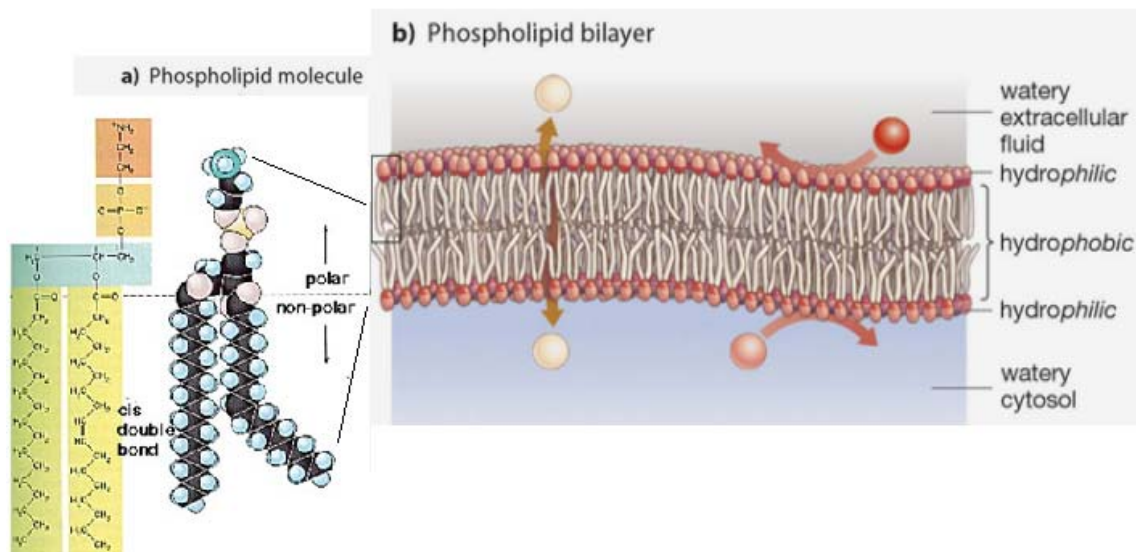


**Figure 1.2** a) Representation and chemical structure of a phospholipid molecule constituting. b) The phospholipid bilayer.

The lipid composition of natural membranes is quite heterogeneous. There are thousands of lipids that are chemically different in their polar head, chain length, degree of unsaturation. For a given membrane, the lipid composition and lipid-protein ratio are relatively well defined, suggesting a correlation between lipid composition and membrane functions (Spector and Yorek, 1985).

Moreover, the lipid distribution between the inner and the outer leaflet of a biological membrane is asymmetrical. The asymmetry of the membrane may play an important role in the proper orientation of membrane proteins (Yamaji-Hasegawa and Tsujimoto, 2006). This asymmetry is not strictly conserved, and several cell types, organelles and cells in different states of activity, probably change their lipid distribution.

To date, little is known about how lipid composition and distribution are controlled and why biological membranes contain so many different lipids. Many biological membranes can adapt to changes in external conditions such as temperature, pressure or long-term exposure to drugs or alcohol, altering their lipid composition or distribution in order to maintain optimal conditions for cell growth (Seelig and Browning, 1978).

In light of some new findings obtained considering the lipid heterogeneity, the “fluid mosaic model”, assuming the lipid membrane as a homogeneous fluid, has currently been revised, and the “mattress model”, firstly proposed by Mouritsen and Bloom (1984) has been introduced. According to this model, lipids and proteins distribute inhomogeneously within the membrane because, due to their variety in size and length,

they have to interact each other in such a way to reduce the exposition of their hydrophobic segments to water (hydrophobic matching). As a consequence, lipid membrane has to be deformed leading to the formation of lipid domains (Bagatolli et al., 2009), or lipid-protein domains. A particular kind of these micro-domains, that in cell biology are called “rafts”, seem to play a role in many biological processes, like endocytosis or protein transport (Edidin, 2003).

The above interpretation leads to a modern view of biological membranes in which the cooperative behavior of lipids and proteins has to be considered.

This aspect becomes even more interesting considering that biological membranes can undergo transitions from ordered to disordered states (melting transition) because of some external perturbations, like a change in pH or salt concentration, or a change of thermodynamic variables like pressure and temperature. Under such perturbations a rearrangement of lipids occurs, in terms of a change in the lateral order of lipids and in the order of their hydrocarbon chains. For native membranes that can occur in proximity of growth or body temperature. This has far reaching consequences on the physical properties of biological membranes, as a change in lipid distribution can change membrane curvature and, in turn, its elastic constants, finally affecting its geometry (size) and permeability properties.

In light of what shown up to this point, it is easily understandable that the cell membrane is a highly complex structure, and a variety of factors should be taken into account to study its properties. For this reason we appeal to simple cell and membrane models to simulate certain properties and conditions found in biological membranes.

## **1.1 MEMBRANE LIPID COMPOSITION**

As mentioned above, biological membranes have a very heterogeneous lipid composition. An example of the lipid composition for different cell membrane is shown in Table 1.1.

**Table 1.1** Approximate lipid composition of different cell membranes.

Lipid	Percentage of Total Lipid by Weight					
	Liver Plasma Membrane	Erythrocyte Plasma Membrane	Myelin	Mitochondrion (inner and outer membranes)	Endoplasmic Reticulum	<i>E. coli</i>
Cholesterol	17	23	22	3	6	0
Phosphatidyl-ethanolamine	7	18	15	35	17	70
Phosphatidylserine	4	7	9	2	5	trace
Phosphatidylcholine	24	17	10	39	40	0
Sphingomyelin	19	18	8	0	5	0
Glycolipids	7	3	28	trace	trace	0
Others	22	13	8	21	27	30

The plasma membranes of bacteria are often composed of a single type of phospholipid and do not contain cholesterol, the most representative among the sterols, which are important lipid components present only in eukaryotic cells.

Eukaryotic cells, in contrast, not only contain large amounts of cholesterol, but present also a great variety of different phospholipids.

Lipids present in nature can vary because of their head groups or their fatty acid chains.

Because of their difference in the head groups, lipids can be distinguished in:

- 1) Phospholipids: lipids containing a phosphate group and a glycerol skeleton as an anchor for the fatty acids. The phospholipids can be further divided into lipids containing nitrogen such as phosphatidylcholine (PC), phosphatidylethanolamine (PE) and phosphatidylserine (PS), and lipids that do not contain nitrogen, such as phosphatidylglycerol (PG) and cardiolipin (CL) (Figure 1.3). Among the lipids shown in Figure 1.3, PC and PE are zwitterionic (neutral net charge), the others are negatively charged.
- 2) Lipid containing backbones different from glycerol. Examples are sphingolipids and glycosphingolipids, mainly found in nerve cells and brain.

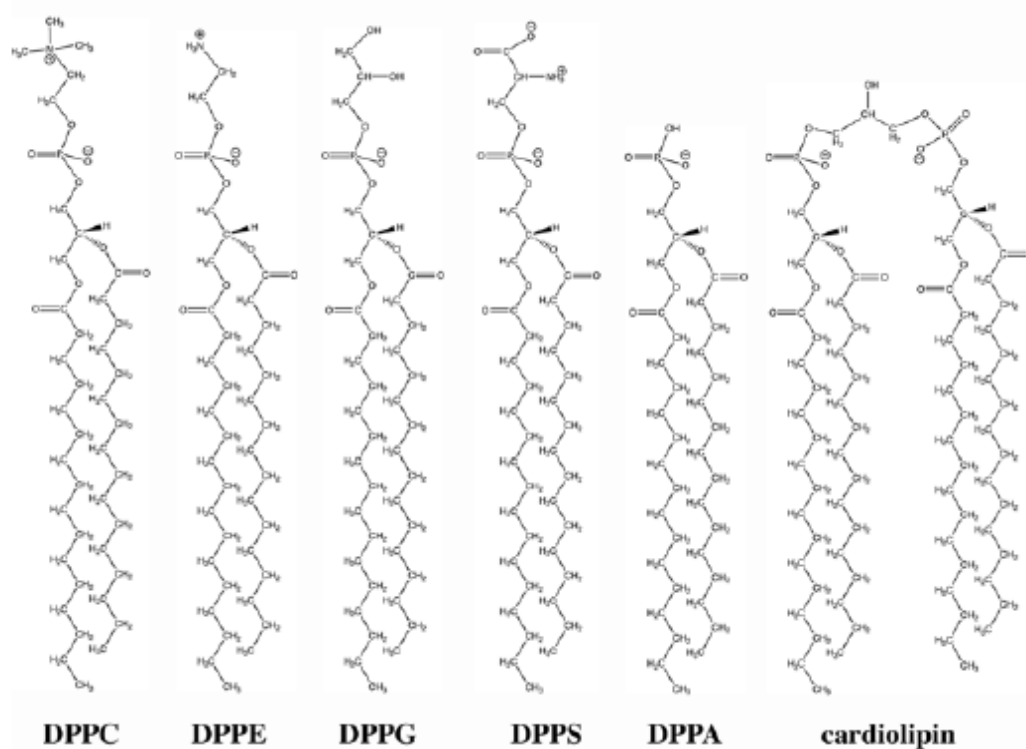


**Figure 1.3** Head group structures of some phospholipids with palmitic fatty acid chains: phosphatidylcholine (DPPC), phosphatidylethanolamine (DPPE), phosphatidylglycerol (DPPG), phosphatidylserine (DPPS), phosphatidic acid (DPPA), and cardiolipin (with four chains and two phosphate groups); from Heimburg (2007).

Lipids in eukaryotic cell membranes are mainly phospholipids containing nitrogen (Seelig and Seelig, 1980). Differences in the lipid chains include differences in their length and degree of unsaturation.

The phospholipids found in cell membranes, prokaryotic (bacteria) and eukaryotic (mammalian) normally contain saturated and *cis*-unsaturated fatty acids, the most abundant of which are saturated palmitoyl (C 16:0) and *cis*-unsaturated oleoyl (C 18:1, *cis*) chains. Phospholipids with a single *cis*-double bond are predominant (Seelig and Seelig, 1977) but lipids containing more than one double bond are encountered quite frequently.

**Table 1.2** Some fatty acids commonly present in membrane lipids (taken from Gennis (1989)).

Trivial name	Chain length: number of double bonds	Position of unsaturations
<b>Lauric</b>	12:0	
<b>Myristic</b>	14:0	
<b>Myristoleic</b>	14:1	9-cis
<b>Palmitic</b>	16:0	
<b>Palmitoleic</b>	16:1	9-cis
<b>Stearic</b>	18:0	
<b>Oleic</b>	18:1	9-cis
<b>Linoleic</b>	18:3	6-cis, 9-cis, 12-cis
<b>Arachidic</b>	20:0	
<b>Arachidonic</b>	20:4	5-cis, 8-cis, 11-cis, 14-cis

The length and degree of unsaturation of lipid chains, as well as the size and charge of polar heads, and their ability to form hydrogen bonds, determine the intermolecular lipid-lipid interactions that is reflected in the packing density of lipids and consequently in the formation of micro- or macro-domains (in this case we refer to them as phases). This, in turn, has an influence on the membrane order transition (see section 1.5) and in its electrostatic potential in the presence of charged head groups.

## 1.2 STRUCTURE OF MEMBRANE LIPIDS

From the upper section it is clear that in order to approach an understanding of biomembranes it is important to understand the detailed structure of the lipid bilayer.

In the following part a detailed description of lipid structures will be given focusing on both the hydrophilic and the hydrophobic regions of membrane bilayer. Figure 1.4 will result useful to understand some common notations used to describe lipid conformation.

### 1.2.1 Polar region.

The polar region at the interface with water includes:

- the head group, with the hydration water tightly bounded to an extended more weakly packed hydration layer;
- the glycerol backbone;
- the ester linkages of the fatty acyl chains.

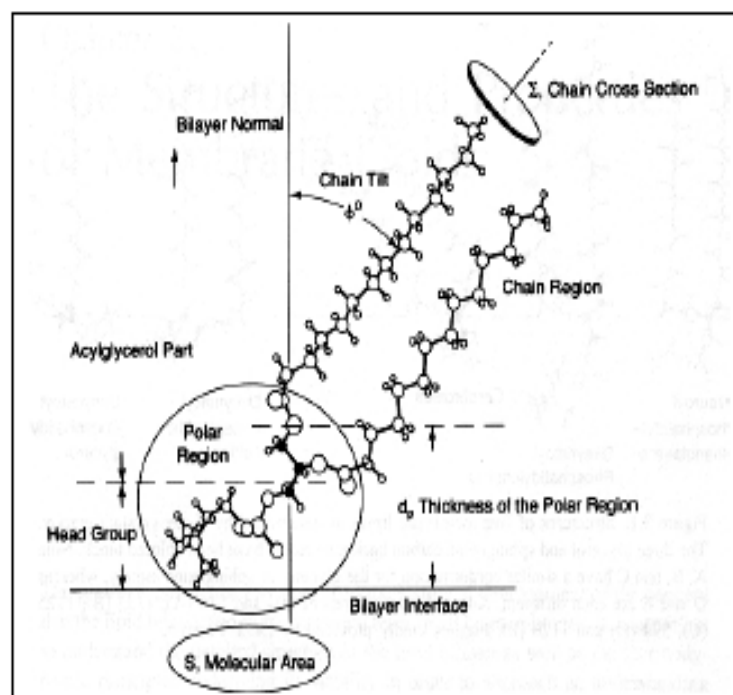


**Figure 1.4.** Schematic of a phosphatidylcholine molecule showing the structural notation defining various regions. Note that the cross-sectional area of the hydrocarbon chain, is taken perpendicular to the chain axis. The cross-sectional area parallel to the plane of the membrane will be, in this case, significantly larger due to the tilt of the chains (from Gennis, 1989).

Because of conformational constraints, the carbonyl group of the *sn*-2 chain is particularly close to the lipid-water interface, while in the *sn*-1 chain it is inserted more deeply in the inner membrane.

Three lipid crystals are shown in Figure 1.5. In all these structures the glycerol backbone is oriented perpendicular to the surface of the double layer, while the polar head group is almost parallel to the membrane surface. Neutron scattering experiments confirm the orientation of the polar heads.

The orientations of the polar heads of double layers of PC, PE and PG are very similar in single crystals, liquid crystalline and gel phases, and independent of the dynamic state of the membrane. The correlation times of the segmental and collective motions of the head groups decrease of more than two orders of magnitude at the gel-liquid phase transition, but the average conformation remains unaffected.



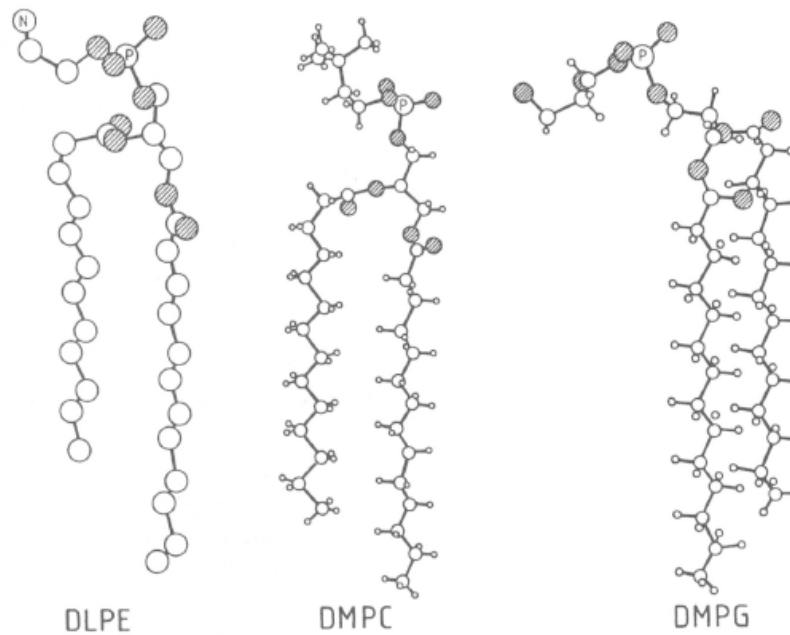


**Figure 1.5** The crystal structures of three phospholipids: 1,2-dilauroyl-sn-3-fosfoetanamina-Glyceria (DLPE), 1,2-dimyristoyl-sn-Glyceria-3-phosphocholine (DMPC), 1,2-dimyristoyl-sn Glyceria-fosfoglicerolo-3-(DMPG). Only one of two possible conformations is shown for each lipid.

### 1.2.2 Role of water.

From NMR and X-ray measurements it has been seen that membrane hydration plays an important role in the head group conformation. A molecule of PC, PE or PG requires a minimum of 11 to up to 16 water molecules to form a primary hydration shell (Borla and Seelig, 1983).

Excess water exchanges with the primary hydration shell. With increasing hydration (10-70 wt% H<sub>2</sub>O) the PO<sup>-</sup>-N<sup>+</sup> phosphocholine dipole undergoes a movement of its cationic end away from the hydrocarbon layer. This explains why the PO<sup>-</sup>-N<sup>+</sup> dipoles in liquid crystalline membranes are generally slightly inclined away from the membrane surface up to an angle of about 30°, and are oriented parallel to the surface in the crystal structure (Seelig and Seelig, 1974).

### 1.2.3 Hydrophobic inner region.

The hydrocarbon chains of lipid bilayers are in an almost liquid state as evidenced by X-ray diffraction, by electron spin resonance spectroscopy and by DSC studies. A quantitative characterization of the hydrocarbon chain order in lipid bilayers is possible,

by means of  $^2\text{H}$ -NMR spectroscopy, selectively deuterating the fatty acyl chains of lipid molecules. The order of the chains can be explained by the rotational isomeric model for hydrocarbon chains. In the region of the constant order parameters, *trans-gauche* isomerizations occur, leaving the hydrocarbon chains basically parallel to each other. This leads to well-ordered bilayers with disordered hydrocarbon chains. The order parameter decrease in the central region is due to an increase in *gauche* states.

The incorporation of *cis* double bond introduces a node in the chain, otherwise being straight, and reduces the chain order compared to the corresponding saturated lipid chain (Figure 1.6). An increase in temperature results in a further decrease in order parameters (Seelig and Seelig, 1977).

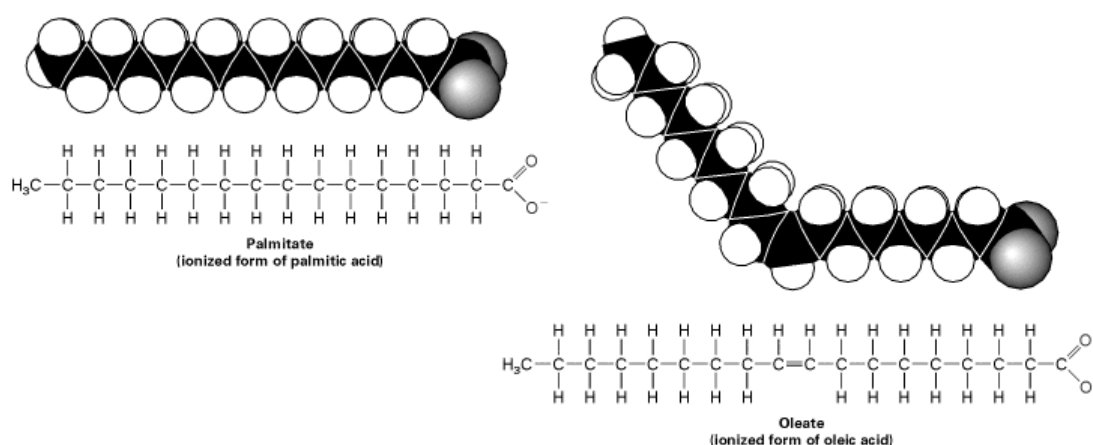


**Figure 1.6** The effect of double bond. Full space models and the chemical structures of the ionized form of the palmitic acid, a saturated fatty acid, and oleic acid, an unsaturated one, are shown. In saturated fatty acids, the hydrocarbon chain is linear; in the oleic acid, the *cis* double bond creates a node in the hydrocarbon chain.

### 1.3 POLYMORPHISM OF LIPIDS

The amphiphilic nature of lipids allows them to spontaneously assemble into organized structures. These phases of matter are called lyotropic liquid crystals and they form the basis of cell walls, biomembranes.

Polymorphism in a mixture of amphiphilic molecules and solvent depends on different parameters of the amphiphilic self, as the ionic character of the polar head, the size and the volume occupied by the head with respect to the parameters of the chain, the presence or absence of surfactants or other salts in the mixture, the pH and ionic strength

of the solution, the purity of the compounds, and temperature, among other factors. The water, which is present in many lyotropic mixtures, plays a significant role in the stability of the different mesophases. Water molecules participate in the ion-dipole interactions and dipole-dipole and hydrogen bonds, involving the hydrophilic groups of the amphiphilic molecules. We can say that there is always a certain amount of bounded water in the structure of amphiphilic molecules, creating a hydration layer around them (Ekwall, 1975).

The hydrophobic effect, a manifestation of the attractive forces between water molecules, is the main force responsible for the spontaneous organization of lipids.

Actually, many different lipid structures have been observed by varying the temperature or/and the lipid concentration, even in the case of systems made of a single kind of lipid. These different phases result from a combination of an optimization of the hydrophobic effect with some geometric packing constraints (Seddon and Templer, 1995).

The best way to illustrate the behavior of an amphiphilic material in water is to show a phase diagram. A generic phase diagram is shown in Figure 1.7. It shows lipid structure changes with increasing the temperature and/or the concentration of amphiphilic molecules.

For very low concentrations, lipids are present in solution as monomers. Above a critical concentration, monomers aggregate to form micelles. In normal micelles the hydrophobic portion points toward the center of the micelle, away from water. The concentration at which micelles are formed in solution, called critical micelle concentration (CMC), is shown by the dotted line. In addition, a dark line is also shown representing a temperature threshold, referred to as the Krafft temperature, below which very few organized structures are formed, but most of the molecules is diffusely distributed.

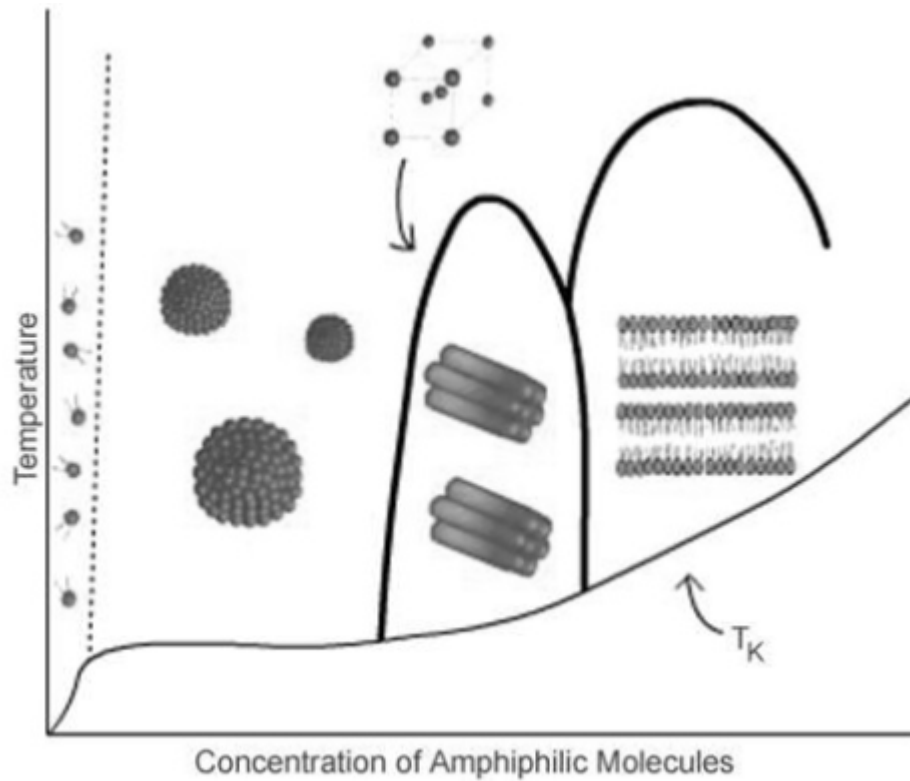


**Figure 1.7** Phase diagram showing structure changes with increasing concentration of amphiphilic molecules (<http://atom.physics.calpoly.edu/>).

At even higher lipid concentration, micelles begin to arrange themselves into different shapes. There are mainly three different classes of lyotropic liquid crystalline structures: lamellar, cubic, and hexagonal phases. Hexagonal and cubic phases are shown in Figure 1.8 and 1.9 respectively.

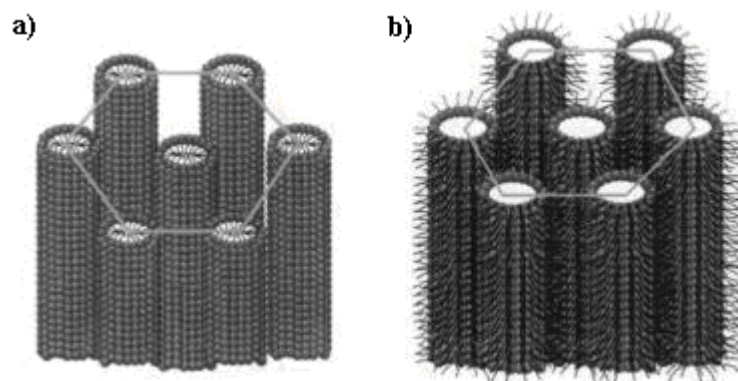


**Figure 1.8** Representation of a hexagonal phase: a) direct structure called  $H_\alpha$  (or E or  $H_1$ ), is characterized by liquid-like ordered hydrocarbon chains inside the cylinders. b) inverted structure known as  $H_\alpha^i$  (or F or  $H_2$ ), is placed inside the cylinders and the chains point outwards.

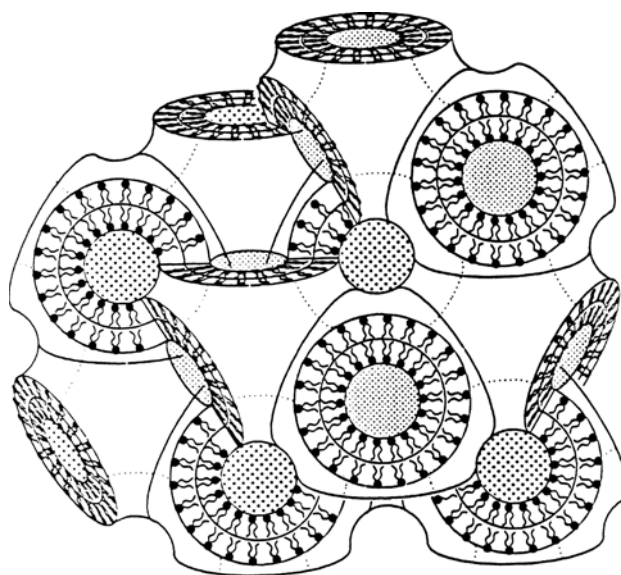


**Figure 1.9** Schematic example of a cubic phase (from Seddon and Templer, 1995). Cubic phases are mostly bicontinuous lipid bilayer structures showing a periodic three dimensional order.

We will focus on the lamellar phase because of its relevance in biology.

In the lamellar phase, the amphiphilic molecules are arranged as a super-molecular aggregates forming layers with a large shape anisotropy (Figure 1.10).

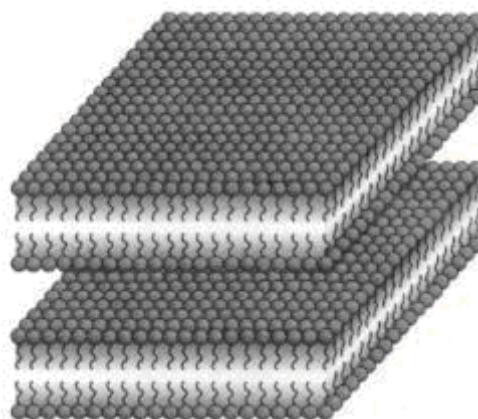


**Figure 1.10** Representation of a lamellar structure (Figueiredo Neto and Salinas, 2005).

This structure is typical of smectic A thermotropic liquid crystals. More double layers are packaged parallel to each other and are separated by a layer of water.

Since the "sheet" layers can easily slide over each other, this phase is less viscous than the hexagonal and cubic ones, at least in the direction of shear, despite its lower water content.

Comparing the thickness of the layers with any other dimension in the plane of the plates, the shape anisotropy is typically larger than 1: 50. Normally, the thickness of the layers is of the order of about twice the length of the main amphiphilic molecule. However, this length may increase after the addition of a non-polar solvent. The thickness also depends on the temperature of the sample (Luzzati et al., 1960).

In a lamellar phase we can distinguish different states because of a decreasing order of the chains by increasing the temperature (see sequence in Figure 1.11):

- Crystalline phase  $L_c$  or  $L_\beta$ , at lower temperatures, is highly ordered in three dimensions, with the hydrocarbon tails of the lipids ordered into all-*trans* configuration (Cevc et al., 1987; Small, 1986).
- Gel phase  $L_{\beta'}$ . It is also called ordered phase. Lipid chains are mainly extended in *trans* configuration and are tilted respect to the membrane normal, with a value close to  $20 \text{ \AA}^2$  for the cross-sectional area per chain.
- Fluid phase  $L_\alpha$ . It is a disordered liquid crystalline phase which is obtained at higher temperatures and in which the paraffin chains are in a quasi-liquid state.

This is the typical phase observed in biologically active membranes (Cevc et al., 1987; Small, 1986).

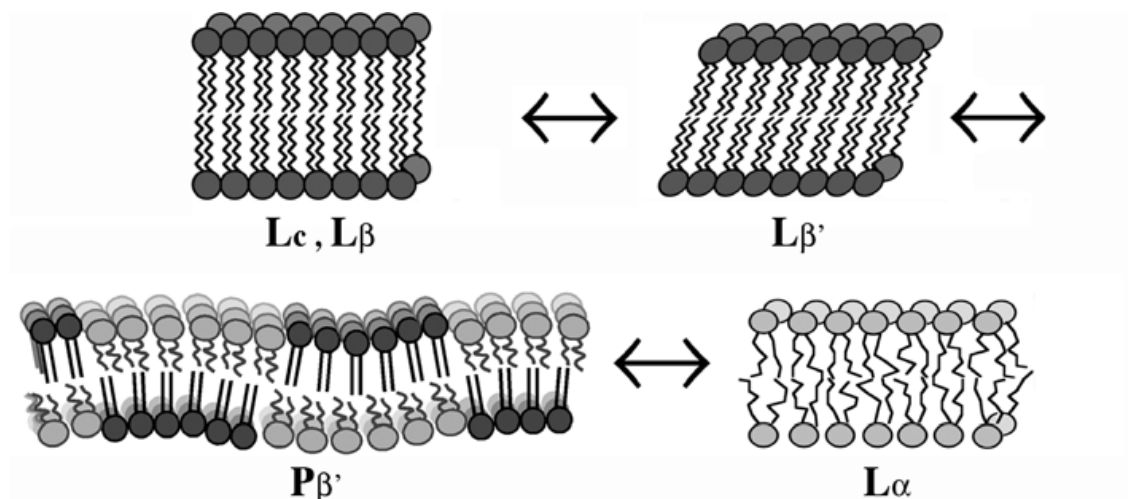


**Figure 1.11** Representation of the structures in lamellar phase: crystalline phase  $L_\beta$  or  $L_c$ , ordered or gel phase  $L_{\beta'}$ , ripple phase  $P_{\beta'}$  and disordered or fluid phase  $L_\alpha$  (from Heimburg, 2007).

Going from the  $L_{\beta'}$  to the  $L_\alpha$  phase, the interfacial area per molecule (area/lipid) expands by 15–30%, volume, packing density and fluidity of the bilayer also increase, the thickness decreases, and the lipid molecules undergo a series of motions including:

*gauche-trans* isomerizations, axial rotation, *out-of-plane* deformation, and lateral diffusion (Peterson and Chan, 1977; Brown et al., 1983; Rommel et al., 1988; Speyer et al., 1989).

Before the occurrence of the complete transition, another structure is observed, the ripple phase  $P_{\beta}$ , in which the surface of the bilayer presents an undulated topology (Tardieu, 1973). These ripples are probably due to the coexistence of gel and fluid lipid domains (Heimburg, 2000), so the lipid chains result partially “melted” and the overall phase show a lower average degree of order compared to the gel phase.

#### **1.4 MEMBRANE MODELS AS AN INVESTIGATIVE RESOURCE**

From the above discussion, it is clear that the study of phenomena involving the cell membrane is very complex and elaborate. For this reason, to explain the structure and dynamics of these systems, membrane models, that simulate some conditions that are found in biological membranes, have been used.

Membrane models present the advantage that they can be specifically composed: they can be composed of specific lipid mixtures, and that means that systematically varying the membrane composition, different interactions can be discovered explaining, for example, for the membrane segregation, or a specific protein can be inserted into the membrane to study its specific function (Walde et al., 2010).

Three essential steps are necessary in building a membrane model: chemical synthesis or isolation of a given lipid, construction of an appropriate model system containing the lipid and, eventually, subsequent incorporation of a particular protein. In doing so, specific membrane models can be developed to clearly characterize the properties of individual lipid components and membranes.

Figure 1.12 shows different membrane model structures obtained by self-organization of amphiphilic molecules. These structures include monolayers at air-water interface, supported monolayers, and bilayers.

In particular, *bilayers* can have planar or spherical shape. The aqueous compartments on both sides provide the opportunity to study the transmembrane movement of molecules and the electrical properties of membranes. Spherical shaped bilayers, also called vesicles or liposomes (in this last case their membrane is composed of lipids present in

biological membranes; Walde et al., 2010), are particularly useful not only for mimicking biological membranes, but because of their closed structure, they are able to reproduce the typical internal-external compartmentalization of biological cells. In this sense, they represent the biological model for excellence.

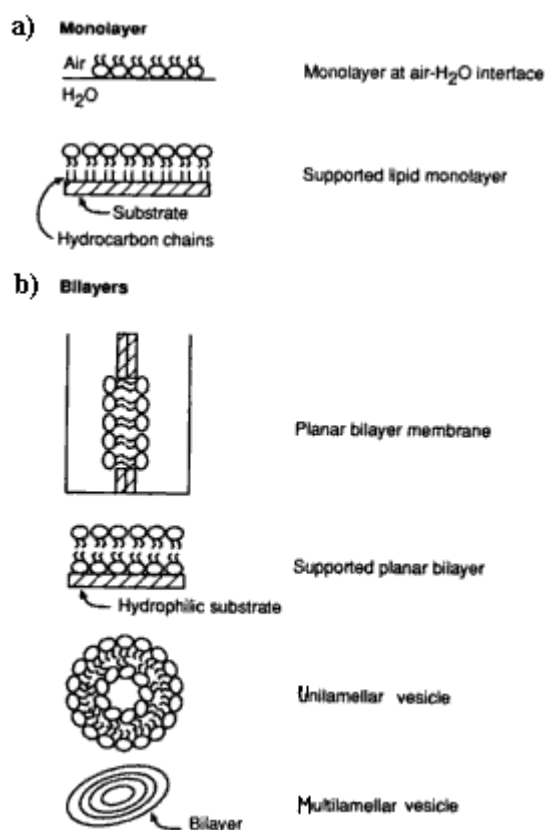


**Figure 1.12** Biological model structures. a) monolayers, b) bilayers. Both monolayers and bilayers are useful models of biological membranes.

Vesicles can vary in size and lamellarity.

*Multilamellar vesicles (MLVs)*, are composed of concentric multi-bilayer structures, very similar to the concentric layers of an onion, that are interdispersed by thin aqueous layers. They are formed by direct hydration of a lipid film by mechanical agitation, such as mixing with the *vortex*. Their use is limited to physical studies about the organization of the double layer, because only about 10% of lipids is concentrated on the outer layer of a *MLV*.

From *MLVs*, *small unilamellar vesicles (SUVs)* can be obtained by ultrasonic irradiation. They are vesicles whose walls have a single lamella and whose diameter does not exceed



100 nm. Even though they present the advantage of being unilamellar, their use is limited because of their small diameter, and therefore a surface curvature not comparable with those of biomembranes.

A more suited model for investigations are *large unilamellar vesicles (LUVs)*, whose diameter can range between 100 nm and 1  $\mu\text{m}$ . These vesicles, having diameters comparable to those of biomembranes, show certainly membrane properties that are closer to those of the real systems than *MLVs* or *SUVs*.

In recent years, much attention has been given to the *giant unilamellar vesicles (GUVs)*. They are even more interesting model systems than *LUVs*, as they have the same size of a biological cell (their diameter can range from 1 to more than 100  $\mu\text{m}$ ), so they represent a real suitable biomimetic system. Due to their large size, *GUVs* better reflect the curvature of the biological membrane and in this context, it has been thought that their size can lead to the identification of new chemical and physical properties not found in *SUVs* and *LUVs*, regarding, for example, the permeability of bio-molecules and macromolecules (Fischer et al., 2000).

Moreover, their large size makes possible the injection of chemicals in the aqueous interior, through the use of special techniques of micromanipulation, so they can be made gradually more complex to better mimic real biological cells. In addition, due to their big size, *GUVs* can be observed by light microscopy, while conventional vesicles need an electron microscope. A detailed description of preparation methods and investigation techniques employed in this work will be given in Chapter 3. The study of membrane models is then useful to understand the properties and the working mechanisms of the living cell membranes. A good overview on the topic can be found in Walde (2002) and Walde et al. (2010).

## **1.5 PHASE TRANSITION IN LIPID MEMBRANE**

Lipid membranes undergo order or melting transitions. For biological membranes this can happen near the growth or body temperature (10-25  $^{\circ}\text{C}$ ).

Many techniques, including differential scanning calorimetry (DSC) or spectroscopic methods as nuclear magnetic resonance, can be used to measure the temperature at which such transitions occur.

In the melting process, the molecules absorb heat (enthalpy) and the entropy increases due to the increase in the number of possible chain configurations. The melting processes is cooperative, meaning that the lipids do not melt independently of each other. The absorption of heat is typically monitored by measuring the heat capacity, that is the amount of heat absorbed per degree temperature increase. The heat capacity at constant pressure is defined by

$$C_p = (dH=dT)_p \quad (1.1)$$

It is shown in Figure 1.13, where at the melting temperature,  $T_m$ , it displays a pronounced maximum.

At low temperatures lipids are in the gel phase, presenting an ordered triangular lattice and chains that are mainly in a all-trans configuration. This phase is also called solid-ordered phase,  $s_o$ . At high temperatures the system undergoes a transition to a fluid phase, also called liquid-disordered phase,  $l_d$ , as there is not any order neither in the lattice nor in the chains with many *gauche-trans* isomerizations (Heimburg, 2007; Figure 1.13).

This transition takes place into the membrane plane, but other transitions may occur involving the third dimension because of some changes in the curvature of the bilayer. Such transitions are particularly important close to the melting regime, because in this regime many membrane properties are amplified.

One example is the pretransition of membranes, that occurs a few degrees below the main transition and show a low cooperativity of the lipids. Between the pretransition and the main transition, the ripple phase appears (Figure 1.13).

Size, charge, and the ability to form hydrogen bonds of polar heads, determine the intermolecular lipid-lipid interactions that are reflected in the packing density of lipids and in the transition temperature of lipid membranes from gel to liquid crystalline phase.

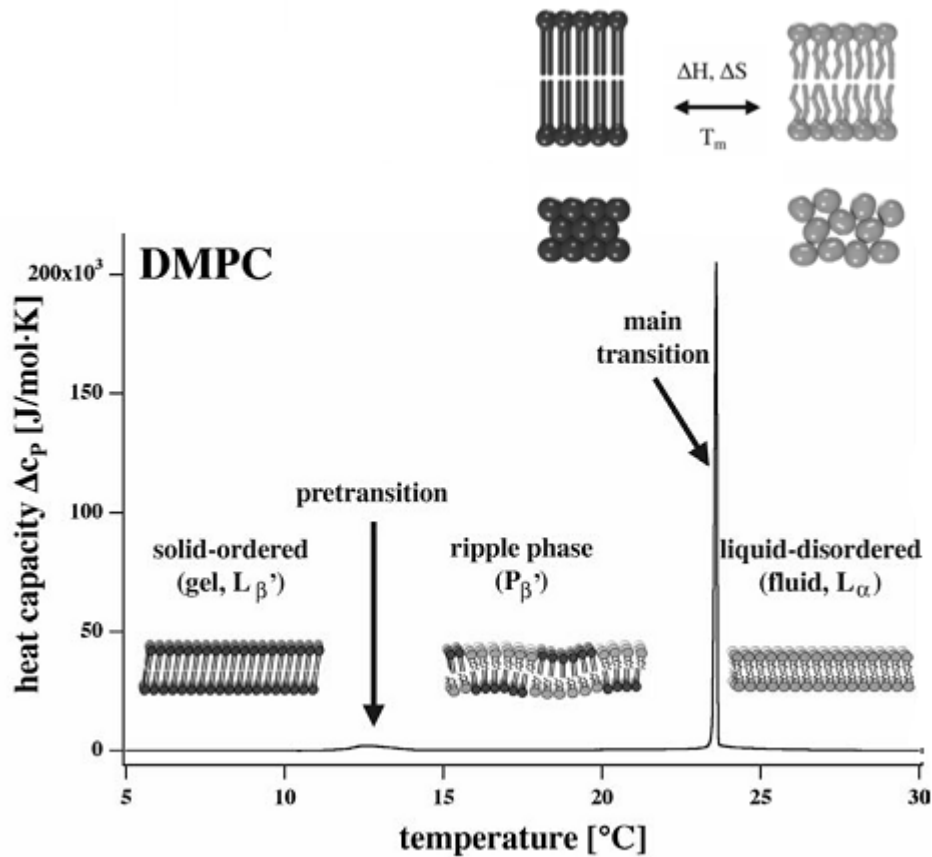


**Figure 1.13** Calorimetric melting profile of dimyristoyl phosphatidylcholine (DMPC). The melting curve displays two peaks called pretransition ( $T_p$ ) and main transition ( $T_m$ ). Below the pretransition one finds the solid-ordered phase (gel phase), between pretransition and main transition the ripple phase is found (see the text). Above the main transition one finds the liquid-disordered state (fluid phase). The ripple phase most likely is an intermediate between the gel and fluid phase. A schematic picture of lipid melting from a solid-ordered to a liquid-disordered phase is also shown. Top: The order within the lipid chains is lost upon melting. Bottom: The crystalline order of the lipid head groups is also lost and the matrix undergoes a solid–liquid transition (adapted from Heimburg, 2007).

Also the chain length and insaturation affects the order transition process: increasing chain length induces an increase of the melting temperature, as is clearly illustrated in Figure 1.14, where  $T_m$  values as a function of the chain length are reported for different phosphatidylcholines (Heimburg, 2007).

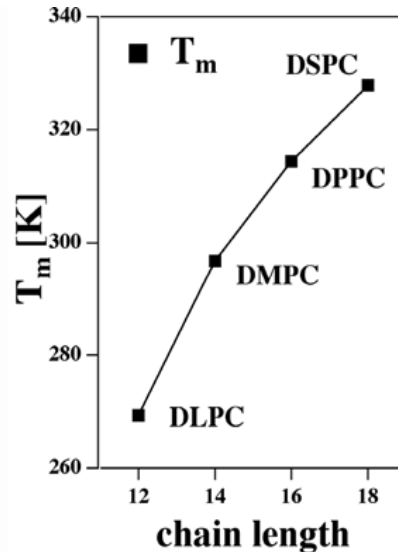


**Figure 1.14** Melting temperature,  $T_m$ , as a function of the chain length (adapted from Heimburg, 2007).

Lipid melting occurs in a very narrow temperature regime and this is significant of some cooperative events that lead to cluster and domain formation. Then, the knowledge of gel-liquid crystal phase transitions is of great importance for the understanding of the formation of lipid domains discussed above (section 1.1).

Below, in Figure 1.15, an example of a phase diagram for the water-dimyristoylphosphatidylcholine (DMPC) system is illustrated.

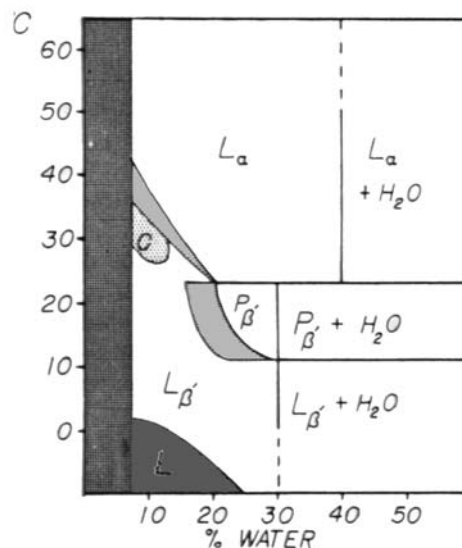


**Figure 1.15** Phase diagram for the water-dimyristoylphosphatidylcholine (DMPC) system.

## 1.6 MEMBRANE FLUIDITY

### 1.6.1 Headgroups and water dipoles as probes.

Membrane fluidity is related to the viscosity of the membrane that a probe experiences when moving in the lipid bilayer. Different techniques can be used to test such molecular motions like NMR (Bloom et al., 1991) or ESR spectroscopy (Marsh, 1981). These techniques measure either the time-averaged orientation of the probe with respect to the bilayer director (the order parameter  $S$ ) or a relaxation time after disturbance.

Another technique recently introduced is paraelectric spectroscopy which is based on the relaxation of permanent dipoles under the excitation of an oscillating external electric field. Hydrated lipid bilayers represent a composite dipole system because both the polar headgroups of lipids and bound water molecules (without which the bilayer would not exist) have permanent dipoles and constitute an intrinsic probe for measuring electrical features as the dipole density and the dipole mobility of the membrane surface in the radio frequency range (1-1000 MHz). Headgroup dipoles seem to respond uniformly to the external excitation which means that the average surroundings are the same for all headgroups. On the other hand the hydration water consists of dipoles whose response could best be described by an exponentially decaying distribution of relaxation frequencies.

The rotation of the headgroup dipole moment senses modifications in the molecular packing within the bilayer because of the difference between the molecular area and the chain cross section (see Figure 1.4). Temperature dependant relaxation frequency measurements (Klöggen et al., 1996) have shown that polar headgroup and hydration water dipoles exhibit a slow continuous increase of the relaxation frequencies with increasing temperature. This trend for the headgroup mobilities is caused by the temperature dependant decrease of the packing density within the bilayer and the reduction of ambient friction in the water that the headgroup dipoles experience during their rotations. This increase is interrupted by a small pronounced jump when the membranes undergo a cooperative transition into a new conformation with an altered packing density. This is the case for DMPC bilayer at  $T_m = 23^\circ\text{C}$  where the membranes pass from the gel to the fluid transition.

### 1.6.2 Diffusion of lipids in membranes.

Lipids inside membranes can undergo different diffusion processes, the diffusion coefficients depending on the lipid nature (Figure 1.16):

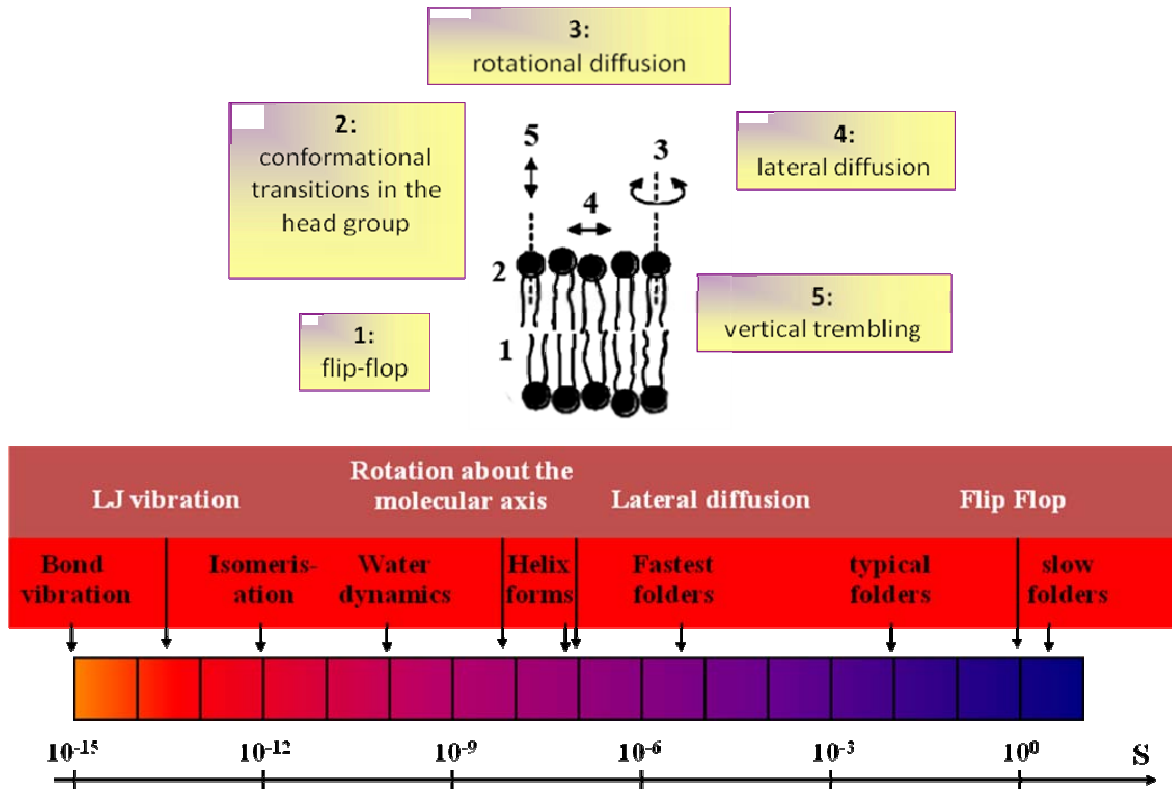


**Figure 1.16** Different diffusion process and relative times.

Above their transition temperature  $T_m$ , lipids can freely move inside the membrane plane and the lateral diffusion coefficient is very fast ( $\sim 7 \times 10^{-8} \text{ cm}^2/\text{s}$ ; Saxton and Jacobson, 1997; Haustein and Schwille, 2007).

Flip-flop processes, on the contrary, are quite slow because the transfer of lipids between the two leaflets would mean that the polar head group has to go across the hydrophobic region. So, generally this event takes a long time (even hours), but it results faster for lysolipids (having only one chain). Moreover, Raphael et al. (2001), have demonstrated that in case of density equilibration between the two leaflets of the bilayer (as in the case of area relaxation processes that follow vesicle shape changes), the relaxation is considerably faster, by assuming the possibility of a convective flow of lipids via transient pores.

In biological membranes, this process can be accelerated by some proteins present in membrane called flippases (Smith and E. Oldfield, 1984).

Lipids can also exchange between different vesicles, as in the case of LUVs. The exchange can occur:

- *via* free monomers, and the process is called Ostwald ripening (Madani and Kaler, 1990; see also section 5.1 for more details).
- *via* vesicle collisions. This process is often followed by aggregation and fusion phenomena (Armengol and Estelrich, 1995).

## 1.7 CURVATURE, ELASTIC CONSTANTS AND FLUCTUATIONS

Membranes are typically not flat rigid sheets but often display curvature when they form vesicles and organelles. They are soft and display both fluctuations in area and curvature. Further, when membranes are asymmetric they may curve spontaneously.

### 1.7.1 Elastic constants and curvature.

Many membrane properties depend on the elastic constants of the bilayer. Therefore their measurements can give information on cell functions and lead to vesicle optimization for several applications.

On a mesoscopic level, membranes can be described by the geometric properties and physics of elastic fluids. Classical descriptions have been given by Canham (1970), Helfrich (1973), and Evans (1974 and 1981). The elastic energy results from three deformation modes: a) compression-extension mode, b) shear mode, and c) curvature mode. All deformations can be formed from a combination of these three basic deformations (Figure 1.17):

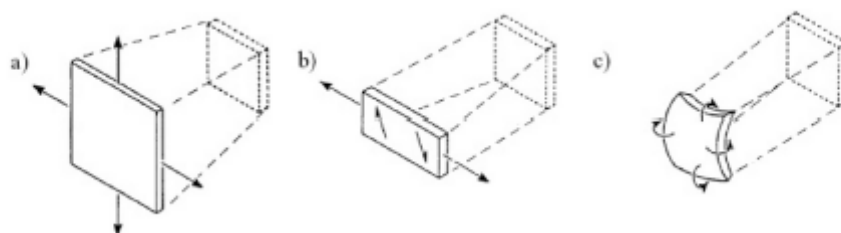


**Figure 1.17** The three possible deformation modes: a) compression-extension mode, b) shear mode, and c) curvature mode. From Bloom et al. (1991).

- The compression-extension mode, is an elastic deformation characterized by a compression modulus,  $\chi$  (in J/m<sup>2</sup>) (Figure 1.17a).

The associated energy per surface,  $H_{ext}$ , depends quadratically on the variation of the surface area,

$$H_{ext} = \frac{1}{2} \chi \left( \frac{\Delta A}{A} \right)^2 \quad (1.2)$$

where  $\chi$ , the compression modulus, is about 0.2 J /m<sup>2</sup> for vesicles, as estimated by micropipette aspiration technique (Olbrich et al., 2000; Puech et al., 2003) and  $\Delta A/A$  is the relative variation of the surface area associated with the deformation.

This variation never exceeds 8 % as beyond this point, pores open and the vesicle lyses at a critical tension around 10<sup>-3</sup>N/m.

- The shear mode is a deformation in the plane of the membrane at constant area (Figure 1.17b). The associated energy per unit surface area,  $H_{shear}$ , is obtained from Hooke's law and gives:

$$H_{shear} = \frac{1}{2} \mu (\lambda^2 + \lambda^{-2} - 2) \quad (1.3)$$

where  $\lambda = (L_0 + \Delta L)/L_0$  is the lateral extension rate and  $\mu$  the shear modulus. In the case of fluid membranes, the energy is negligible: with constant area, the lipids can diffuse freely and do not resist shearing. This deformation becomes important however in the case of more complex systems such as when the membrane is associated with the cytoskeleton.

- The curvature term combines all deformations which are not in the plane of the membrane or which do not occur on a constant surface (Figure 1.17c). It is the dominant deformation of the three:

$$H_{curv} = \frac{1}{2} \kappa (c_1 + c_2 + c_0)^2 + \kappa_G c_1 c_2 \quad (1.4)$$



where  $c_1 = 1/R_1$ , and  $c_2 = 1/R_2$  are the principal curvatures of the membrane, and  $R_1$ ,  $R_2$  are the two principal radii in perpendicular direction.  $c_0$  is the spontaneous curvature, that is the local curvature of the membrane without mechanical constraint. This term corresponds to a possible asymmetry of the membrane due to differences in the lipid composition in the two leaflets of the membrane. The product  $c_1c_2$  is the Gaussian curvature. The Gauss-Bonnet theorem shows that the integrated product over the surface of the vesicle is a topological invariant. Deformations applied to the surface of the vesicle generally do not alter the topology. Therefore, the term characterized by the Gaussian curvature  $\kappa_G$  is frequently neglected.  $\kappa$  is the bending rigidity modulus of the curvature. It depends on the temperature and the composition of the membrane. Numerous techniques to measure this modulus exist, such as by Fourier analysis of the vesicle shape (Peterson et al., 1992; Pécrciaux et al., 2004; Méléard et al., 1992; Kummrow et al., 1991).

Other methods study the elastic behavior of the membrane after mechanical deformation by electrical field (Bacri et al., 1996) or by micropipette aspiration (Olbrich et al., 2000).

The energy associated with the integrated curvature over the whole membrane is given by the following hamiltonian (Helfrich, 1973; Evans, 1974):

$$H = \oint H_{curv} dA = \oint \left( \frac{1}{2} \kappa (c_1 + c_2 + c_0)^2 \right) dA \quad (1.5)$$

To this hamiltonian additional corrections were later added to take into account the asymmetry of the bilayer and its thickness. However, this hamiltonian does not allow for the existence of structure within a bilayer, nor the fact that two monolayers can have two different surface areas, which could induce an additional curvature (Döbereiner, 2000). These effects will be discussed below together with the area difference elasticity model (ADE) (Sackmann, 1994).

Some typical values for the compression modulus, the shear modulus, and the curvature modulus of biological materials are given in Table 1.3 and compared to standard materials.

**Table 1.3** Some typical values for the compression modulus, the shear modulus, and the curvature modulus.

Material	Compression Modulus $\chi$ (J/m <sup>2</sup> )	Shear Modulus $\mu$ (J/m <sup>2</sup> )	Curvature Modulus $\kappa$ (J)
Red blood cell	10 <sup>-5</sup>	6 x 10 <sup>-6</sup>	2-70 x 10 <sup>-20</sup>
Lipid bilayer	100-700 x 10 <sup>-3</sup>	0	4-40 x 10 <sup>-20</sup>

- The lateral tension,  $\sigma$ , is an intensive parameter associated with the vesicle area,  $\sigma = \partial F / \partial A$  where  $F$  is the free energy of the membrane. Two regimes can be defined as a function of the extension: the enthalpic and the entropic regime. The enthalpic regime corresponds to large extensions whereas the entropic regime corresponds to small extensions.

In the enthalpic regime, the membrane has already undergone a large extension, and so further stretching increases the average surface area per lipid. When the membrane is expanded, its area increases with  $\Delta A$ , which increases the elastic term,  $H_{ext}$ . If the shear mode is neglected, the elastic energy per surface area can be written as follows:

$$H = H_{ext} + H_{curv} = \frac{1}{2} \chi \left( \frac{\Delta A}{A} \right)^2 + \frac{1}{2} \kappa (c_1 + c_2 + c_0)^2 + \kappa_G c_1 c_2 \quad (1.6)$$

The total elastic energy of the membrane is therefore  $HA$ . The tension is then

$$\sigma = \frac{\delta(HA)}{\delta(\Delta A)} \quad (1.7)$$

### 1.7.2 Membrane fluctuations.

The origin of this tension is enthalpic. However, this equation is only valid for tensed membranes (Figure 1.18 b), when vesicle area and projected area are equal (Figure 1.18c).

Experimentally, vesicles are often not tensed and can then undergo large thermal fluctuations because of their low bending modulus  $\kappa$  (Figure 1.18a).

The concept of “fluctuation” is very important in biology. The most relevant phase in lipid bilayers, the fluid phase, is the one with the largest fluctuations.

At a molecular level, local fluctuations can affect passive permeability of solutes through the membrane or help proteins in their functions reducing the activation energy of the process (Nagle and Tristram-Nagle, 2000).

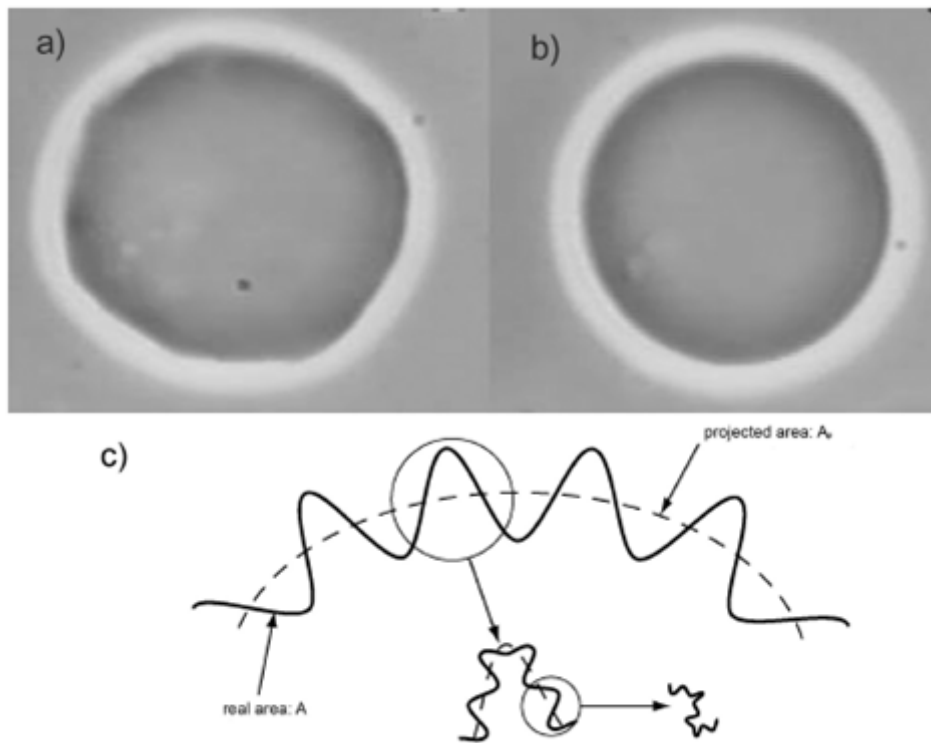


**Figure 1.18** GUV under light microscope a) Floppy vesicle: The membrane fluctuations are optically visible. b) Tensed vesicle: The vesicle appears perfectly round and no fluctuations are optically detected. c) Schematic representation of a fluctuating membrane.  $A$  represents the real area, while  $A_p$  represents the projected area. (Helfrich, 1984).

If considered to a mesoscopic level, fluctuations can be adaptive for cell shape changes and give rise to an additional forces between membranes.

In aqueous solution, collisions with water molecules make the membrane fluctuate around an average position. Hence, the observed area (e.g. by microscopy) does not correspond to the real surface of the vesicle.

The higher the difference between projected and real area is, the more the vesicle fluctuates and the lower its membrane tension is.

In the general case, it was shown experimentally (Olbrich et al., 2000) and theoretically (Wintz et al., 1996) that the area excess  $\Delta A/A$  can be expressed as a function of the membrane tension by adding the two contributions of the fluctuations (entropic, low

stretching regime) and the elasticity (enthalpic, high stretching form). The variation of the surface excess area  $\Delta A/A$  between an initial state with zero tension and a final state with a tension  $\sigma$ ,  $\Delta\alpha = \alpha_0 - \alpha$ , results from both the flattening of membrane fluctuations and the extension of the membrane (Olbrich et al., 2000):

$$\Delta\alpha = \frac{k_B T}{8\pi\kappa} \ln(1 + cA\sigma) + \frac{\sigma}{\chi} \quad (1.8)$$

where  $c = 1/24\pi$  and  $A$  is the area of the vesicle (if we suppose that area and volume remain constant).

## **1.8 TEMPERATURE DEPENDENCE OF MEMBRANE PHYSICAL PROPERTIES**

Besides changes in enthalpy and entropy, phase transition also results in an increase of lipid area of about 25% and an increase of the membrane volume of about 4% and this an effect on many physical properties.

For example, it has been shown by Heimburg (1998) and Ebel et al. (2001) that the elastic constants all depend in a simple manner on the heat capacity of the membrane that assumes high values in the transitions of membranes (see Figure. 1.13). This means that within transitions, elastic constants assume high values too and membranes are very elastic. They are soft, easy to bend and easy to compress.

Everything that is related to the elastic constants will respond very sensitively to changes in temperature and other variables like pH, calcium content etc. especially near transition points. This can explain many properties of lipid bilayers.

As an example, the hydrophobic core of lipid membranes should neglect polar molecules to cross the membrane – this is the case for ions and big molecules (that usually cross the membrane thanks to protein channels) – nonetheless pure lipid membranes exhibit a high permeability for water molecules (Finkelstein, 1987; see also section 5.3 for a detailed description of permeability in membranes).

In fact, lipid layers are very thin and due to fluctuations in the membrane there is always some finite likelihood that spontaneous pores are formed; pore formation is a function of

the lateral compressibility and therefore this likelihood is dramatically increased in the phase transition temperature regime of lipid membranes where the compressibility is high, explaining for the enhanced membrane permeability close to  $T_m$ .

Since biological membranes display such transitions close to body or growth temperature, this is of quite high significance (Papahadjopoulos et al., 1973; Nagle and Scott, 1978). Figure 1.19 shows the permeability of artificial membranes for a fluorescence dye as a function of temperature compared to the heat capacity. One can recognize that the permeability is closely related to the heat capacity.

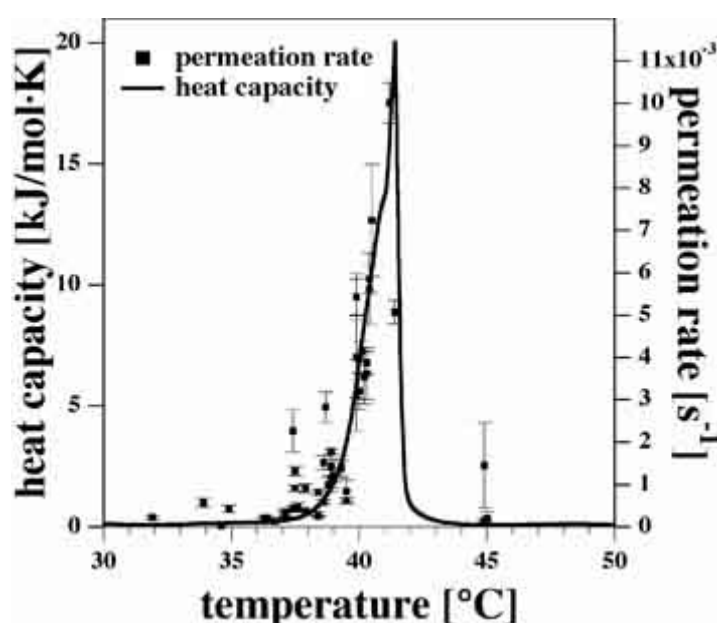


**Figure 1.19** Permeability of a lipid vesicles for a fluorescent dye as a function of temperature compared to the melting profile (Blicher et al., 2009).

## 1.9 VESICLE SHAPE

### 1.9.1 The ADE model.

The different shapes observed changing external conditions as osmotic pressure or temperature, are due to a search of the system for the lowest free energy.

For symmetrical membranes, in which the two monolayers are the same, the flat conformation has the minimum free energy, but for closed vesicles, that cannot be flat, the lowest energy is related to the physical properties of the the bilayer. The shape of the vesicles can be obtained by minimizing their bending energy and considering a non local

elasticity model  $\bar{\kappa}$  (Döbereiner, 2000) that accounts for the asymmetry between the two leaflets, due to the fact that the inner leaflet is more compressed than the external one, and to the different numbers of molecules  $N^+$  and  $N^-$  in the outer and inner monolayer, that leads to a preferred area difference  $\Delta A_0 = (N^+ - N^-) a_0$ , being  $a_0$  the area per lipid molecule, between the two monolayers. This is the so called Area Difference Elasticity model (ADE) model.

The obtained phase diagram depends on three parameters:

1) the dimensionless volume which describes the swelling state of the vesicle:

$$v = \frac{V}{\left(\frac{4}{3}\right)\pi\left(\frac{A}{4\pi}\right)^{\frac{3}{2}}}. \text{The denominator would be the volume of the vesicle if it were}$$

spherical.

2) the ratio between the two elastic moduli  $q = \bar{\kappa} / \kappa$  (Heinrich et al., 1993).

3) The dimensionless area difference between the two leaflets:  $\Delta a_0 = \frac{\Delta A_0}{8\pi d \left(\frac{A}{4\pi}\right)^{3/2}}$

Figure 1.20a shows a phase diagram resulting from varying only parameters,  $v$  and  $\bar{\Delta a}_0$ . This last is the dimensionless effective area between the two leaflets given by the sum of spontaneous and area difference curvature  $\bar{\Delta a}_0 = \Delta a_0 + (1/2\pi q)c_0$ .

For a physical interpretation of the phase diagram one has to relate the above variables to physical observables. One of this is the temperature.

An increase in temperature from an initial value  $T_0$  leads to a thermal expansion of the area of the two monolayers. The expansion coefficients of the two monolayers can be different, then an asymmetric factor  $\gamma$  has to be introduced. Even a very small asymmetry can have considerable influence on the temperature trajectory. The physical reason is that shape changes not only depend on the absolute change in area, but also on the variation in the area difference between monolayers: if the outer monolayer expands more than the inner one, budding formation can be observed; on the contrary a more relevant increase in the inner monolayer induces discocytes-to-stomatocytes transition.

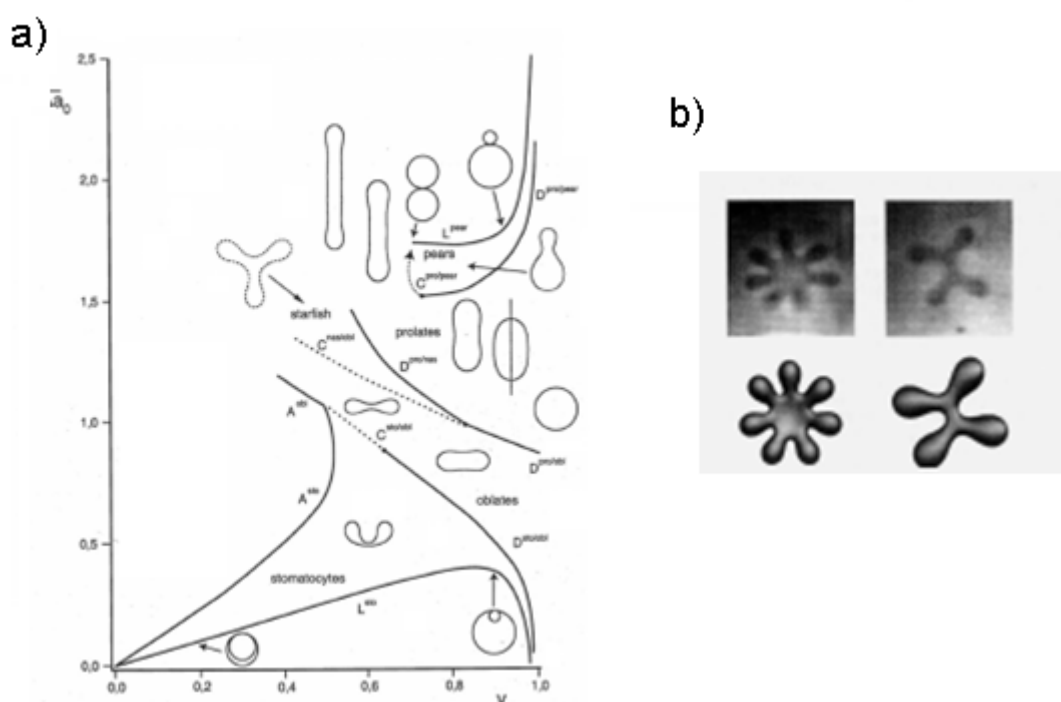


**Figura 1.20** a) Phase diagram of possible vesicle shapes in the ADE model, parameters are the reduced volume  $v$  and the area difference between the two leaflets  $\overline{\Delta a_0}$ . From (Sackmann, 1994). b) Starfish-shaped vesicle. From (Lipowsky and E. Sackmann, 1995).

So far many of the temperature transitions observed experimentally are not explainable by theory. This is the case for example of temperature-induced budding, where has been observed that a temperature increase leads continuously to a pear with a weak up-down asymmetry and then to a vesiculated shape (Lipowsky and E. Sackmann, 1995). Such a discrepancy could be explained by the presence of metastable shapes due to the long relaxation times near an instability for long-wave length bending fluctuations. The decay of this metastable shape occurs as soon as the energy barrier becomes comparable to the thermal energy  $\kappa_B T$ .

### 1.9.2. Adhesion.

In adhesion phenomena two aspects have to be considered: the macroscopic, i.e. involving the whole shape, and the mesoscopic aspects, this last referring to fluctuations in the vicinity of the substrate.

**1.9.2.1 Macroscopic model.**

From a macroscopic point of view, adhesion can be considered adding an adhesion energy contribution  $F_a = -WA^*$  to the bending energy (Eq. 1.5), where  $A^*$  is the adhesion patch of the vesicle adhering to the substrate, and  $W$ , the contact potential, is defined as

$$W = \gamma(1 - \cos\theta) \quad (1.9)$$

Where  $\gamma$  is the membrane tension and  $\theta$  the contact angle. In principle, knowing the membrane tension and measuring the contact angle, the adhesion energy can then be deduced (Seifert and Lipowsky, 1990).

**1.9.2.2 Mesoscopic model.**

The mesoscopic model takes into account the thermal fluctuations of vesicles and all the forces involved in the vesicle-substrate interaction.

Such interaction forces are both attractive and repulsive forces (Van der Waals interaction energy, repulsive forces). Furthermore the contribution of thermal fluctuations has to be considered.

**1.9.2.3 Adhesion transition.**

Also for bound vesicles, as for free vesicles, a variety of shapes can be obtained and arranged in a phase diagram (Figure 1.21).

The most characteristic aspect of such a phase diagram is the line separating bound from free vesicles.

Experimentally, adhesion transition can be observed by changing the temperature. A temperature decrease induces also  $W$  to decrease. Therefore, a bound vesicle can become free upon cooling the system, providing an initial situation of the vesicle close to the adhesion transition.



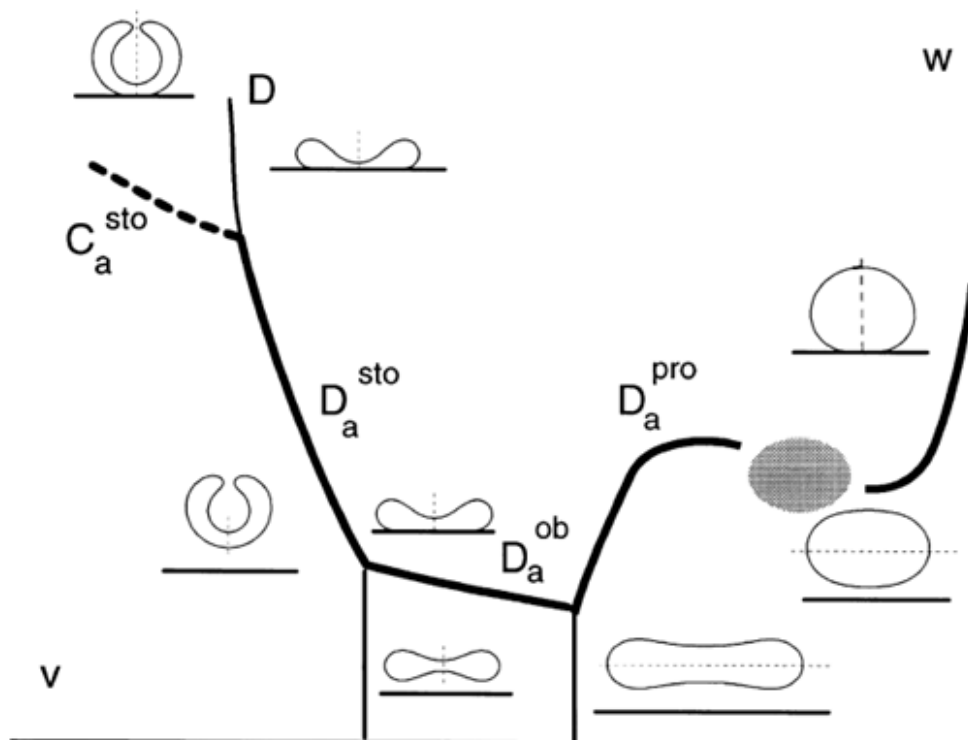


**Figure 1.21** Schematic phase diagram with free and bound shapes at constant area and volume. The heavy lines show the adhesion transition at  $W = W_a$ , which can be discontinuous ( $D_a^{pro}$ ,  $D_a^{ob}$  and  $D_a^{sto}$ ) or continuous ( $C_a^{sto}$ ). In the dashed region, non-axisymmetric bound shapes are relevant. The dashed straight lines across the shapes denotes the axis of symmetry (Lipowsky and Sackmann, 1995).

## **CHAPTER 2**

### **Interaction between millimeter waves and biological systems**

Pervasive use of electromagnetic waves in modern society has strong potential implications for human health. Wide-spread use of microwaves (MWs) in wireless communication have already stimulated interest in the scientific community and led scientists to the discovery of considerable effects at 2  $\mu\text{m}$  (150 THz) (Wells et al., 2005a; Wells et al., 2005b) and 333 mm (900 MHz) (Hillert et al., 2008; Wiholm et al., 2009).

Current studies are focusing on the extremely high frequency microwave region of the electromagnetic spectrum, that spans 30-300 GHz or wavelengths from 10 to 1 mm, and is formally designated as the millimeter-wave (MMW) band. The attention is devoted in particular to the 50-80 GHz sub band, due to its current applications in biomedicine (in the so called MMW therapy (Pakhomov et al., 1998; Rojavin and Ziskin, 1998; Pakhomov et al., 2000; Rojavin et al., 2000; Radzievsky et al., 2004) and its next use in wireless communication technologies (Marcus et al., 2005; Lawton, 2008, LeVine, 2009).

MMWs are strongly absorbed by dipole-oriented molecules, such as water and phospholipids (Enders and Nimitz, 1984; Liburdy and Magin, 1985; Cametti et al., 1988; Beneduci, 2008a; Ramundo-Orlando et al., 2009). At 60 GHz, a commonly utilized millimeter wave frequency, the absorption coefficient for water, tissue media, and skin tissue ranges from 50 to 55  $\text{cm}^{-1}$ , with almost all energy being absorbed within 0.4 mm (Zhadobov et al., 2008). This strong absorption has been exploited for more than a half century for simple heating of biological tissue, but MMWs may also produce more subtle effects at power levels well below the existing safe exposure limit of  $1\text{mW}/\text{cm}^2$  (ICNIRP, 1998; Chou and D'Andrea, 2005; Beneduci, 2008a).

In fact, numerous experimental studies have shown that MW may induce a variety of biological effects at low power densities that cannot arise from heating (Pakhomov et al., 1998; Ramundo-Orlando, 2010). A resonant-like or frequency-dependent interaction mechanism has been theoretically suggested (Fröhlich, 1988) and, in a few notable cases, observed experimentally (Pakhomov et al., 1998). Despite the evidence cited above, no conclusive experimental proofs demonstrate the nonthermal nature of the MW-induced effects. Two main intriguing and challenging questions are still unsolved. On the one hand, it is to be definitely established what biological structures are the site of interaction. On the other hand, the mechanisms on which the above nonthermal biological effects are based, must be provided. These two questions are strictly related.

In this chapter after an introduction on the fundamental aspects of the interaction of MMWs with matter, an overview from the earlier to the most recent state of the art will be given, in terms of the hypotheses of mechanism proposed and the biological effects observed up to now.

## 2.1 FUNDAMENTALS ON THE INTERACTION OF MILLIMETER WAVES WITH MATTER

Millimeter waves belong to the non-ionizing portion of the electromagnetic spectrum. At those frequencies, photons are not able either to alter intermolecular structure or to break any kind of intermolecular bond, in a single hitting process. In fact, the greatest quantum energy (300 GHz), is  $1.2 \cdot 10^{-3}$  eV, while the energy of the weakest hydrogen bond is 0.08 eV. The wavelengths are much longer than atomic or molecular structures, but comparable with those of biological object or electrical circuits. Basically, the interaction of radiofrequencies (RF) and microwaves (MW) with matter, can be said of two types: macroscopic and microscopic. Maxwell's equations, whose solutions describe the distribution of electric and magnetic fields within and out a given object, express a macroscopic interaction (Cheng, 1989).

### 2.1.1 The macroscopic model.

In the macroscopic theory of electromagnetic fields, the field within matter, is fully described by two vectors, the electric field vector  $\vec{E}$  and the magnetic field vector  $\vec{H}$ .

The macroscopic properties describing the interaction with the electromagnetic fields are expressed by the complex dielectric permittivity  $\hat{\epsilon}$  and complex magnetic permeability  $\hat{\mu}$ . Because biological systems are not magnetic materials, the complex permeability can be approximated to be unitary  $\hat{\mu}=1$ .

The permittivity defines the interaction of the electric field vector with matter and can be expressed as

$$\hat{\epsilon} = \epsilon' - j\epsilon'' \quad (2.1)$$

where  $\epsilon'$  is the dielectric constant and  $\epsilon''$  is the loss factor (Von Hippel, 1954).

The electric constant  $\epsilon'$  is a measure of the ability of a given medium, to store electric field energy. The loss factor  $\epsilon''$ , describes the portion of energy dissipated within the material.

The complex dielectric permittivity is a measure of how easy polarisable is a given material. The polarization per unit volume or electric dipole moment per unit volume,  $\vec{P}$ , of the material, is indeed proportional to the external electric field, through the relation

$$\vec{P} = [\hat{\epsilon}(\nu) - 1]\epsilon_0\vec{E} \quad (2.2)$$

The loss factor  $\epsilon''$  can be related to the conductivity of a given material,  $\sigma$ , by the following:

$$\epsilon'' = \frac{\sigma}{\omega\epsilon_0} \quad (2.3)$$

where  $\epsilon_0$  is the permittivity of the free space,  $\epsilon_0 = 8.85 * 10^{-12} F/m$  and  $\omega = 2\pi\nu$  is the angular frequency of the radiation.

Materials can be basically divided into two groups, depending on the values of conductivity and dielectric constant, namely conductors and dielectrics.

A perfect conductor is the one exhibiting an infinitive conductivity value,  $\sigma = \infty$ .

Similarly, a perfect dielectric has a zero conductivity value,  $\sigma = 0$ , then is lossless and the propagation of electromagnetic waves through it, occurs without attenuation. Free space is a perfect dielectric. Non perfect dielectrics satisfy the condition:  $\sigma < \omega\epsilon_0$ . The electromagnetic waves propagating through a non perfect dielectric are attenuated at a rate depending on permittivity, and they are often referred as lossy dielectrics. Biological materials belong to this group.

### **2.1.2 Reflection and transmission of a wave at the boundary between two media.**

Let's describe the general case of interaction, in which the biological system is formed by stratified layers of different materials and the MMW impinges onto the interface that separates the generic layers of media  $i$  and  $j$ , at a generic angle of incidence  $\vartheta$ . Let's

assume that the wave is planar, the dimensions of the system are large compared to the wavelength of the radiation and that the interface is planar, too. Let the generic media  $i$  and  $j$ , be characterized by different dielectric material properties, respectively indicated by  $\hat{\epsilon}_i$  and  $\hat{\epsilon}_j$ . Two phenomena arise at this interface: 1. the wave will be reflected at an angle of reflection  $\vartheta$ ; 2. the wave will be transmitted at an angle of transmission that is prescribed by the Snell's law (Figure 2.1):

$$\frac{\sin \vartheta}{\sin \varphi} = \frac{\sqrt{\hat{\epsilon}_i}}{\sqrt{\hat{\epsilon}_j}} \quad (2.4)$$

Depending on the properties of the system, the electromagnetic energy of the transmitted wave can be variably absorbed. Eventually, a biological effect could arise if the energy absorbed is used by the system to perturb some of its functional properties. For this reason, it is important to consider how does the millimeter radiation, propagates into a system.

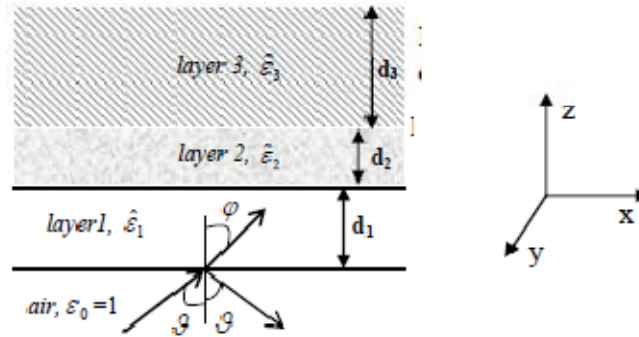


**Figure 2.1** Plane millimeter wave propagating through air that impinges at angle  $\vartheta$  on a three-layered system. The scheme shows what happens at the first interface air/layer 1. The transmitted wave at angle  $\varphi$  propagates into layer 1 until it will be partly reflected and partly transmitted at the 2nd interface between layer 1 and 2 and so on for the third interface (not shown) (from Beneduci, 2008a).

### 2.1.3 Propagation of waves within matter.

A wave passing through a lossless material travels at a speed  $v$  given by the following:

$$v = \frac{1}{\sqrt{\epsilon\mu}} = \frac{1}{\sqrt{\epsilon_0\mu_0} * \sqrt{\epsilon_r\mu_r}} = \frac{c}{\sqrt{\epsilon_r\mu_r}} \quad (2.5)$$

The ratio, speed light through the vacuum over speed light trough a transparent material, is called refraction index  $n$  and it is given by:

$$n = \left( \frac{c}{v} \right) = \sqrt{\epsilon_r \mu_r} \cong \sqrt{\epsilon_r} \quad (\mu_r = 1 \text{ in perfect dielectrics}) \quad (2.6)$$

Since  $\epsilon_r$  is a complex quantity, also  $n$  is correctly described by a complex expression:

$$n = n_1 - jn_2 \quad (2.7)$$

In this case, the real part,  $n_1$  is the ratio of the velocity of the waves propagating through the two media. The imaginary portion  $n_2$ , represents the absorption of the waves in the media. As already mentioned, the velocity of a wave travelling through a medium, depends also on the wavelength of the radiation  $\lambda$ , then also the refraction index will depend on  $\lambda$ .

To clarify the meaning of the real and imaginary part of the refraction index, let us suppose an electromagnetic wave, a plane wave to simplify, propagating in the  $x$  direction of a Cartesian reference frame, in a material with refraction index given by Eq. (2.8), then

$$\vec{E} = \vec{E}_0 e^{j\omega(t - \frac{x}{v})} = \vec{E}_0 e^{j\omega(t - \frac{nx}{c})} = \vec{E}_0 e^{j\omega \left[ t - (n_1 - jn_2) \frac{x}{c} \right]} = \vec{E}_0 e^{-\frac{\omega n_2 x}{c}} e^{j\omega(t - n_1 \frac{x}{c})} \quad (2.8)$$

The latter equation represents a wave propagating in the  $x$  direction at a velocity  $v = \frac{c}{n_1}$ , whose amplitude  $\vec{E}_0'$ , is exponentially attenuated along the propagating axis by a quantity:

$$\vec{E}_0' = \vec{E}_0 e^{-\frac{\omega n_2 x}{c}} \quad (2.9)$$

The quantity  $\frac{\omega n_2}{c}$  is called *absorbition coefficient* of the given material, related to electromagnetic waves having pulsation  $\omega$ . Its reciprocal  $\delta = \frac{c}{\omega n_2}$ , which has a length dimensions, is called *depth of penetration* or *attenuation path*, representing the way to be done by the wave, in order to have its own amplitude reduced by  $\frac{1}{e}$  with respect to the initial one.

Equation (2.9) prescribes that the attenuation of the amplitude of the radiation is proportional to the frequency and to the conductivity of the material. Furthermore, for two systems having different dielectric properties at a given frequency, the greater is the value of the imaginary part of the complex refractive index of the material, the smaller is the penetration depth. Equivalently, the radiation at frequency  $\nu$ , penetrates less in those materials that have large dielectric loss factor and then, large conductivity. Then, we can speak about low- and high-loss dielectric materials.

As a valuable case, let us consider the dielectric properties of water, methanol, ethanol and propanol, at 70 GHz and at 25°C, reported in Table 2.1.

As can be seen, the penetration depths of the 70 GHz millimeter radiation into these systems are very different. Water is the liquid possessing the highest dielectric loss (most dispersive) and accordingly, at this frequency, the penetration depth is the lowest in this medium. One can easily estimate that, when the 70 GHz wave has travelled a path equal to  $3\delta$  ( $< 1$  mm) in pure water, its amplitude will be reduced by about 95% its initial value.

**Table 2.1** Dielectric properties of water and some lower alcohols at 70 GHz and at 20°C (adapted from Beneduci, 2008a)

	$\epsilon'$	$\epsilon''$	$\kappa$	$\delta$ (mm)	$\tau_D$ (ps)	$\Delta\epsilon$
H <sub>2</sub> O	9.93	17.56	2.26	0.30	8.26	72.3
CH <sub>3</sub> OH	4.63	2.39	0.54	1.26	51.5	26.6
CH <sub>3</sub> CH <sub>2</sub> OH	3.47	0.98	0.26	2.62	163	19.8
CH <sub>3</sub> CH <sub>2</sub> CH <sub>2</sub> OH	3.00	0.80	0.19	3.60	329	16.7

#### 2.1.4 Electrical Properties of Biological Materials in MMWs range.

Biological materials, from the point of view of the interactions with electromagnetic fields, are lossy dielectrics (Grant, 1983). Their permeability,  $\mu$ , is equal to that of free



space. Their permittivity is complex, at frequencies above a few tens of KHz scalar, and varies depending on the materials composition, temperature and field frequency.

The dielectric properties are greatly influenced by water, which has a prominent role for biological systems. It governs for example, the formation of all the membranes by interacting with the polar head group of the phospholipids. It stabilizes the polar molecules by means of solvation effects. It plays a fundamental role in the folding of a globular protein into its native structure. It participates in the catalytic mechanism of many enzymatic reactions.

Water assumes also a crucial role in the interaction between millimetre waves and biological systems. Indeed, the dielectric properties of tissue, cells and aqueous solutions in the GHz frequency range, are essentially determined by those of water.

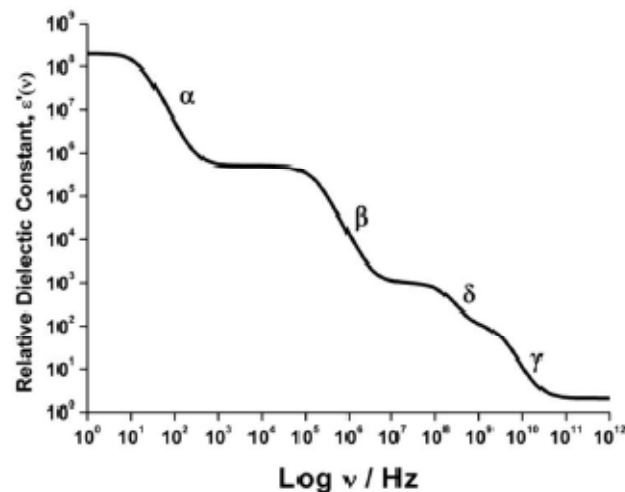


**Figure 2.2** Relative dielectric constant  $\epsilon'(\nu)$  of a typical tissue as a function of the frequency from 0 up to 300 GHz.  $\alpha$ ,  $\beta$ ,  $\delta$  and  $\gamma$  are the relaxation regions respectively occurring in the KHz, MHz and GHz frequency range. (Curve simulated by a tetra-Debye equation with relaxation time constants of 10<sup>-2</sup> s, 10<sup>-6</sup> s, 5 $\times$ 10<sup>-10</sup> s and 5 $\times$ 10<sup>-11</sup> s (from Beneduci, 2008a).

Figure 2.2 indicates the dielectric behaviour of practically all tissues of high water content. Two remarkable features stand out: unusually high permittivity values at low frequencies, and four relaxation regions  $\alpha$ ,  $\beta$ ,  $\delta$ , and  $\gamma$ . If properties change with frequency, we name such properties “dispersive” and the phenomena of frequency dependence itself “dispersion”.

Membrane relaxation causes the  $\alpha$  dispersion and inhomogeneous structures causes  $\beta$  dispersion, i.e., the polarization resulting from the charging membranes through intra

and extracellular fluids. A small additional relaxation ( $\delta$ ) between  $\beta$  and  $\gamma$  dispersion is probably caused in part by rotation of amino acids, partial rotation of charged side groups of proteins and the relaxation of protein bound water which occurs somewhere between 1 and 5 GHz. The  $\gamma$  dispersion is caused by water and extends above 100 GHz, in the millimeter range.

Water appears in two forms as free water and bound water. The relaxation of free water takes place at a frequency of approximately 18 GHz at 37 °C, and the relaxation frequency is a function of temperature. An increase in the temperature causes an increase in the relaxation frequency. Bound water has many definitions, according to the experimental techniques being employed to investigate it. A suitable general designation would be to refer to bound water as molecules held in non random orientations at or near the surface of a macromolecule. Considerable differences of opinion exist as to how much water in the vicinity of the macromolecule may be considered to be different from free water. The relaxation frequency of bound water depends on the molecule the water is attached to, and on the solvent viscosity.

### **2.1.5 Frequency dielectric response of water.**

The frequency dependence of the permittivity of a dipolar material at MMW, is in general determined by the orientation of molecular dipoles that tend to align along the direction of the applied time-varying electric field, against the action of the friction forces produced by the surrounding environment. Generally, this mechanism describes the orientation polarization of the material induced by the field. The response of the dipoles to the electric field is not instantaneous and this causes their reorientation to lag behind it. The kinetic of orientation is thus dependent on the frequency of the field. Intuitively, one can think that the angular velocity at which the molecular dipoles rotate, is basically dependent on the shape of the molecules, on the viscosity of the surrounding medium and on the temperature.

If one analyzes the behavior of the real,  $\epsilon'(\nu)$ , and imaginary part,  $\epsilon''(\nu)$ , of the complex dielectric permittivity of a condensed system, as a function of the frequency of the applied electric field, one obtains the so called dielectric spectrum or relaxation spectrum.

The dipolar dielectric spectra of water is in Figure 2.3, that is relative to water at 303 K. Three distinct frequency regions can be identified. The region at which the dielectric

constant suddenly decreases and the loss factor has a maximum. It has been previously called dispersion region. The maximum variation of the dielectric constant in this process is called dielectric step ( $\Delta\epsilon$ ).

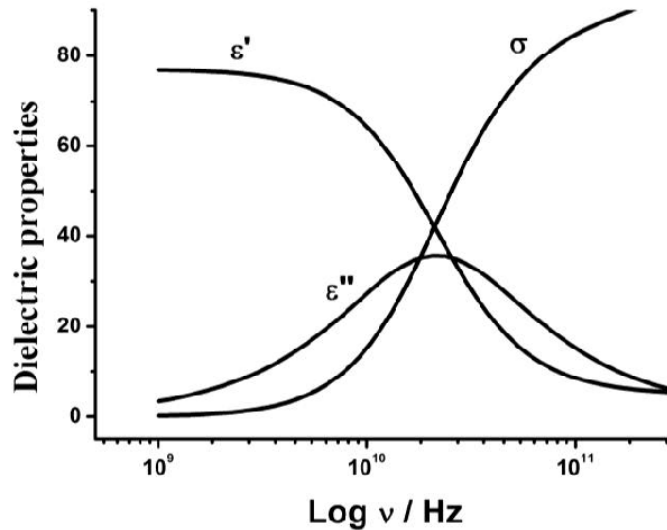


**Figure 2.3** Relative dielectric constant  $\epsilon'$  ( $\nu$ ) , relative loss factor  $\epsilon''(\nu)$  and dielectric conductivity  $\sigma$  ( $\nu$ ) (S/m) of water at 303 K as a function of the frequency (from Beneduci, 2008a).

The frequency  $\nu D$  of maximum dielectric loss, is the characteristic frequency of the system at which the relaxation occurs. The corresponding time constant,  $\tau D = 1/2\pi\nu D$ , is called relaxation time.

For water at 30°C  $\nu D = 20$  GHz and  $= 7.44 D \tau$  ps (Beneduci, 2008b).

Before and after this region,  $\epsilon'(\nu)$  does not change significantly, assuming fairly constant values, approximately equal to the static dielectric constant,  $\epsilon'(0)$  and to the dielectric constant at infinite frequency,  $\epsilon'(\infty)$  , respectively. A qualitative explanation that can be applied to is that, when the frequency is low compared to the angular velocity of the rotational motion of the dipoles, they have enough time to reorient. In this case,  $\epsilon'(\nu)$  approaches the static value, with  $\epsilon'(\nu)$  near to the highest value and  $\epsilon''(\nu)$  near to the lowest one. On the contrary, when the frequency of the field is high compared to the characteristic relaxation frequency, the molecular dipoles have not enough time to reorient and no orientation polarization occurs. Thus, either  $\epsilon'(\nu)$  or  $\epsilon''(\nu)$  assume low values. The dielectric relaxation thus occur when the orientation motions of the molecular dipoles are matched by the field, that is when the angular

frequency of the external electric field approaches the angular velocity of rotation of the dipoles in the system.

It is also interesting to analyze the dependence of the dielectric conductivity  $\sigma(\nu)$  on the frequency (Figure 2.3). At the relaxation frequency it abruptly increases as it would be expected from the Kramers-Kronig relation (Von Hippel, 1966).

A model that describes the frequency dependence of the complex dielectric permittivity, has been introduced by Debye and is described by the Debye equation (Von Hippel, 1966).

To a good approximation the dielectric properties of water in this region can be represented by a single Debye equation:

$$\varepsilon = \varepsilon' - j\varepsilon'' = \varepsilon_{\infty} + \frac{\varepsilon_s - \varepsilon}{1 + j\omega\tau_D} \quad (2.10)$$

Where  $\varepsilon_s$  is the static permittivity of the pure liquid and  $\varepsilon$  is the plateau value to which  $\varepsilon'$  would fall at frequencies much higher than  $\tau_D^{-1}$  assuming that no further dispersion occurs.

Measurements on water carried out within the past few years, show, however, that further dispersion does occur in the far infrared.

One sure fact that does stand out is that the processes of viscosity and dielectric relaxation are just as strongly related for pure water as they are for the solutions of biological macromolecules in water. The variation of relaxation time with temperature for pure water is consistent with an activation enthalpy of around 16 kJ/mole which, for biological solutions, indicates that hydrogen bond breakage is the rate determining step in dielectric relaxation.

## **2.2 BIOPHYSICAL MECHANISM OF INTERACTION**

### **2.2.1 Thermal vs Non-Thermal Effects.**

When the frequency of the applied electric field is close to the characteristic relaxation frequency of the system (that of water), the water dipoles change orientation continuously following the change of the field. This motion can produce a macroscopic

temperature increase of the system, by a mechanism in which the electromagnetic energy absorbed is dissipated into heat. Thermal effects occur provided the field strength is high enough to cause a certain time-dependent polarization of the system. The standard quantity adopted to specify the absorption of EM energy is the Specific Absorption Rate (SAR). It specifies the time rate at which the absorption of EM energy is transformed into another form of energy in the unit mass of irradiated system (W/Kg) (Stuchly et al., 1996; Chou et al., 1996). The SAR is proportional to the conductivity  $\sigma$  of the system, at the frequency of exposure, to the square of the internal electric field strength and is inversely proportional to the density,  $\rho$  of the object:

$$SAR = \frac{\sigma}{2\rho} |\vec{E}_i|^2 \quad (2.11)$$

The SAR can also be expressed in terms of the temperature gradient  $\Delta T$ , induced in the irradiated system,

$$SAR = C_H \frac{\Delta T}{t} \quad (2.12)$$

where  $CH$  is the specific heat of the system (in Joule/K Kg) and  $t$  is the time in seconds. This definition implies that the temperature changes induced are linearly dependent on the SAR. Correspondingly, the heat production is proportional to  $|\vec{E}_i|^2$ . Then, one can estimate the value of  $\Delta T$  at low power exposure conditions from the values of  $\Delta T$  determined at high SAR levels, by a simple extrapolation of the data.

Equation (2.12) provides us a simple experimental method in order to identify the limit value of SAR at which no temperature rise occurs in the exposed system. The safety standard limits of exposure adopted in West Countries are based on the thermal mechanism prescribed by Eq. (2.12). However, such a method of evaluation of health hazards caused by EMR exposure, does not take into account any possible mechanism, of non-thermal nature, that could arise in the system and that could significantly affect its biological properties.

### **2.2.2 Hypothesis of the Mechanism.**

Interaction energy between water and microwaves is far below the thermal motion, i.e., at intensities where no orientation of polar molecules in solution can be achieved by the radiation. The question is therefore how these small external stimuli can affect the biological functions of a system (Schwan, 1977; Weaver and Astumian, 1990; Adair, 2003).

H. Fröhlich some decades ago theoretically suggested a mechanism of interaction between MMWs and living systems (Fröhlich, 1988). He proposed that a living cell can be modelled as an ensemble of small electric oscillators exhibiting cooperative functions. These oscillators are highly ordered, charged and polarized structures of dynamic nature and could be biomolecules and other cellular structures such as ordered water embedding membranes and organelles. Cooperativity and dynamic information processing would be possible by a mechanism known as Fröhlich's coherent excitation of a single mode of oscillation in which the oscillators vibrate collectively and coherently, involving the entire system. The excitation can be achieved if the energy flux density supplied to the system exceeds a threshold. Non thermal effects due to microwaves irradiation can occur provided the energy required for the excitation is self-sustained by the system, e.g. by metabolic processes. The theory prescribes that the system can store the energy until the relevant single mode of vibration is excited. In this case, the external field would act as a trigger supplying just the small amount of energy required to built up the coherent oscillation. Fröhlich has shown that biological membranes might oscillate at frequencies in the GHz region and therefore that they are very probable candidate target-structures of microwaves.

Fröhlich's conjecture provides the theoretical basis for rationalizing the claimed non thermal microwave effects induced on active biological systems (Webbs and Booth, 1969; Pakhomov, 1998; Belyaev et al., 2000; Belyaev, 2005; Beneduci et al. 2005; Beneduci, 2007; Beneduci, 2009; Siegel and Pikov, 2010). This theory however does not hold for passive systems for which no energy storage can in general take place. An alternative model that explains how biological membranes should be especially sensitive to microwaves also in the absence of metabolic input, was proposed by Bond and Wyeth (Bond and Wyeth, 1986). They suggested that the coupling between the radiation and the membrane changes the order parameter associated with the lipid matrix. Such a coupling mechanism can shift the ordered-to-fluid transition to a critical point, i.e., the

transition is interpreted as a continuous second order phase transition. This model is based on collective oscillations due to long range order parameter fluctuations when the membrane system is close to the critical point. Such collective oscillations differ from those prescribed by Fröhlich, because they can occur also in passive membrane systems where non metabolic energy flux is present. The criticality of the system is manifested with the anomalous increase of some membrane response functions, such as the lateral compressibility, directly related to the membrane permeability, the repeat bilayer distance, etc. (Bond and Wyeth, 1986).

Despite numerous evidences show the influence of low power millimetre waves on biological systems (see section 2.3 below), no conclusive experimental proofs have been brought in favour of a non-thermal nature of the interaction.

## **2.3 BIOLOGICAL EFFECTS OF MILLIMETER WAVES**

Since the first work of Webbs and Dodds (1968) on the influence of microwave radiation on the cell growth of escherichia coli bacterium, many other scientists have been investigating the effects of MMWs on biological systems (Pakhomov et al., 1997; Belyaev et al., 2000; Belyaev, 2005; Beneduci et al. 2005; Beneduci, 2007; Alekseev et al., 2009; Beneduci, 2009; Siegel and Pikov, 2010). For a comprehensive overview on the topic we remind to the reviews of Pakhomov (1998) and recently Ramundo-Orlando (2010).

### **2.3.1 Biological membrane is the primary target of MMWs.**

Strong evidence show that biological membranes are likely to be the main target of microwaves with frequency in the range 1-80 GHz (Fröhlich, 1988; Pakhomov, 1998; Ramundo-Orlando, 2010). Ionic transmembrane current seems to be influenced by microwave exposure. For instance, Brovkovich et al. observed a significant activation of the  $\text{Ca}^{2+}$  pump in the sarcoplasmic reticulum of the skeletal muscle cells and in those of the rat heart exposed to 61 GHz radiation at  $4 \text{ mW/cm}^2$  (Brovkovich et al., 1991).

Geletyuk et al. found significant alterations in the transport of calcium ions across the single  $\text{Ca}^{2+}$ -activated  $\text{K}^+$  channel of kidney cells exposed to nonthermal 42.25 GHz radiation (Geletyuk et al., 1995). In related works authors attributed to water the capacity

to transfer electromagnetic radiation information because of a change in size and concentration of clusters of water interacting by hydrogen bonds (Fesenko 1995a and 1995b). This capability of water has been also studied by Cojocaru et al. (2005). From their study on the direct exposition of water, these authors concluded that water is the main acceptor of MMWs.

Frequency specific and reversible effects has been reported on the Cl<sup>-</sup> transmembrane current in cells of the *Nitellopsis obtusa* giant algae exposed to microwaves in the 41-76 GHz frequency range at a power density of 5 mW/cm<sup>2</sup> at which thermal increase was restricted to < 1 °C (Kataev et al., 1993). Besides the effects observed on ionic membrane transport, results from other investigations show that *in vitro* exposure of human cells in the 42-78 GHz frequency range may result in nonthermal induced changes on cell membranes, such as reversible externalization of phosphatidylserine in keratinocyte and murine melanoma cells (Szabo et al., 2006).

Our group has reported of some significant morphological alterations in leukaemia (Beneduci et al., 2007) and breast cancer (Beneduci et al., 2005) cells (Figure 2.4 and Figure 2.5).

An intrinsic or direct effect of the radiation (non-thermal effects) have been claimed to fully explain some experimental findings, even in the presence of thermal effects, like the increase in cation permeability (K<sup>+</sup>, Na<sup>+</sup>) observed in erythrocytes exposed to low frequency microwaves up to 8.42 GHz (Liburdy 1984). This effect occurred however, only when erythrocyte preparations were exposed to the radiation at temperatures close to the erythrocyte membrane phase transition point (Liburdy 1985), indicating that membrane phase transition could play a significant role in microwaves induced biological effects.



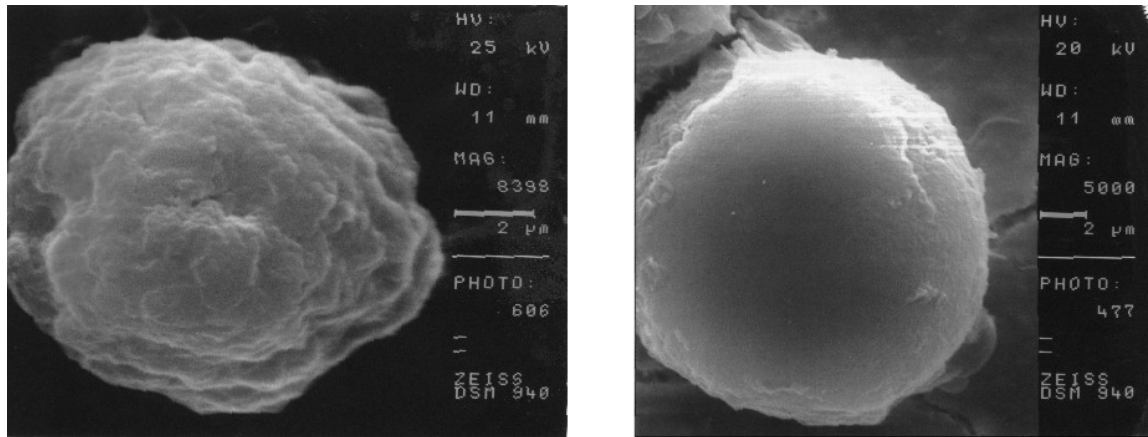


**Figure 2.4** Scanning electron microscopy of K562 cells as they appear before (left) and after MMW irradiation (right). Control K562 cells present ruffled membranes. MMW irradiation has an evident smoothing effect on the K562 cells that appear rounded and smoothed after irradiation (from Beneduci et al., 2007).

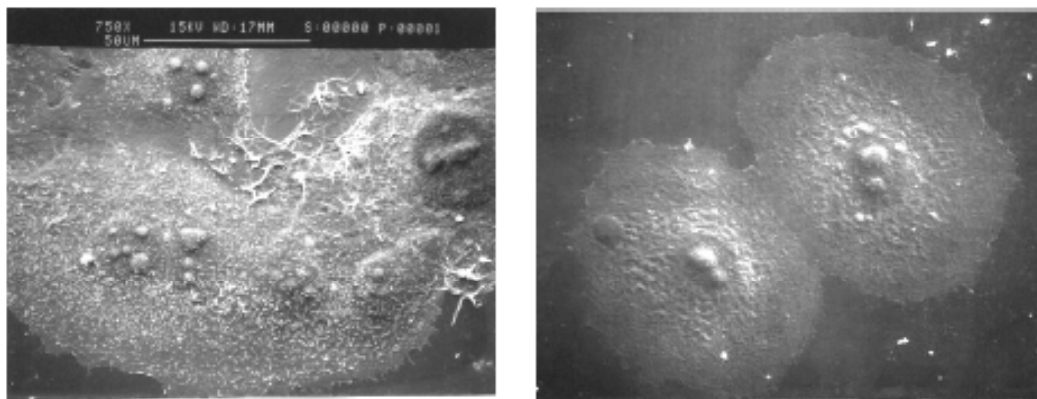


**Figure 2.5** Scanning electron microscopy of MCF-7 cells as they appear before (left) and after MMW irradiation (right). MMW irradiation causes a noticeable decrease in the number of microvilli that cover the surface of non irradiated MCF-7 cells (from Beneduci et al., 2005).

Very recently, Siegel and Pikov have reported an increased cellular membrane permeability and nanoporation in epithelial and neuronal cells in vitro after 60 GHz short term exposure at 10-50 mW/cm<sup>2</sup> (Siegel and Pikov, 2010) (Figure 2.6).

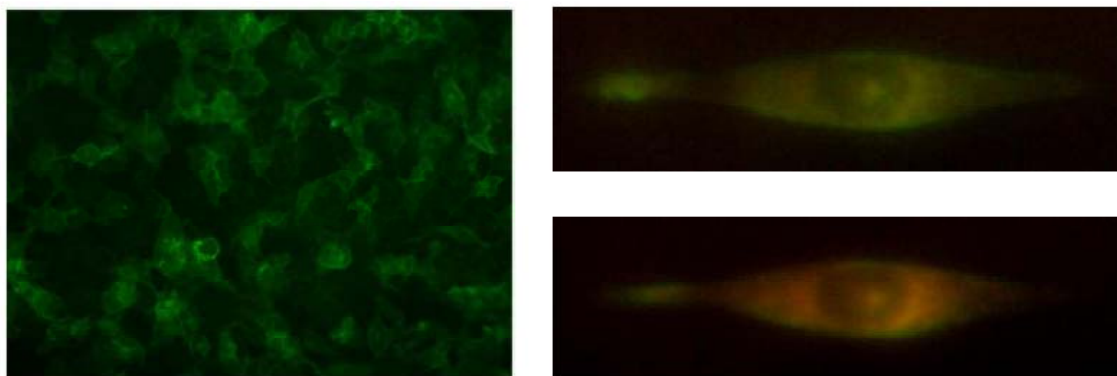


**Figure 2.6** Left. Photograph of H1299 cell field expressing lipid bound fGFP at cell membrane (transfected with pEGFP-F vector). Right. Photograph of single fGFP expressing cell in oxonol and PBS before (top) and during (bottom) millimeter wave exposure. The shift from green to red fluorescence indicates the increase in cellular membrane permeability leading to depolarization of oxonol (oxonol migrates from the outside into the inner leaflet and bounds to fGFP) (from Siegel and Pikov, 2010).

Some evidence of the microwave effects on model membrane systems, have also been reported in addition to those observed on active biological systems. Zhadobov et al. studied the effects of short-term low-power 60 GHz radiation exposure on phospholipid monolayer films at different exposure conditions (Zadhobov et al., 2006). They observed that microwave radiation at 60 GHz significantly increased the lateral pressure of the phospholipid monolayer even at power densities as low as  $9 \mu\text{W}/\text{cm}^2$ , independently on the other exposure parameters. However, they concluded that the changes in the lateral pressure did not involve a statistical significant phospholipid microdomain reorganization. Ramundo-Orlando et al. reported that irradiation of phospholipid cationic vesicles at 130 GHz pulsed wave can affect the permeability of the vesicles by a nonthermal mechanism (Ramundo-Orlando et al., 2007). This effect was strongly dependent on the time-averaged incident intensity ( $I_{\text{av}}$ ) and on the pulse repetition rate. Recently, our group have shown that exposure of giant unilamellar vesicles (GUVs) at 53.57 GHz and average SAR up to  $0.55 \text{ W}/\text{Kg}$ , induces shape changes of GUVs, diffusion of the fluorescent dye D-8-ANNEPS into the membrane bilayer and increased attraction between vesicles (Ramundo-Orlando et al., 2009). It has been advanced the hypothesis that exposure of GUVs to millimetre waves mainly affects the membrane-water interface of vesicle causing the above perturbations.

## **CHAPTER 3**

### **Experimental techniques and devices**

In this chapter the theoretical and technical aspects concerning the preparation and characterization of biomimetic systems used in this work, are illustrated.

The last section is dedicated to a technical description of the exposure devices employed.

### 3.1 VESICLE PREPARATIONS

All phospholipids are insoluble in water and simple mixing of lipid and water doesn't result in spontaneous small or giant unilamellar vesicle formation. In the late sixties Reeves and Dowben investigated the effects of swelling thin lipid films in aqueous solutions (Figure 3.1), and developed a protocol for making giant multilamellar vesicles (Reeves and Dowben 1968).

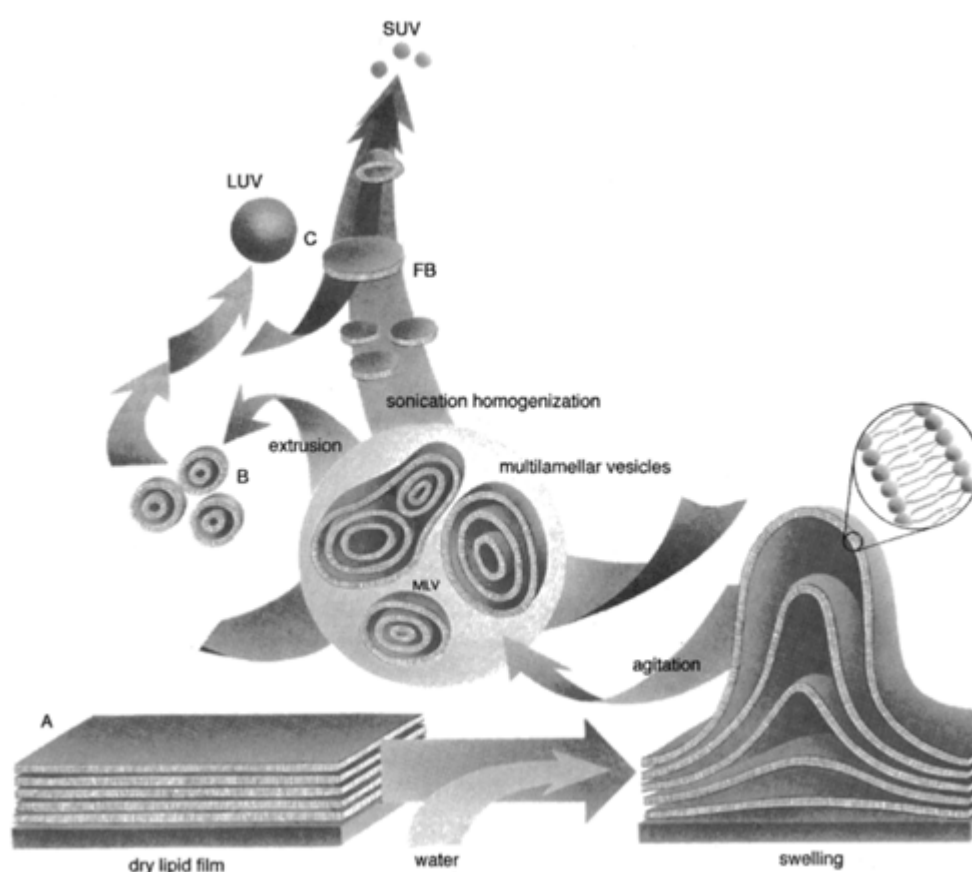


**Figure 3.1** Evolution of Vesicles: The figure shows how one arrives at different classes of vesicles beginning from a stack of lipid bilayers obtained by hydration of a dry lipid film (swelling process). Practicing a protocol of hydration followed by agitation one is able to build a wide variety liposomes depending on experimental needs (Avanti Polar Lipids).

Since then variations on vesicle formation have been developed and many different preparation methods currently exist. One must predetermine the type of liposome needed for a measurement taking into account factors such as size, composition, and membrane sensitivity.

Here we describe the two methods used to construct vesicles in this work, one for production of giant unilamellar vesicles (GUV's) (diameter  $>10\ \mu\text{m}$ ) and the other for large unilamellar vesicles (LUV's) (diameter 100 nm).

There are a few features that are common to both giant unilamellar vesicle and large unilamellar preparation techniques. The initial step to creating vesicles here is to create a lipid film. One does this by depositing a volume of lipid solubilized in an organic solvent; usually chloroform, into a container (in the case of extrusion of LUVs), or onto a conductive surface (in the case of electroformation GUV). In both cases, based on the amount of lipids deposited and the type of container that it is deposited into, one dries the prepared lipid solution under vacuum until dry. Finally, vesicle formation takes place with the addition of aqueous solution to the lipid film (swelling process; Figure 3.1). In order to obtain vesicles with different size one must now vary the preparation procedures significantly.

### **3.1.1 Large unilamellar vesicle preparation by extrusion technique.**

One is able to produce uniform submicron sized unilamellar vesicles using a technique called extrusion. It is the method of choice for producing well defined, small ( $< 80\ \text{nm}$ ) and large (80nm-1 $\mu\text{m}$ ) unilamellar vesicles. Here high pressure is used to force a dispersion of multilamellar vesicles through pores with a well-defined pore size. Repeated cycling of the vesicle dispersion through the filters reduces the number of lamellae per vesicle. In the end the extrusion process gives expected results, unilamellar lipid bilayers with a narrow distribution of vesicle sizes having a mean diameter near the filter's pore size (Figure 3.2a).

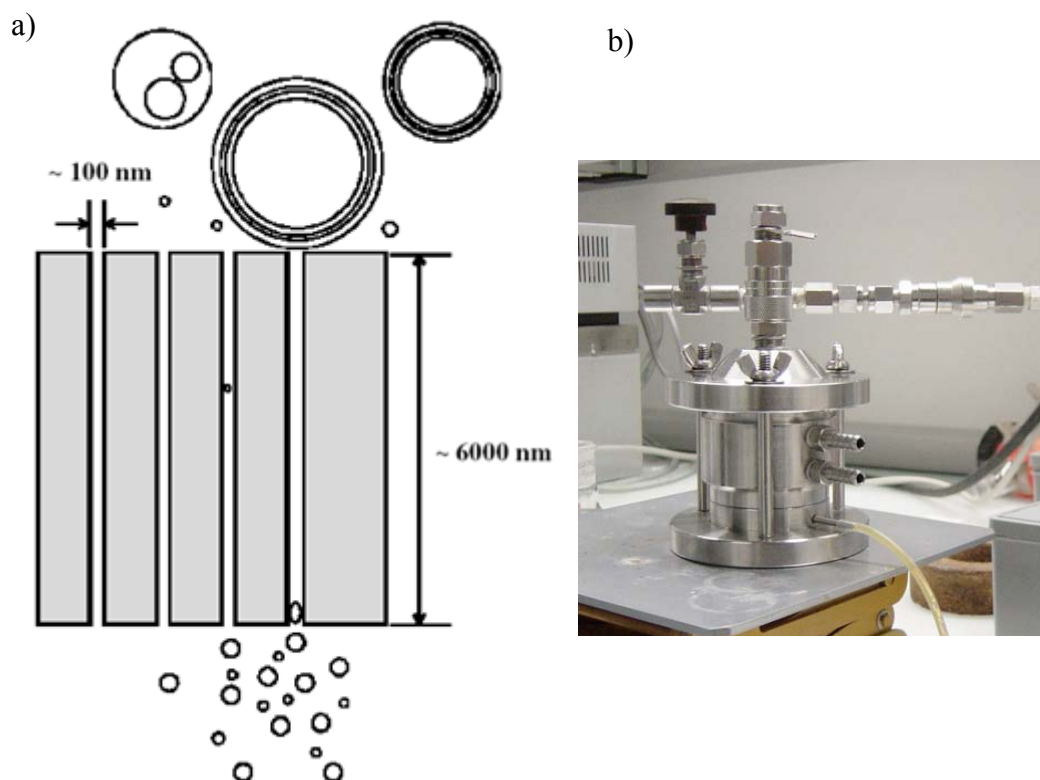


**Figure 3.2** Extrusion technique. a) A dispersion of multilamellar vesicles is forced through pores with a well-defined pores size to obtain homogeneous unilamellar vesicles; b) Lipex Extruder (Northern Lipids) used to produce large unilamellar vesicles (LUVs).

### 3.1.2 Giant unilamellar vesicle preparation by electroformation.

Giant vesicles are ideal objects to model cell bodies, particularly with respect to size (similar to that of biological cells,  $\sim 20 \mu\text{m}$ ) and composition. The great advantage of their direct visualization under a microscope, has led to a widely diffuse use of these systems to mimic certain aspects of biomembranes (Figure 3.3) and recently an outstanding numbers of papers have been devoted to new improved methods for their preparation.

In Figure 3.4 it is shown the inside cover of an issue of *ChemBioChem* dedicated to our review on preparations and applications of giant unilamellar vesicles (Walde et al., 2010). For a detailed description of the preparation methods of GUVs we remind to this work, attached at the end of this thesis.

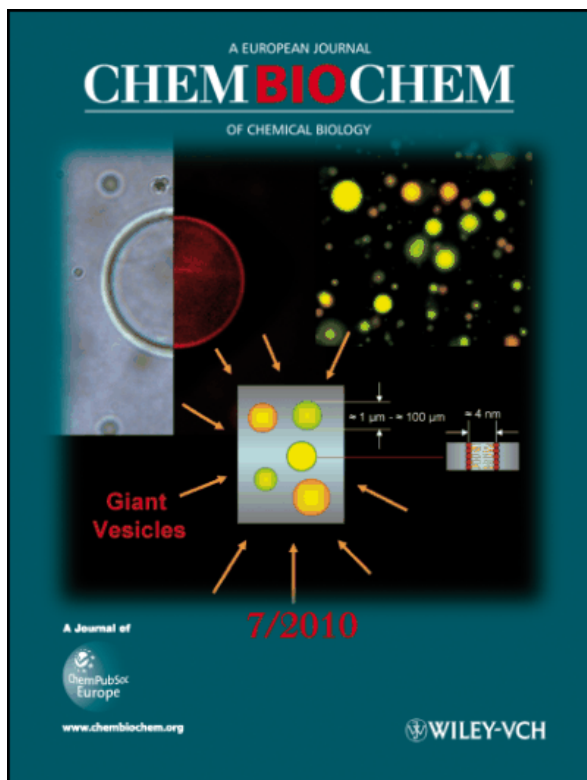


**Figure 3.4** Inside cover of *ChemBioChem* issue of May 2010, dedicated to our review on preparations and applications of GUVs (Walde et al., 2010). The picture shows giant phospholipid vesicles containing different lipid- and water-soluble fluorescent probes and a scheme indicating typical vesicle dimensions.

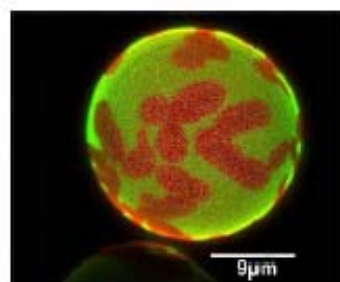


**Figure 3.3** Confocal microscopy image of a 33:67 DLPC:DPPC mixture at 26 °C, showing domain formation (gel domains in red, fluid domains in green). Adapted from Seeger et al. (2005).

## 3.2 ANALYTICAL METHODS

To investigate the physical aspects of vesicles we chose to use a series of complementary experimental techniques. To investigate the interaction of MMWs at the membrane-water interface we performed Deuterium Nuclear Magnetic Resonance measurements ( $^2\text{H-NMR}$ ). Dynamic light scattering measurements (DLS) and fluorescence spectroscopy were used to determine, respectively, changes in vesicle radius and size distribution of vesicles, and membrane permeability, in LUVs, which are invisible to the microscope. Thus direct visualization of the submicroscopic processes measured with DLS was performed on GUVs by optical microscopy.

**3.2.1 <sup>2</sup>H Nuclear Magnetic Resonance.**

Nuclear Magnetic Resonance (NMR) spectroscopy is a sort of absorption spectroscopy. A sample in a magnetic field may absorb, in appropriate conditions, electromagnetic radiation in the radiofrequency (rf) region and the peculiarities of the sample influence the absorbed frequencies. Protons and neutrons, like the electron, have a spin angular momentum, which can take values of + ½ and - ½. We can say that a nucleus with unpaired protons and neutrons will have an overall spin, with the number unpaired contributing ½ to the overall nuclear spin quantum number,  $I$ . When this is larger than zero, a nucleus will have a spin angular momentum and an associated magnetic moment,  $\mu$ , dependent on the direction of the spin. It is this magnetic moment that gives rise to an NMR experiment. The spin quantum number,  $I$ , determine the number of orientation that a nucleus can have, when immersed in an external and uniform magnetic field, according to the formula  $2I+1$ ; for instance, nuclei having  $I=1/2$  have two possible orientation to which two energy levels can be associated, and the difference in energy ( $\Delta E$ ) is given by:

$$\Delta E = \frac{h\gamma}{2\pi} B_0 \quad (3.1)$$

Where  $h$  is the Planck's constant. This relation states that the difference in energy  $\Delta E$  is proportional to  $B_0$ .

The fundamental NMR equation, relating the applied radiofrequency  $\nu_1$  to the intensity of the magnetic field is:

$$\nu_1 = \frac{\gamma}{2\pi} B_0 \quad (3.2)$$

where  $B_0$  is the intensity of the static magnetic field,  $\gamma$  is a fundamental nuclear constant called gyromagnetic ratio; practically it is the proportional constant between the magnetic moment  $\mu$  and the spin number  $I$ :

$$\gamma = \frac{2\pi\mu}{hI} \quad (3.3)$$



When the above relation is satisfied, taking in account that  $\Delta E = h\nu$ , the system is into resonance; energy is absorbed by the given nucleus which jumps to the higher energy level and a spectrum can be recorded (Abragam, 1961).

### 3.2.1.1 NMR of Anisotropic media.

The behavior and the properties of matter, strongly depend on the arrangement of its microscopic constituents. One can distinguish two different kind of order in the structure of matter:

- Positional order
- Orientational order

The first one, refers to the distribution of the mass center of molecular groups constituting matter.

Oriental order refers to the spatial orientation of non spherical molecules. In a crystalline solid, molecules are distributed as to a tridimensional network, while in a liquid they are randomly arranged. A liquid crystal has the typical properties of both liquids and crystals, in which the orientational order is not completely associated with tridimensional positional order. NMR spectra of either solid compounds or liquid crystals, allow to study molecular motions and spatial orientation (Breitmaier, 2002). The study of the quadrupole coupling is particularly useful in analyzing the deuterium nuclei belonging to the systems we have been investigating.

### 3.2.1.2 Quadrupolar Interaction.

Nuclei having spin number  $I \geq 1$ , show a non spherical charge distribution. This asymmetry is described by an electric quadrupole moment,  $eQ$ , which influences the relaxation time and as a consequence, the broad-line shape and the coupling with near nuclei.

The quadrupolar interaction arises from the interaction of the electric quadrupole moment with the electric field gradient (EFG) occurring around the nucleus. Mathematically, the electric field gradient (EFG) is the hessian matrix (the matrix of the second derivatives) of the electrical potential  $V$ :

$$V_{ij} = \frac{\partial^2 V}{\partial x_j \partial x_i} \quad (3.4)$$

It is an important structural property of a crystalline solid, where it is defined at the location of a nucleus. The EFG is non-zero only if the charges surrounding the nucleus violate cubic symmetry and therefore generate an inhomogeneous electric field at the position of the nucleus. The individual components  $V_{ij}$  form a symmetrical and traceless tensor.

Deuterium nucleus we used in our observation, posses spin number  $I=1$ . If deuterium nucleus is immersed into a static magnetic field, it shows 3 different energy levels and a quadrupole moment different from zero ( $2,73 \times 10^{-21} \text{cm}^{-1}$ ), although relatively small, dominate over the other interactions (dipolar, spin-spin and chemical-shift interaction), except for the Zeeman interaction. Hence the Hamiltonian for Deuterium NMR spectra of liquid crystals will be given by:

$$H=H_Z + H_Q \quad (3.5)$$

The quadrupole moment adds a further perturbation to the energy levels, which are under the external magnetic field  $H_0$ .

Considering the first perturbative order, the Hamiltonian can be written as:

$$H = \omega_0 I_z + \frac{e^2 q Q}{4I(2I-1)} (3I_z^2 - I^2) \quad (3.6)$$

Thus, because of the quadrupole perturbative term, the unique spectral frequency generated by Zeeman effect, splits into two frequencies  $\nu_1$  e  $\nu_2$ .

The difference between these frequencies is generally called quadrupole splitting and, for uniaxial systems, it is given by:

$$\Delta\nu = \frac{3}{2} \frac{e^2 q Q}{h} \frac{3 \cos^2 \theta - 1}{2} \quad (3.7)$$

where  $\theta$  defines the orientation of the direction of field  $H_0$  respect to the principal axis of EFG of the deuterium nucleus.

Hence, the spectrum coming out from a deuterium, being either in a single crystal or in an oriented sample, will consist in a doublet having a splitting depending on the  $\theta$  angle as shown in Figure 3.5.

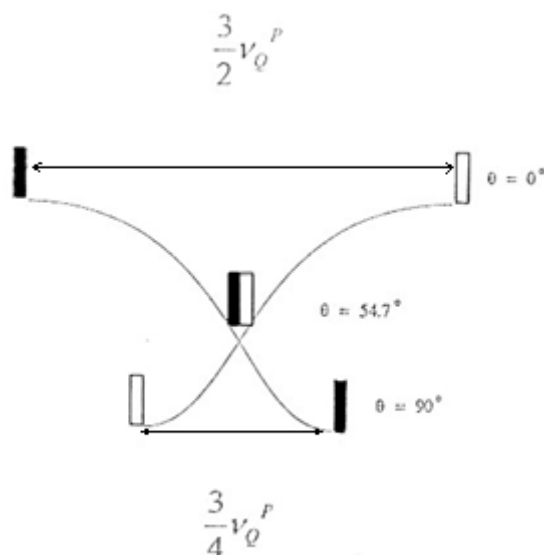


**Figure 3.5** Separation of the peaks as a function of  $\theta$ .

Within a sample containing deuterium, in which there is no motion, unless aligned under the external fields influence or surfaces effects, a spherical isotropic distribution of (x)- $^2\text{H}$  bonds exists. Thus the spectral powder pattern is the superposition of all possible orientation (all possible values), as illustrated in Figure 3.6.

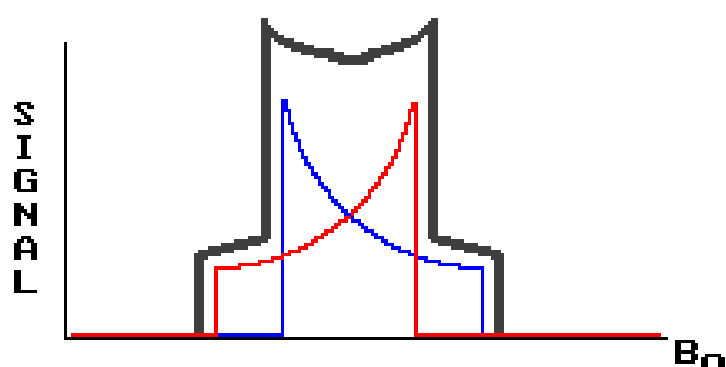


**Figure 3.6** Deuterium spectral pattern.

The principal axis system of the EFG tensor is a molecule fixed coordinate system. When some dynamical motion take place inside the system, modulation of the angle  $\theta$

occurs, so that if these motions are on a timescale short compared to  $1/\Delta\nu$ , the observed quadrupolar splitting will be:

$$\langle \Delta\nu \rangle = \frac{3}{2} \frac{e^2 q Q}{h} S \quad (3.8)$$

where  $S = \frac{1}{2} \langle 3 \cos^2 \theta - 1 \rangle$ , is the order parameter.

### 3.2.2 Dynamic Light Scattering.

Dynamic light scattering (DLS), another non invasive analytical method, is particularly useful for samples containing homogenous particle size and shape. One is able to determine information about the size and size distribution of vesicles from a sample measurement.

When a beam of light passes through a colloidal dispersion, the particles or droplets scatter some of the light in all directions. When the particles are very small compared with the wavelength of the light, the intensity of the scattered light is uniform in all directions (Rayleigh scattering); for larger particles (above approximately 250nm diameter), the intensity is angle dependent (Mie scattering).

If the light is coherent and monochromatic, as from a laser for example, it is possible to observe time-dependent fluctuations in the scattered intensity using a suitable detector such as a photomultiplier capable of operating in photon counting mode.

These fluctuations arise from the fact that the particles are small enough to undergo random thermal (Brownian) motion and the distance between them is therefore constantly varying. Constructive and destructive interference of light scattered by neighboring particles within the illuminated zone gives rise to the intensity fluctuation at the detector plane which, as it arises from particle motion, contains information about this motion. Analysis of the time dependence of the intensity fluctuation can therefore yield the diffusion coefficient of the particles from which, via the Stokes Einstein equation, knowing the viscosity of the medium, the hydrodynamic radius or diameter of the particles can be calculated (Berne and Pecora, 1976).

As such, light scattering allows us to maintain the integrity of the system without the addition of impurities of dyes, or adding markers to our sample.

Non invasive back light scattering was used to determine vesicle size distribution as a result of a given extrusion procedure.

We perform two series of measurements. One on a control system, and another on the exposed sample. Comparisons of the two measurements, during and after the radiation exposure, give us information about changes in the size and polydispersity of the vesicles as a result of the interaction of the membranes with the millimeter waves.

### 3.2.2.1 Basic equations.

The fluctuating signal, originating from the random motion of particles in a liquid phase and the associated alterations in the intensity of the scattered light over time, were processed by the autocorrelation function:

$$C(t), C(t) = Ae^{2\Gamma t} + B \quad (3.9)$$

where  $t$  is the time delay,  $A$  is an optical constant determined by the instrument design.  $\Gamma$  is one of the two moments of the distribution and is related to the relaxation of the fluctuations by:

$$\Gamma = Dq^2 \quad (\text{rad/sec}) \quad (3.10)$$

where  $D$  is the translational diffusion coefficient in  $\text{cm}^2/\text{s}$  and  $q$  is the scattering vector. The value of  $q$  is calculated from the scattering angle  $\theta$  (e.g.  $90^\circ$ ), the wavelength of the laser light  $\lambda_0$  e.g. 635 nm), and the index of refraction  $n$  (e.g. 1.33) of the suspended liquid, according to the equation:

$$q = (2\pi n/\lambda_0)2\sin(\theta/2) \quad (3.11)$$

Particle size is related to  $D$  for simple common shapes like a sphere, ellipsoid, cylinder and random coil. Of these, the spherical assumption is most useful in the greatest number of cases. For a sphere,

$$D = \frac{k_B T}{3\pi\eta(t)d} \quad (\text{cm}^2/\text{sec}) \quad (3.12)$$

Where  $\kappa_B$  is Boltzmann's constant ( $1.38054 \cdot 10^{-16}$  ergs/deg),  $T$  is the temperature in K,  $\eta(t)$  (in centipoise) is the viscosity of the liquid in which the particle is moving, and  $d$  is the particle diameter. This equation assumes that the particles are moving independently of one another.

The other momentum is  $\mu_2$  that is proportional to the variance of the intensity weighted distribution according the Eq. (3.13):

$$\mu_2 = (D^{*2} - D^{*2})q^4 \quad (3.13)$$

and it is used to calculate the polydispersity  $= \mu_2/\Gamma^2$ . Polydispersity has not units.

Analysis of the autocorrelation function in terms of particle size distribution is done by numerically fitting the data with calculations based on assumed distributions. A truly monodisperse sample would give rise to a single exponential decay to which fitting a calculated particle size distribution is relatively straightforward. In practice, polydisperse samples give rise to a series of exponentials and several quite complex schemes have been devised for the fitting process. One of the methods most widely used today is known as Non-Negatively Constrained Least Squares (NNLS).

Particle size distributions can be calculated either assuming some standard form such as log-normal or without any such assumption. In the latter case, it becomes possible, within certain limitations, to characterize multimodal or skewed distributions. The size range for which dynamic light scattering is appropriate is typically submicron with some capability to deal with particles up to a few microns in diameter. The lower limit of particle size depends on the scattering properties of the particles concerned (relative refractive index of particle and medium), incident light intensity (laser power and wavelength) and detector/optics configuration.

### **3.2.3 Fluorescence spectroscopy.**

Fluorescent spectroscopy has been used in this work to measure the membrane permeability of LUVs to calcein, a fluorescent dye with an excitation and emission wavelengths of 490/511 nm. The fluorescent dye is entrapped into liposomes at self-quenching concentrations. Upon leakage the dye is diluted in the outer aqueous compartment leading to an increase of the fluorescence signal.

The visible region of the spectrum comprises photon energies of 36 to 72 kcal/mole, and the near ultraviolet region, out to 200 nm, extends this energy range to 143 kcal/mole. Ultraviolet radiation having wavelengths less than 200 nm is difficult to handle, and is seldom used as a routine tool for structural analysis.

The energies noted above are sufficient to promote or excite a molecular electron to a higher energy orbital. Consequently, absorption spectroscopy carried out in this region is sometimes called "electronic spectroscopy". A diagram showing the various kinds of electronic excitation that may occur in organic molecules is shown in Figure (3.7). Of the six transitions outlined, only the two lowest energy ones (left-most, colored blue) are achieved by the energies available in the 200 to 800 nm spectrum.

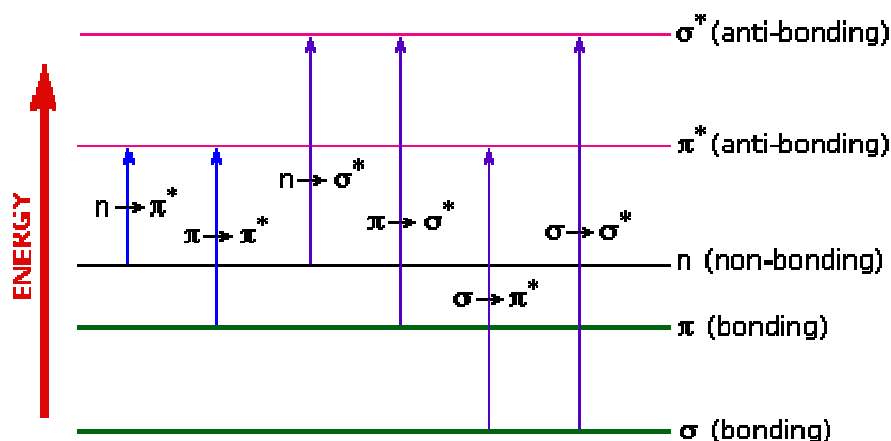


**Figure 3.7** Diagram showing the various kinds of electronic excitation that may occur in organic molecules.

As a rule, energetically favored electron promotion will be from the highest occupied molecular orbital (HOMO) to the lowest unoccupied molecular orbital (LUMO), and the resulting species is called an excited state.

When sample molecules are exposed to light having an energy that matches a possible electronic transition within the molecule, some of the light energy will be absorbed as the electron is promoted to a higher energy orbital. An optical spectrometer records the wavelengths at which absorption occurs, together with the degree of absorption at each wavelength. The resulting spectrum is presented as a graph of absorbance (A) versus wavelength. Absorbance usually ranges from 0 (no absorption) to 2 (99% absorption), and is precisely defined in context with spectrometer operation.

The absorbance of a solution increases as attenuation of the beam increases. Beer's Law states that absorbance is directly proportional to the path length,  $b$ , and the concentration,  $c$ , of the absorbing species according the equation:

$$A = \epsilon bc \quad (3.14)$$

Where  $\epsilon$  is a constant of proportionality, called the absorbtivity.

### **3.2.4 Phase Contrast Microscopy.**

Experiments on giant vesicles were performed using optical microscopy. In particular, phase contrast microscopy has been employed here to aid visualization of the vesicles under the microscope, without the addition of stains or dies in our samples.

Microscopic objects that are distinguished from their surround only by a difference of refractive index lose their Becke line and disappear when brought exactly into focus (Zernike, 1958) – the Becke line is a bright halo of light that appears around the perimeter of a particle when the indices of refraction of the particle and the surrounding medium are different or when the microscope is defocused). Phase contrast microscopy generates images in which contrast depends on the difference between the refractive index of observed object and the surrounding medium. In conventional dark-field microscopy, an annular aperture is introduced in the focal plane of the condensor and an annular beam-stop is placed in the back focal plane of the objective. When there is no sample in the microscope, light that passes through the condensor annulus is absorbed by the beam-stop in the objective and the image appears "dark".

However, a phase object (an object with a different refractive index) scatters some of the light passing through it. This scattered light is not blocked by the annular beam-stop in the objective and forms a bright image of the object (Figure 3.8).



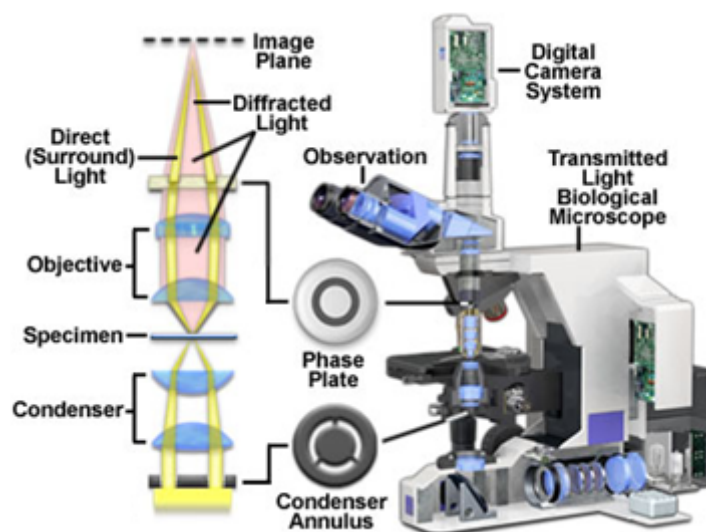


**Figure 3.8** Cut-away diagram of a modern upright phase contrast microscope, including a schematic illustration of the phase contrast optical train. Partially coherent illumination produced by the tungsten-halogen lamp is directed through a collector lens and focused on a specialized annulus (labeled condenser annulus) positioned in the substage condenser front focal plane. Wave-fronts passing through the annulus illuminate the specimen and either pass through undeviated or are diffracted and retarded in phase by structures and phase gradients present in the specimen. Undeviated and diffracted light collected by the objective is segregated at the rear focal plane by a phase plate and focused at the intermediate image plane to form the final phase contrast image observed in the eyepieces (from [www.microscopyu.com](http://www.microscopyu.com)).

### 3.3 INSTRUMENTS FOR IRRADIATING TREATMENTS

The instruments employed to irradiate membrane models were manufactured in Russia by the International Microwave Group composed by physicists, engineers, biologist and medical doctors of Nizhny Novgorod University. Today the company joined TEBAID, a universities consortium for applied biotechnologies, in which University of Calabria has a partnership.

#### 3.3.1 Wide band (53,57-78,33 GHz) noise source generator.

As a source of noise radiation it was used the instrument called AMPHIT.

This instrument irradiates in continuous wave mode (CW) the wide frequency band 53,37- 78,33 GHz. The output power is of the order of  $\mu\text{W}$ . Figure 3.9b reports the section of the instrument. The adaptor card (6) sends the right DC to the Diode (4), which generates the extremely high frequencies (EHF) putting them into the main

waveguide (2). Part of this radiation ends to the pyramidal absorber (5) and the remaining is conveyed to the output (1).

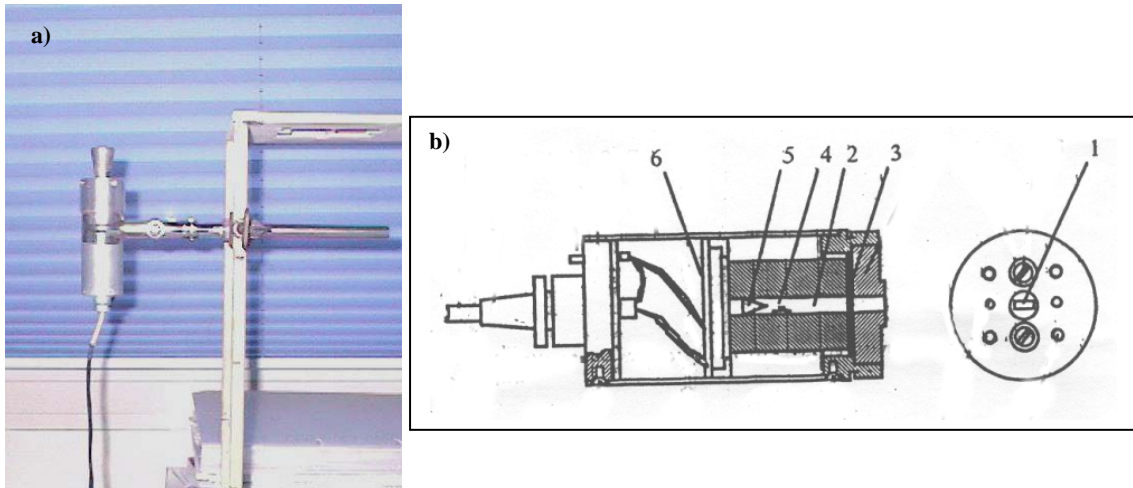


**Figure 3.9** a) A photograph of the instrument called AMPHIT. b) Section view of the “noise” generator AMPHIT. It emits continuous wave mode (CW) from 53,57 to 78,33 GHz. On the left the axial section is showed. On the right is the radial section. See text for description.

Power density is regulated with respect to the distance from the conical antenna of the instrument, by the following relation:

$$\rho = \rho_0 \left( \frac{d_0}{d + d_0} \right)^2 \quad (3.15)$$

where  $d_0=4,3$  cm,  $\rho_0=2,7 \cdot 10^{(-17)}$  is the power emitted for every irradiated Hz (W/Hz) and  $S_0=2,01$  cm<sup>2</sup> is the surface area of the conical antenna (Figure 3.10).

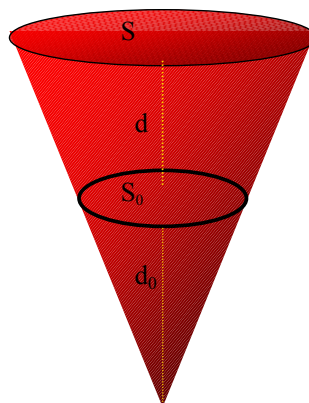


**Figure 3.10** Schematic view of the radiation pattern.

In Figure 3.11 the radiating power of AMPHIT is reported as function of the frequency. Such measure was performed by means of a microwave radiometer, previously developed in our laboratory. As could be noted, the emission of the instrument is not constant with the frequency, but it is comprised between  $10^{-17}$  W/Hz and  $10^{-19}$  W/Hz.

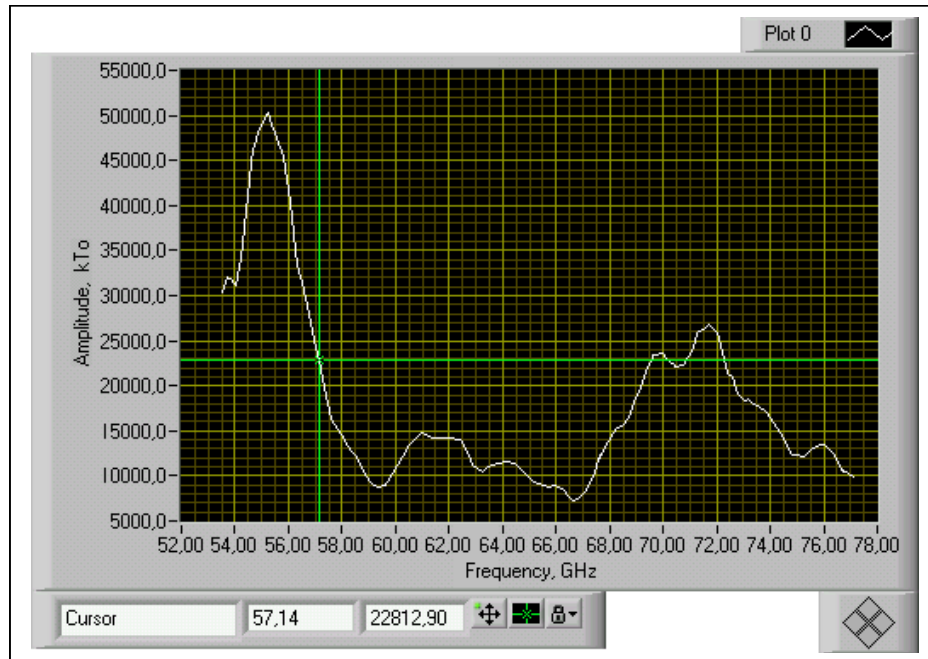


**Figure 3.11** Radiating power of AMPHIT as a function of frequency. The power level is different at different frequencies.

### 3.3.2 The IMG-56/76.

The unit called IMG-56/76 (Figure 3.12) is a very powerful tool for irradiating samples and has many peculiarities that is worth to mention. The working range of the instrument is from 52 to 72 GHz, having an output power between 0,15 and 0,45 mW.

IMG-56/76 can work in three main modes:

1. **Wide Band Mode:** in this mode the instrument emits covering all possible operating frequency in the working range 52-72 GHz.
2. **MONOCHROMATIC:** the operator can choose a frequency, in the working range of the instrument, and irradiate at that frequency.
3. **SCAN:** the instrument makes a scan of the frequencies between 52 and 72 GHz. Then it is able to detect the less reflected frequency which in turn must be the most absorbed one. In other words this device can reveal the maximum absorbed frequency of a system, in its own operating frequency range. Two sub-mode of the

scan mode are possible. Within the first one the instrument detect the 13 more absorbed frequencies and then manually, the operator can choose among them. In the second mode, called AUTOSCAN, the most absorbed frequency automatically is selected. In particular in this irradiation mode, the instrument scans all possible frequencies (from 52 to 72 GHz) every minute, and irradiates at the most absorbed frequency.

Furthermore this device can modulate the emitted frequency.



**Figure 3.12** The IMG-56/76 generator.

## **CHAPTER 4**

**Phase transition in multilamellar vesicles  
under MMWs: a  $^2\text{H}$  NMR study**

This chapter reports very original experiments made by using the  $^2\text{H}$ -NMR spectroscopy to probe the variation induced by prolonged millimeter wave irradiation on model membranes close to their main phase transition temperature.

This research idea originally took place after some electronic microscopy investigations, in which it was observed, by our research group, that morphological alterations of certain tumor membrane cells, (K-562 chronic leukemia), appeared after irradiation treatment (see section 2.3). In addition many papers report change in membrane properties after irradiation (see Chapter 2).

As already highlighted in Chapter 1, biological membranes are even more sensitive to external perturbations when close to a “critical temperature” that for natural membranes is their growth or body temperature, while for model membranes is the main phase transition temperature of the lipids they are made of, and this fact has led us to investigate particularly the effect of low power millimeter wave radiations on membrane models close to the lipid main phase transition temperature.

## 4.1 INTRODUCTION

Here we have studied the impact of MW on pure phospholipid membranes made of 1,2-Dimyristoyl-sn-glycero-3-phosphatidylcholine- $^2\text{H}_2\text{O}$  (DMPC/ $^2\text{H}_2\text{O}$ ) multilamellar vesicles (MLVs) that serve as biomimetic membranes. Samples were exposed in the 53-78 GHz frequency range, at Specific Absorption Rate (SAR)  $< 12$  mW/Kg. A new experimental setup, described in section 4.2.4, was assembled in order to irradiate the model membranes meanwhile recording their  $^2\text{H}$  NMR spectra. We have used deuterium nuclear magnetic resonance spectroscopy ( $^2\text{H}$ -NMR, see section 3.2.1) of heavy water to determine the properties of the membrane polar interface and their changes as a response to MW in strictly controlled temperature conditions. Heavy water can be appropriately used as a probe of membrane surface geometry and is particularly suitable for studying membrane phase transitions because a change in water quadrupole splitting ( $\Delta\nu_Q$ ) can be related to changes in bilayer structures (Davis, 1983; Chidichimo et al., 1985; Nagle and Tristram-Nagle, 2000). In fact, for unoriented MLVs (powder sample),  $\Delta\nu_Q$  is measured by the distance in Hz between the principal peaks of the powder spectrum (see section 3.2.1.2) and is given by (Chidichimo et al., 1985):

$$\Delta\nu_Q = \frac{3}{4}\nu_Q|S| \quad (4.1)$$

where,  $\nu_Q$  is the quadrupole coupling constant equal to 220 KHz;  $S$  is the water molecular order parameter averaged over the fast anisotropic molecular reorientations and is a direct measure of the ordering of water molecules at the polar interface (Cheng et al., 2003). It brings information on the dynamic processes involved at the membrane/water interface and is therefore sensitive to the membrane phase.

This experimental strategy is also linked to the hypothesis that water is the primary site of interaction with microwaves (Fröhlich, 1983).

The study of the effect of low power millimeter waves on the phase transition of multilamellar vesicles has resulted in a manuscript, actually under revision for publication.

## **4.2 MATERIALS AND METHODS**

### **4.2.1 Materials.**

1,2-Dimyristoyl-sn-glycero-3-phosphatidylcholine (DMPC) was purchased from Sigma Aldrich with a 98.8 % purity and used without further purification. <sup>2</sup>H<sub>2</sub>O was obtained from Cambridge Isotope Inc. having a purity of 99.98 %.

### **4.2.2 Sample preparation.**

Multilamellar vesicles (MLVs) were prepared as described elsewhere (Chidichimo et al., 1985). Samples, containing  $11 \pm 1$  water moles per mole of lipids ( $n_w$ ) were investigated. They were weighted and stored at 37 °C for three days. Before performing the exposure treatment, <sup>2</sup>H NMR spectra were recorded over 48 h to ensure the time stability of the observed splitting. After any exposure, samples were weighted to check out for water evaporation.

### 4.2.3 $^2\text{H}$ -NMR acquisitions.

Deuterium spectra were acquired with a Bruker Avance 300 spectrometer at 46.52 MHz using a phase cycled quadrupole echo sequence with  $\pi/2 = 7 \mu\text{sec}$ ,  $\tau_2 = 50 \mu\text{sec}$  and a recycle delay of 1 s followed by Fourier transformation. 32 to 128 transients were averaged with a spectral width of 30 KHz. A 20 Hz exponential multiplication was performed on the free-induction decay (FID).

Phase transition was monitored with a precision on T of  $\pm 0.2 \text{ }^\circ\text{C}$ , controlled by the Bruker VT 2000 unit. Samples were brought in the  $L_\alpha$  phase, above  $T_m$ , and their temperature was gradually decreased in steps of  $0.2 \text{ }^\circ\text{C}$  in order to enter into the  $P_\beta$  phase. For each new T value, the systems were equilibrated for at least 30 min prior to acquisition. The reverse process ( $P_\beta$  to  $L_\alpha$ ) was studied increasing the temperature in the same way.

### 4.2.4 Real-time NMR acquisition under exposure.

MW exposure was performed by means of a microwave wide-band generator (Amphit-32, MicroMedTech, Nizhny Novgorod, Russia) in the 53.57-78.33 GHz range (see section 3.3.1). The frequency-dependent emission spectrum of this generator (Figure 3.11), measured by a radiometer (IMG Panorama, MicroMedTech, Nizhny Novgorod, Russia), exhibited several relative maxima and minima with output power in the range 5-20  $\mu\text{W}$ . This radiation source was chosen due to its wide-band characteristic and its use in biomedicine (Pakhomov et al., 1998; Radzievsky et al., 2004). To allow real time detection of NMR spectra during exposure, the MW generator was connected to a diamagnetic cylindrical waveguide of variable length terminating with a dielectric Teflon antenna inserted into the NMR probe with a vertical coil (Figure 4.1). The dielectric antenna was inserted into a 10 mm glass tube, containing a sample tube of 5 mm. The waveguide was kept outside the NMR acquisition volume to avoid interference with the radiofrequency signal of the coil. Spectra recorded with this set-up show that the antenna did not affect the measurement. Sham exposure conditions correspond to the same set-up but with the generator turned off (Incident power density = 0). NMR spectra were acquired in real-time in strictly controlled temperature conditions.



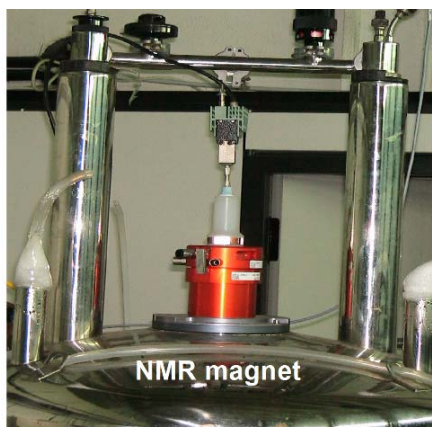


**Figure 4.1** MW exposure set-up for  $^2\text{H}$  NMR measurements in real time. The whole irradiating system is inserted in the NMR magnet.

#### 4.2.5 Dosimetry.

The exposure set-up was made up of different modules of circular waveguides (internal radius of 2 mm), feeding at one end by the MW source and terminated on the other end with a dielectric antenna (Figure 4.2). The dielectric antenna was made up of Teflon, with a radius of 3 mm and height of 40 mm (Figure 4.2a). At the end of the dielectric antenna the NMR tube (internal radius 3 mm, height 15 mm) filled with the sample (thickness between 3-5 mm, depending on the sample preparation) is positioned (Figure 4.2).

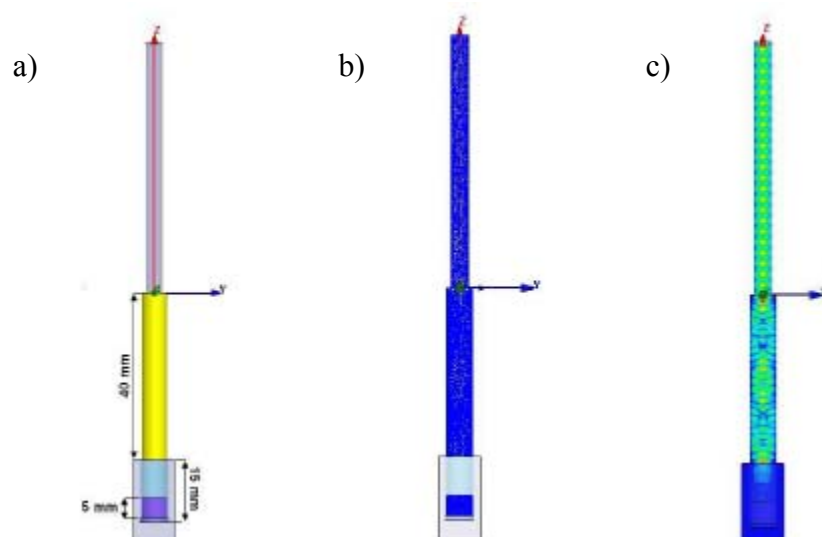


**Figure 4.2** Model of the scenario. a) The MMWs applicator (a circular waveguide terminated with a dielectric probe) inserted into a NMR tube with the exposed sample (radius 3 mm and height 3-5mm). b)

Tetrahedral mesh generated by the FEM Method; c) Electric field amplitude of the model in the xz plane of the structure ( $f = 74$  GHz, input power 1 W).

The power deposition pattern inside the sample was evaluated numerically by using Ansoft HFSS, a commercial code based on the Finite Element Methods (FEM) (Jin, 1999), running on a typical laptop (2 GB RAM).

Due to the wide range investigated, several simulations were carried out considering different medium complex relative permittivities,  $\epsilon = \epsilon' - j \epsilon''$ , while the density was  $\rho = 1110$  kg/m<sup>3</sup>. In Table 4.1 the assumed parameters are reported, being  $\omega = 2 \pi f$ ;  $\epsilon_0 = 1 / (36 \pi \times 10^9)$  F/m and  $\epsilon'' = \sigma_{eq} / \omega \epsilon_0$ . Permittivity values of DMPC membranes at these frequencies are unknown. We have therefore assumed that they can be described by those of the analogous membrane system 1,2-Dioleoyl-sn-Glycero-3-Phosphocholine (DOPC), for which they have been measured in the 0.2-1.2 THz frequency range (Tielrooij et al., 2009). We have calculated the dielectric properties at frequencies  $< 0.2$

THz simulating a double-Debye dispersion equation  $\hat{\epsilon}(f) = \epsilon_\infty + \frac{\Delta\epsilon_1 2\pi\tau_D}{1+i2\pi f\tau_D} + \frac{\Delta\epsilon_2 2\pi\tau_2}{1+i2\pi f\tau_2}$

with  $\Delta\epsilon_1 = 8.8$ ,  $\Delta\epsilon_2 = 0.89$ ,  $\epsilon_\infty = 2.3$ ,  $\tau_D = 8$  ps and  $\tau_2 = 121$  fs that holds for DOPC membrane at  $n_w = 9$  in the range 0-1.2 THz (Tielrooij et al., 2009).

According to the FEM method, the region of interest was divided in tetrahedral elements (134891); the mesh generation (Figure 4.2b) was based both on the material wavelength  $\lambda_m$  (at 53.57 GHz  $\lambda_m = 2.5$  mm, at 74 GHz  $\lambda_m = 1.3$  mm) refinement and on the length based mesh refinement; thus the length of the tetrahedral elements were refined until they were below a specified value. In this case we adopted as the maximum length of a tetrahedron (i.e. the length of its longest edge)  $l = 0.5$  mm.

In particular the following dosimetric parameters were calculated (Calabrese et al., 2006):

- $|E_u(x,y,z)|$ : the local electric field amplitude per unit incident power [V/m]. This was evaluated at each node of the computing domain Figure 4.2c).
- $SAR_u(x,y,z) = \sigma_{eq} |E_u|^2 / 2\rho$ : the local absorbed power per unit mass and per unit incident power [W/kg]. This is also the local specific efficiency, and it is zero outside the sample ( $\sigma_{eq} = 0$ ). It is understood that, should the incident power be  $P_0 = 1$  W, the local absorbed power per unit mass would be  $P_0 \times SAR_u(x,y,z) = SAR(x,y,z) =$  specific absorption rate [W/kg].
- $AV_u$ : the average  $SAR_u(x,y,z)$  over the sample [(W/kg)/W].

**Table 4.1** Electromagnetic parameters adopted in numerical simulations.

medium	$f$ [GHz]	$\epsilon_r$ <sup>a</sup>	$\epsilon_r$ <sup>'a</sup>	$\sigma_{eq}$ <sup>b</sup> [S/m]
DMPC- $^2\text{H}_2\text{O}$	53.57	4.3	3.0	8.9
(MLVs) $n_w=11$	65.00	4.0	2.6	9.4
	74.00	3.8	2.3	9.5
quartz glass (NMR tube)		3.78		
teflon		2.10		

<sup>a</sup>Calculated by a double-Debye equation  $\hat{\epsilon}(f) = \epsilon_\infty + \frac{\Delta\epsilon_1 2\pi\tau_D}{1+i2\pi f\tau_D} + \frac{\Delta\epsilon_2 2\pi\tau_2}{1+i2\pi f\tau_2}$  with  $\Delta\epsilon_1 = 8.8$ ,  $\Delta\epsilon_2 = 0.89$ ,  $\epsilon_\infty = 2.3$ ,  $\tau_D = 8$  ps,  $\tau_2 = 121$  fs.

<sup>b</sup>Calculated by  $\sigma_{eq} = 2\pi f \epsilon_0 \epsilon_r''$

## 4.3 RESULTS

### 4.3.1 MW induced effect on the membrane main phase transition.

Figure 4.3a shows a sequence of  $^2\text{H}$ -NMR spectra acquired at different temperatures across the main phase transition temperature  $T_m$  (25.5 °C) of the DMPC- $^2\text{H}_2\text{O}$  membrane having a water/lipid mole ratio ( $n_w$ ) of 11. The spectra a and b are typical powder patterns of the fluid phase ( $L_\alpha$ ). When the system reaches  $T_m$ , a clear discontinuity in the lineshape occurs and the spectrum becomes a singlet, typical of the ripple  $P_\beta$  phase (spectrum d) (Pope et al., 1981). The  $L_\alpha \rightarrow P_\beta$  phase transition can be advantageously monitored by the decrease of the water splitting upon cooling, as shown in Figure 4.3b. The discontinuity near  $T_m$ , at which the splitting drops to  $\approx 110$  Hz, reflects the discontinuity in the NMR lineshape. A reduced splitting effectively indicates a loss of water order (Eq. 4.1) that becomes maximum at the main phase transition. It must be noted that  $\Delta\nu_Q$  decreases in the fluid phase and increases in the ripple phase as the temperature decreases (Figure 4.3a sequences a-c and d-g, respectively).

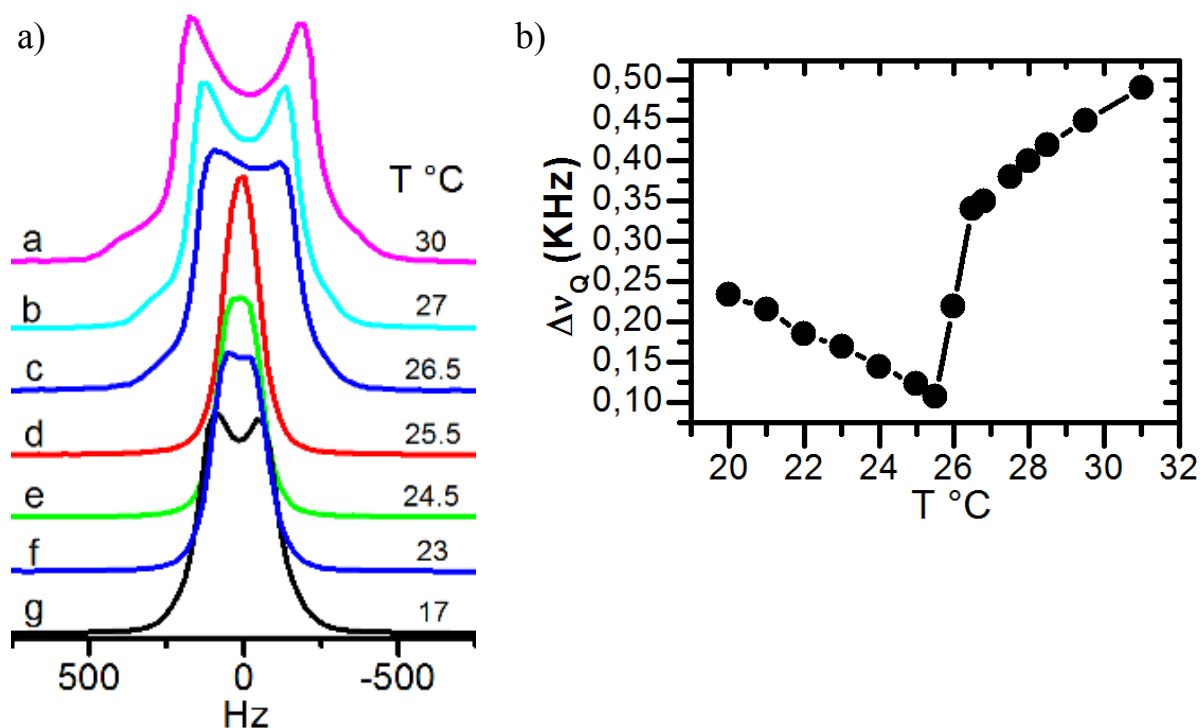


**Figure 4.3** DMPC- $^2\text{H}_2\text{O}$  membrane phase transition. a) Sequence of  $^2\text{H}$ -NMR spectra for the DMPC- $^2\text{H}_2\text{O}$  membrane with  $n_w = 11$  acquired at different temperatures across the fluid/ripple first order transition (a-c, fluid phase; d-g ripple phase). b) Heavy water quadrupole splitting temperature dependence, across the transition point. At  $T_m = 25.5$  °C, a discontinuity occurs due to the transition from the fluid ( $L_\alpha$ ) to the ripple ( $P_\beta'$ ) phase.

In order to evaluate the potential effects of MW on the membrane at different temperatures, a real-time exposure set-up was conceived (see section 4.2.4).  $^2\text{H}$ -NMR spectra were acquired during the exposure experiments by strictly controlling and accurately adjusting the temperature of the membrane samples inside the probe. The response of the DMPC- $^2\text{H}_2\text{O}$  membrane to MW, was first evaluated near the transition point, at 25.0 °C. In these conditions, the membrane was in the ripple phase close to  $T_m$  (Figure 4.3a and b). The results of the exposure experiment are summarized in Figure 4.4 where the dependence of  $\Delta\nu_Q$  on the exposure time and temperature is reported for the sham and MW exposed samples. No significant changes were observed after 3 h of exposure on both samples neither in the lineshape, that still exhibited the characteristic singlet of the ripple phase (Figure 4.3a spectra d and e), nor on the width of the signal. It should be further noted that, at constant temperature, both samples showed a long term thermal stability. Next, the temperature was gradually raised above  $T_m$ , still under

exposure, in order to induce the transition to the fluid phase. The splitting increased in both samples as expected, but significantly less in the MW exposed one (Figure 4.4).

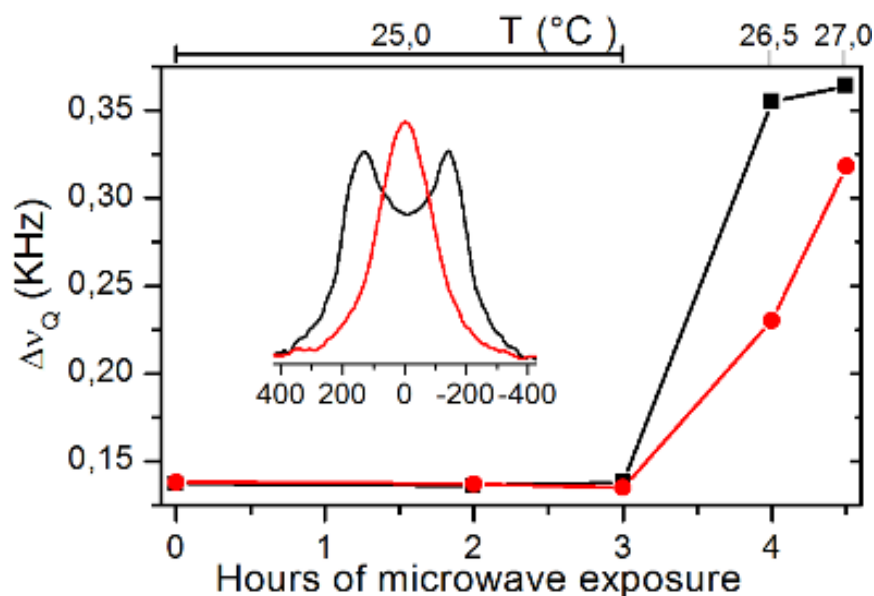


**Figure 4.4** Effects of MW on the  $P_{\beta'} \rightarrow L_{\alpha}$  transition. Heavy water quadrupole splitting as a function of the microwave exposure time and temperature for the DMPC- $^2\text{H}_2\text{O}$  membrane ( $n_w=11$ ). No effects were observed in the first 3 hours ( $T = 25.0$  °C) on the sham (black line) and microwave exposed (red line) samples. The inset shows the spectra acquired for the sham (black spectrum) and the microwave exposed (red spectrum) samples at  $26.5$  °C ( $T > T_m$ ). The transition to the fluid phase occurred only in the sham exposed sample (doublet).

Moreover, the inset in Figure 4.4 clearly shows that, at  $26.5$  °C, the sham sample (black line) got into the  $L_{\alpha}$  phase, as visible from the doublet appearance, while the MW exposed one was still in the  $P_{\beta'}$  phase (red singlet), even though  $T > T_m$ . Under microwave exposure conditions, a doublet was observed only after a further temperature increase up to  $27$  °C. This phase transition temperature delay is to be clearly attributed to the radiation that acts against the opposite thermal trend.

In order to confirm the microwave induced upward shift of the transition point, the response of the membrane was studied on the fluid phase side of the transition region as a function of the exposure time and temperature (Figure 4.5 a and b). The effect of the radiation was analyzed qualitatively by observing the 1 h interval spectral sequence reported in Figure 4.5a relative to the first 4 h of exposure, keeping  $T=27$  °C (close to  $T_m$ ). Relevant changes in the lineshape were observed only for the MW exposed system and revealed an overall reduction of the water order. This effect is quantitatively shown

in Figure 4.5b, where the water splitting dependence on the exposure time is displayed for the sham (black line) and microwave (red line) exposure conditions. During the first 4 h, the splitting of the sham exposed sample did not change, indicating a long term thermal stability. In contrast, under microwave exposure, a time-dependent decrease of the splitting was found, reaching a maximum (from  $\approx 350$  to  $\approx 240$  Hz) at 4 hours. Subsequently, the temperature was gradually lowered (but still kept above  $T_m$ ) and, after an initial slight reduction at  $26.5^\circ\text{C}$ , a significant splitting increase was observed.

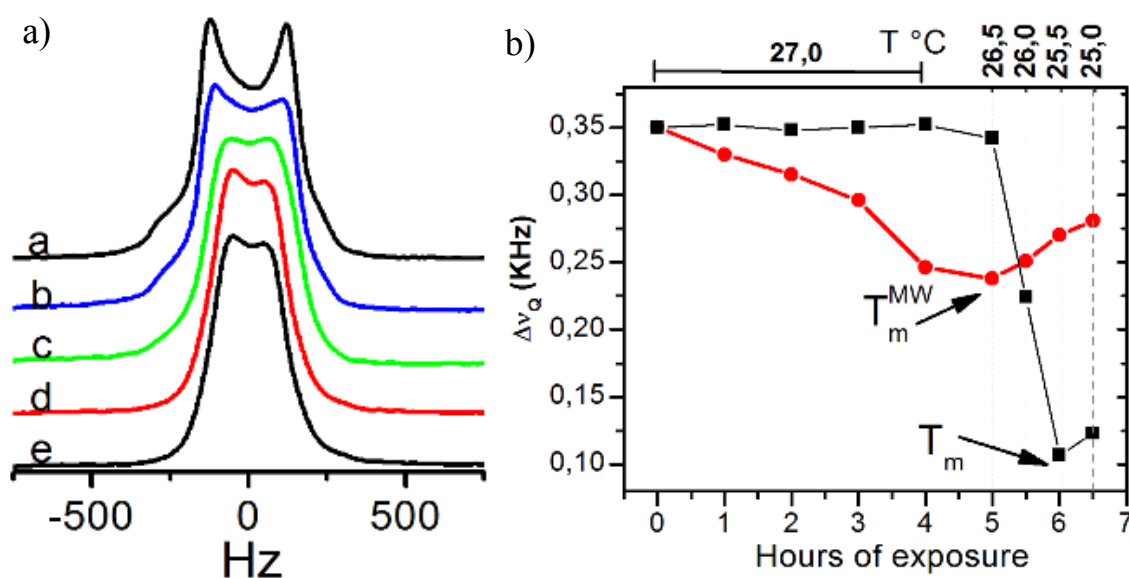


**Figure 4.5** Effects of MW on the  $L_\alpha \rightarrow P_\beta$  transition a) Deuterium NMR lineshape changes for the DMPC- $^2\text{H}_2\text{O}$  membrane ( $n_w = 11$ ) induced by microwaves at constant  $T = 27^\circ\text{C}$  as a function of the exposure time (see Figure 4.3a for comparison). b) Quadrupole splitting of water ( $^2\text{H}$ ), as a function of the exposure time and temperature for the sham (■) and microwave exposed (●) samples. Microwaves induce an upwards shift of the transition point. Black and red lines are drawn to show the different trends.

This trend is qualitatively analogous to that observed in the sham exposed sample during the  $L_\alpha \rightarrow P_\beta$  phase transition (Figure 4.3b and 4.5b, black line), but the minimum splitting was shifted to a higher temperature under microwave exposure. On the other hand, the lineshape changes discussed in Figure 4.5a, are qualitatively similar to those observed on the sham exposed system during the  $L_\alpha \rightarrow P_\beta$  transition (Figure 4.3a), even though the doublet did not completely disappear under MW exposure.

These results do effectively indicate that the microwave exposed DMPC membrane is pointing towards a transition point at  $T_m^{MW} \approx 26.5^\circ\text{C} > T_m$ . It must be noted, however,

that the discontinuity in the splitting and in the lineshape observed in the microwave exposed membrane is less pronounced compared to that in the unperturbed system.

### 4.3.2 Dosimetric study.

The effects described above are clearly nonthermal since the radiation always acts to contrast the opposite thermal trend. On the other hand, no induction of heating is expected due to the very low incident power densities used. The electromagnetic power absorbed by the sample inside the NMR probe, calculated by performing extensive dosimetric simulations, are summarized in Table 4.2 (and Figure 4.6). It reports the average (AV) Specific Absorption Rate values (SAR) at three different frequencies in the GHz range investigated, for the whole sample as well as for different layers of the sample along the direction of propagation of the radiation. Each layer is 1 mm thick; the layer 1 identifies the sample top while the layer 5 (or 3) the bottom one.

**Table 4.2** SAR values for different sample layers in case of 1W (average) and 20 $\mu$ W input power.

$f$ [GHz]	Layers	$AV_u^*$ (W/kg)	$AV_u^\dagger$ (whole sample) (W/kg)	$SAR^\ddagger$ (mW/kg) 30 $\mu$ W input power
53.57	1	322.6	86.0	9.7
	2	59.7		1.8
	3	28.2		0.8
	4	17.2		0.5
	5	30.5		0.9
65.00	1	244.9	68.9	7.3
	2	60.7		1.8
	3	24.9		0.7
	4	13.2		0.4
	5	27.4		0.8
74.00	1	381.1	133.9	11.4
	2	141.7		4.3
	3	66.6		2.0
	4	43.8		1.3
	5	101.7		3.1
74.00 <sup>§</sup>	1	281.8	168.7	8.5
	2	122.3		3.7
	3 (bottom)	143.7		4.3

\* Average SAR per 1 W incident power for each 1 mm thick sample layer into which the sample has been divided along the z axis;  $^\dagger$  Average SAR per 1 W incident power for the whole sample;  $^\ddagger$  SAR values scaled down to 20  $\mu$ W incident power corresponding to the maximum power emitted by the Amphit-32 generator;  $^\S$  Calculated on a 3 mm thick sample for an output power of 20  $\mu$ W

The results show that, as expected due to the high conductivity of the membrane system (Table 4.1), the  $\text{AV}^{\text{u}}$  SAR values are higher on the top of the sample (Figure 4.6a and b) and decrease approaching the bottom layer (Figure 4.6a); the latter is higher than the next internal layer because of the coupling with the walls of the quartz sample holder. In Table 4.2, the corresponding SAR at the maximum input power applied (20  $\mu\text{W}$ ), is reported too. Finally, the results for a 3 mm sample thick at 74 GHz (higher SAR condition) are also shown. The SAR levels are in all cases much lower than 1.6 W/kg, the currently accepted safety limits for nonthermal effects (ICNIRP, 1998).

From our knowledge, we have reported the first experimental proof of a nonthermal effect of microwaves on a biological membrane.

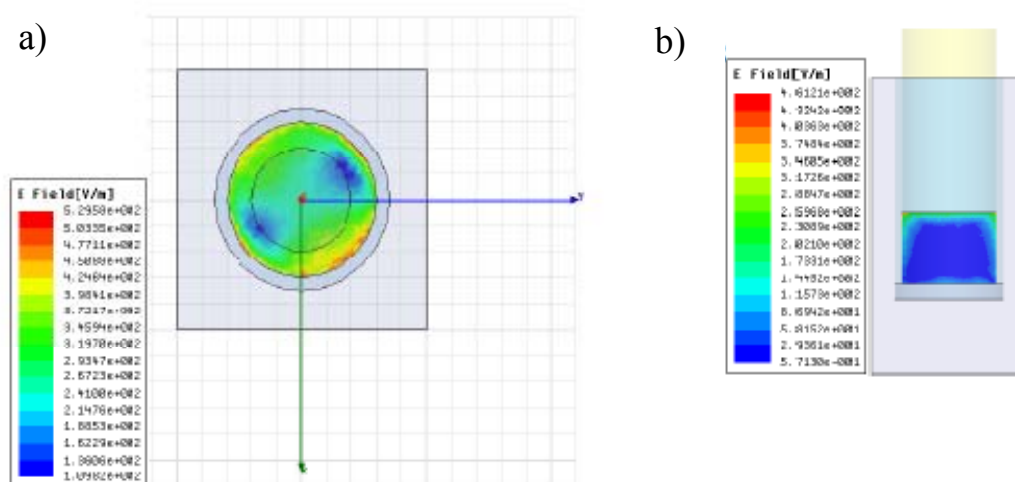


**Figure 4.6** Local electric field amplitude per unit incident power [V/m]. a) Electric field amplitude on the top layer and b) on the yz plane of the exposed sample ( $f = 74$  GHz, input power 1 W).

### 4.3.3 Theoretical interpretation.

The crucial questions are: i. How can these small amounts of MW energy ( $< k_{\text{B}}T$ ) affect the membrane behaviour in such a relevant way? ii. Which are the biophysical phenomena involved in the MW-membrane interaction? A possible mechanism based on the theory of the phase transition in phospholipid bilayer systems is provided here. Let's recall, therefore, that the ordered/fluid transition is of first order type. This can be clearly seen by the discontinuity of the splitting reported in Figure 4.3b. However, phospholipid membranes show precritical (or pretransitional) phenomena near the transition point



such as the nonlinear increase of the membrane permeability (Papahadjopoulos et al., 1973; Doniach, 1978; Nagel and Scott, 1978) and the anomalous swelling (Richter et al., 1999). Another pretransitional phenomenon is the non linear decrease of the water order parameter when approaching  $T_m$ , shown in Figure 4.3b. Precritical phenomena have been described by thermal fluctuations of the orientational order parameter associated to the lipid chains (Jähnig, 1981a and 1981b), as well as by lateral packing density (Ipsen et al., 1990) and membrane area fluctuations (Hawton and Doane, 1987). Near the transition point, fluctuations increase and this, in turn, results in a non linear increase of some membrane response functions, as those cited. The precritical phenomena are interrupted by the intervening of the first order transition, so that the membrane does not reach the critical (or pseudocritical) temperature ( $T_c$ ) at which the response functions would diverge (Jähnig, 1981a).

First order phase transitions that exhibit precritical behaviour (weakly first order) can be treated with the general theory of Landau as they would be of second order (Jähnig, 1981a). Landau's theory is based on the universal behaviour of many-particle systems near the phase transition, i.e., the decrease of the order parameter as  $(T - T_c)^x$  and the increase of the order parameter fluctuations as  $|T - T_c|^{-x}$ , where  $x$  is the critical exponent. This behaviour is determined by the onset of cooperativity (or long range order) at the transition point that is preceded by the pretransitional increase of the order parameter fluctuations. The term precritical is used to stress the analogy between this type of phase transition and those of second order for which the order parameter exhibits a continuous change (Jähnig, 1981a).

$^2\text{H}$ -NMR studies have shown that heavy water/phospholipid membrane systems exhibit a reduction of the water order parameter approaching  $T_m$  (Hawton and Doane, 1987). This interesting and universal behaviour has been explained by the increase of the thermal fluctuations of the area per lipid molecule near the transition point (Hawton and Doane, 1987). It has been suggested that the water orientational order averages to zero in regions of the bilayer where area fluctuations exceed a value  $\Delta A_0$  corresponding to the size of one or few water molecules. In these interfacial regions, the membrane surface can be considered more soft in relation to its reduced ordering capability on water molecules. Area fluctuations can therefore be interpreted as fluctuations between hard and soft membrane local states.

The orientational order parameter of water was used in the context of Landau's theory, to describe the phase transition. For a mode with Landau free energy =  $kT/2$ , the normalized time-averaged water quadrupole splitting ( $\frac{\Delta v_Q}{\Delta v_0}$ ) is proportional to the inverse of the area fluctuations:

$$\frac{\Delta v_Q}{\Delta v_0} = \Delta A_0 \left(\frac{2}{\pi}\right)^2 \left(\frac{a}{kT}\right)^x |T - T_c|^x \quad (4.2)$$

where,  $\Delta v_0 = 1.22$  KHz, is the quadrupole splitting at high temperatures where no fluctuations occur, i.e., far from the precritical region, and  $a > 0$  is a phenomenological coefficient derived from the free energy density expansion in terms of the order parameter (Jähnig, 1981a, Hawton and Doane, 1987). It essentially affects the curvature of the free energy parabola around the equilibrium state and therefore, the precritical behaviour of the system (Jähnig, 1981a). The normalized splitting in Eq. (4.2) is the probability that area fluctuations in the headgroup region are smaller than  $\Delta A_0$ . As the temperature approaches the critical point, this probability goes to zero. This can be seen in Figure 4.7a showing the fitting of our normalized splitting values by Eq. (4.2). The black line is the best fit of the data for the sham exposed system (■), giving the results reported in Table 4.3, in good agreement with the theory (Jähnig, 1981a) and the results presented by Hawton and Doane (1987). In the fitting analysis, the only parameter constraint was  $\Delta A_0 \geq 6.16 \text{ \AA}^2$ , being this the van der Waals area of a water molecule (Finney, 2001).

The results of the same fitting analysis for the microwave exposed sample (Figure 4.7a, ●), are also reported in Table 4.3. For clarity, the critical temperatures for the  $L_\alpha \rightarrow P_{\beta'}$  and  $P_{\beta'} \rightarrow L_\alpha$  transitions, are respectively indicated in Figure 4.7a with the symbols  $T_c^{L\alpha}$  and  $T_c^{P\beta'}$  for the sham sample and with  $T_c^{L\alpha}(MW)$  and  $T_c^{P\beta'}(MW)$  for the exposed one.

The fitting analysis shows that under microwave exposure there is i. an upward shift of the critical temperatures and ii. a broadening of the transition region. In particular,  $T_c^{P\beta'}(MW)$  is shifted close to  $T_m^{MW}$ , so that the critical point is closer to the transition point and consequently, the phase transition under microwave exposure behaves more like one of second order.

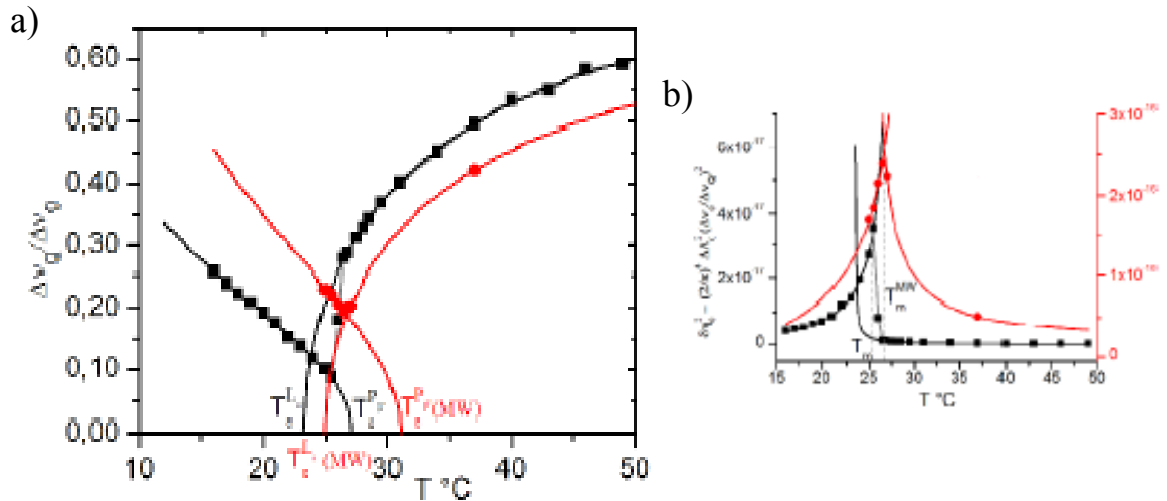


**Figure 4.7** Effect of microwaves on the membrane dynamic behaviour near the transition. a) Under MW exposure, the change of the order parameter of water in DMPC-<sup>2</sup>H<sub>2</sub>O ( $n_w = 11$ ) at  $T_m$  is less pronounced (●), the transition temperature, as well as the critical temperatures  $T_c^{L\alpha}$  and  $T_c^{P\beta'}$  respectively for the  $L_\alpha \rightarrow P_{\beta'}$  and  $P_{\beta'} \rightarrow L_\alpha$  transitions, are shifted upward and the transition region is broader compared to the unperturbed, sham exposed membrane (■). Solid lines are the best fits of the data performed by Eq. (4.2) that gives the results reported in Table 4.2. b) Strength of the order parameter fluctuations  $\delta\eta_0^2$ , as a function of temperature. In the sham exposed membrane (■), the pretransitional increase is interrupted by the intervening of the first order transition at  $T_m$ . In the microwave exposed sample (●), the criticality of the membrane is greatly enhanced near the transition point that is shifted to a higher temperature ( $T_m^{MW}$ ) compared to the unperturbed, sham exposed membrane. It can be also seen that the critical temperature of the fluid to ripple transition is shifted very close to  $T_m^{MW}$  (Table 4.3). Data points for the MW exposed sample correspond to the largest normalized splitting observed during exposure.

**Table 4.3** Fitting results of the normalized splitting by Eq. (4.2).

DMPC- <sup>2</sup> H <sub>2</sub> O		$T_c$ (°C)	$\chi$	$a$ (Jk <sup>-1</sup> m <sup>-1</sup> )	* $\Delta A_0$ (Å)
$n_w = 11$					
Sham	$L_\alpha \rightarrow P_{\beta'}$	$23.8 \pm 0.2$	$0.49 \pm 0.04$	$(1.5 \pm 0.03) \times 10^{-4}$	$7.62 \pm 0.07$
	$P_{\beta'} \rightarrow L_\alpha$	$27.2 \pm 0.3$	$0.46 \pm 0.02$	$(2.5 \pm 0.04) \times 10^{-4}$	$12.9 \pm 1.9$
MW	$L_\alpha \rightarrow P_{\beta'}$	$24.8 \pm 0.2$	$0.51 \pm 0.03$	$(6.0 \pm 0.1) \times 10^{-5}$	$6.17 \pm 0.8$
	$P_{\beta'} \rightarrow L_\alpha$	$30.1 \pm 0.6$	$0.48 \pm 0.02$	$(7.0 \pm 0.6) \times 10^{-5}$	$12.2 \pm 2.1$

\*The parameter  $\Delta A_0$  was set  $> 6.16 \text{ \AA}^2$

According to Jähnig (1981b), the membrane response,  $\delta\eta$ , to a small external force,  $\delta\phi$ , can be expressed as  $\delta\eta = \chi\delta\phi$  where  $\chi$  is the response function dependent on  $T$ . The membrane response function is proportional to the strength of the order parameter fluctuations,  $\delta\eta_0^2$  (Jähnig, 1981b):

$$\chi = \frac{\delta\eta_0^2}{k_B T} = \frac{1}{a|T-T_c|} \quad (4.3)$$

where

$$\delta\eta_0^2 = \frac{k_B T}{a} \frac{1}{|T-T_c|} \quad (4.4)$$

In terms of our observable ( $\Delta\nu_Q$ ), a relation is found between  $\frac{\Delta\nu_0}{\Delta\nu_Q}$  and  $\delta\eta_0^2$  by combining Eq. (4.2) and (4.4) ( $x=1/2$ , see Table 4.3):

$$\delta\eta_0^2 = \left(\frac{2}{\pi}\right)^4 \left(\frac{\Delta\nu_0}{\Delta\nu_Q}\right)^2 \Delta A_0^2 \quad (4.5)$$

where,  $\frac{\Delta\nu_0}{\Delta\nu_Q}$ , the inverse of the normalized splitting, is the probability that area fluctuations are greater than  $\Delta A_0$ . From Eq. (4.3) and (4.5), the response function can be expressed in terms of the measurable quantity  $\frac{\Delta\nu_0}{\Delta\nu_Q}$ :

$$\chi = \frac{\delta\eta_0^2}{k_B T} = \left(\frac{2}{\pi}\right)^4 \frac{\left(\frac{\Delta\nu_0}{\Delta\nu_Q}\right)^2 \Delta A_0^2}{k_B T} \quad (4.6)$$

As  $T$  approaches  $T_c$ , the response function diverges. In the case of a precritical first order transition, a discontinuity occurs in the response function at  $T=T_m$ , that interrupts the pretransitional increase.

Figure 4.7b shows the strength of the membrane area fluctuations as a function of  $T$ , for the unperturbed (■) and MW exposed (●) systems. The straight lines have been obtained by fitting the experimental points with Eq. (4.5) and taking into account the value of  $\Delta A_0$  and  $a$  found in the previous fitting analysis. Under MW exposure, the pretransitional phenomena are markedly enhanced compared to the sham exposed membrane. From Eq. (4.6), it is obvious that the membrane response function behaves in an analogous way as  $\delta\eta_0^2$ .

It is worth noticing that a “threshold” value of the microwave energy is required in order to observe a significant increase of the response function (i.e., a reduction of the water

order parameter). For instance, the point at 37 °C of Figure 4.7b was obtained after about 3 h of exposure. Hence, a defined work must be done on the membrane to change its precritical behavior. As shown in the dosimetric study, this work is small compared to the thermal energy. Actually, this is not very surprising considering that, the energy needed to induce the fluid to gel phase transition by applying osmotic pressures on different PC systems, is  $< k_B T$  (Parsegian et al., 1986).

## 4.4 DISCUSSION

### 4.4.1 Membrane-MW interaction: a microscopic interpretation.

Membrane-MW interaction must involve a coupling between some polarized states of the lipid bilayer and the MW electric field,  $E_{MW}$ . We have previously assumed that membrane area fluctuations occur between hard and soft polar surface states. Thus, fluctuations in the membrane polarization do occur in the pretransitional regions due to collective interactions. When the transition is approached from above, fluctuations of the lateral density of lipid chains lead to transient (dynamic) gel phase domains within the fluid phase which increase as closer is  $T$  to  $T_m$  (Ipsen et al., 1990). Hence, at least near the transition point, a two states description of the membrane polarizability can be done, as early suggested (Bond and Wyeth, 1986). One can assume that  $E_{MW}$  affects the population of these two polarized states and, consequently, the overall polarization,  $P$ . In this case, the electric susceptibility  $\chi$  represents a useful response function for describing the effect of the radiation:

$$\chi = \left( \frac{\partial P}{\partial E_{MW}} \right)_T \propto \frac{1}{a|T-T_c|} \quad (4.7)$$

It is worth considering what is the primary mechanism of interaction by taking into account the structure of the membrane components and, above all, their characteristic relaxation dynamics. Different temperature-dependent relaxation times including the range of MW frequencies ( $10^{-7}$  to  $10^{-12}$  s) (Jähnig, 1981a), have been measured in membrane systems. Membrane area fluctuations involve a macroscopic reorganization of the mesophase that typically occurs with slower relaxation dynamics than the

characteristic time of the MW radiation (Jähnig, 1981a). Also the fluctuation of water molecules between the two above mentioned phase domains, which occurs at the characteristic time of water diffusion, are too slow to interact with microwave. The local motions of water molecules, having typical relaxation frequencies in the range 0.1-9 ps (Beneduci, 2008; Tielrooij et al., 2009), need then to be considered. A further coupling mechanism of the radiation with the membrane can occur, as early suggested (Bond and Wyeth, 1986), due to the local dipole fluctuations of the C-H bonds which fall in the range  $10^{-10}$ - $10^{-11}$  s (Doniach, 1978). However, due to the large dielectric permittivity of water at these frequencies (Beneduci, 2008), it is expected that the interaction with its permanent dipoles should play a predominant role. One important local fluctuation of the water molecules, occurring in the neighborhood of  $T_m$ , has been pointed out by Westlund and collaborators (Westlund, 2000; Sparmann and Westlund, 2003; Aman et al., 2003) who were able to justify both the evolution of  $^2\text{H}$  (water) and  $^{14}\text{N}$  (choline group) NMR quadrupole interactions and the typical relaxation times of the magnetization by considering the variation of water distribution among two interfacial regions in which the local water orientational order parameter would have opposite sign. These two regions have been, for simplicity, identified as the phosphate and the choline binding sites. In this case,  $\Delta\nu_Q$  is expressed by a weighted sum of the contribution of bound water at each site:

$$\Delta\nu_Q = \frac{3}{4}\nu_Q |P_{B_-}S_{B_-} + P_{B_+}S_{B_+}| \quad (4.8)$$

considering that  $P_{B_-} + P_{B_+} = P_B$  and  $P_{B_-}S_{B_-} + P_{B_+}S_{B_+} = P_B S_B < 0$ , where,  $S_{B_{\mp}}$  (-0.0372 and +0.0120) are the orientational order parameters of water at the - (phosphate) and + (choline) interface regions.  $P_{B_{\mp}}$  are the mole fractions of bound water ( $S_B \neq 0$ ) in the corresponding binding sites and  $P_B = \frac{n_B}{n_B + n_F}$ , being  $n_B$  and  $n_F$  the moles of bound and free water per mole of lipid, respectively.

Eq. (4.8) shows that the quadrupole splitting of heavy water is sensitive to changes in the relative populations of bound water at the two sites. A small increase of the fraction of water at the choline site, for instance, causes a net decrease of the splitting because the total order parameter is negative (Westlund, 2000; Sparmann and Westlund, 2003). The model gives a good interpretation of the temperature dependence of the quadrupole

splitting in terms of the variation of the water populations at the phosphate and the choline sites, even in the case where all the water molecules can be considered bound to the polar groups (hydration regime:  $P_B = 1$ ). It has also been suggested that an increase in the hydration of the choline site at the expense of the phosphate one is related to the tilting of the P-N dipole with respect to the interface normal (Aman et al., 2003).

The exchange mechanism of the water molecules between these two groups appears then to be very important in the vicinity of the main phase transition, since the P-N dipole tilting is correlated with the appearing of  $L_{\beta'}$  domains into the  $L_{\alpha}$  phase. If microwaves interact with the water exchange between the phosphate and choline sites, such an hypothesis could explain the strong influence of the radiation on the main phase transition. It has been shown that the bound water reorientation autocorrelation function reveals a fast and a slow decaying component, each contributing to a partially averaged quadrupole interaction (Aman et al., 2003). The fast part has been attributed to the anisotropic local reorientation of water molecules when they change hydration site at the same lipid molecule, while the slow decaying component is due to the lateral diffusion motion of water molecules between different lipid headgroups (Aman et al., 2003). The fast relaxation mechanism (few ps) falls in the range of high frequency MW and may provide the dipole interactions triggering with the microwave radiation. Even being only a speculation, useful for further deep investigations, this idea may also explain the small MW effect on the membrane detected far from  $T_m$  (Figure 4.4 at 37 °C) where area fluctuations are very small (close to zero) and the system is in a pure fluid phase (as already visible at 30°C in Figure 4.3a spectrum a).

Finally, microwaves change the energetic of the bilayer. A similar effect is caused by incorporating cholesterol or proteins in the membrane (Jähnig, 1981b). In the simplified statistical-mechanical model of the fluid-gel phase transition in PC membranes proposed by Doniach, both  $T_c$  and  $T_m$  are linearly dependent on the inter-chain van der Waals attraction potential (Doniach, 1978). Therefore, any agent affecting this potential, like a change of the phospholipid hydration, may also affect the above temperatures, as we have observed in the case of MW exposure.

## 4.5 CONCLUSION

This work provides strong evidence of the extreme sensitivity of biological membranes to low power long term MW exposure near the phase transition point. We believe that the molecular mechanism advanced here, by which the radiation affects DMPC membrane, may play a common and crucial role in all the effects observed both *in vitro* and *in vivo* as a consequence of microwave exposure.



## **CHAPTER 5**

**Physical properties of large and  
giant unilamellar vesicles affected by MMWs**

In Chapter 2 (section 2.3) we have reported of many studies about the effects of low power millimeter waves on the physical properties of biological membranes, in terms of alterations of lateral pressure (Zhadobov et al., 2006), diffusion of molecules (Ramundo-Orlando et al., 2009) or membrane permeability (Ramundo-Orlando et al., 2007; Siegel and Pikov, 2010).

An active role of water molecules, considered to be the main target of the MMW radiations (Cojocaru et al., 2005), and other dipolar residues surrounding the membranes, has been advanced in explaining for the observed phenomena (Cojocaru et al, 2005; Ramundo-Orlando, 2009); nonetheless, no clear evidence has been reported up to now.

In this chapter further experiments to test the influence of MMWs on the properties of lipid membranes are illustrated. While the above mentioned studies have mainly focused on the alteration of membrane processes at a cellular level, like ion channels functionality, or on membrane structural changes (Ramundo-Orlando 2010), the very original contribution of the experiments here presented, is that we have followed MMW-induced changes in membrane properties by directly monitoring the behavior of water. These experiments have aimed to elucidate the role of water in affecting the physical properties of biological membranes under exposure.

Lipid vesicles of different composition and size were used to investigate the effects of low power millimeter waves on some physical properties like changes in size, physical stability and membrane permeability to water and other molecules, like calcein.

In this study large and giant unilamellar vesicles (LUVs and GUVs) were used. They represent more suited biomimetic systems compared to the multilamellar vesicles used before (Chapter 4), as they are unilamellar, like a biological plasma membrane, and have a more homogenous size distribution thanks to their preparation techniques (for further details see Chapter 3).

The need to use both these unilamellar systems arises from, at least, two main reasons:

- 1) Different vesicle sizes can affect the curvature properties of membrane bilayers (see Chapter 1) and consequently their response to radiation;
- 2) One biomimetic system can turn out more suited than the other ones for some specific studies. For example, LUVs are widely used to encapsulate molecules inside vesicles (we used them to encapsulate calcein molecules in the experiment on

membrane permeability), whereas this is not possible with GUVs prepared by the electroformation technique. On the other hand, the advantageous visualization of GUVs under a microscope has allowed the instantaneous and direct visualization of the osmotic permeability of vesicles and the effect of radiation exposure on this property, where for LUVs this would have been possible only by using a stopped-flow device, currently not available in our laboratory.

## **5.1 SIZE CHANGES AND PHYSICAL STABILITY OF LUVs UNDER RADIATION EXPOSURE.**

### **5.1.1 Introduction.**

Vesicle size is of fundamental importance in regulating the *in vivo* circulation of liposomes. Vesicles bigger than 100 nm are removed from circulation by cells of the mononuclear phagocytic system (Szoka, 1990), while smaller vesicles are cleared more slowly than their larger counterparts. Consequently, changes in vesicle size can have dramatic effects on the *in vivo* behavior of liposomes.

One of the critical characteristics of liposomal systems is their physical stability with time. The general increase in the size of vesicles with time is called aging processes, referring to the physical instability of such systems with time (Armengol and Estelrich, 1995; Madani and Kaler, 1990; Olsson and Wennerstroem, 2002). In fact vesicles are not thermodynamically stable but metastable kinetically trapped systems and therefore their size and lamellarity can change with time.

Aging processes can occur mainly through two mechanisms:

- 1) Fusion of vesicles, that usually occurs as a consequence of aggregation phenomena (Armengol and Estelrich, 1995) for vesicles in the gel state.
- 2) Exchange of amphiphile monomers between vesicles of different sizes, leading to a change in the size distribution. The diffusion favors the growth of large vesicles and dissolution of small ones (Madani and Kaler, 1990). The driving force for this process is the curvature energy and smaller the droplet larger the enhancement of the monomer solubility (Olsson and Wennerstroem, 2002).

This process, called Ostwald ripening in classical colloidal systems, becomes relevant only for amphiphiles with a high monomer solubility ( $10^{-8}$  M), which is the case for short-chain lipids (Walde, 2004).

Here we used dynamic light scattering to monitor the average size as well as the polydispersity of LUVs made of DLPC (1,2-dilauroyl-*sn*-glycero-3-phosphocholine) 100 nm in size, during and after the exposure to low power millimeter waves. The vesicles are prepared in pure water so that the very simple composition can facilitate the interpretation of the observed phenomena.

### **5.1.2 Materials and Methods.**

Chloroform was purchased from Sigma-Aldrich and was of the highest quality commercially available. The water used in all sample preparations was purified by a Millipore Milli-Q cartridge system. 1,2-dilauroyl-*sn*-glycero-3-phosphocholine (DLPC) was purchased from Avanti Lipids in powdered form.

#### **5.1.2.1 Sample preparation.**

The procedure for obtaining extruding liposomes has been described previously (Hope et al. 1985; Mayer et al. 1986; Huster et al. 1997) and in Chapter 3 of this thesis. Briefly, DLPC was dissolved in chloroform and placed in a round-bottomed flask. The solvent was removed in a rotary evaporator. After drying under vacuum overnight, the residual lipid film was hydrated with high purity water to obtain a final concentration of 10 mM and subjected to three sonication-vortex-mixed cycles. The suspension was subjected to ten freeze-thaw cycles to produce MLV. The freeze thaw procedure reduces the lamellarity of the vesicles (Mayer et al., 1986). Large unilamellar vesicles were prepared by extruding the MLVs ten times through 400 nm polycarbonate filters, followed by ten passages through 200 nm filters and ten passages through 100 nm filters, always under nitrogen gas pressure, using a 10 ml Thermobarrel Extruder T.001 (Lipex Biomembranes, Vancouver, Canada) (MacDonald, 1991). Lipid concentrations were determined in triplicate by phosphorous analysis.

The final extruded DLPC samples appeared to be translucent. Before performing the exposure treatment, light scattering characterizations of the samples were performed.

The average diameter of the vesicles was  $113.8 \pm 1.1$  nm, with a minimum value of 100.5 nm and a maximum value of 125.1 nm.

For the light scattering measurements samples were diluted 10 fold.

### **5.1.2.2 DLS acquisitions.**

The effective diameter, that is an average size of the particles in the sample, and the polydispersity, that is a measure of the non uniformity that exists in the particle size distribution, were measured in LUVs by QELS (quasi-elastic light scattering) in a 90Plus/BI-MAS Multi Angle Particle Sizing analyzer (Brookhaven Instruments). The light source for the instrument is a Spectra-Physics, Model 124B, 15-mW, linearly polarized, HeNe laser. The laser and optical components are all mounted on a vibration isolation table.

The index matching fluid being used to surround the sample cell is Cargille Fluid S1056 (blended siloxanes with a refractive index of 1.45). A Millipore peristaltic pump is used to circulate and filter the index matching fluid through a 0.45- $\mu$ m membrane filter to remove any dust or particles that might interfere with the scattering experiment. A Neslab RTE-5DD refrigerated, circulating bath is used to maintain a constant temperature of  $25 \pm 0.1$  °C in the sample cell and surrounding liquid.

Data were collected and later analyzed with software supplied with the instrument. For each sample, data were acquired – typically for a duration of 10 min – for 5 runs at a scattering angle of 90°. The count rate was monitored to exclude runs containing artifacts due to infrequent passage of dust particles through the scattering volume.

A typical window showing results from light scattering measurements of a DLPC-LUV sample, is presented below (Figure 5.1).

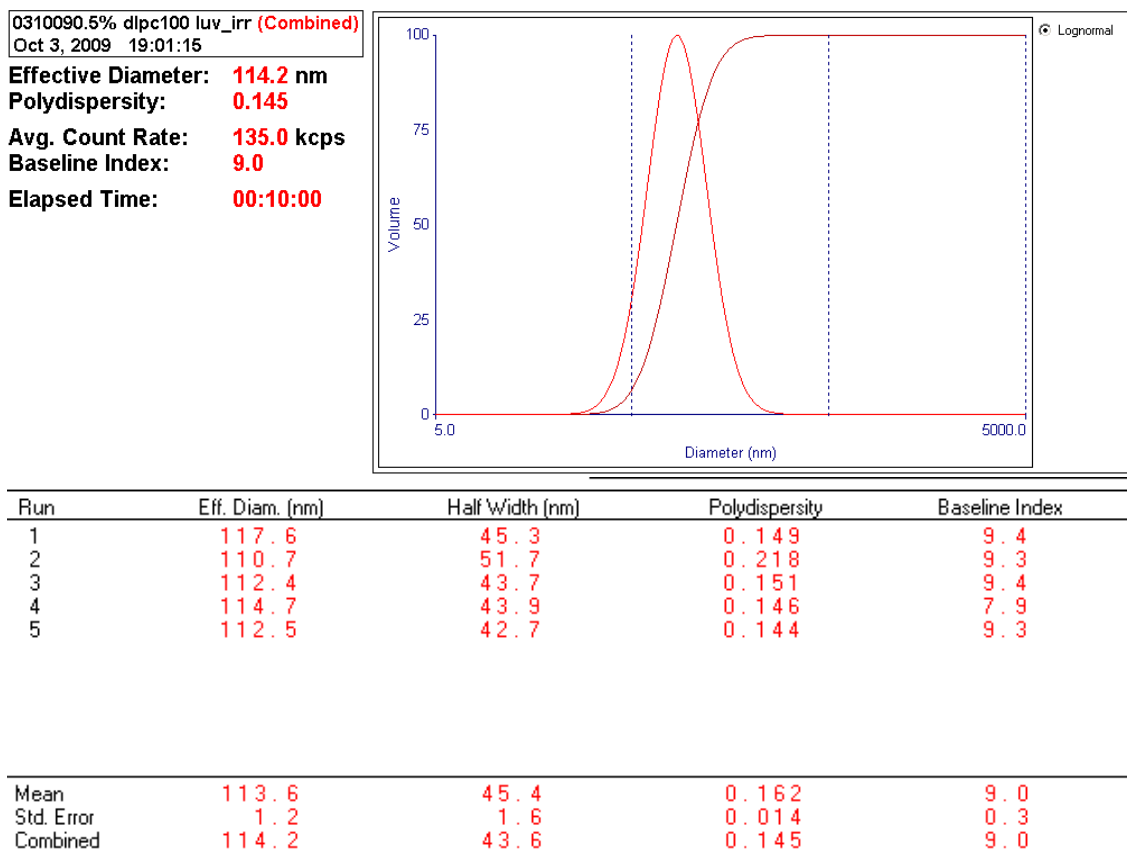


**Figure 5.1** Typical window where dynamic light scattering results for DLPC-LUVs appear.

### 5.1.2.3 Exposure set-up.

Vesicles were irradiated for 4 hours by wide band through IMG-56/76. The working range of the instrument is from 52 to 72 GHz, having an output power between 0,15 and 0,45 mW. The exposure time was chosen based on our previous experiments on multilamellar vesicles (see Chapter 4).

The experimental set-up is shown in Figure 5.2.

Samples were prepared introducing 300  $\mu$ l of the diluted solution containing LUVs into 10 mm glass tubes. A cylindrical dielectric antenna connected to the IMG 56/76 generator was also introduced in the glass tube, in such a way that the solution was homogeneously exposed to irradiation. The assembled system was then sealed with parafilm to avoid evaporation of the water solution. Measurements recorded with and without the inserted antenna show that its presence did not alter vesicle size. Sham exposure conditions correspond to the same set-up but with the generator turned off (Incident power density = 0). Both the sham and exposed samples were immersed in a water bath at the temperature of 25 °C and before performing the experiments they were

left to homogenize for two hours at the desired temperature. DLS measurements were acquired in controlled temperature conditions at  $25.0 \pm 0.05$  °C.

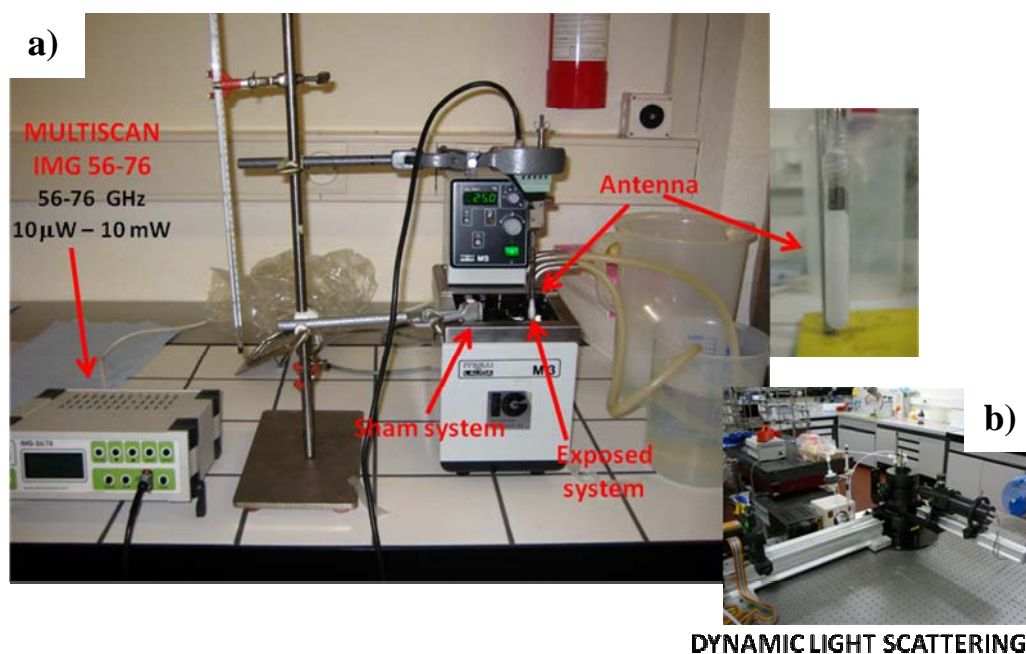


**Figure 5.2** a) Exposure set-up for irradiation of DLPC LUV<sub>100</sub> by multiscan IMG 56-76. A particular of the inserted antenna into a 10 mm glass tube containing the sample is also shown. b) Dynamic light scattering instrument used to monitor physical stability of vesicles. All the experiments were performed at the temperature of 25 °C.

#### 5.1.2.4 Dosimetry.

As for the dosimetric calculations, we remind to the section 4.2.5, even though a more proper dosimetric study needs to be conducted for the specific experimental set-up.

An independent experiment was performed to test eventual thermal effects of the radiation on LUVs by using a device, called rheo-magnet, appositively conceived at the laboratories of ETH Zürich, able to detect changes in the temperature with a instrumental resolution of  $\pm 0.1$  °C. During 4 hours of exposure of vesicles suspension at 25 °C, no temperature variations were detected.

#### 5.1.3 Results.

Figure 5.3 shows the relative increase of the effective vesicle diameter as a function of time for the exposed (red line) and the sham (blue line) systems.  $X_i$  is the effective diameter at the exposure time  $t$  and  $x_0$  is the effective diameter at the exposure time  $t_0=0$

(initial vesicle size). Arrows in the graphic indicate the time  $t_0$ , at which the radiation treatment started and the time at which the radiation was switched off, after 4 hours of treatment. Further exposure did not result in any significant change of the observed parameter (data not shown). Samples were also monitored after the end of the treatment and data taken after 1 hour and 14 hours are shown. All the data presented result from triplicate measurements of three independent experiments.

During the exposure time an analogous increase in the vesicle diameter was observed in both the exposed and the sham system. Thus, no significant effects on the size of the vesicles were observed during the exposure time and also, after one hour the end of the treatment. In contrast, after 14 hours storage, while the diameter increase in the sham exposed LUVs was about 14%, in the treated sample it was only about 8%. This is a significant difference that should be attributed to MMWs exposure, that seemed to affect the aging process.

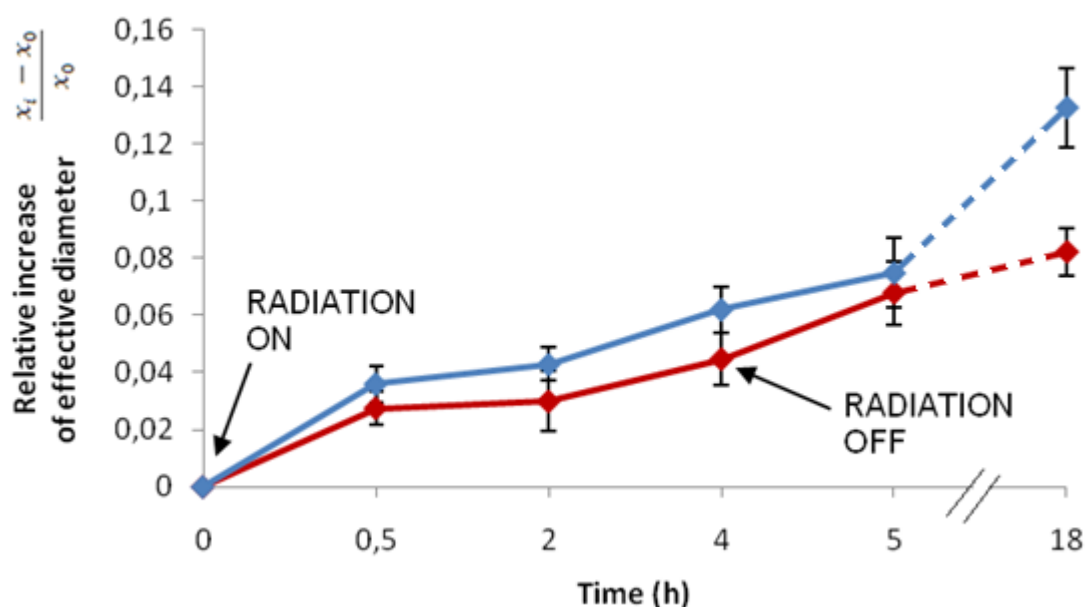


**Figure 5.3** Relative increase of the effective vesicle diameter as a function of time for the exposed (red line) and sham (blue line) system.  $x_i$  is the effective diameter at the exposure time  $t$  and  $x_0$  is the effective diameter at the exposure time  $t_0=0$ . The arrows indicate the time  $t_0$ , at which the radiation treatment started, and the time at which the radiation was switched off, after 4 hours of treatment. Error bars denote the standard deviation obtained from three independent experiments.



When the potential effects of microwaves were evaluated in terms of the vesicle polydispersity (Figure 5.4), no significant differences of this parameter were observed between sham and exposed vesicles.

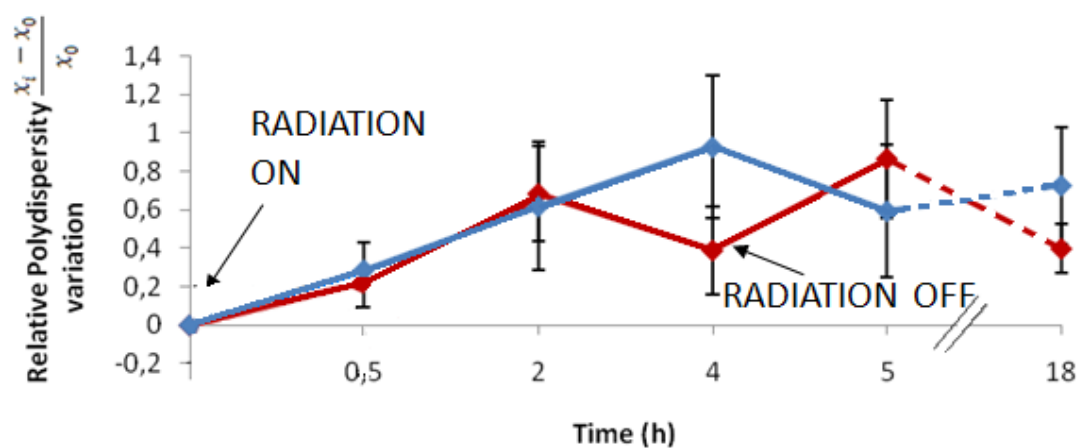


**Figure 5.4** Relative polydispersity variation as a function of time for the exposed (red line) and sham (blue line) system.  $x_i$  is the polydispersity of the sample at the exposure time  $t$  and  $x_0$  is the polydispersity at the exposure time  $t_0=0$ . The radiation treatment was switched off after 4 hours of treatment and samples monitored one hour and 14 hours after the end of the exposure treatment. Error bars denote the standard deviation obtained from three independent experiments.

We therefore note, in general, that the increase of the vesicle size with time due to the aging processes (especially for the sham exposed vesicles), is not accompanied by any change in polydispersity.

#### 5.1.4 Discussion.

Experiments were performed at room temperature (25°C), then well above the main phase transition temperature of DLPC ( $T_m = -1,8$  °C), therefore the vesicles were in their fluid phase. As stated in the introduction, the mechanisms contributing to the increase of the effective vesicle diameter are fusion of liposomes and Ostwald ripening. The first one appears to be less probable because it occurs mainly when vesicles are in the gel phase. The latter occurs for monomer solubility above  $10^{-8}$  M (Walde, 2004), as it is the case for DLPC whose monomer solubility is  $9 \cdot 10^{-8}$  M (data from Avanti Polar Lipids). Therefore, vesicle ripening can be reasonably brought into play for the observed changes (Madani and Kaler, 1990; Olsson and Wennerstroem, 2002).

In surfactant sonicated vesicle suspensions, aging process occurs at two distinct stages: an initial one, more rapid, within a few hours from sample preparation, and a second long-term one lasting several weeks. The first one is due to the supersaturation produced by sonication that can be addressed to both heating of the solution and production of many small vesicles or other aggregates with a high surface curvature. These last aggregates are formed as a consequence of the monomer concentration readjustment after sonication and grow with time. When supersaturation becomes small the second stage begins, that occurs via monomer ripening.

In Figure 5.3 the first stage is clearly visible in the first five hours in both the sham and the exposed systems with no statistical significant differences between them. Hence, the first stage of the aging process appears to be not affected by the exposure. In contrast, however, the second stage, evaluated after 14 h storage of the vesicle suspensions, was observed only in the sham system.

Moreover, as noted above, the increase of the vesicle size in the sham system did not involve any increase in the polydispersity of vesicles (Figure 5.4). Therefore, the observed increase cannot be explained only by a size decrease of the smaller vesicles that release monomers in favor of the larger ones, but it should involve their break up.

Interestingly, however, the second stage of the Ostwald ripening did not occur in MMW-exposed vesicle suspensions. We can therefore advance the hypothesis that radiation prevents this process in neutral DLPC-liposomes through the stabilization of the smaller vesicles, that would not be prone anymore to release their phospholipid monomers and/or aggregates in favor of the larger vesicles, thereby inhibiting the aging process.

This experiment was performed on a very simple system consisting of a single-lipid vesicle suspension in high purity water. Madani and Kaler (1990) reported of aging processes in charged vesicular dispersion formed by sonication of either pure water or electrolyte solutions and found that ripening processes are favored in pure water due to the high monomer solubility, whereas are suppressed in the presence of electrolytes because of a lowering of the surfactant solubility.

As already reported in section 2.1 and 4.4.1, water is mainly involved in the interaction with millimeter waves, because relaxation times of local motions of water molecules are in the range of MMW frequencies, and also because water has a larger dielectric permittivity compared to the other molecules (lipids) present in solution (Finney, 2001).

Many authors agree that a possible explanation of the effects induced by MMWs involves some structural changes at the membrane-water interface (Cojocaru et al, 2005; Ramundo-Orlando et al., 2009) and our findings on the  $^2\text{H}$  NMR measurements of irradiated lipid membranes have definitely showed a reduction of the water ordering at the membrane interface, that can be traduced in a dehydration effect of the membrane (see Chapter 4).

Zhang et al. (2006), have showed that there is a correlation between hydration and membrane curvature; in particular, higher bilayer curvature leads higher hydration, because of a lower packing density of the lipid headgroups (Hof et al., 1994), or in other words, an increased area/lipid ratio.

The inhibition of ripening process by radiation, may be caused by the same membrane dehydration effect previously observed on  $^2\text{H}$  labeled MLVs (Chapter 4). In fact, a dehydration induces a curvature decrease that, as seen in section 5.1.1 (Olsson and Wennerstroem, 2002), contrasts Ostwald ripening.

Finally, it is also worth noting that the results reported here confirm the non-thermal nature of the observed effects, in that, a thermal increase would increase membrane hydration (section 1.6), favoring therefore the ripening process.

## **5.2 CALCEIN PERMEABILITY IN LUVS UNDER RADIATION EXPOSURE**

### **5.2.1 Introduction.**

The permeation of calcein across the phospholipid bilayer membrane is a key phenomenon in the detection of liposome physical properties.

Calcein (Figure 5.5) has been widely known as a fluorescence probe due to the self-quenching ability of the calcein molecules themselves at higher concentrations (Alle et al., 1980; Lopez et al., 1998; Davidsen et al., 2003; Kuboi et al., 2004; Shimanouchi et al., 2007). Calcein-release from vesicles can be monitored directly by increasing fluorescence intensity and have been utilized as an effective index to characterize the membrane properties of (model) biomembranes and to evaluate the interaction between the closed bilayer lipid membrane and target materials such as proteins (Davidsen et al., 2003; Kuboi et al., 2004), peptides (Shimanouchi et al., 2007), and (model)

biomembranes (Felix et al., 2002). In addition, the calcein-release phenomena have been investigated with regard to design of a drug-delivery system.

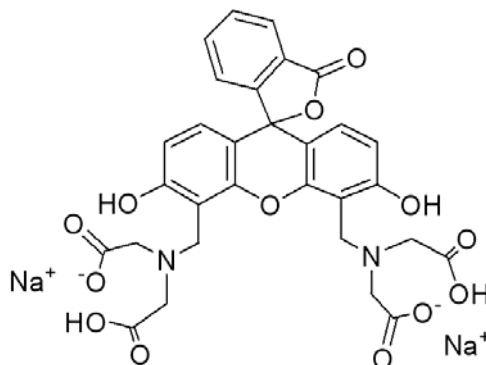


**Figure 5.5** Calcein molecular structure Molar mass = 622.55 g/mol; Permeability coefficient =  $(1.88 \pm 0.8) \times 10^{-10} \text{ cm/s}^{-1}$ ; Emis  $\lambda = 511 \text{ nm}$ ; Exc  $\lambda = 490 \text{ nm}$ ).

Calcein permeation appears to be controlled by the membrane fluidity: immobilization of liposome on the solid surface affects the permeability of calcein, probably due to the change in the packing density of lipid molecules within the phospholipid membrane accompanying the deformation of liposome (Shimanouchi et al., 2009).

In this experiment calcein was used to monitor the influence of low power millimeter waves on the membrane permeability. Big molecules like calcein have a very small permeability compared to smaller molecules like water:  $1.88 \times 10^{-11} \text{ cm/s}$  (Shimanouchi et al., 2009) and to  $\sim 3 \times 10^{-3} \text{ cm/s}$  respectively (Figure 5.6).

Exposure experiments were carried out either far and near the lipid phase transition temperature, where, from our findings on multilamellar vesicles (see Chapter 4), the radiation effect is expected to be enhanced because of the higher sensitivity of the system at  $T_m$  (see section 1.8).

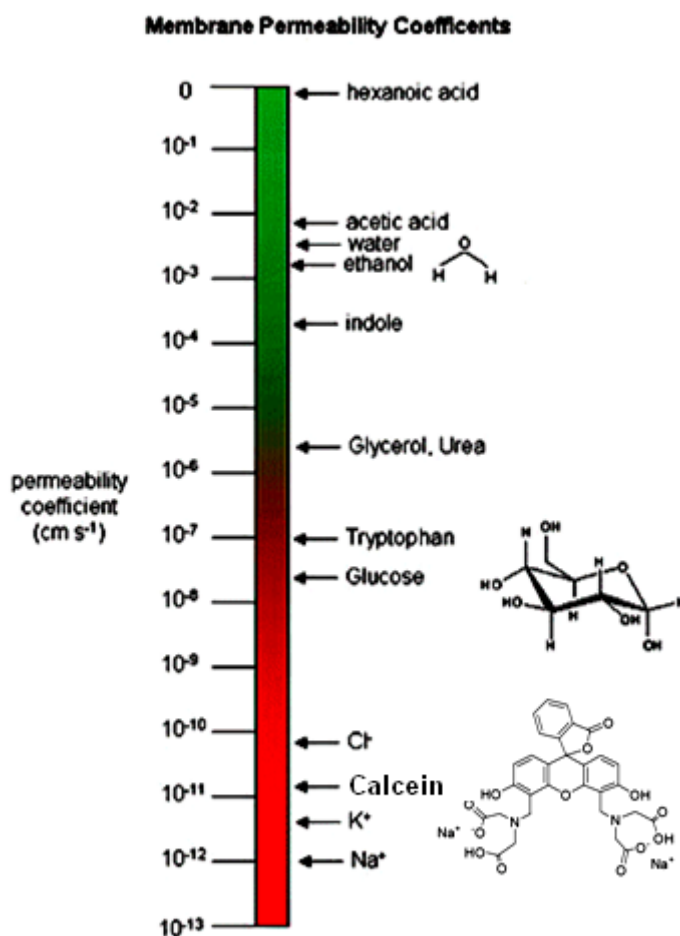


**Figure 5.6** Permeability coefficient of molecules and ions crossing lipid bilayer.

To this aim, two different lipids were used: 1-palmitoyl-2-oleoyl-sn-glycero-3-phosphocholine (POPC), which has a  $T_m = -2$  °C, and therefore it is used in the fluid phase; and 1-stearoyl-2-oleoyl-sn-glycero-3-phosphocholine (SOPC) whose transition temperature is at  $T_m = 6$ °C, and then is more suited for performing experiments near the main transition. We monitored calcein permeability to LUVs made of POPC or SOPC 100 nm in size during and after 4 hours of exposure to low power millimeter waves. Calcein leak out was measured by using a fluorescence reader. Radiation didn't seem to affect membrane permeability even in the case in which exposure was performed close to  $T_m$ , where permeability is enhanced and the system should be more sensitive to irradiation (see section 1.8).

## **5.2.2 Materials and Methods.**

### **5.2.2.1 Materials.**

1-palmitoyl-2-oleoyl-sn-glycero-3-phosphocholine (POPC) and 1-stearoyl-2-oleoyl-sn-glycero-3-phosphocholine (SOPC) were purchased from Avanti Lipids in chloroform solution. Calcein disodium salt, Triton X-100, Sepharose R4B200, were purchased from Sigma-Aldrich (Seelze, Germany). NaCl was purchased from Acros Organics (Geel, Belgium), chloroform from J.T. Baker (Deventer, Holland). All other reagents of analytical grade were purchased from Sigma-Aldrich (Seelze, Germany). The water used in all sample preparations was purified by a Millipore Milli-Q cartridge system.

If not otherwise indicated, all methods were performed at room temperature and procedures are valid for both POPC and SOPC vesicles.

### **5.2.2.2 Sample preparation.**

POPC and SOPC LUVs containing calcein were prepared in a similar manner to that described above for LUVs in pure water solution, with the only difference being that the solution with which the lipids were hydrated was 50 mM calcein,  $\text{pH} = 7.4$ ; pH measurements were accomplished with a pH 62 Standard pH Meter (Instrumenten Gesellschaft AG, Zürich, Switzerland). A final solution of POPC or SOPC 5 mM was obtained. The size distribution was determined via dynamic light scattering (DLS) using a BI 90 Plus - 9kpsdw32 (Brookhaven Instruments Cooperatin, Holtsville, NY, USA).

### **5.2.2.3 Separation of vesicles and free calcein solution.**

The vesicles were separated from the free calcein solution with a Sepharose TM-column (Figure 5.7). The Sepharose TM-column was 25 cm high with a diameter of 1 cm and was builded up in glass tube. To achieve a constant flow a reservoir with iso-osmotic NaCl solution 137 mM was installed prior to the glass tube and a peristaltic pump Pharmacia P-3 (Pharmacia Ltd., Earlington London, UK) was attached afterwards.

For achieving iso-osmotic solutions, the osmolarity of both calcein and NaCl solutions were determined using a TM Micro-Osmometer, Model 3MO (Advanced Instruments Inc., Nordwood, MA, USA) and resulted to be 251 Osm. pH was adjusted if necessary.

The flow time for the vesicle fraction was determined gravimetrically (free flow = 0.38 ml/min).

Elution samples were taken over an interval of 3 minutes and fractions collected by visual detection. The dilution factor of the column was determined applying the Stewart assay (see section 5.2.2.4).

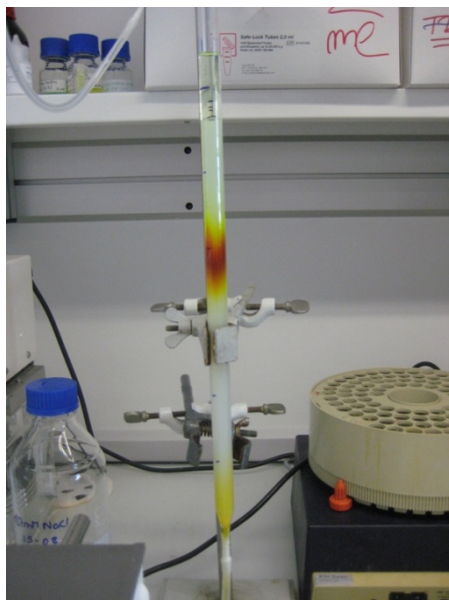


**Figure 5.7** Separation of free calcein (upper band in the chromatographic column) from loaded POPC LUVs (lower band).

#### **5.2.2.4 Stewart assay.**

The Stewart assay was performed according to Torchilin (2003).

#### **Stewart assay standard curve.**

The optical density  $od$  (VIS 485 nm) of two independent POPC dilution series were Measured with a spectrophotometer PerkinElmer Lambda 20 (PerkinElmer R, Waltham, MA, USA) the optical density (OD), (VIS 485 nm) over an interval of 350-600 nm using 1 cm quartz cells and chloroform as reference substance.

The standard curve was strongly linear over the whole concentration range (0.00–0.05 mg/ml) (Figure 5.8).

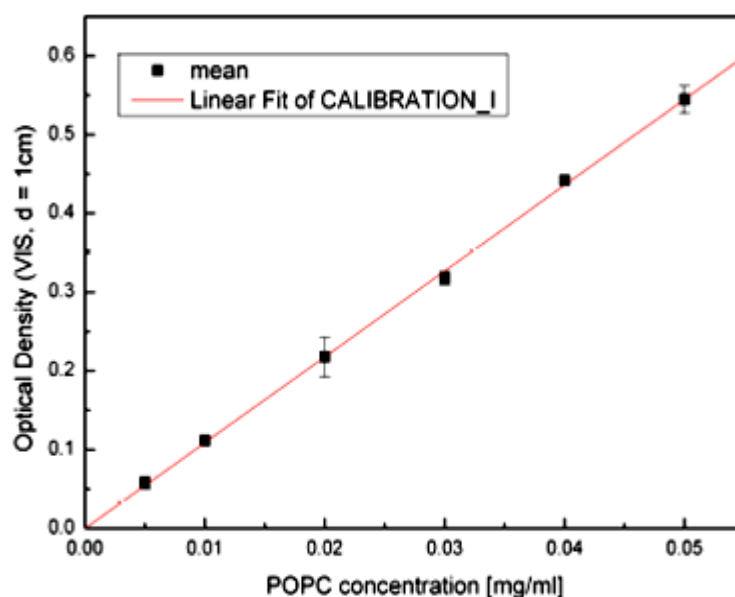


**Figure 5.8** Stewart assay standard curve. POPC was solved and diluted with chloroform, which was also utilized as reference substance. The optical density od (VIS 485 nm) was read using 1 cm quartz cuvettes. The POPC concentration can be determined from this curve.

#### **POPC concentration determination.**

Two independent samples were measured after the first separation. The mean POPC concentration of these two vesicle fractions was 258  $\mu\text{M}$ . Considering the initial POPC concentration (5 mM POPC) the dilution factor of the column was determined to be approximately 20 x.

#### **5.2.2.5 Calcein-release measurement.**

##### **Calcein fluorescence intensity (FI) standard curve.**

A calcein standard curve was reordered with a FL 600 Microfluorescence Reader (BioTek R, Winooski, VT, USA) using a black 96 wells microtiterplate (Firma, Ort, Land). Calcein excitation wavelength is at 490 nm and emission wavelength at 511 nm. The goal of such a curve is to determine the linear region where the fluorescence intensity is directly proportional to calcein concentration.

Three independent calcein dilution series were prepared. A calcein stock solution (80 mM calcein in 10 mM phosphate buffer, pH 7.4) was diluted with iso-osmotic buffer (10 mM phosphate, 210 mM NaCl, pH 7.4). The dilution series ending at 156 nM calcein taking 15 steps to reach it (Figure 5.9)



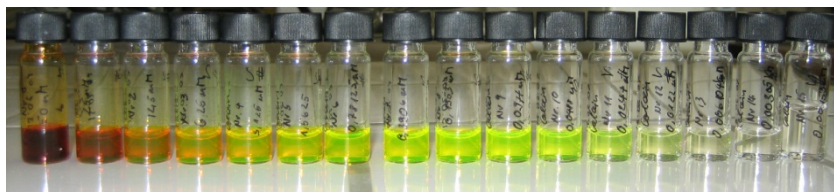


**Figure 5.9** Dilution series of 80 mM calcein solution ending at 156 nM.

Of each dilution 3 x 200  $\mu$ L were transferred on a 96 wells microtiterplate and read. The results showed small FI at 80 mM calcein, increasing exponentially to a maximum at 500  $\mu$ M calcein and descending exponentially with increasing dilution leading in a linear region at 2.5  $\mu$ M calcein (see Table 5.1 and Figure 5.10).

**Table 5.1** Calcein dilution series design including FI results.

Calcein concentration ( $\mu$ M)	Fluorescence intensity 200 $\mu$ L sample
$80 \times 10^3$	624
$40 \times 10^3$	3571
$20 \times 10^3$	14767
$10 \times 10^3$	37108
5000	58461
2500	71195
500	77039
100	69610
20	40397
10	26497
5	14392
2.5	7923
1.25	3898
0.625	1957
0.3125	922
0.15625	483

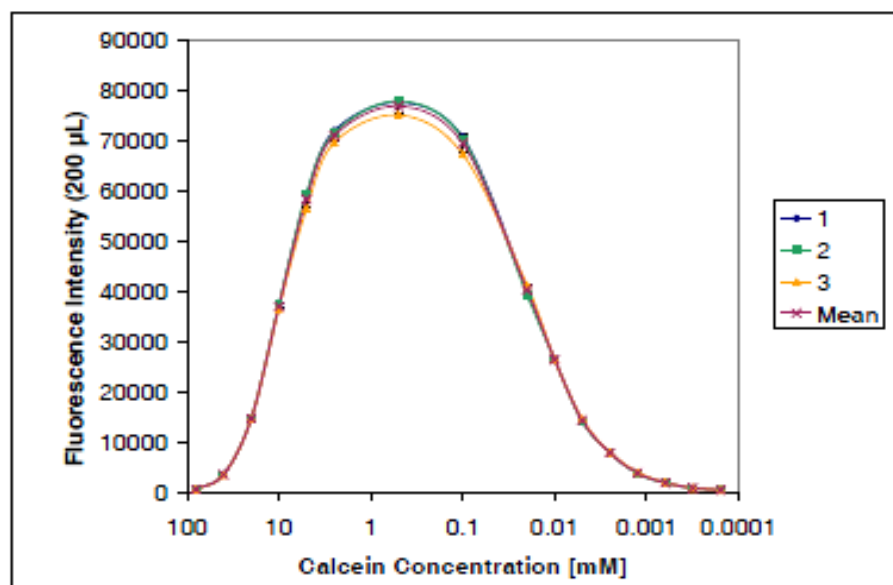


**Figure 5.10** Calcein standard curve in 10 mM phosphate buffer.

Two things have been shown with this standard curve:

1. The maximum self quenching effect of calcein is found at 80 mM of the dye. This perfectly fits with Benachir et al. (1995).
2. The linear region starts at 2.5  $\mu\text{M}$  (Figure 5.11).

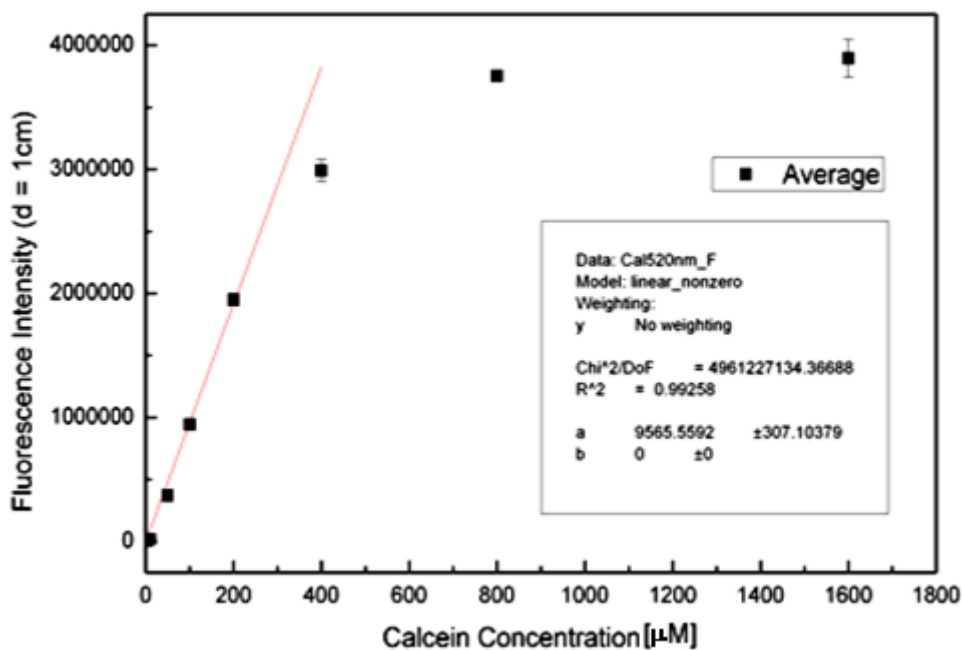


**Figure 5.11** Fluorescence intensity as a function of calcein concentration. Fluorescence intensity of calcein is directly proportional to its concentration up to 2.5  $\mu\text{M}$ .

**Calcein fluorescence intensity (FI) measurements.**

Our standard curve describing the fluorescence intensity as a function of calcein concentration showed that the fluorescence intensity of calcein is directly proportional to its concentration up to 2.5  $\mu\text{M}$ . The LUV dispersion was diluted 1:30 with NaCl in order to ensure a dye concentration less than 2.5  $\mu\text{M}$  after total release from all the vesicles.

Total calcein concentration is achieved by adding appropriate amount of Triton X-100 (10 %) causing lysis of POPC vesicles and therefore total release of entrapped calcein.

The high concentration (80 mM) of the encapsulated marker led to self-quenching of its fluorescence, resulting in low background fluorescence intensity of the vesicle dispersion ( $I_B$ ). Release of calcein led to the dilution of the dye into the medium and could therefore be monitored by increasing fluorescence intensity with time ( $I_F$ ). The experiments were normalized relative to the total fluorescence intensity ( $I_T$ ) corresponding to the total release after complete disruption of all the vesicles by Triton X-100 (10 %). The results of the leakage experiments are presented as the percentage of released calcein, calculated according to:

$$\% \text{ release} = 100(I_F - I_B)/(I_T - I_B) \quad (5.1)$$

**5.2.2.6 Exposure set-up.**

Vesicles were irradiated for 4 hours by wide band through IMG-56/76. The working range of the instrument is from 52 to 72 GHz, having an output power between 0,15 and 0,45 mW. The exposure time was chosen based on our previous experiments on multilamellar vesicles (see Chapter 4).

The experimental set-up for both the experiments with POPC and SOPC LUVs, is shown in Figure 5.12.

The samples were prepared introducing 2 ml of the solution containing LUVs into a 2.3cm x 2.3cm x 2.3cm poly(methyl methacrylate) (PMMA) box – liquid thickness  $\sim$  4 mm allowed the total exposure of the sample to the radiation (radiation penetration is of a few millimeters: see Chapter 2).

A conical dielectric antenna connected to the IMG 56/76 generator was put on the top of the chamber at a distance of 8 cm. Sham exposure conditions correspond to the same set-up but with the generator turned off (Incident power density = 0). Both the sham and exposed samples were immersed in a water bath at the temperature of 25  $^{\circ}\text{C}$  for the experiments with POPC LUVs and of 6.5  $^{\circ}\text{C}$  (0.5  $^{\circ}\text{C}$  above SOPC main phase transition

temperature  $T_m=6^\circ\text{C}$ ) for the experiments with SOPC LUV<sub>100</sub>. Before starting to perform the experiments, samples were left to homogenize for two hours at the desired temperature. Fluorescence measurements were acquired in controlled temperature conditions at  $25.0 \pm 0.05^\circ\text{C}$ .

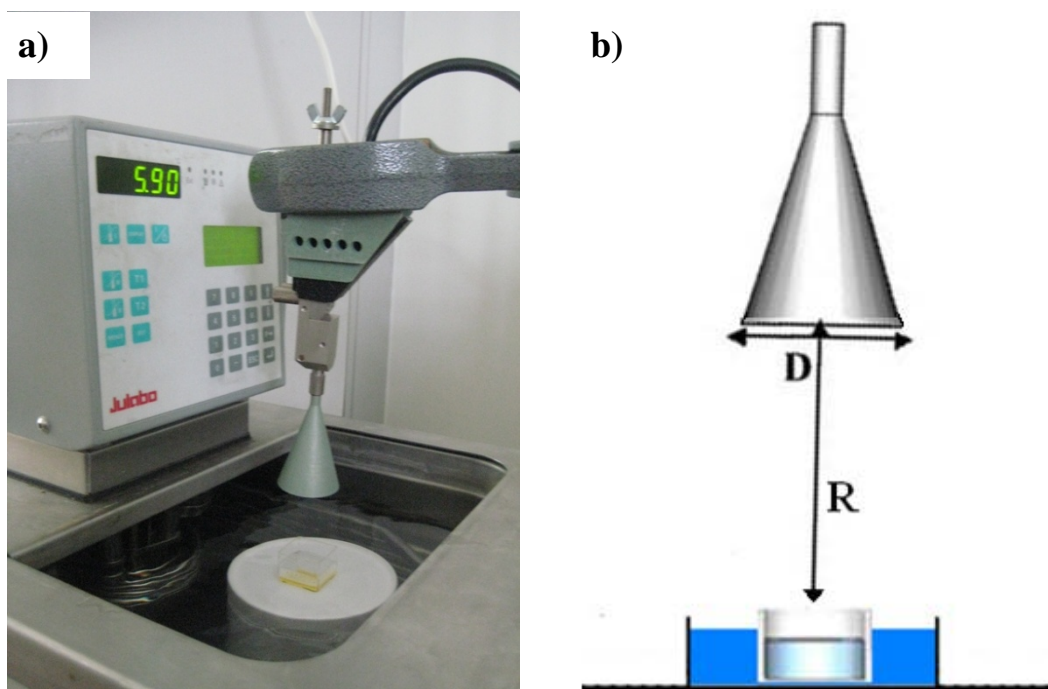


**Figure 5.12** a) Exposure set-up for irradiation of SOPC LUV<sub>100</sub> by multiscan IMG 56-76. Sham and exposed samples were immersed each in a water bath at the temperature of  $6.5^\circ\text{C}$  ( $0.5^\circ\text{C}$  above SOPC main transition temperature  $=6^\circ\text{C}$ ), and before performing the fluorescence measurements they were left to homogenize for two hours. Fluorescence measurements were acquired in controlled temperature conditions at  $25.0 \pm 0.05^\circ\text{C}$ . b) Diagram of the experimental set-up including the horn antenna, the exposure chamber and the water bath. Dimensions:  $D=34\text{ mm}$ ;  $R=8\text{ cm}$ . In this figure is also shown that the sample was exposed from the top. The same experimental set-up was used for POPC LUV<sub>100</sub> but at a temperature of  $25^\circ\text{C}$ .

### 5.2.2.7 Dosimetry.

As for the dosimetric calculations we remind to Ramundo-Orlando et al. (2009), even though a more proper dosimetric study needs to be conducted for the specific experimental set-up.

An independent experiment was performed to test eventual thermal effects of the radiation on LUVs by using a device, called rheo-magnet, appositively conceived at the laboratories of ETH Zuerich, able to detect changes in the temperature with a

instrumental resolution of  $\pm 0.1$  °C. During 4 hours of exposure of vesicles suspension at 25 °C, no temperature variations were detected.

### 5.2.3 Results.

Figure 5.13 shows the percentage of released calcein as a function of time for the exposed (red line) and the sham (blue line) systems, calculated according to Eq. (5.1). In the graphics the arrows indicate the time  $t_0$ , at which the radiation treatment started and the time at which the radiation was switched off, after 4 hours of treatment. The samples were monitored after the end of the treatment and data taken after 1 hour are shown. Data shown result from triplicate measurements of three independent experiments.

During and after the exposure time a slight increase in the percentage of calcein release was observed in both the exposed and the sham system, due to normal time-course of calcein leakage (Shimanouchi et al., 2009). This means that no significant effects on the calcein permeability were observed during the exposure time and also, after one hour the end of the treatment. With this kind of experiments it was not possible to follow the time-course of radiation effects, as calcein release reached a plateau (Shimanouchi et al., 2009) in a few hours in both the samples (data not shown).

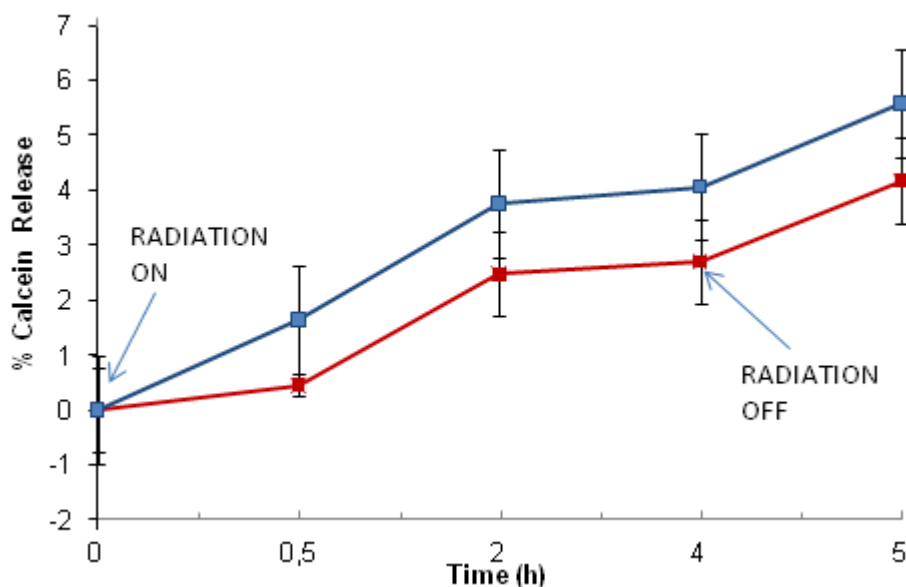


**Figure 5.13** Percentage of calcein release as a function of time for exposed (red line) and sham (blue line) POPC LUVs (100 nm) systems. The arrows indicate the time  $t_0$ , at which the radiation treatment started, and the time at which the radiation was switched off, after 4 hours of treatment. Error bars denote the standard deviation obtained from three independent experiments.

The same trend was observed for SOPC LUVs<sub>100</sub>, even performing the exposure close to SOPC main phase transition temperature (data not shown).

In conclusion, these experiments have shown that MMWs don't affect calcein permeability through the membrane. Besides, our measurements showed large standard deviations that prevents any conclusion from these experiments. We can simply conclude that, under the experimental conditions used, the method was not suited for detecting eventual MMW effects membrane permeability of LUVs.

### **5.3 WATER OSMOTIC PERMEABILITY IN GUVS UNDER RADIATION EXPOSURE**

#### **5.3.1 Introduction.**

Our first interest in GUVs was inspired by the idea to get some “direct” evidences, visible under a light microscope, of effects of MMWs on lipid vesicles and membrane properties. In the first case we were just interested in understanding if the radiation could be able to affect the shape and geometry of GUVs.

Related to the second aspect, membrane properties, we moved from our experiments on LUVs, where we observed that the ripening process, commonly occurring in vesicles made of short-chain lipids as DLPC, was inhibited by the radiation. The interpretation for this effect was that of a change in the physical properties of the membrane (increased membrane rigidity) induced by the action of radiation on water bound molecules. Therefore, the idea was to add some other evidences proving that the radiation could be able to increase lipid membrane rigidity. An increased membrane rigidity for example could have some consequences on the ability of vesicles to change their shapes and size when undergoing an osmotic stress. In effect, it has been proved that there is a correlation between membrane rigidity and water permeability in lipid membrane (Lande et al., 1995).

Water and solute permeability across the bilayer membrane have been extensively studied over years (Xiang and Anderson, 1994; Lande et al., 1995; Paula et al., 1996). According the widely accepted solubility-diffusion model for describing the transport of small molecules across a homogeneous single slab membrane, the permeability

coefficient,  $P$ , of the molecule is inversely proportional to the bilayer thickness,  $d_c$ , according to the relation:

$$P=KD_C/d_c \quad (5.2)$$

where  $K$  is the partition coefficient of the molecule and  $D_C$  is the diffusion coefficient in the membrane. Recently this model has been put into discussion by Mathai et al., (2008). They followed the water permeability of water through lipid membrane and found that, in single component bilayers, it is mainly determined by the area per lipid molecule, while the role of bilayer thickness is secondary. These results were already predicted by MD simulation studies using saturated PC lipids (Sugii et al., 2005). Moreover, many studies suggest that tighter packing of lipids leads to a reduced water permeability through the membranes (Lande et al., 1995; Negrete et al., 1996), as when cholesterol is inserted inside the membrane (Lande et al., 1995). Mathai et al. (2008) explained for such effect by observing a decrease in area occupied by the lipids in the presence of cholesterol, even though, an additional contribution for the decrease, arising from the partition coefficient, was also taken into account.

Since the area/lipid is a surface property of lipid bilayers, it has been suggested that the rate limiting step for water permeability is at the water-lipid interfacial region (Mathai et al., 2008). A new model has then been proposed that develops the initial idea by Diamond and Katz (1974) of a three slab model, one hydrocarbon and two interfacial slabs, suggesting an interfacial steric blockage mechanism (Nagle et al., 2008).

Water permeability through lipid membranes of vesicles can be measured by abruptly subjecting the vesicles to an increase of external osmotic pressure (Jansen and Blume, 1995; Bucher et al., 1998). It can be done, for example, by adding a glucose solution to a pure water vesicle suspension.

From Fick's law, the rate at which small molecules cross the membrane by simple diffusion is proportional to the permeability coefficient,  $P$ , according to the following relation:

$$J=P\Delta c(t) \quad (5.3)$$

where  $J$  is the flux and  $\Delta c(t)$  is the concentration gradient.

From Figure 5.6, it can be seen that the permeability coefficient of water is about 5 orders of magnitude bigger than glucose, therefore water molecules cross lipid membranes faster than glucose molecules.

The exit of water due to the osmotic gradient results in a decrease of liposomal volume that can be measured by fluorescence techniques, in case a fluorescent dye is entrapped in vesicles, or by light scattering (Lande et al., 1995; Mathai et al., 2008). A direct visualization of the change in the volume of vesicles is even possible by light microscopy in case giant vesicles are used.

In this experiment, phase contrast microscopy was used to monitor the influence of low power millimeter waves on water permeability through lipid membranes. We irradiated DLPC (1,2-dilauroyl-*sn*-glycero-3-phosphocholine) GUVs prepared in pure water for 4 hours and then monitored shape and size distribution changes upon abruptly adding a glucose solution.

Vesicle size shrinkage was significantly reduced in samples exposed to MMWs compared to the sham systems. At the light of the recent findings about the mechanism of water permeability through lipid membranes and the molecular interpretation of the effects observed by our group on multilamellar vesicles affected by MMWs (see Chapter 4), an explanation involving water behavior at the interfacial region of the membrane is provided.

### **5.3.2 Materials and Methods.**

#### **5.3.2.1 Materials.**

Chloroform and methanol were purchased from Sigma-Aldrich and were of the highest quality commercially available. D-glucose, was from Fluka (Switzerland). The water used in all sample preparations was purified by a Millipore Milli-Q cartridge system. 1,2-dilauroyl-*sn*-glycero-3-phosphocholine (DLPC), 1-palmitoyl-2-oleoyl-*sn*-glycero-3-phosphocholine (POPC), egg phosphatidylcholine (egg PC) and cholesterol were purchased from Avanti Lipids.

#### **5.3.2.2 Sample preparation.**

DLPC GUVs were prepared with the electroformation method (Bucher et al., 1998 and Walde et al., 2010), originally developed by Angelova and Dimitrov (1986; Angelova et al., 1992; Angelova, 2000). The investigation chamber, the same described in Bucher et



al., (1998), contained two parallel platinum wire electrodes (diameter 0.5 mm), separated at a distance of 3 mm (Figure 5.14a). About 1  $\mu\text{l}$  of a solution of DLPC (0,5 mg/ml) in chloroform: methanol (9:1, v/v) were applied onto each of the two platinum wires. After drying overnight, 1.2 ml pure water was added and an alternating electric field was applied at 10 Hz, and gradually increasing voltage from 100 mV to 500 mV in 50 mV steps for the first 30 minutes, and in 100 mV or 500 mV steps up to 2 V. After two hours giant vesicles were formed (Figure 5.14b).

All the steps of vesicle preparation and exposure were performed at 25 °C; this temperature is above the main phase transition one of DLPC, so that the phospholipids were in their liquid crystalline state.

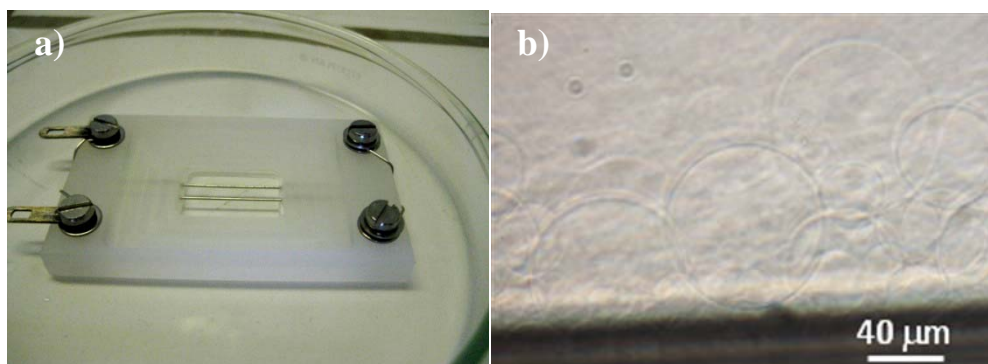


**Figure 5.14** a) Chamber with Pt wires for the electroformation of b) DMPC GUVs (Angelova and Dimitrov, 1986).

### 5.3.2.3 Osmotic vesicle shrinkage.

Osmotic effects were observed after that vesicles were formed from lipid films as described above. Vesicles were formed by using 1.05 mL of water. Afterward 150  $\mu\text{L}$  of a 10 mM solution of glucose were added to build up the desired concentration gradient between the aqueous interior of the vesicle and the bulk solution (the total final volume in the investigation chamber was 1.2 mL).

### 5.3.2.4 Microscopic equipment.

The vesicles were observed with a Nikon inverted microscope with a 60 $\times$  objective with ELWD 0.3 lenses using the phase contrast mode. The microscope was equipped with an optical condenser, a standard optical camera (Nikon). The images were acquired using

the analysis control software and are presented as collected: no image processing was applied.

#### **5.3.2.5 Exposure set-up.**

Vesicles were irradiated by wide band through IMG-56/76 by using a conical horn antenna with 34 mm maximal diameter ( $D$ ). The working range of the instrument is from 52 to 72 GHz, having an output power between 0,15 and 0,45 mW. The exposures were carried out directly under the microscope with the chamber placed on its stage. The distance ( $R$ ) of the centre of the chamber from the horn antenna was 8 cm and the incidence angle was  $45^\circ$  (Figure 5.15).

In this situation, an upward irradiation is applied on the samples, which enhances the efficiency of the exposure due to the reduction of the multiple reflections between the chamber and the horn antenna and to the reduction of the field disturbance due to the wave reflections from the workbench (Zhao et al., 2005).

#### **5.3.2.6 Experimental procedure.**

After the electro formation, vesicle shape stability was monitored for 2 hours and the size distribution of vesicles was measured at least twice. No variation in shape, size and number of vesicles were observed.

A quantitative estimate of vesicle size distribution was made from the acquired images by using the software provided by the manufacturer.

To this aim we selected different zones on each platinum wire and measured the diameter of vesicles parallel to the platinum wire. To account for all the vesicles present on the selected region, the focus plane was gradually changed until complete disappearance of vesicles.

All the measurements were automatically collected by the software which provided a histogram showing the distribution of vesicle size. As an example the size distribution of GUVs obtained from EPC/cholesterol lipid mixture is reported in Figure 5.16.

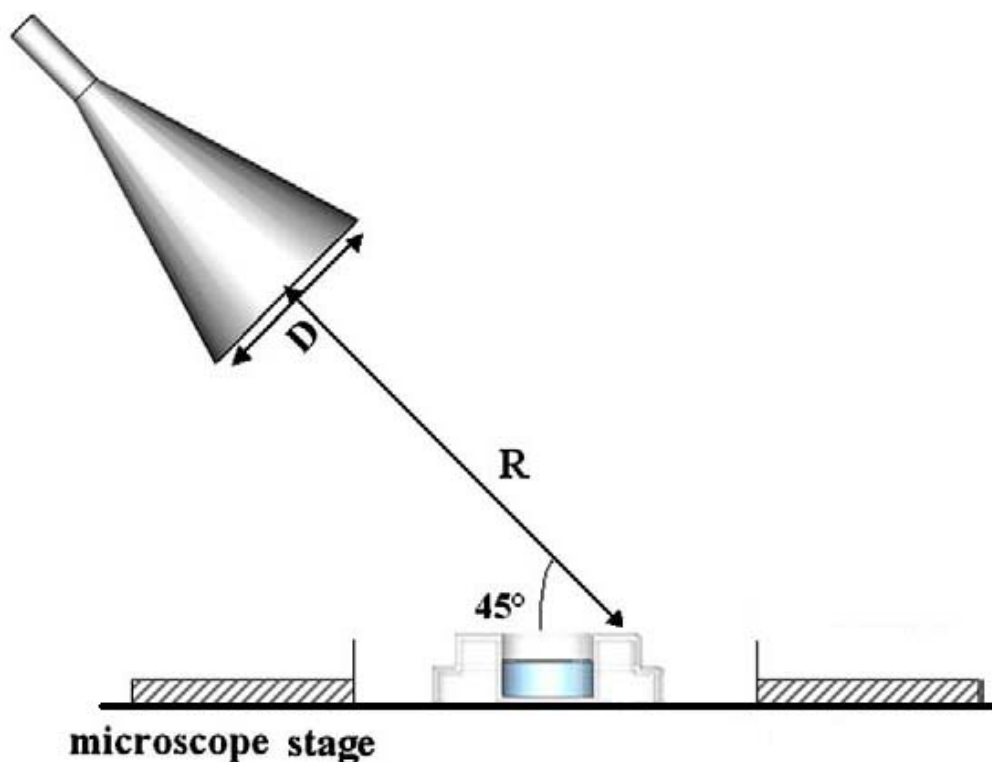


**Figure 5.15** Diagram of the experimental set-up used for the exposure of GUVs to 52-72 GHz radiations, including the horn antenna and the exposure chamber. Dimensions:  $D=34$  mm;  $R=8$  cm. In this figure is also shown that the sample was exposed from the top.

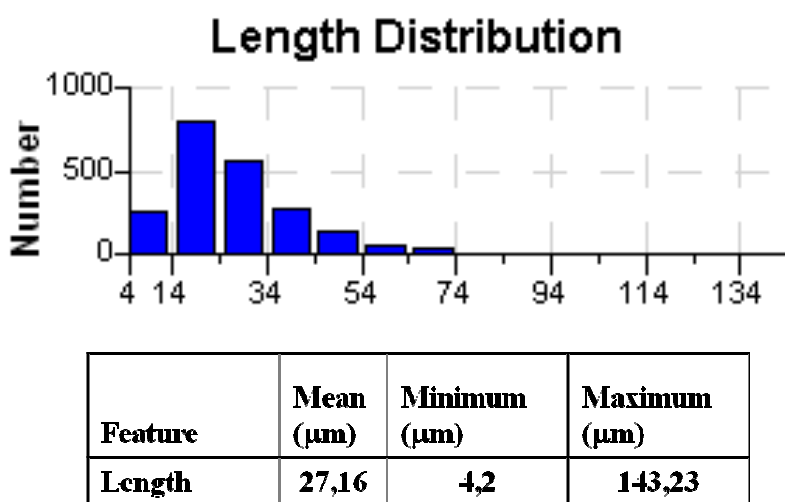


**Figure 5.16** Size distribution of giant unilamellar vesicles obtained from EPC/CHOL (70/30 %wt) lipid mixture.

For the exposures we used the same chamber in which the vesicles were electroformed. The vesicle suspension (1.05 ml) was subjected to either 52-72 GHz radiation or sham exposure, that corresponds to the same set-up but with the generator turned off (Incident power density = 0). The irradiation was turned on consecutively for 4 hours (this exposure time was chosen based on our previous experiments on multilamellar vesicles, see Chapter 4). At the end of irradiation vesicle size distribution was measured immediately and again after 20 minutes. Successively 150  $\mu$ L of a glucose solution 10 mM were added to the vesicle suspension, and vesicle size distribution was measured 5 and 30 minutes after the addition of glucose.

Data shown refer to the best ones of three independent experiments.

### **5.3.2.7 Dosimetry.**

As for the dosimetric calculations we remind to section 5.2.2.7.

## **5.3.3 Results.**

### **5.3.3.1 Formation of giant vesicles.**

In a first series of experiments we used different lipids and lipid-cholesterol mixtures to standardize the electroformation procedure with our electroformation chamber, carefully checked if the formation of giant vesicles was reproducible and setting up the procedure to measure vesicle size distribution by light microscopy.

After testing the more appropriate AC field parameters (frequency and voltage) for vesicle formation of single component GUVs made of POPC or DLPC, that resulted to be 10 HZ and gradually up to 2V, giant vesicles of gradually increased complexity were prepared, using lipid mixtures or adding cholesterol in the lipid membrane and testing their influence in affecting the AC field parameter for a successful production of vesicles.

Table 5.2 reports the outcome of giant unilamellar vesicles formation by electrosweeling method at different POPC/CHOL (%wt) ratios from an initial lipid solution 0,5 mg/ml in chloroform/methanol (9:1).

**Table 5.2** GUVs obtained from different POPC/CHOL mixtures.

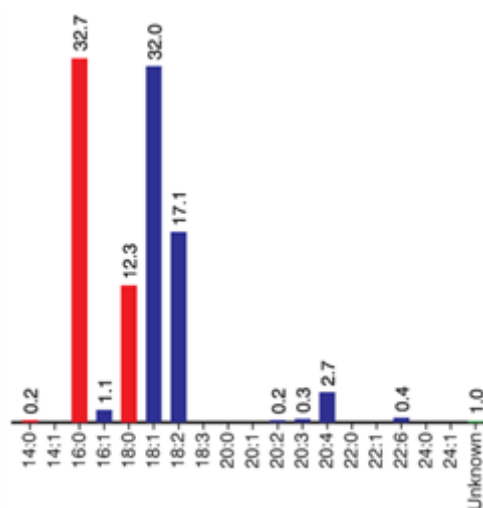
RATIO POPC/CHOL (%wt)	CHCl <sub>3</sub> (ml)	MeOH (ml)	FORMATION	REMARKS
95:5	160	20	+	Voltage increase up to 3 V
90:10	80	10	+	Voltage increase up to 4 V
80:20	80	10	++	Successful formation only increasing the voltage up to 6 V
70:30	80	10	++	Successful formation only increasing the voltage up to 6 V
50:50	80	10	-	Voltage increase up to 6 V

Formation of liposomes: ++, very successful preparations; +, with success; -, lower yield and/or smaller sizes giant liposome found.

From these experiments two main considerations can be concluded:

- Increasing amount of cholesterol inhibits giant vesicles formation at low voltage;
- 50 wt% of cholesterol definitely inhibits giant vesicles formation even increasing voltage to very high values (> 6V).

As for testing the influence of lipid mixtures on the frequency and voltage parameters we used egg yolk PC, in which several fatty acids are present according to the distribution reported in Figure 5.17.

**Figure 5.17** Fatty acid distribution in Egg PC (taken from [www.avantlipids.com](http://www.avantlipids.com)).

In this case, voltage and frequency values to obtain GUVs were the same as in single components lipids (10 HZ and up to 2V), but interestingly, when CHOL was added to

lipid mixtures, even higher values than those applied in POPC/CHOL mixtures were necessary to successfully obtain giant unilamellar vesicles (see sequence in Figure 5.18).

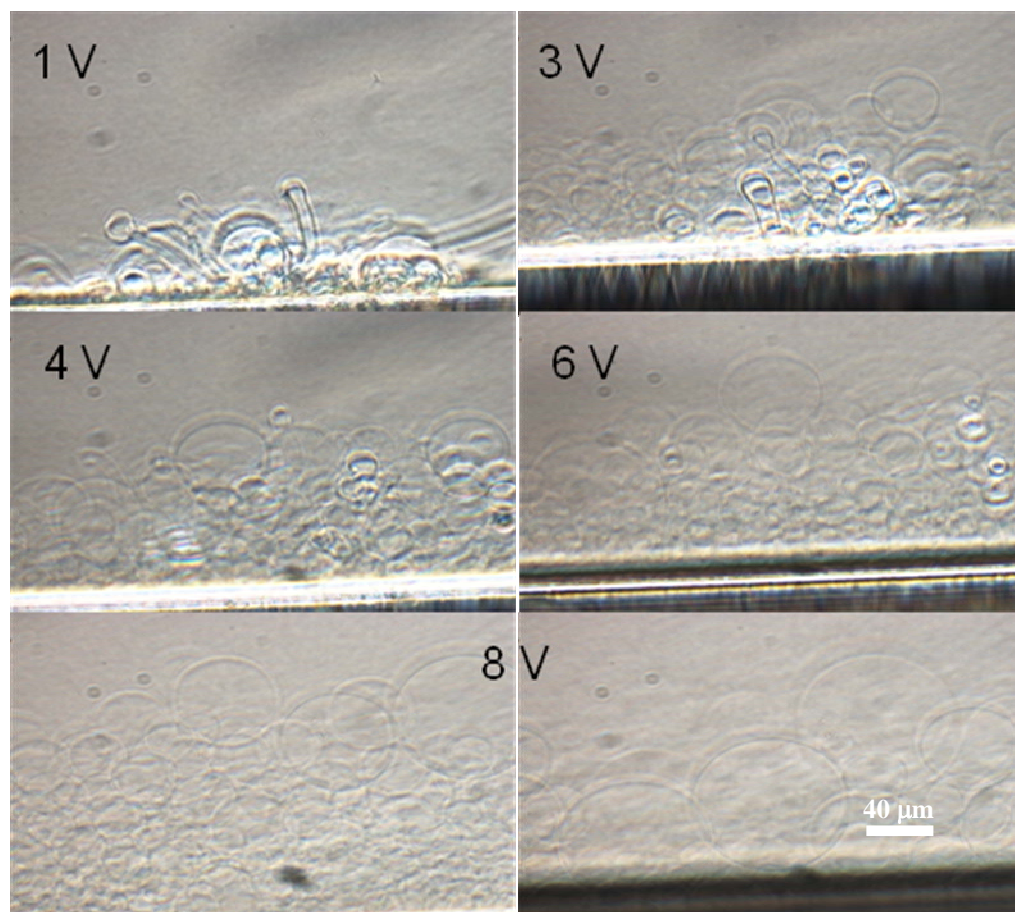


**Figure 5.18** Sequence showing the effect of increasing voltage in EPC/CHOL (70/30) lipid mixture: at 1V during the electroformation process mainly myelin figures due to natural swelling of lipids (Walde, 2004) are still present; increasing voltages (3,4,6 V) gradually reduce the presence of tubular shape vesicles and induce the formation of giant vesicles, finally obtained applying a voltage of 8V.

From the experimental observations some general conclusions can be drawn. It can be concluded that electroformation of GUVs is strongly affected by:

- Voltage applied: at the beginning of the electroformation process voltage has to be increased very slowly, both for more and less rigid systems. The final voltage value has been chosen according to the lipid mixtures: lipid solutions which present elements that induce more rigidity to the membrane, like cholesterol (Lande et al., 1995), need the application of higher voltages in the final electroformation step. Moreover, voltage strongly affects the final vesicle sizes, so that the mean size of vesicles can be regulated according to the applied voltage.

- Lipid composition (rigidity of the system inhibits vesicle formation);
- Other factors like uniformity and thickness of the deposited dry lipid film (data not shown).

### 5.3.3.2 Osmotic Effects of Giant DLPC Vesicles.

In this experiment, DLPC GUVs prepared in pure water (Figure 5.19a), were subjected to an osmotic pressure by addition of a glucose solution 1,25 mM to the vesicle suspension. The osmotic gradient between the internal pure water solution of GUVs and the external glucose solution, immediately led to a shrinkage and shape change in vesicles (Figure 5.19b).

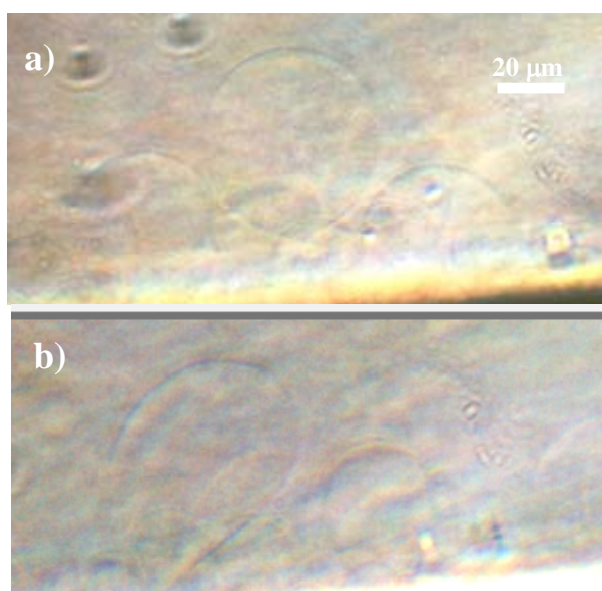


**Figure 5.19** a) Electroformed DLPC GUVs in pure water; b) same vesicles under osmotic pressure; picture is taken 5 minutes after the addition of a glucose solution 1,25 mM. A change in the shape of vesicles and a shrinkage of their sizes are clearly visible from comparison.

Size distribution of vesicles in pure water was measured after checking for vesicles stability. The histogram illustrated below (Figure 5.20a) shows a mean vesicle diameter of 23 μm.

The addition of glucose to the vesicle suspension, after 4 hours of exposure condition simulation, abruptly decreased the size of vesicles already after 5 minutes (Figure 5.20b) and after 30 minutes the mean diameter of vesicles was reduced to 16 μm (Figure 5.20c) that corresponds to 31% shrinkage of vesicles size compared to the initial vesicle size distribution.

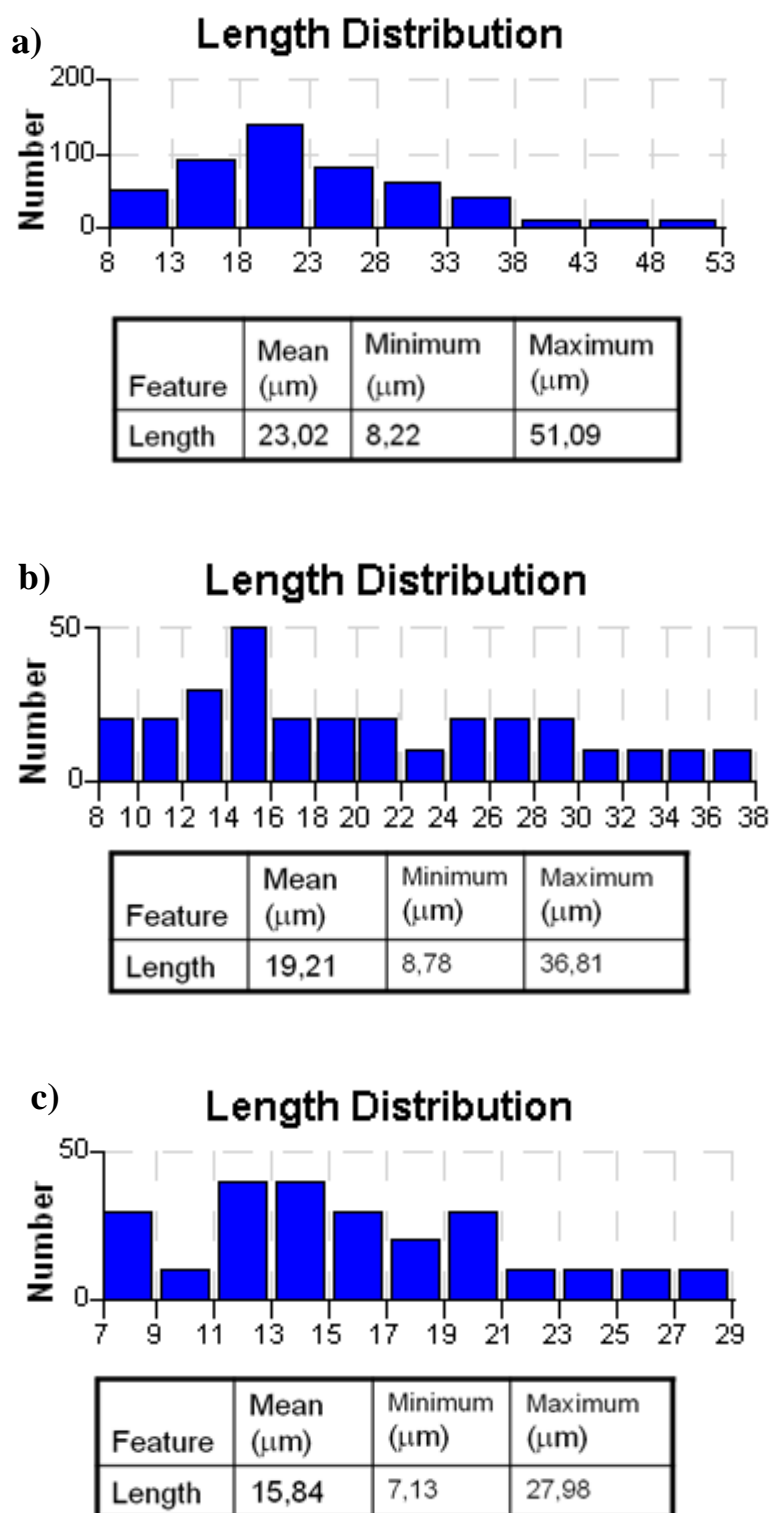


**Figure 5.20** a) Size distribution of DLPC GUVs in pure water; b) Vesicle size distribution measured 5 minutes and c) 30 minutes after the addition of a glucose solution 1,25 mM. A reduction of about 32 % of vesicle mean diameter compared to the initial one was observed.



It is worth to note also that osmotic pressure seems to affect mainly big vesicles, as can be noted by comparing minima and maxima diameters before and after the glucose addition. The maximum value of the vesicle diameter is significantly reduced while the minimum value is constant over the time. This effect is also visible looking at the histograms: in Figure 5.20a it resembles a skewed-right size distribution, while in Figure 5.20b and c a more homogeneous distribution of vesicle sizes is observed.

### **5.3.3.3 Millimeter wave effects on water osmotic permeability of Giant DLPC Vesicles**

On a another electroformation chamber, where vesicles were formed in the same conditions and following the same experimental procedure as described above, vesicle size distribution was measured before (Figure 5.21a) and after (Figure 5.21b) 4 hours of exposure to MMW radiations. No evident effects were observed in terms of morphological changes or vesicle size distribution (compare Figure 5.21a and b) during the exposure and 30 minutes after turning off the radiation. Then, a glucose solution 1,25 mM was added to the exposed system solution, but despite the significant shape change and rapid reduction of vesicle size observed in the sham sample, after 5 minutes the addition it was not observed any significant change in the shape and in the size of the vesicles and 30 minutes after the percentage of vesicle size shrinkage induced by the internal-external osmotic gradient was reduced only to about 5% the original value (compare Figure 5.21a and c).

Moreover, the shape of the size distribution is not affected significantly neither by the radiation nor by the following addition of glucose, and all the histograms show the same initial skewed-right distribution.

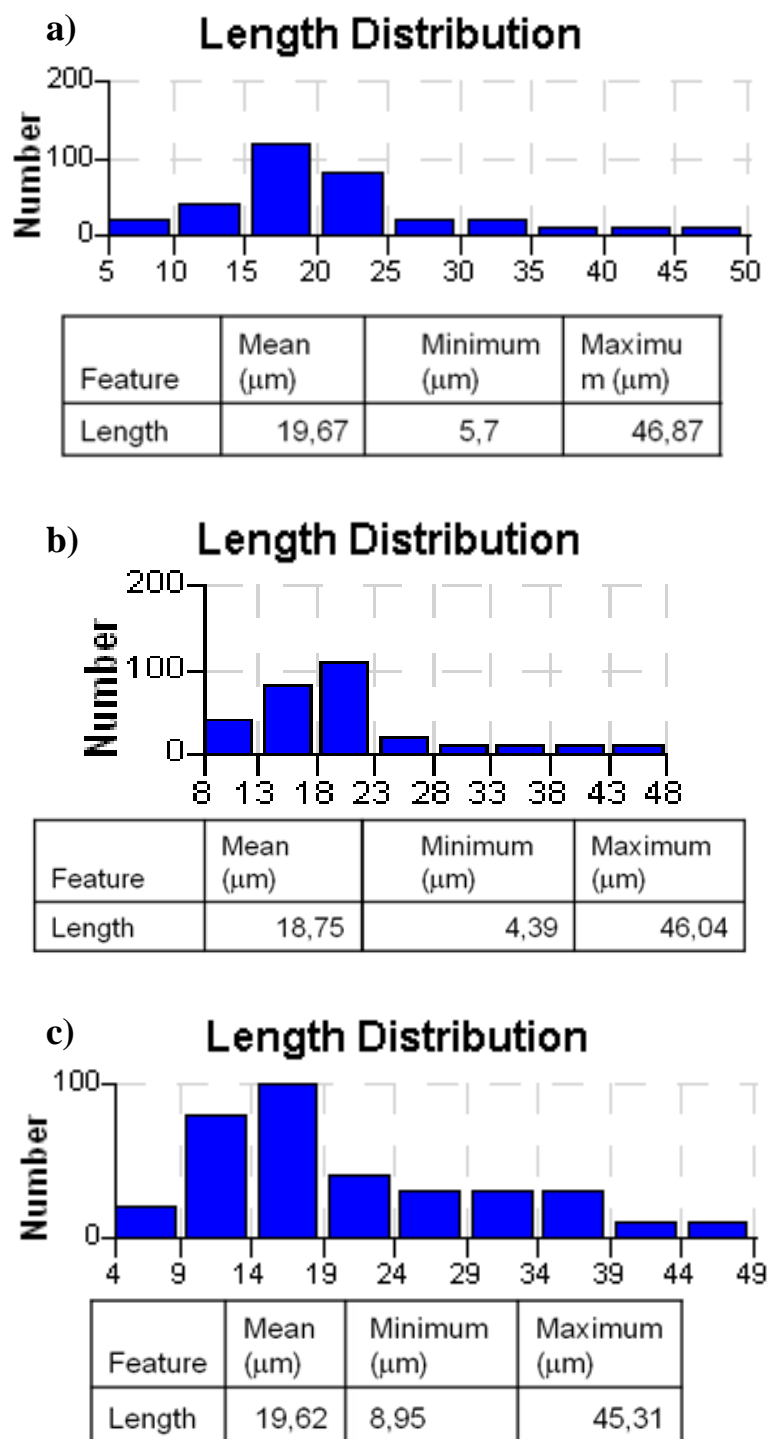


**Figura 5.21** Size distribution of DLPC GUVs a) in pure water, b) after 4 hours of vesicle exposure to MMWs; c) 30 minutes after the addition of a glucose solution 1,25 mM. No differences in the size distribution were observed during and after irradiation. A reduction of about 5 % in the mean size of the exposed vesicles was observed under osmotic pressure.

### **5.3.4 Discussion.**

The exposure of GUVs to a millimeter wave radiation with an output power of a few mW, did not result in any change in the morphology or geometry of vesicles.

Nonetheless, under osmotic pressure, exposed vesicles showed a different behavior compared to the sham ones. These last were very sensitive to the osmotic gradient induced by the addition of glucose and a shrinkage of 31 % of the vesicle size was observed already 30 minutes later. In contrast, exposed vesicles, that seemingly were not affected by the radiation, exhibited a different response of water permeability through the membrane under osmotic pressure, resulting in a vesicle size shrinkage of only 5%.

Our results seem to be in contrast with previous findings on GUVs subjected to MMWs at an output power of 39 MW (Ramundo-Orlando et al. 2009), where, under exposure, vesicles exhibited clear changes in their geometry. A faster movement of free vesicles during irradiation compared to a sham situation (no irradiation) period was also observed.

It has been suggested that for resonances to have an important effect on the biological systems, a significant energy transfer must be allowed during the coupling with the electromagnetic field (Adair, 2002). Even though this was not the case, according to the authors, the above results indicated that giant vesicles could exhibit vibrational resonances at MMW frequency.

It is worth to note that even if the exposure set-up and the irradiating frequency we used are very similar to those adopted by these authors, the output power of the radiation is significantly lower. This means that under the low power exposure conditions we applied, the coupling with electromagnetic field might not result in the same effects they observed in giant vesicles.

Nonetheless, their molecular interpretation of these phenomena, according to which the action of MMWs would be at the membrane–water interface, could explain for the reduced water permeability we observed in the exposed system, being, as suggested by Mathai et al. (2008), the membrane-water interface the rate limiting step for water permeability in single lipid component membranes.

Moreover, it has been suggested that physical changes, like an increase in membrane tension or higher curvatures of the membrane, could be linked to an enhancement in hydration depth (polarity) of the lipid bilayer (Zhang, 2006); in these last cases the area per lipid molecule should increase (see section 1.6).

In our experiment, the reduction of water permeability following the exposure to MMWs, could then be explained by an action of the radiation on the membrane hydration that reduces the area per lipid molecule.

This hypothesis is confirmed by our previous studies on the exposure to MMWs of MLVs close to the main phase transition point (see Chapter 4).

In that case the radiation induced a reduction of the water ordering at the membrane interface, and when the system was close to its main phase transition temperature, this caused a transition to the gel phase, which notoriously presents a smaller area per lipid compared to the respective fluid phase. In addition, some studies suggest that a reduction in water permeability is linked to a reduction in membrane fluidity (Lande et al., 1995), that also occurs when the system passes to a gel phase.

In that case we explained for the observed effects by claiming a redistribution of water molecules among the binding sites at the membrane-water interface (see Chapter 4).

This molecular interpretation is consistent with the hypothesis of a reduction of the area/lipid to explain for the decrease of the water permeability.

The present experiment confirms our previous results and provides further consistent proofs to support the hypothesis of an action of MMWs at the membrane-water interface and the important role that water plays in such interaction.

## **5.4 CONCLUSION**

In this chapter we have shown our study on the effects of the radiation on the physical properties of membranes (physical stability and permeability) by monitoring shape and size changes in vesicles in absence and presence of MMWs radiation.

Changes in shape and size of vesicles, can be induced by varying the area/volume ratio (see section 1.9). This can be done in several ways:

1. by inducing an osmolarity difference between the outer and the inner medium of the vesicle (Farge and Devaux, 1992);
2. by addition of lipids to one of the leaflets (Jie et al., 1998);
3. by temperature variation.

In the case of LUVs experiments, this has been done by spontaneous addition of lipid monomers from smaller to bigger vesicles through the so-called Ostwald ripening (see

section 5.1); in the case of GUVs, Ostwald ripening cannot be observed because this is a curvature dependent mechanism and smaller the vesicles more probable this process is – we should keep in mind that we are comparing large vesicles of 100 nm with giant vesicles in the range 10-100  $\mu\text{m}$ . Therefore, to induce shape and size transformation in GUVs we have introduced an osmolar gradient between the internal and external solution of vesicles (section 5.3)

Nonetheless the same mechanism which explains for the inhibition of the ripening process, can explain the decrease of water permeability of membrane too: a change of polarization states of water induced by the radiation that causes a partial dehydration of the membrane and consequently a greater packing density (increased membrane rigidity). In fact, irradiation seems to reduce water permeability by increasing membrane rigidity, in a manner similar to that observed when cholesterol is inserted in the membrane bilayer ( Lande et al, 1995).

We also induced shape changes in GUVs upon temperature variation, but because of some interesting observations during the standardization procedure, we decided to go in more details in the study of the temperature dependence of vesicle shapes. To these interesting results we have dedicated the next chapter (Chapter 6).

## **CHAPTER 6**

**Cooling rate effects on phase shape transition in GUVs**

As explained in Chapter 1, giant vesicles can be considered the paradigm of biomimetic systems. Their big size, comparable to that of a real cell, has allowed the direct observation under a microscope of many relevant biological phenomena.

At the same time, the reductionist approach they offer, focusing on a simple and specific composition of the lipid bilayer, compared to the complex structure of a real system, has made possible the identification of many physical mechanisms and even a quantitative explanation for such phenomena, that has represented an interesting challenge for many physicists and chemists (Walde et al., 2010).

For example, the quest for an understanding of the different shapes that erythrocyte cells assume when undergoing transformations under external perturbations (Fischer et al. 1978), is one of the reasons for studying giant vesicles.

Our first interest in GUVs was inspired by the idea to get some “direct” evidences, visible under a light microscope, of the effects of MMWs on lipid membrane properties.

In particular we wanted to prove MMW effects on membrane properties by monitoring how they affected shape changes in GUVs.

Shape changes in vesicles can be induced by varying the area/volume ratio of vesicles (see Chapter 1 and section 5.4). In giant vesicles the two most diffuse methods to induce such variations are:

1. By inducing an osmolarity difference between the outer and the inner medium of the vesicle (Farge et al., 1992) that is responsible for a change of vesicle volume at constant area;
2. By varying the temperature. A temperature variation in vesicles affects the packing density of lipids (and also has some consequences on the fluidity properties of the membrane) that is responsible for a change in the area/volume ratio and a consequent change in vesicle shape (see Chapter 1).

Our study on the effects of radiation on GUVs are described in the previous chapter (see section 5.3). In particular, from the experiments on water osmotic permeability in GUVs under radiation exposure, it resulted that shrinkage processes were strongly reduced after irradiating the system for 4 hours, because of a reduced water permeability through the membrane. This effect has been associated to an increase in membrane rigidity.

We also were interested in verifying whether radiation would have been able to induce some changes in the packing density of membranes – as deduced from the experiments on LUVs (see section 5.1) – by affecting the normal change in the packing density (and then in vesicle shape), induced by temperature. Moreover, as radiation effect is particularly enhanced in the vicinity of phase transition, as confirmed by our NMR studies on multilamellar vesicles (Chapter 4), we were particularly interested in studying MMW effects on the phase shape transition of GUVs .

Nevertheless, during the standardization procedure, we observed that vesicles showed a different behavior according to the rate at which temperature was changed and then we decided to devote more attention to this phenomenon.

The very interesting outcomes of such study are illustrated in this chapter.

## **6.1 INTRODUCTION**

Here we will show our study on the phase shape transition of ITO glass supported GUVs by cooling the system at different rates. A variety of effects have been observed in dependence of the scan speed, like pore, bud and pearl-chain formations (Doebner, 2000), all resulting in the final breaking up of the mother vesicle. Such effects are observed only in proximity and through the main phase transition, but not far from it. Even more interesting, rupture effects have been observed only above a “threshold” scan rate of 0.2 °C/min.

These observations inevitably evoke the question of non-equilibrium phenomena in interacting vesicle dynamics and, related to this, the relaxation processes of the system to recover an equilibrium situation (Franke et al., 2009a). Non-equilibrium effects are still not completely understood and topic of discussion in current research (Seifert, 1999).

The cooling rate “threshold” we have found by changing the temperature across the main phase transition, somehow, marks the boundary between equilibrium and non-equilibrium dynamic processes in adherent vesicles, where complete rupture of the vesicle occurs, and provides an estimation of the relaxation times of the cooperative area fluctuations occurring in adherent membranes at the phase transition.



The need to use adherent vesicles is bivalent: first, such a system can serve as a model for studying the nontrivial kinetics of biological situation of adhesion of membranes under ramped forces, getting a contribution to the dynamic unbinding of these cells (Bongrand, 1995); second, unbinding transition of vesicles in an equilibrium regime, let us to get some thermodynamic information about the system and to calculate relaxation times of vesicle cooperative area fluctuations (Franke 2009b; Grabitz, 2002, Wunderlich, 2007).

This relaxation time is used for comparison with the relaxation time estimated by changing the cooling rate. This comparison supports the hypothesis that membrane adhesion may play a major role in regulating relaxation processes in biomembranes.

This work provides a simple method to have an estimation of relaxation times of cooperative processes at the transition temperature in biological membranes.

### **6.1.1 Equilibrium and non-equilibrium dynamics in vesicles.**

Giant vesicles are characterized by a slow dynamics, in the range of seconds. This makes possible to directly observe under a microscope dynamical aspects in vesicles.

Vesicle dynamics can be distinguished in dynamics of equilibrium and non-equilibrium phenomena.

Equilibrium dynamics comprises the dynamic fluctuations around mean shapes, like in the case of prolate-oblate transition (see Chapter 1). Non-equilibrium phenomena can be further distinguished in two classes: 1. The relaxation to a new shape after a perturbation; an example is the decay of a metastable shape such as budding or pearl chain processes induced by a temperature change (see Chapter 1 and Döbereiner, 2000a); 2. by non-equilibrium states generated by external fields, such as hydrodynamic flow (Seifert, 1999).

### **6.1.2 Relaxation times in vesicles.**

In general, vesicle shape transformations occur when, after changing some external conditions, the system can relax to a new favorable equilibrium state (that is the state showing a minimum in the free energy). The time the system needs to recover its equilibrium situation is the so called relaxation time.

Sometimes, the relaxation time  $\tau_i$  is related to state variables (as enthalpy) by a simple single exponential function of time

$$\frac{d\varphi_i}{dt} = \varphi_{i,u} \exp\left(-\frac{t}{\tau_i}\right) \quad (6.1)$$

However, most of the time, the situation is made more complex because of the presence of many relaxation processes, that usually interact each other. According to Onsager (1931), thermal fluctuations of the system can be seen as a perturbation from its equilibrium and we can conclude that fluctuations and relaxation processes have the same timescale.

Relaxation processes have been studied by many authors by various techniques. Some relaxation times found for different lipid and model systems are reported in table 6.1. The reason for the many different relaxation values are: 1. different physical process involved – for instance, it is well known that trans-gauche isomerization happens in ns time scale and diffusion processes in 100 ns time scale (see section 1.6.2); 2. not accuracy of experiments; 3. different sensitivity of the investigation technique.

The above cited relaxation processes occur at an atomistic or molecular level and then require the use of spectroscopic techniques. But it is worth to appreciate that dealing with fluctuations, a molecular description can have sense only if considering statistical distribution functions. Sometimes a mesoscopic approach can result more advantageous for the understanding of such phenomena, as they imply some cooperativity of the system.

For example, when studying membrane phase transitions, it has been shown that such fluctuations dramatically increase. In particular this effect is enhanced in proximity of domains interfaces (Heimburg, 2007) and this can have far reaching consequences on the elastic properties of the membrane. Since such an increase in fluctuations, also relaxation behavior of membranes is expected to change in the transition regime.

Table 6.1 Relaxation times,  $\tau$ , found for different lipid models (sometimes multi-steps processes, with different  $\tau$ , have been found).

LIPID	$\tau_1$ (T)	$\tau_2$ (T)	REMARKS	REFERENCES
DSPC MLV	2.4 s			Van Osdol (1991b)
	18 s (54,81 °C)	103 s (54,93 °C)		Schiewek et al. (2010)
DPPC MLV	3.89 s			Van Osdol et al. (1991b)
	45 s			Grabitz et al. (2002)
	34 s (41,65 °C)	110s (41,60°C)	DPPC has a sharper transition compared to DSPC	Schiewek et al. (2010)
DMPC MLV	30 ms			Tsong and Kanehisa (1977)
	2,04 s			Van Osdol (1991)
	35 s			Grabitz et al. (2002)
	20 s (24.05-24.19 °C)	100 s (24.05-24.19 °C)	T interval even smaller than DPPC because of the very high cooperativity of the transition	Schiewek et al. (2010)
	100 ms , 10 ms	3s		Elamrani and Blume (1983)
DMPA MLV	5-10 s	20-45 s	Cooperativity lower than PC and then T interval broader	Schiewek et al. (2010)
	26 s (50 °C)	60-80 s		Schiewek et al. (2010)
DMPE MLV	40 ms		SV (somicated vesicles) have broadened melting profile and consequently short time are expected	Gruenewald (1980)
DMPC&DPPC SUV	2 ms	20 ms		Wunderlich et al. (2009)
D15PC/DOPC SUV	80ms		Relaxation amplitude shows a broad low maximum at $T_m$ and relaxation time is quite constant over much of the transition region: different behavior than MLV. These results are similar for DMPC LUV	Van Osdol et al. (1991a)
DPPC LUV	<10 s	>10-15 s		Pott et al. (2002)
SOPC GUV	30 ms		Lifetime of macropores	Dimova et al. (2007)
	0.5-3 s		Relaxation time of vesicles with excess area	Leiter et al. (2009b)
Egg-PC GUV	5 s			
DPPC GUV				

Some examples of similar relaxation times from biology are also reported, as the fluctuations in lipid domains in lung surfactants (relaxation time of 50-130 ms), transition of proteins (100 ms), ion release through potassium channels (10 ms) (Heimburg, 2007). In particular it has been found that erythrocytes and erythrocyte ghosts have relaxation time in the range 0.4 and 9 s. These times can be attributed to hemolysis but also to cooperative melting events. These data are very interesting because lipid models are very close to these structures. However, in general, due to the complexity of real biological membranes (many different kinds of lipids and proteins that spread heat capacity and relaxation times values), heat capacities are low and fluctuations occur locally and not on a global scale (cooperative processes).

Many of these studies came to the conclusion that relaxation times dramatically increase at the main phase transition (Grabitz et al., 2002; Seeger et al., 2007; Heimburg, 2007).

Grabitz et al.(2002), have proposed a thermodynamics model that relates the heat capacity to the relaxation times of cooperative processes close to the chain melting transition of lipids and have found that the relaxation time is maximum at the main phase transition,  $T_m$ .

Wunderlich et al. (2009) have found current fluctuations in the fluid phase of 2 ms and during the phase transition of 20 ms. So the relaxation time near  $T_m$  is 10 times slower than away from it. The existence of fluctuations far and near  $T_m$  means that the nature of the mechanism is the same but the physical state of the membrane affects the intensity of the phenomenon.

Even though relaxation times can be attributed to processes occurring in the order of ps, they have found that fast relaxation processes contribute for less than 10% to the relaxation processes at the phase transition, therefore only cooperative domain fluctuations can be taken into account (Grabitz et al., 2002; Seeger et al., 2007). According the theory of Grabitz, the system is composed by an ensemble of highly cooperative sub-systems, which change energy each other inducing enthalpy fluctuations. When close to  $T_m$  some systems are already in the opposite phase. This means that phase transition occurs as a single step process.

Recently a pressure perturbation calorimetry (PPC) study has been performed to evaluate the number of processes involved for time scales  $>10s$  (slow processes), related to lipid phase transition (Schiewek et al., 2010). Relaxation times in the seconds range

have been found (see table 6.1). Nevertheless, in contradiction with the data from Grabitz et al., about 50% of the heat uptake was due to processes not resolved by the instrument, and therefore concerning faster relaxation times, showing that a multiple step process occurs at the phase transition.

Even though the reduced lipid concentration in GUVs doesn't allow to apply the commonly employed techniques (spectroscopic or calorimetric techniques) to get information about the relaxation times, the direct visualization under a microscope, has allowed the monitoring of thermal shape fluctuations (Pott et al., 2002) and the measurement of area relaxation times, by applying electric fields (Riske et al., 2006; Dimova et al., 2007) or by vesicle quenching induced by temperature (Leirer et al., 2009b).

Nonetheless, to our knowledge, not so much is known about the relaxation processes in case of adhering giant unilamellar vesicles.

This work provides a simple method to have an estimation of the relaxation times of the cooperative processes in glass supported GUVs through  $T_m$ , and elucidates the role that adhesion plays in regulating relaxation process in biological membranes.

## **6.2 MATERIALS AND METHODS**

### **6.2.1 Materials.**

Chloroform and acetonitrile were purchased from Sigma-Aldrich and were of the highest quality commercially available. The water used in all sample preparations was purified by a Millipore Milli-Q cartridge system.

1,2-dimyristoyl-*sn*-glycero-3-phosphocholine (DMPC) was purchased from Avanti Lipids.

### **6.2.2 Sample preparation.**

DMPC GUVs were prepared with the electroformation method originally developed by Angelova and Dimitrov (1986; Angelova et al., 1992; Angelova, 2000). The investigation chamber was made from two 25mm×45mm glass slides covered with

indium tin oxide (ITO) (Estes et al., 2005) with their conductive faces facing each other, separated by a 1.6 mm thick rectangular frame of poly-dimethylsiloxane (PDMS) with a 10mmx10mm central hole, the whole sandwiched between two thin metal slides holed in the middle, provided by the workshop of the ETH, Zürich (Figure 6.1a).

GUVs were electroformed from lipid films spin-coated on the ITO glasses. In this case, DMPC was dissolved in chloroform : acetonitrile (95:5 v/v), at a concentration of  $3.75 \text{ mg ml}^{-1}$ . Approximately 0.25 ml of this solution was deposited on the conductive face of the ITO glass, and spin-coated at 1200 rpm for 5 min. The lipid films were then dried under vacuum ( $\approx 8 \text{ Mbar}$ ) for 2 h to remove traces of solvent.

Distilled water was injected through a hole in the PDMS spacer, and 10 Hz 1.2 V (peak-to-peak) was immediately applied between the two ITO glasses. The formation of giant vesicles was then observed by light microscope. After approximately 2 h, vesicles between 20 and 90  $\mu\text{m}$  in diameter were formed (Figure 6.1b). All the steps of vesicle preparation were performed at  $37 \text{ }^\circ\text{C}$ , well above the main phase transition temperature of DMPC ( $\approx 23^\circ\text{C}$ ), so that the phospholipids were in their liquid crystalline state.

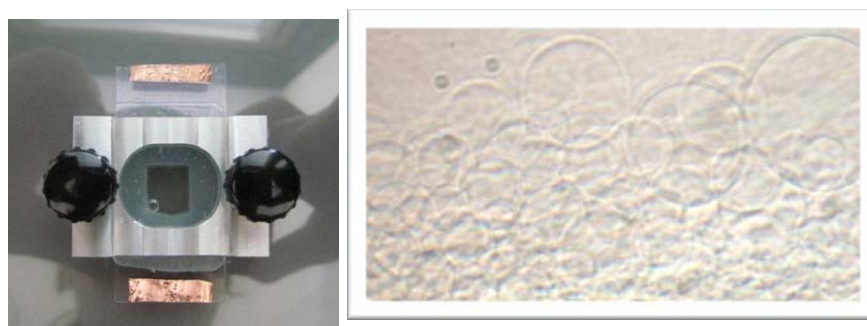


**Figure 6.1** a) ITO chamber and b) DMPC GUVs formed by the electroformation technique (Estes et al., 2005).

### 6.2.3 Experimental set-up.

The experimental set-up is illustrated in Figure 6.2.



**Figure 6.2** Experimental set-up for the study of shape phase transition in DMPC GUVs.

The experiments were performed using the same electroformation chamber with optical access from the bottom and the top. During the experiments, the temperature was controlled with the aid of an Instec's basic hot and cold stage system (Boulder, Colorado), consisting of a hot and cold stage, a STC200 temperature controller, with a temperature resolution of  $\pm 0.1$  °C, and WinTemp - a Windows based software. An additional sample chamber cooling accessory (liquid nitrogen cooling accessory) was required for below ambient operations. Temperature measurements were performed with a thermocouple within the experimental chamber.

Vesicles were observed with a Leica DM LP microscope with a 50 $\times$  objective using the phase contrast mode. The videos and images were acquired using a standard digital video-camera (Canon) and pictures are presented as collected: no image processing was applied.

#### **6.2.4 Experimental procedure.**

After electroformation at 37 °C, the system was gradually cooled down to 26 °C (still above DMPC main transition temperature of  $\approx 23$  °C) and vesicles were monitored for 1 hour: no variations in shape, size and number of vesicles were observed.

Before starting the experiments we standardized the heating/cooling system by observing shape changes of free vesicles with different morphology.

As an example, we report changes observed in a tubular vesicle upon several cooling/heating cycles at a rate of 0.2 °C/min (Figure 6.3).

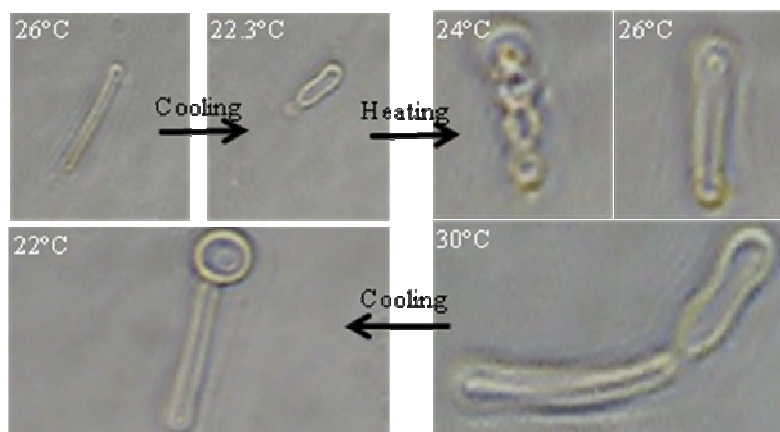


**Figure 6.3** Monitoring of a free tubular vesicle cooling and heating the system at a rate of 0.2 °C/min.

## 6.3 RESULTS

### 6.3.1 Phase transition induces rupture of adhered vesicles above a temperature threshold.

We have studied the shape transformations of DMPC GUVs supported on a ITO glass surface during the fluid-to-gel phase transition, under different cooling rates.

When cooling at a rate of 0,2 °C/min we observed only some fluctuations and a few modifications of the vesicles that became more spherical in size. Moreover some vesicles became smaller and disappeared. We think that this last effect was most probably due to some fluctuations that occurred in vesicles or around them, causing the detachment of vesicles from the others and from the glass. So, in this case, adhesion forces have to be taken in account (Franke et al., 2009b). Nonetheless, no differences, in terms of evident shape modifications and rupture of vesicles, were observed going through the main phase transition  $T_m$  from 26 to 18 °C (Figure 6.4).



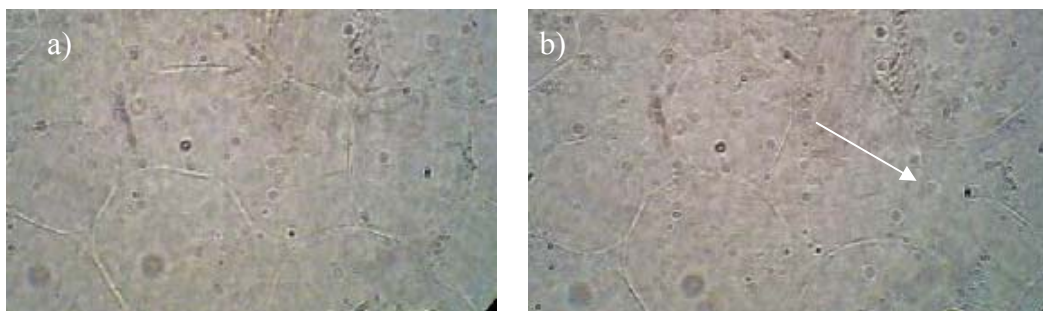


**Figure 6.4** Glass supported DMPC GUVs a) before (26°C) and b) after (18°C) cooling the system through DMPC main phase transition ( $T_m=22.7$  °C in this system – see section 6.3.3) at a rate of 0.2 °C/min. The arrow in b) shows the point where a vesicle present in a) detached from the glass surface due to a decrease in its adhesion area by going through  $T_m$ .

When the cooling rate was increased above 0.2 °C/min, completely different behaviors of vesicles were observed. Such difference was already visible at 0.3 °C/min but it was very well observed at a temperature ramp rate of 0.5 °C/min.

When the system passed through the phase transition temperature, vesicles started to show first some fluctuations followed by irregular shapes and formation of pores that led either to direct rupture of the vesicles with formation of liposomal segments, or expulsion of daughter vesicles with formation of pear like structures and buds that brought to pearl chain formations, all resulting in a final irreversible vesicle breakdown (Figure 6.5).

This effect was dramatically enhanced increasing the temperature ramp rate to 15 °C/min, where complete rupture of vesicles was visible immediately after starting the cooling process.

On the other hand, whenever it was possible to find some vesicle presenting an irregular shape but still almost intact, the following heating of the system above  $T_m$  induced vesicle changes from an irregular to a smooth morphology assuming in the end almost a spherical shape.

The variety of phenomena observed is dependent on: 1. membrane curvature; 2. vesicle size; 3. vesicle surrounding (vicinity to other vesicles).

Vesicles in contact with others were more subjected to rupture because of the pressure from the other vesicles. Bigger vesicles were the first to go to rupture, and pore formations occurred in zones where the membrane curvature was bigger. Some small vesicles were even able to survive to the rupture process.

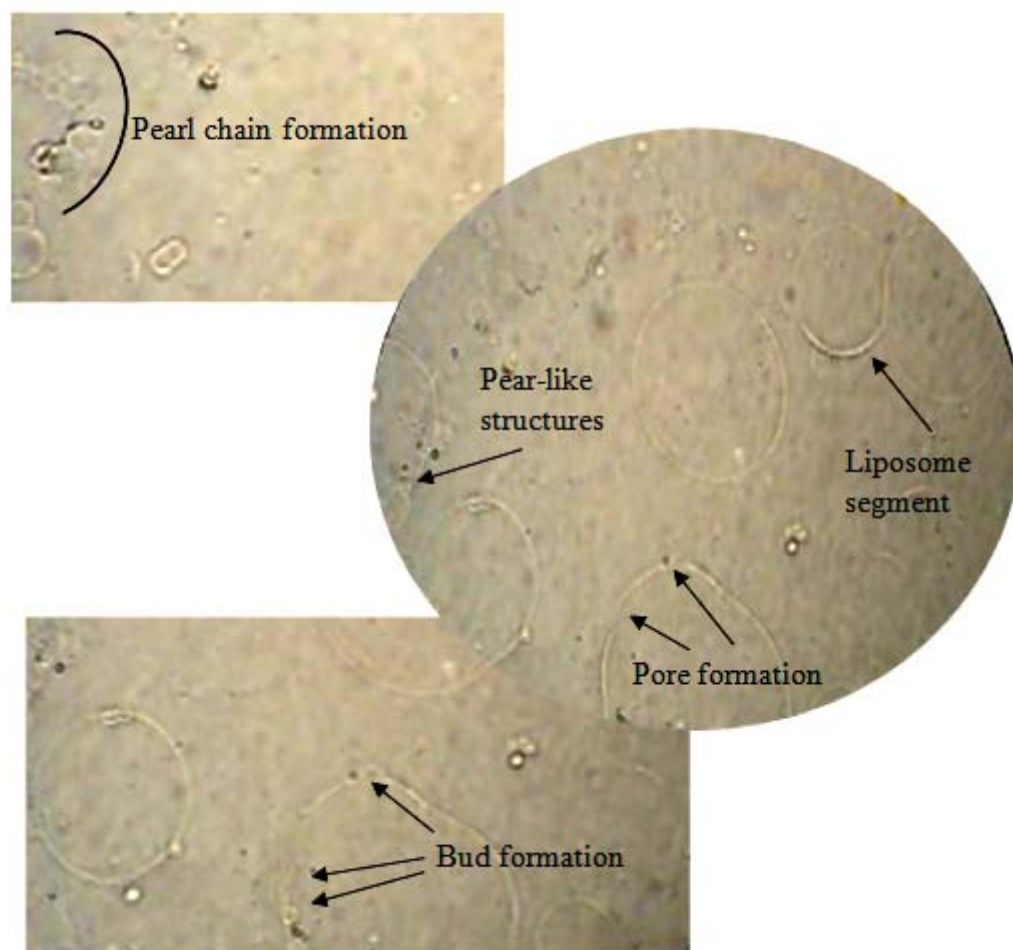


**Figure 6.5** Glass supported DMPC GUVs going through DMPC main phase transition ( $T_m=22.7\text{ }^\circ\text{C}$  in this system – see section 6.3.3) at a rate of  $0.5\text{ }^\circ\text{C}/\text{min}$ . Arrows show pore, bud and pearl-chain formations, all resulting in irreversible vesicles breakdown.

From these results it is clear that in order to observe the above effects, two conditions had to be fulfilled:

1. the system had to go across  $T_m$ ;
2. the cooling rate had to exceed a “threshold” estimated to be  $0.2\text{ }^\circ\text{C}/\text{min}$ .

The kinetics nature of this phenomenon may be attributed to the relatively slow relaxation dynamics of the membrane area vesicle reorganization at the main phase transition point, compared to the rate at which the transition region is spanned by cooling the system.

Therefore, the knowledge of the ramp rate threshold, above which membrane breakdown can be observed, allows an estimation of the membrane cooperative fluctuation relaxation time.

This value can be verified by independent calculation of the fluctuation relaxation time by measuring the variation of vesicle adhesion area going through  $T_m$  (Franke et al., 2009; Grabitz et al., 2002; Wunderlich et al., 2009) in equilibrium condition, as described in the following sections.

### **6.3.2 Temperature evolution of the adhesion area.**

The use of adhered GUVs to a glass support has turned out to be very convenient because the temperature evolution of the adhesion area of vesicles in an equilibrium regime let us to get some thermodynamic information about the system and to calculate the relaxation time of the vesicle area cooperative fluctuations (Franke 2009 adhesion; Grabitz, 2002, Wunderlich, 2007).

Generally, the transition gel-to-fluid phase is associated with an increase in vesicle area of about 20–25 % and in vesicle volume of about 4% (Julicher et al., 1993; see also section 1.3); the same, an area decrease of 25% during the fluid-to-gel transition has been observed (Leirer et al., 2009b).

Franke et al. (2009) showed that, following the melting process of adhered GUVs, the adhesion area (adhesion disk) of vesicles grew until when they reached the fluid phase, and the final adhesion area equaled the gel-fluid excess area. A similar experiment was performed by Gruhn et al.(2006), by an osmotic control of the excess area.

In order to calculate the adhesion area of vesicles through the fluid-gel phase transition in thermodynamic equilibrium conditions, we monitored an isolated vesicle cooling the system at a rate of only 0.2 °C/min (at which no vesicle ruptures were observed).

Our observable was the equatorial size of adhered vesicles, then the vesicle diameter we measured was neither the diameter of a free vesicle,  $R$ , nor the one of the adhesion area,  $a$ , but a combination of both (Figure 6.6a and 6.9a ).

Therefore we don't know how these two parameters vary with temperature. The only information available is the radius of the vesicle in the gel phase: in fact, when the system reached the gel phase, vesicle detached from the glass surface and the mid-plane size we measured immediately before the detachment can be, with a good

approximation, considered as the effective diameter of the vesicle, as the adhesion deformation contribution is negligible (Figure 6.6b).

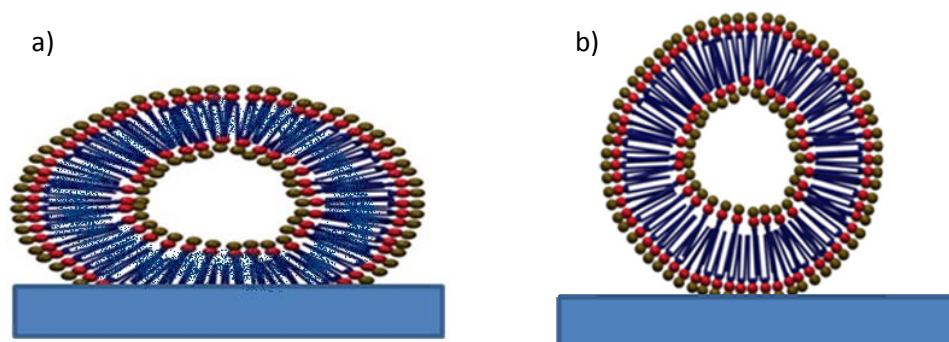


**Figure 6.6** Cartoon of a glass supported DMPC GUV in its a) fluid phase, where the excess area (the area increase respect the gel phase) is spreaded on the glass and the vesicle assume an ellipsoid shape, and b) gel phase, where the vesicle is almost detached from the surface and assume a spherical shape.

We used this value to extrapolate the  $a/R$  ratio dependence on temperature as illustrated in the following.

Lai et al. (2002) have shown for DMPC GUVs adhered to a glass support, that the degree of deformation,  $a/R$ , is a temperature-dependent decreasing function of the mid-plane diameter of vesicles. They measured the degree of deformation as a function of vesicle diameter at the temperature of 22.5 °C and we reported their data to extrapolate the  $a/R$  ratio of our vesicle at this temperature (Figure 6.7).

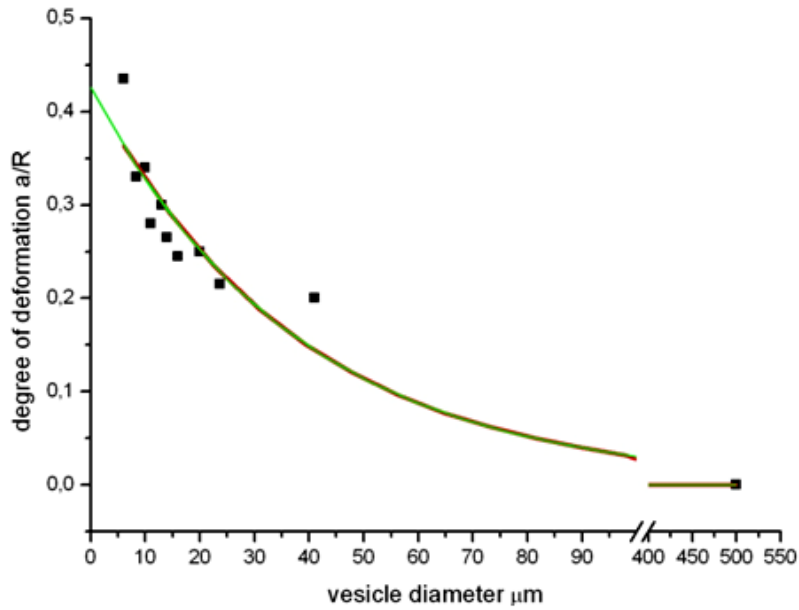


**Figure 6.7** The degree of deformation, ( $a/R$ ), at DMPC's  $T_m=22.5$  °C, against vesicle diameter of glass supported DMPC GUVs. (■) are the experimental data taken from Lai et al. (2002), the red line is the best fitting of experimental data and the green line is the simulation curve we used to calculate the  $a/R$  ratio of our vesicles at  $T=22.5$  °C.

From the exponential decay simulated curve

$$\frac{a}{R} = 0.42557e^{-\left(\frac{\kappa}{37.9802}\right)} \quad (6.2)$$

for the vesicle diameter we measured  $R=22.765$   $\mu\text{m}$ , the  $a/R$  value at  $22.5$  °C is  $0.1283$ .

Lai et al.(2002) have also demonstrated the degree of deformation dependence on the temperature for a fixed vesicle size of  $\sim 8\mu\text{m}$ .

To obtain the  $a/R$  ratio against temperature behavior for our vesicle ( $R=22.765$   $\mu\text{m}$ ) we assumed that the degree of deformation vs temperature behavior is independent on the vesicle size and adapted the data from Lai et al.(2002) for our vesicle ( $a/R=0.1283$  at  $T=22.5$  °C) (Figure 6.8).

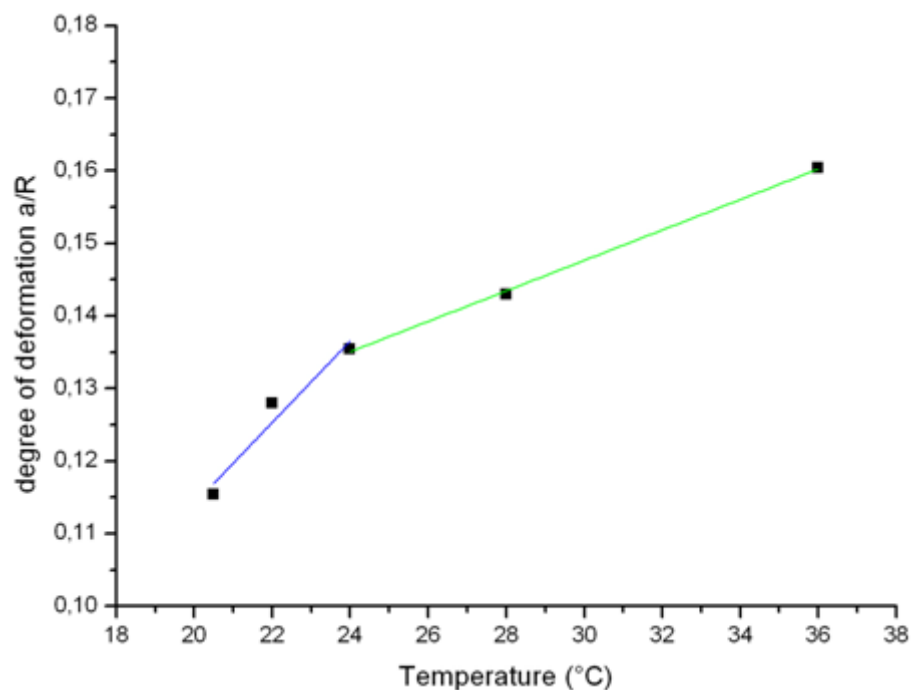


**Figure 6.8** The degree of vesicle deformation  $a/R$  against the increase of temperature for DMPC GUVs adherent to a glass support. (■) are the experimental data taken from Lai et al. (2002) adapted to a  $a/R$  ratio = 0.1283 at 22.5 °C. The blue and green lines are the best fitting of reported data.

To calculate the adhesion radius,  $a$ , from  $a/R$  ratio, we still need to consider how  $R$  vary with temperature.

As the vesicle area decreases by decreasing the temperature through  $T_m$ , but vesicle volume changes can be considered negligible (Kas et al., 1991; Lai et al., 2002), to calculate  $R$  at different temperatures, we calculated the volume of the vesicle in its gel phase, which has a spherical shape (see Figure 6.6b), and assumed it to be also the volume of the vesicle in its fluid phase (where it is adherent to the glass support). Nonetheless, this time we treated the vesicle as an ellipsoid (see Figure 6.6a), whose axes are  $L_1$ ,  $L_2$ , and  $L_3$  (Figure 6.9b).

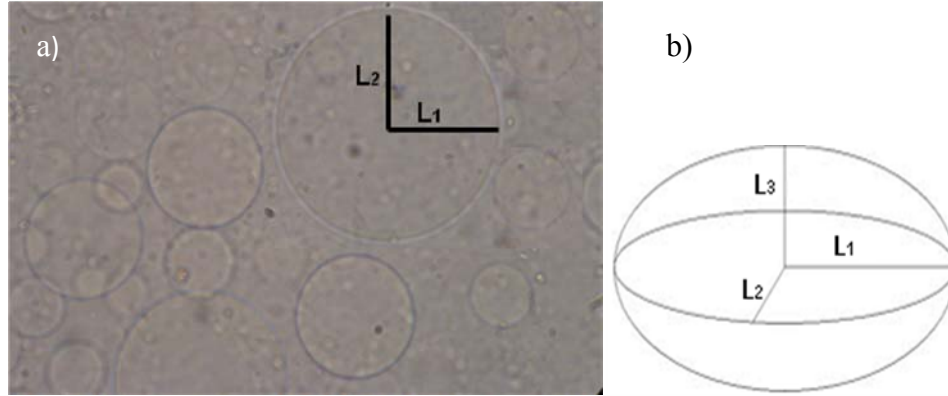


**Figure 6.9** a) View from the top of DMPC GUVs on a glass support: the two axes,  $L_1$  and  $L_2$  of vesicles have the same length and b) the vesicle can be approximate to an ellipsoid with  $L_1=L_2=L$  (spheroid).

In particular, from our measurements,  $L_1$  and  $L_2$  resulted to have the same length, therefore the vesicle can be approximated to a spheroid (see Figure 6.9b).

From the volume and from the values of  $L_1=L_2=L$  measured at different temperatures during the cooling process through the phase transition, we can derive  $L_3$ .

We then use Knud Thomsen's formula to find the ellipsoidal surface area:

$$SA_{Ellipsoid} = 4\pi \left[ \frac{(L_1 L_2)^{1.61} + (L_1 L_3)^{1.61} + (L_2 L_3)^{1.61}}{3} \right]^{1/1.61} \quad (6.3)$$

The above equation is an approximate solution to the general spheroid equation with an error of 1.06% (McGahon et al., 2007):

$$\left( \frac{x}{2L_1} \right)^2 + \left( \frac{y}{2L_2} \right)^2 + \left( \frac{z}{2L_3} \right)^2 = 1 \quad (6.4)$$

This surface area can be assumed to be the same surface area of a spherical vesicle of radius  $R$ :

$$SA_{Sphere} = SA_{Ellipsoid} = 4\pi R^2 \quad (6.5)$$

Therefore

$$R = \sqrt{\frac{SA_{\text{Ellipsoid}}}{4\pi}} \quad (6.6)$$

From the  $a/R$  ratio and from  $R$  we can finally calculate the temperature dependence of the radius of the contact zone,  $a$ , during phase transition and consequently the adhesion area.

In Figure 6.10 the adhesion area calculated,  $A_{\text{adh}}$ , is plotted against temperature. The adhesion area decreases along with the cooling process trough  $T_m$  linearly over a temperature range of  $\Delta T_m = 0.3$  °C (Figure 6.10).

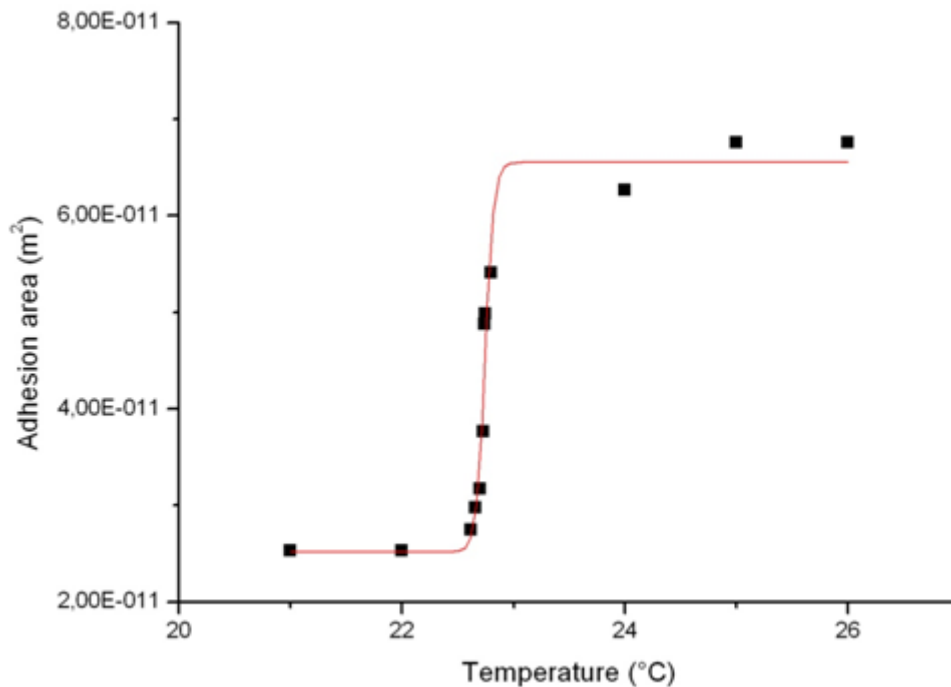


**Figure 6.10** Variation of the adhesion area during fluid-gel transition ( $\Delta T_m = 0.3$  °C). The same behavior was observed in other vesicles at different sizes. (■) are the calculated values and the red line is the best fitting.

### 6.3.3 Mechanical and Thermodynamic Coupling.

A good measure of the transitions of these systems are the corresponding responses to changes in one or more parameters such as pressure or temperature. The response function to temperature change at constant pressure, is the isobaric heat capacity:



$$C_p = (dH / dT)_p \quad (6.7)$$

where  $dH$  is the infinitesimal variation of enthalpy following an infinitesimal change of the temperature  $dT$ .

This is often used to characterize the phase behavior of liquid to gel transition.

As for GUVs, calorimetry measurements are not possible because of the low concentration of lipids in solution. Nevertheless Figure 6.10 allows us to calculate heat capacity using a linear relationship, first demonstrated by Heimburg (1998), between excess area changes,  $\Delta A(T)$ , and the excess enthalpy changes,  $\Delta H(T)$ , during lipid phase transition (Eq. (6.8)):

$$\Delta A (T) = \gamma_A \Delta H (T) \quad (6.8)$$

with  $\gamma_A$  being a phenomenological constant =  $0.89 \text{ m}^2/\text{J}$  that has the same values for all lipids (Heimburg, 2007).

Combining Eq. (6.7) and (6.8), we can calculate the heat capacity  $C_p$  of the membrane from its change in area during lipid melting using equation (Eq.(6.9)):

$$C_p = \frac{dH}{dT} = \gamma_A^{-1} \frac{dA}{dT} \quad (6.9)$$

and accounting for the total number of lipids in the vesicle. In Figure 6.11 the calculated molar heat capacity profile, taking  $\gamma = 0.89 \text{ m}^2 \text{ J}^{-1}$  (Heimburg, 2007) and an average size of a single lipid in the fluid phase of  $0.60 \text{ nm}^2$  for DMPC (Lipowsky and Sackmann, 1995) is shown.

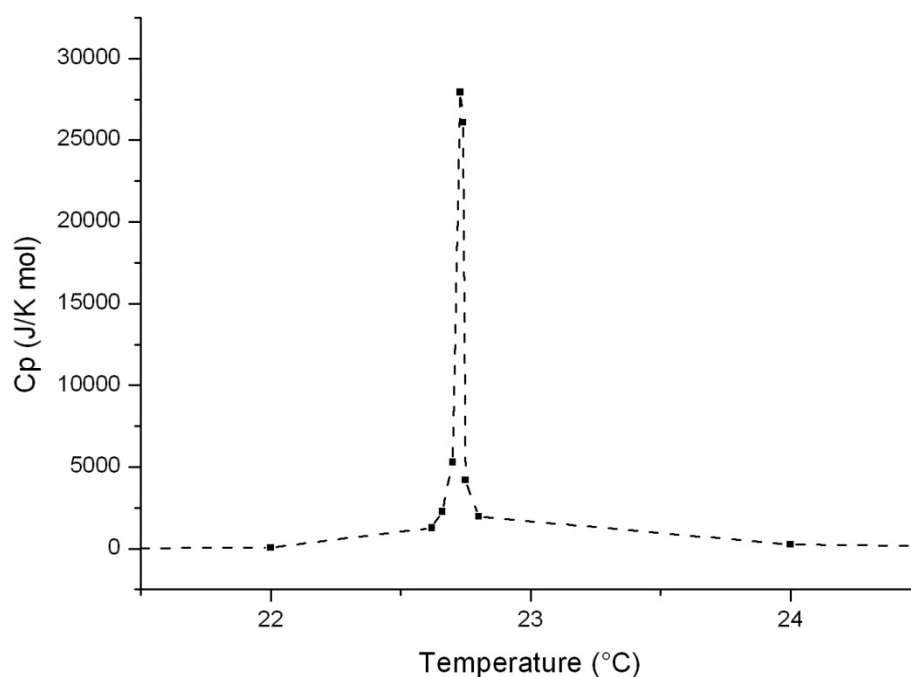


**Figure 6.11** Heat capacity profile (■; black dotted line is drawn to show the trend) of DMPC GUVs during the fluid-gel transition. From the graphics it can be seen that the main transition point is at  $T_m=22.7^\circ\text{C}$ .

### 6.3.4 Relaxation process.

In the previous section we showed that enthalpy and area are proportional functions in the transition temperature regime.

It has been also found that exists a proportional relation between relaxation time and excess heat capacity (Grabitz et al., 2002, Heimburg, 2007).

As shown in Eq. (6.7), the excess heat capacity  $C_p$  is a function of the fluctuations in enthalpy, but simultaneously, it is also a function of the entropy (Eq. (6.10)):

$$C_p = T \cdot dS/dT \quad (6.10)$$

The thermodynamic forces can be derived from the entropy potential.

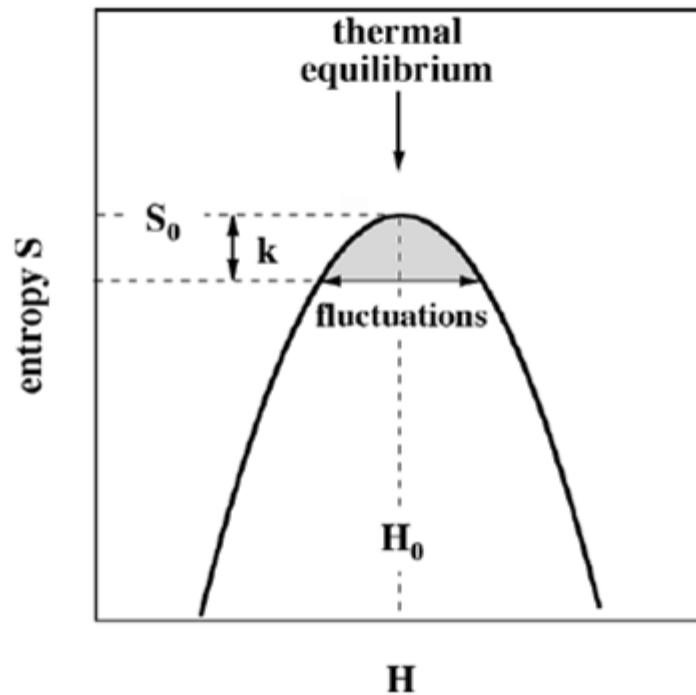


**Figure 6.12** Entropy as a function of the enthalpy of a lipid membrane.

The theory is based on the assumption that the distribution of enthalpy states at a given temperature can be described by a Gaussian distribution. This is correct when the system displays a continuous transition that is neither of first-order nature nor at a critical point

$$P(H - \langle H \rangle) = \frac{1}{\sigma\sqrt{2\pi}} e^{-(H - \langle H \rangle)^2 / 2\sigma^2} \quad (6.11)$$

where  $H$  is the enthalpy,  $\langle H \rangle$  is the mean enthalpy, and  $\sigma^2 = \langle H^2 \rangle - \langle H \rangle^2$  is the variance. The Gibbs free energy depends logarithmically on this distribution (Lee et al., 1991):  $G = RT \ln P$ . Using this, one finds that the entropy  $S$  can be approximated as a harmonic potential

$$S(H - \langle H \rangle) \approx -\frac{R(H - \langle H \rangle)^2}{2\sigma^2} \quad (6.12)$$

where  $R$  is the gas constant.

Throughout a melting transition, changes in area, volume, and enthalpy are proportional, and therefore, one only finds one independent fluctuation given by  $R = H - \langle H \rangle$ . The thermodynamic force driving the lipid sample back to equilibrium (after a perturbation) is given by  $X = dS/d(H - \langle H \rangle)$ , and the flux of heat by  $J = d(H - \langle H \rangle)/dt$ . This is in fact the observable in our calorimetric experiments. According to Onsager (1931a;1931b), the flux is proportional to the thermodynamics force. Therefore

$$\frac{d(H - \langle H \rangle)}{dt} = -L \frac{R(H - \langle H \rangle)}{\sigma^2} \quad (6.13)$$

using the phenomenological constant  $L$ . This leads to a simple differential equation that is solved by an exponential decay

$$(H - \langle H \rangle) = (H - \langle H \rangle)_0 \exp\left(-\frac{t}{\tau}\right) \quad (6.14)$$

introducing the relaxation time  $\tau$ . Using the identity  $C_p = (H - \langle H \rangle)^2/RT^2 \equiv \sigma^2/RT^2$  (fluctuation theorem), one arrives at

$$\tau = \frac{T^2}{L} c_p \quad (6.15)$$

where  $T$  is the temperature. The constant  $L$  has to be obtained from experiments. For the details of the derivation, we refer to Heimburg (2007).

From this formula we are able to calculate the relaxation time from the calculated value of  $C_p$ .

$L$  should be derived experimentally, but in case of GUVs this is obviously not possible. Therefore we used some values of  $C_p$  and  $\tau$  from literature to calculate it.

In particular we considered the heat capacity calculated from Franke et al. (2009) in an analogous way to ours, by considering  $C_p$  proportionality with the excess area during phase transition, and the relaxation time is taken from Leirer et al. (2009b). This is the

area relaxation of GUV vesicles after a fast temperature quench ( $10\text{ }^{\circ}\text{C/s}$ ) from the fluid to the gel phase (in this case there is a consequent pore opening, therefore the area relaxation corresponds to pore lifetime).

For a  $C_p \approx 18\text{ KJ/molK}$  and  $\tau = 5\text{ s}$ , the resulting value for  $L$  is  $3.6 \cdot 10^8\text{ JK/mol s}$ , that is of the same order of magnitude of other previous measured  $L$  for MLVs and LUVs (Heimburg, 2007).

Figure 6.13 reports heat capacity profile (black line) and relaxation times (red line) of DMPC GUV.

The most important outcome of this figure is that relaxation times, heat capacity and consequently all the mechanical properties of vesicles related to it, as the excess area, are enhanced at the transition temperature. The maximum value of  $\tau$  for our vesicle at the transition temperature is  $\sim 7 \pm 1\text{ s}$ .

This value is the mean value of  $\tau$  calculated from two vesicles of different sizes.

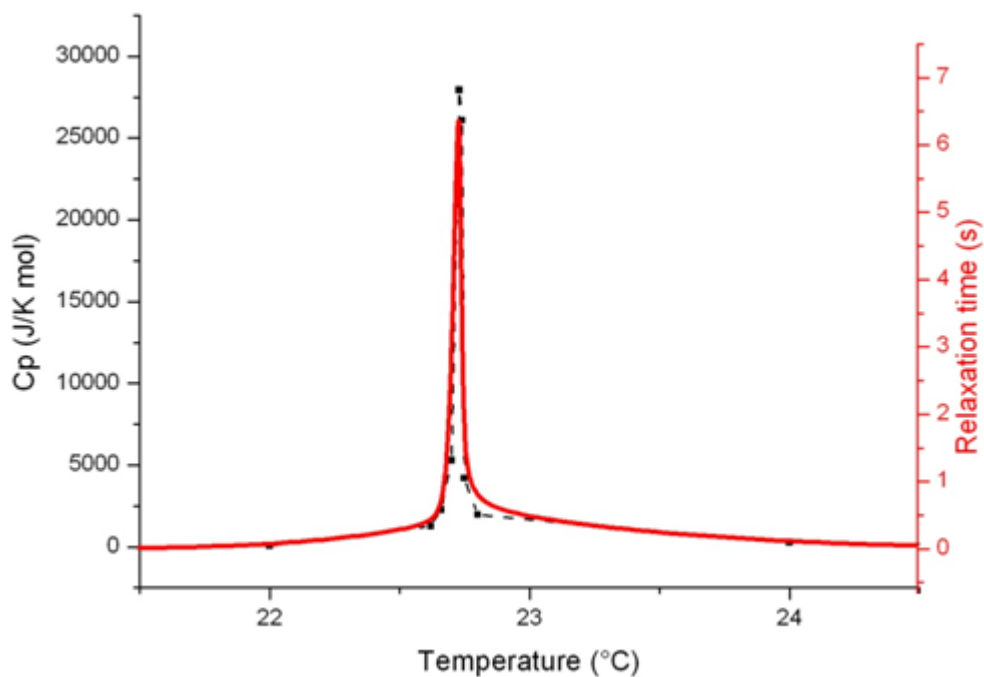


**Figure 6.13** Heat capacity profile (■; black dotted line is drawn to show the trend) and relaxation times (red line) of DMPC GUV during the fluid-gel transition. The maximum value of  $\tau$  for our vesicle at the transition temperature is  $\sim 7 \pm 1\text{ s}$ . This value is the mean value of  $\tau$  calculated from two vesicles of different sizes.

## 6.4 DISCUSSION

### 6.4.1 Cooperative relaxation processes in GUVs.

In this study we have induced fluid to gel transition by applying different cooling rates and we have found that a series of phenomena starting with pore formation and ending up with the complete rupture of vesicles occurred only above the threshold value of 0.2 °C/min.

All these facts have led us to consider some kinetics processes occurring in the membrane and the relative relaxation times. In particular, as such effects were strictly dependent on the temperature, as they were not observed far from the main transition point, we focused on the relaxation times at  $T_m$ , where, as already mentioned in the section 6.1.2, their value is incredibly enhanced.

As already outlined in section 6.1.2, according to Onsager (1931), each thermal fluctuation of the system, can also be seen as a perturbation of its equilibrium followed by a relaxation process. Therefore the timescale of thermal fluctuations and relaxation processes are the same.

The relaxation time we have found by the calculated value of  $C_p$ , is the time of vesicle area fluctuations at the transition temperature. A study in support of our finding has been conducted by Leirer et al. (2009b). They induced a very fast fluid to gel transition (10 °C/s) in a free-floating DPPC vesicle. Cooling led to an area decrease and vesicle shrinkage, but because of the fast cooling rate, volume had not time to change; at the same time, as the vesicle was already spherical and taut, that means that it already had the maximum volume/area ratio, shape transformations had no reason to occur (see Chapter 1) and the only way to shrink the surface was to expel some volume through pore formation (fission of vesicles). Subsequently they measured the time the pore remained opened and found that the overall pore lifetime occurred in a time of  $5 \pm 0.3$  s. It's interesting to note that in their work the fission process happened simultaneously with gel phase domain appearance. This means that phase coexistence can represent a driving force for membrane fission. A possible explanation for this is that the increase in area fluctuations, which are maximized in the transition phase, are responsible for the pore formation; this last was originated, probably, at the boundaries between gel and fluid phases arising during the phase transition (Leirer et al., 2009a; 2009b).

Since relaxation time reflects the organization of lipids, one would expect that pore nucleation, opening and closing have the same time evolution of lipid relaxation (Leirer et al., 2009a; 2009b; Wunderlich et al., 2009).

This value, therefore, corresponds also to the time of membrane area relaxation after the temperature quench, and it is in excellent agreement with the value we have found in our experiment.

Comparison of our results to the relaxation times found in this study and to morphological relaxation phenomena found in earlier studies on GUVs, reveals an universal relaxation behaviour in GUVs.

#### **6.4.2 Role of adhesion in area fluctuations and related relaxation times.**

To explain for the “threshold” effect, we have to think that complete rupture of vesicles occurs only when the transition region, in our case  $\Delta T_m = 0.3^\circ\text{C}$  (see Figure 6.10), is spanned in less than 7 s: in this case the system would not have time to relax explaining for vesicle breaking up.

Nevertheless, this scenario would present for a cooling rate  $\Delta T_m/\tau = 0.3^\circ\text{C}/7\text{s} = 2.57^\circ\text{C}/\text{min}$  while we start to observe rupture of vesicles already at a cooling rate of  $0.3^\circ\text{C}/\text{min}$ , that would involve a relaxation time of 60s.

This means that some other contribution, responsible for a slower area relaxation, has to be taken into account.

In fact, what we have not considered until now is the adhesion of vesicle to the glass support.

Some studies have reported of vesicle deformation on planar substrates as a function of temperature and in some cases, vesicle rupturing on the surface has been observed, but not correlation between deformation and rupturing has been determined up to now (Gillmore et al. 2009).

A C-RICM (confocal reflectance interference contrast microscopy) study, in combination with cross polarized light microscopy, has showed the presence of strong physical interactions between adherent DMPC vesicles and pure fused silica substrate at the main phase transition of DMPC bilayer, due to the electrostatic interactions between the silanol group ( $-\text{SiOH}$ ) of pure fused silica substrate, that carries a net negative charge at pH 7.4, and the headgroup of DMPC lipids that is in short range from the fused

silica substrate and contains both a quaternary amine with a permanent positive charge and phosphate group with a negative charge (see Chapter 1) (Lai et al., 2002; Dimitrova et al., 1997). It has also been reported that only van der Waals forces are sufficient to mediate the colloidal adhesion of PC based vesicles on non-deformable substrates in relatively high ionic strength (Seifert et al., 1990). There is a third force involved in the adhesion energy, a repulsive interaction known as undulation force, that has resulted from the thermal fluctuation of membrane away from the fused silica substrate, but it is suppressed by the electrostatic attraction and van der Waals forces at  $T_m$  (Lai et al., 2002). Moreover, it has been showed that adhesion energy is enhanced at fluid-to-gel phase transition because of an increase in the elastic modulus (Lai et al., 2002; Dimova et al., 2000; Chan et al., 2002).

Our interpretation of the observed effects is that the interaction between the bilayer and the substrate makes vesicle contact zone more rigid than the rest of the bilayer and therefore the thermal area fluctuations in that region result slower. As a consequence, relaxation times in that part of the membrane are longer.

A study on the lateral diffusion coefficients of a BODIPY tail-labeled lipid in free-standing giant unilamellar vesicles (GUVs) and supported phospholipid bilayers (SPBs) has revealed that the lipid mobility in free-standing bilayers ( $D = 7.8 \pm 0.8 \mu\text{m}^2 \text{s}^{-1}$ ) is significantly higher than in the bilayer created on the solid support ( $D = 3.1 \pm 0.3 \mu\text{m}^2 \text{s}^{-1}$ ) (Przybylo et al., 2006).

In our case, all these effects still don't represent a limit for relaxation processes that occur far away the transition temperature after applying a cooling rate of  $0.3 \text{ }^\circ\text{C}/\text{min}$ , because the global relaxation times are anyway faster than the perturbation we applied, but the situation change when the system is cooled across the main transition temperature, because both, area relaxation time and adhesion energy, are strongly enhanced.

We can think that there are two different relaxation times at  $T_m$  in the vesicle: one for the "free" bilayer, that has a relaxation time of  $\sim 7\text{s}$ , and another one, which arises from the reduced thermal area fluctuations at the contact zone; therefore, in this case, a further contribution must be added to the area relaxation time at  $T_m$  ( $\sim 7\text{s}$ ), which is responsible for a relaxation time  $> 7\text{s}$ . The relaxation time at the contact zone can be considered the cooling rate limiting relaxation time that we have observed.



### 6.4.3 Mechanism of vesicle rupturing.

We still have to answer the question: how does the rupturing of vesicles occur?

A mechanism for explaining such effect is illustrated in Figure 6.14.

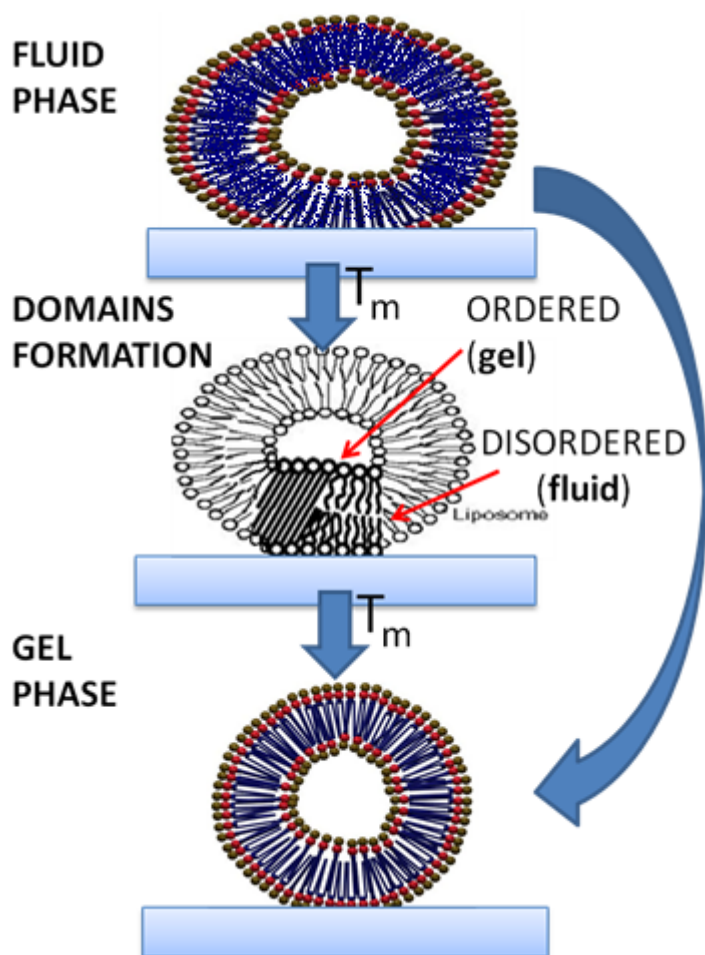


**Figure 6.14** An hypothesis of mechanism for explaining rupturing of vesicles during the fluid-to-gel transition above a cooling rate of  $0.2\text{ }^{\circ}\text{C}/\text{min}$ .

When the transition to the gel phase starts to occur, gel domains nucleate and start to expand all over the vesicle wall; the thermal area fluctuations associated to this process, however, are slower at the contact zone than in the rest of the vesicle and this will result in the formation of some defects at the boundaries between the different zones, that probably will result in the formation of pores, as previously suggested (Leirer et al., 2009a; Wunderlich et al., 2009).

In an analogous study of Singh et al. (1998) on glass supported diacetylenic and DSPC vesicles, they have reported that, when vesicles were brought below  $T_m$  at a cooling rate of  $1^\circ\text{C}/\text{min}$ , some dark spots were observed from which GUVs started to collapse; they referred to them as defects of the membrane, exactly like we suggest, that were the starting point for vesicles rupture, resulting in aggregate formations of not well defined morphology.

Moreover they observed that vesicles with large radius of curvature were more stable and a further decrease of the temperature was necessary to obtain their disintegration.

This explains our observations on the membrane-curvature dependent effects and why rupturing didn't occur at the same time for all the vesicles.

This phenomenon could also call the issue of a microscopic thermal gradient inside the vesicle: in fact, even though the very small aqueous volume inside the chamber should ensure an homogenous environment (that is also confirmed, within the error, by the cross monitoring of the internal chamber temperature by using a thermocouple), we have to consider that gel domain nucleation starts at the contact zone, since the glass support is in direct contact with the cooling stage; therefore bigger vesicles could need more time to equilibrate at the new temperature.

## **6.5 CONCLUSION**

A clear understanding of the physical principles governing dynamics and properties of biological membranes, is of primary importance for the explanation of all the functions in which the plasma membrane is involved, whose role goes by far beyond the simplified view of a barrier that compartmentalizes the inside of a biological cell.

This kind of study can be approached both at an individual molecule level, as the interaction with lipids may regulate the functions of proteins and enzymes, or at a mesoscopic level, because a macromolecular vision allows a better understanding of biological processes such as endocytosis, exocytosis, diffusion and transport of substances inside or outside the cell, and all the other processes governed by a "cooperative behavior" of the membrane, meaning, for example, domain formations, phase changes and membrane permeability variations, pore formations and so on.

In this context, thermodynamics plays a decisive role.

Through a thermodynamics and/or kinetic approach, important information can be extracted concerning the physical parameters responsible for these processes, such as elastic constants, line tension or relaxation times. A monitoring of these parameters by changing thermodynamic variables like pressure, temperature or changes in pH, allows, ultimately, a control over the involved biophysical processes.

The use of adhered vesicles as a model for studying the nontrivial kinetics of adhesion of membranes under ramped forces in biological systems, gets a contribution to elucidate the role of adhesion in regulating the relaxation processes of these cells.

## **CONCLUSION**

In this work we have used biomimetic membrane systems to study the interaction between low power millimeter waves and biological membranes.

At high power densities, MMWs induce thermal effects due to the absorption of water. More interesting, they induce a variety of biological effects at low power densities, that are considered non-thermal, and that may be explained, at a molecular level, by an involvement of water molecules at the membrane interface. However, no conclusive experimental evidence that biomembranes exhibit remarkable sensitivity to this radiation has been provided up to now.

The experiments here presented have been appositely conceived to elucidate the effects of low power MMWs on biological membranes, and their nature, by monitoring water behavior in mediating the membrane/radiation interaction.

This study gives a crucial contribution to this research field because:

- The results reported here establish an influence of low power MMWs on interfacial properties of lipid membranes.

By monitoring, through  $^2\text{H}$  NMR spectroscopy, deuterated water in a multilamellar lipid/water system, we have observed that if the membrane is brought into close proximity to the transition point, microwaves (53-78 GHz at a density power of the order of  $\mu\text{W}/\text{cm}^2$ ), induce a reduction of water ordering at the membrane interface, an upward shift of the main phase transition temperature and a broadening of the transition region.

Moreover, we have studied the effects of wide band MMWs (52-72 GHz and output power in the range 0.15-0.45 mW) on vesicle physical stability, in terms of vesicle size and size distribution changes, of 100 nm large unilamellar vesicles (LUVs), by dynamic light scattering. An inhibition of the aging processes (Ostwald ripening), that usually occur in these vesicles because of their thermodynamic instability, has been showed.

In the end, giant unilamellar vesicles (GUVs), have been used to study the effect of millimeter waves on membrane water permeability under osmotic stress, by monitoring vesicle shape and size distribution with a phase contrast microscope. The observed decrease in the water membrane permeability of irradiated samples provides

further consistent proofs in support of the hypothesis of an action of MMWs at the membrane-water interface and the important role that water may play in such interaction.

- The non-thermal nature of the observed effects has also been established.

Radiation effects on the membrane phase transition in multilamellar vesicles (MLVs) can be explained in terms of an increase in membrane polarizability. This effect, among other consequences, induces an upward shift of the main phase transition temperature. In other words we can say that irradiation causes a “dehydration” of the membrane stabilizing its gel phase.

Also the inhibition of the ripening process and/or aggregation phenomena in LUVs induced by low power MMWs, may be explained in terms of a dehydration of the membrane. In fact membrane dehydration induces a curvature decrease that, as seen in section 5.1, is the rate determining step in Ostwald ripening aging process (Olsson and Wennerstroem, 2002).

In the end, a change of the polarization states of water induced by the radiation, can also explain for the reduced water permeability of irradiated GUVs, being the membrane-water interface the rate limiting step for water permeability in single lipid component membranes (Mathai, 2008). In this case, a partial dehydration of the membrane may cause an increase of packing density (increased membrane rigidity) that is inversely related to water permeability (Lande et al, 1995). MMWs exposure seems to reduce water permeability by increasing membrane rigidity, in a manner similar to that observed when cholesterol is inserted in the membrane bilayer (Lande et al, 1995).

Thus, all the results reported here confirm the non-thermal nature of the observed effects, in that, a thermal increase would increase membrane hydration.

- Our spectroscopic study by  $^2\text{H}$  NMR, has allowed a better understanding of the molecular mechanisms of MMW radiation/biological membrane interaction.

In the context of the study MMW-multilamellar vesicles interaction, the high sensitivity of NMR spectroscopy has allowed the specific monitoring of deuterated water bound to the membrane. This has led to a microscopic interpretation of the

membrane-microwave interaction involving the redistribution of water molecules among the binding sites of phospholipid headgroups.

In conclusion, this thesis provides strong evidence of the sensitivity of biological membranes to low power long term MW exposure.

We believe that the molecular mechanism advanced here, by which the radiation, mediated by water, affects lipid membranes, may play a common and crucial role in all the effects observed both *in vitro* and *in vivo* as a consequence of microwave exposure.

In the context of the characterization of biomimetic membrane models, a study on the shape phase transition of glass supported GUVs has been also performed.

Cell adhesion represents a crucial step for a variety of biological processes, such as vesicle fusion, intracellular trafficking (exo- and endo-cytosis) or wound healing (Bongrand, 1988).

A thermodynamic and kinetic study of the phase shape transition of adhered GUVs at different cooling rates, has led to the conclusion that membrane adhesion may play a major role in regulating relaxation processes in biomembranes.

This work, moreover, provides a simple method to estimate relaxation times of cooperative processes in biological adherent membranes at their transition temperature.

## BIBLIOGRAPHY

- A. Abragam. *The Principles of Nuclear Magnetism*, Clarendon Press, Oxford, 1961.
- R.K. Adair. Vibrational resonances in biological systems at microwave frequencies. *Biophys. J.* 82:1147-1152, 2002.
- R.K. Adair. Biophysical limits on athermal effects of RF and Microwave radiation. *Bioelectromagnetics*, 24:39-48, 2003.
- T.M. Alle, L.G. Cleland. Serum-induced leakage of liposome contents. *Biochim. Biophys. Acta.*, 597:418-426, 1980.
- K. Åman, E. Lindahl, O. Edholm, P. Håkansson and P.O. Westlund. Structure and dynamics of interfacial water in a  $L_{\alpha}$  phase lipid bilayer from molecular dynamics simulations. *Biophys. J.*, 84:102-115, 2003.
- M.I. Angelova, D. Dimitrov. Liposome electroformation. *Faraday Discuss. Chem. Soc.*, 81:303-311, 1986.
- M.I. Angelova, Liposome electroformation. In: P.L. Luisi, P. Walde (Eds), *Giant Vesicles, Perspectives in Supramolecular Chemistry.*, vol. 6, pp:27-36. Wiley, Chichester, 2000.
- M.I. Angelova, S. Soléau, P.Méléard, J.F. Faucon, P. Bothorel. Preparation of giant vesicles by external AC electric field. Kinetics and applications. *Prog. Colloid & Polym. Sci.*, 89:127-131, 1992.
- X. Armengol and J. Estelrich. Physical stability of different liposome compositions obtained by extrusion method. *J. Microencapsul.*, 12:525-535, 1995.
- J.C. Bacri, V. Cabuil, A.C. Cebers, C Menager, and R. Perzynski. Flattening of ferro-vesicles undulations under a magnetic field. *Europhysics Letters*, 33:235-240, 1996.
- L.A. Bagatolli and P.B.S. Kumar. Multicomponent membranes: Experimental techniques and phase behavior. *Soft Matter*, 5:3234-3248, 2009.
- I.Y. Belyaev. Non-thermal Biological Effects of Microwaves. *Microwave Review*, 11:13-29, 2005.
- I.Y. Belyaev, V.S. Shcheglov, E.D. Alipov, and V.D. Ushakov. Nonthermal effects of extremely high-frequency microwaves on chromatin conformation in cells in vitro-



Dependence on physical, physiological, and genetic factors. *IEEE Trans. Microwave Theory and Techniques*, 48:2172–2179, 2000.

A Beneduci, G. Chidichimo, S. Tripepi, E. Perrotta, F. Cufone. Antiproliferative effect of millimeter radiation on human erythromyeloid leukemia cell line K562 in culture: Ultrastructural- and metabolic-induced changes. *Bioelectrochemistry*, 70:214-220, 2007.

A. Beneduci, L. Filippelli, K. Cosentino, G. Chidichimo. “5th International Workshop on Biological effect of EMF”, Palermo, 2008.

A. Beneduci, G. Chidichimo, S. Tripepi, E. Perrotta. Transmission electron microscopy study of the effects produced by wide-band low-power millimeter waves on MCF-7 human breast cancer cells in culture. *Anticancer Res.*, 25:1009-1014, 2005.

A. Beneduci. Review on the mechanisms of interaction between millimeter waves and biological systems. In E.M. Bernstein (Eds), *Bioelectrochemistry Research Developments*, pp:35-80, Nova Science Publishers, New York, 2008a.

A. Beneduci. Which is the effective time scale of the fast Debye relaxation process in water? *J Mol Liq.*, 138:55-60, 2008b.

A. Beneduci. Evaluation of the potential in vitro antiproliferative effects of millimeter waves at the therapeutic frequencies on RPMI 7932 human skin malignant melanoma cells. *Cell Biochem. Biophys.*, 55:25-32, 2009.

B. Berne and R. Pecora. *Dynamic light scattering with applications to chemistry, biology and physics*, Wiley-Interscience, New York 1976.

A. Blicher, K. Wodzinska, M. Fidorra, M. Winterhalter and T. Heimburg. The temperature dependence of lipid membrane permeability, its quantized nature, and the influence of anesthetics. *Biophys. J.*, 96:4592-4597, 2009.

M. Bloom, E. Evans and O.G. Mouritsen. Physical properties of the fluid lipid-bilayer component of cell membranes : a perspective. *Quart. Rev. Biophys.*, 24:293-397, 1991.

J.D. Bond and N.C. Wyeth. Are membrane microwave effects related to a critical phase behaviour? *J. Chem. Phys.*, 85:7377-7379, 1986.

P. Bongrand. *Physical Basis of Cell-Cell Adhesion*, CRC, Boca Raton, 1988.

P. Bongrand. Adhesion of cells. In: R. Lipowsky and E. Sackmann (Eds) *Structure and Dynamics of Membranes*, Vol. IB, pp:755-803, Elsevier, Amsterdam, 1995.

F. Borle, J. Seelig. Hydration of Escherichia coli lipids. Deuterium T1 relaxation time studies of phosphatidylglycerol, phosphatidylethanolamine and phosphatidylcholine. *Biochim. Biophys. Acta*, 735:131-136, 1983.

E. Breitmaier. *Structure elucidation by NMR in organic chemistry: a practical guide*, Third revised edition, J. Wiley & Sons, 2002.

V.M. Brovkovich, N.B. Kurilo, V.L. Barishpol. Action of millimeter-range electromagnetic radiation on the  $\text{Ca}^{++}$  pump of sarcoplasmic reticulum. *Radiobiologia*, 31:268-271, 1991 (in Russian).

M.F. Brown, A.A. Ribeiro, G.D. Williams. New view of lipid bilayer dynamics from  $^2\text{H}$  and  $^{13}\text{C}$  NMR relaxation time measurements. *Proc Natl. Acad. Sci USA*, 80:4325-4329, 1983.

P. Bucher, A. Fischer, P.L. Luisi, T. Oberholzer, P. Walde. Giant vesicles as biochemical compartment: the use of microinjection techniques. *Langmuir*, 14:2712-2721, 1998.

M.L. Calabrese, G. D'Ambrosio, R. Massa, G.A. Petraglia. High-efficiency waveguide applicator for in vitro exposure of mammalian cells at 1.95 GHz. *IEEE Trans. Microwave Theory and Techniques*, 54:2256-2264, 2006.

C. Cametti, F. De Luca, M.A. Macri, B. Maraviglia, P. Sorio. Audio to microwave frequency dielectric study of the pretransition region in DPL-water systems. *Liquid Crystals*, 3:839-845, 1988.

P. B. Canham. The minimum energy of bending as a possible explanation of the biconcave shape of the human red blood cell. *J. Theor. Biol.*, 26:61-81, 1970.

G. Cevc, D. Marsh. *Phospholipid bilayers*, Wiley/Interscience, New York, 1987.

V. Chan, K.T. Wan. Thermal induced modification of the contact mechanics of adhering liposomes. *Langmuir*, 18:3134-3141, 2002.

D.K. Cheng. *Field and wave electromagnetic*, Ed. Addison-Wesley Pub. Co, 1989.

J.X. Cheng, S. Pautot, D.A. Weitz and X.S. Xie. Ordering of water molecules between phospholipid bilayers visualized by coherent anti-Stokes Raman scattering microscopy. *PNAS*, 100:9826-9830, 2003.

- G. Chidichimo, A. Golemme, J.W. Doane, P.W. Westermann. Investigation of ribbon lyotropic structures by deuterium magnetic resonance. *Phys. Rev. Lett.*, 48:1950-1954, 1985.
- C.K. Chou, Bassen H., J. Osepchuk, Q. Balzano, R. Petersen, M. Meltz, R. Cleveland, J.C. Lin, L. Heynick. Radio frequency electromagnetic exposure: Tutorial review on experimental dosimetry. *Bioelectromagnetics* 17:195-208,1996.
- C.K. Chou, J. D'Andrea. *IEEE Standard for Safety Levels With Respect to Human Exposure to Radio Frequency Electromagnetic Fields, 3 kHz to 300 GHz*. 2005.
- A.F. Cojocaru, N.L. Cojocaru and Zh.I. Burkovetsakaya. Mechanisms of water-mediated action of weak radio-frequency electromagnetic radiation on biological objects. *Biophysics*, 50:S141-S156, 2005.
- J. Davidsen, K. Jorgensen, T.L. Andersen, O.G. Mouritsen. Secreted phospholipase A2 as a new enzymatic trigger mechanism for localized liposomal drug release and absorption in diseased tissue. *Biochim. Biophys. Acta*, 1609:95-101, 2003.
- J.H. Davis. The description of membrane lipid conformation, order and dynamics by <sup>2</sup>H-NMR. *Biochim. Biophys. Acta*, 737:117-171, 1983.
- P.F. Devaux, M. Seigneuret. Specificity of lipid-protein interactions as determined by spectroscopic techniques. *Biochimim. Biophys. Acta*, 822:63-125, 1985.
- J.M. Diamond and Y. Katz. Interpretation of nonelectrolyte partition coefficients between dimyristoyl lecithin and water. *J. Membr. Biol.*, 17:121-154, 1974.
- M.N. Dimitrova, H. Matsumura, V.Z. Neitchev. Kinetics of protein-induced flocculation of phosphatidylcholine liposomes. *Langmuir*, 13:6516-6523, 1997.
- R. Dimova, B. Pouligny, C. Dietrich. Pretransitional effects in dimyristoylphosphatidylcholine vesicle membranes: optical dynamometry study. *Biophys. J.*, 79:340-356, 2000.
- R. Dimova, K.A. Riske, S. Aranda, N. Bezlyepkina, R.L. Knorr and R. Lipowsky. Giant vesicles in electric fields. *Soft Matter*, 3:817-827, 2007.
- N. Divecha, J.H. Clarke, M. Roefs, J.R. Halstead, C. D'Santos. Nuclear inositides: inconsistent consistencies. *Cell. Molec. Life Sci.*, 57:379-393, 2000.

H.G. Döbereiner. Fluctuating vesicle shapes. In: P.L. Luisi, P. Walde (Eds), *Giant Vesicles, Perspectives in Supramolecular Chemistry*, vol. 6, pp:149-168. Wiley, Chichester, 2000a.

H.G. Döbereiner. Properties of giant vesicles. *Current Opinion in Colloid & Interface Science*, 5:256-263, 2000b.

S. Doniach. Thermodynamic fluctuations in phospholipid bilayers. *J. Chem. Phys.*, 68:4912-4916, 1978.

H. Ebel, P. Grabitz, and T. Heimburg. Enthalpy and volume changes in lipid membranes. i. the proportionality of heat and volume changes in the lipid melting transition and its implication for the elastic constants. *J. Phys. Chem. B*, 105:7353-7360, 2001.

M. Edidin. The state of lipid rafts: from model membranes to cells. *Annu. Rev. Biophys. Biomol. Struct.*, 32:257-283, 2003.

P. Ekwall. In: G.H. Brown (Eds), *Advances in liquid crystals*, Academic Press, New York, vol.1, 1975.

K. Elamrani, and A. Blume. Phase transition kinetics of phosphatidic acid bilayers. A pressure-jump relaxation study. *Biochemistry*, 22:3305-3311, 1983.

A. Enders, G. Nimtz. Dielectric relaxation study of dynamic properties of hydrated phospholipid bilayers. *Ber Bunsenges Phys. Chem.*, 88:512-517, 1984.

D.J. Estes, M. Mayer. Electroformation of giant liposomes from spin-coated films of lipids. *Coll. Surf. B Biointerfaces*, 42:115-123, 2005.

E. A. Evans. Bending resistance and chemically induced moments in membrane bilayers. *Biophys. J.*, 14:923-931, 1974.

E. Farge and P.F. Devaux. Shape changes of giant liposomes induced by an asymmetric transmembrane distribution of phospholipids. *Biophys. J.*, 61:347-357, 1992.

M.M. Felix, H. Umakohsi, T. Shimanouchi, M. Yoshimoto, R. Kuboi. Evaluation of interaction between liposome membranes induced by stimuli responsive polymer and proteins. *J. Biosci. Bioeng.*, 93:498-501, 2002.

- E.E. Fesenko, V.I. Geletyuk, V.N. Kazachenko, N.K. Chemeris. Preliminary microwave irradiation of water solutions changes their channel-modifying activity. *FEBS Letters*, 366:49-52, 1995.
- E.E. Fesenko, and A.Ya. Gluvstein. Changes in the state of water, induced by radiofrequency electromagnetic fields. *FEBS Letters*, 367:53-55, 1995
- A.M. Figueiredo Neto, and S.R.A. Salinas. *The physics of lyotropic liquid crystals: phase transitions and structural properties*. Oxford Univ., Oxford, 2005.
- A. Finkelstein. Water movement through lipid bilayers, pores, and plasma membranes. Theory and reality, *Distinguished lecture series of the society of general physiologists*, vol. 4. Wiley, 1987.
- J.L. Finney. The water molecule and its interactions: the interaction between theory, modeling and experiment. *J. Mol. Liq.*, 90:303-312, 2001.
- A. Fischer, T. Oberholzer, P.L. Luisi. Giant vesicles as models to study the interactions between membranes and proteins. *Biochimica et Biophysica Acta*, 1467:177-188, 2000.
- T. M. Fischer, M. Stöhr-Liesen and H. Schmid-Schönbei. Red-cell as a fluid droplet - tank tread-like motion of human erythrocyte-membrane in shear-flow. *Science*, 202:894-896, 1978.
- T. Franke, C.L. Leirer, A. Wixforth, N. Dan, M.F. Schneider. Phase-Transition- and Dissipation-Driven Budding in Lipid Vesicles. *ChemPhysChem*, 10:2852-2857, 2009a.
- T. Franke, C. Leirer, A. Wixforth, and M.F. Schneider. Phase Transition Induced Adhesion of Giant Unilamellar Vesicles. *ChemPhysChem*, 10:2858-2861, 2009b
- H. Fröhlich. Theoretical physics and biology. In H. Fröhlich (Eds), *Biological Coherence and Response to External Stimuli*, pp:1-24, Springer-Verlag, Berlin (DH), 1988.
- K. Gawrisch, K. Arnold, T. Gottwald, G. Klose, F. Volke. Deuterium NMR studies of the phosphate water interaction in dipalmitoylphosphocholine-water systems. *Stud.Biophys.* 74:13-14, 1978.
- V.I. Geletyuk, V.N. Kazachenko, N.K. Chemeris, E.E. Fesenko. Dual effects of microwaves on single  $\text{Ca}^{2+}$ -activated  $\text{K}^+$  channels in cultured kidney cells. *FEBS Letters*, 359:85-88, 1995.

- R. B. Gennis. *Biomembranes. Molecular structure and function*. Springer, New York, 1989.
- R. Ghosh. P-31 and h-2 nmr-studies of structure and motion in bilayers of phosphatidylcholine and phosphatidylethanolamine. *Biochemistry*, 27:7750-7758, 1988.
- P. Grabitz, V.P. Ivanova and T. Heimburg. Relaxation kinetics of lipid membranes and its relation to the heat capacity. *Biophys. J.*, 82:299-309, 2002.
- E.H. Grant. Molecular interpretation of the dielectric behaviour of biological materials. In M. Grandolfo, S.M. Michaelson and A. Rindi (Eds), *Biological Effects and Dosimetry of Nonionizing Radiation*, NATO Advanced Study Institutes Series. Series A, Life Sciences; vol. 49, pp. 179-194, Plenum Press New York and London, 1983.
- B. Gruenewald, A. Blume and F. Watanabe. Kinetic investigations on the phase transition of phospholipid bilayers. *Biochim. Biophys. Acta*, 597:41-52, 1980.
- T. Gruhn, T. Franke, R. Dimova, R. Lipowsky. Novel Method for Measuring the Adhesion Energy of Vesicles. *Langmuir*, 23:5423, 2007.
- S. Halstenberg, T. Heimburg, T. Hianik, U. Kaatze, and R. Krivanek.. Cholesterol-induced variations in the volume and enthalpy fluctuations of lipid bilayers. *Biophys. J.*, 75:264-271, 1998.
- E. Haustein and P. Schwille. Fluorescence correlation spectroscopy: novel variations of an established technique. *Annu. Rev. Biophys. Biomol. Struct.*, 36:151-169, 2007.
- M.H. Hawton and J.W. Doane. Pretransitional phenomena in phospholipid/water multilayers. *Biophys. J.*, 52:401-404, 1987.
- T. Heimburg. Mechanical aspects of membrane thermodynamics. Estimation of the mechanical properties of lipid membranes close to the chain melting transition from calorimetry. *Biochim. Biophys. Acta Biomembr*, 1415:147-162, 1998.
- T. Heimburg. *Thermal Biophysics of Membranes*. Wiley-VCH, Weinheim, 2007.
- T. Heimburg. A model for the lipid pretransition: Coupling of ripple formation with the chain-melting transition. *Biophys. J.*, 78: 1154-1165, 2000a.
- R. Heinrich, S. Svetina, and B. Zeks. Nonaxisymmetric vesicle shapes in a generalized bilayer-couple model and the transition between oblate and prolate axisymmetric shapes. *Phys. Rev. E*, 48:3112-3123, 1993.

W. Helfrich. Elastic properties of lipid bilayers: theory and possible experiments. *Z. Naturforsch. [C]*, 28:693-703, 1973.

W. Helfrich and R.M. Servuss. Undulations, steric interactions and cohesion of fluid membranes. *Il Nuovo Cimento*, 3:137-161, 1984.

L. Hillert, T. Åkerstedt, A. Lowden, C. Wiholm, N. Kuster, S. Ebert, C. Boutry, S.D. Moffat, M. Berg, B.B. Arnetz. The effects of 884 MHz GSM wireless communication signals on headache and other symptoms: An experimental provocation study. *Bioelectromagnetics*, 29:185-196, 2008.

M. Hof, R. Hutterer, N. Perez, H. Ruf, F.W. Schneider. Influence of vesicle curvature on fluorescence relaxation kinetics of fluorophores. *Biophysical Chemistry*, 52:165-172, 1994.

M.J. Hope, M.B. Bally, G. Webb, P.R. Cullis. Production of large unilamellar vesicles by a rapid extrusion procedure. Characterization of size distribution, trapped volume and ability to maintain a membrane potential. *Biochim Biophys Acta*, 812:55-65, 1985.

D. Huster, A.J. Jin, K. Arnold, K. Gawrisch. Water permeability of polyunsaturated lipid membranes measured by <sup>17</sup>O NMR. *Biophys J*, 73:855-864, 1997

ICNIRP. Guidelines for limiting exposure to time varying electric, magnetic, and electromagnetic fields (up to 300 GHz). *Health Phys.*, 74:494-522, 1998.

J.H. Ipsen, K. Jørgensen and O.G. Mouritsen. Density fluctuations in saturated phospholipid bilayers increase as the acyl-chain length decreases. *Biophys. J.*, 58:1099-1107, 1990.

F. Jähnig. Critical effects from lipid-protein interaction in membranes. I. Theoretical description. *Biophys. J.*, 36:329-345, 1981a.

F. Jähnig. Critical effects from lipid-protein interaction in membranes. II. Interpretation of experimental results. *Biophys. J.*, 36:347-353, 1981b.

P.A. Janmey and P.K.J. Kinnunen. Biophysical properties of lipids and dynamic membranes. *Trends in Cell Biology*, 16:538-546, 2006.

M. Jansen, A. Blume. A comparative-study of diffusive and osmotic water permeation across bilayers composed of phospholipids with different head groups and fatty acyl chains. *Biophys. J.*, 68:997-1008, 1995.

Y. Jie, L. Quanhui, L. Jixing, and O.Y. Zhing-Can. Numerical observation of nonaxisymmetric vesicles in fluid membranes. *Phys. Rev. E*, 58:4730-4736, 1998.

J. Jin. *Electromagnetic Analysis and Design in Magnetic Resonance Imaging*. CRC Press LLC, Florida, USA, 1999.

F. Julicher, R. Lipowsky. Domain-induced budding of vesicles. *Phys Rev Lett.*, 70:2964-2967, 1993.

Käs J, Sackmann E. Shape transitions and shape stability of giant phospholipid vesicles in pure water induced by area-to-volume changes. *Biophys J.*, 60:825-844, 1991.

A.A. Kataev, A.A. Alexandrov, L.L. Tikhonova, G.N. Berestovsky. Frequency dependent effects of the electromagnetic millimeter waves on the ion currents in the cell membrane of Nitellopsis: Non thermal action. *Biofizika*, 38:446-462, 1993 (in Russian).

R. Koynova, M. Caffrey. Phases and phase transitions of the phosphatidylcholines. *Biochimim. Biophys. Acta*, 1376:91-145, 1998.

R. Kuboi, T. Shimanouchi, H. Umakohsi, M. Yoshimoto. Detection of protein conformation under stress condition using liposome as sensor materials. *Sens. Mater.*, 16:241-254, 2004.

M. Kummrow and W. Helfrich. Deformation of giant lipid vesicles by electric fields. *Phys. Rev. A*, 44:8356-8360, 1991.

R. Kwok and E. Evans. Thermoelasticity of large lecithin bilayer vesicles. *Biophys. J.*, 35:637-652, 1981.

A.C.K. Lai, K.T. Wan and V. Chan, Substrate-induced deformation and adhesion of phospholipid vesicles at the main phase transition. *Biophys. Chem.*, 99:245-258, 2002.

M.B. Lande, J.M. Donovan, and M.L. Zeidel. The relationship between membrane fluidity and permeabilities to water, solutes, ammonia, and protons. *J. Gen. Physiol.*, 106:67-84, 1995.

G. Lawton. Wireless HD Video Heats Up. *Computer*, 41:18-20, 2008.

J. Lee, J. Kosterlitz. Finite-size scaling and Monte Carlo simulations of first-order phase transitions. *Phys. Rev. B*, 43:3265-3277, 1991.



- G. Le Goff, M.F. Vitha, R.J. Clarke. Orientational polarisability of lipid membrane surfaces. *Biochem. Biophys. Acta Biomembr.*, 1768:562-570, 2007.
- C. Leirer, B. Wunderlich, V.M. Myles, M.F. Schneider. Phase transition induced fission in lipid vesicles. *Biophys. Chem.*, 143:106-109, 2009a.
- T. Leirer, B. Wunderlich, A. Wixforth, M.F. Schneider. Thermodynamic relaxation drives expulsion in giant unilamellar vesicles. *Phys Biol.*, 6:1478-3975, 2009b.
- S. LeVine. *The Active Denial System. A Revolutionary, Non-lethal Weapon for Today's Battlefield*, pp:1-17. Washington, DC: National Defence Univ., 2009.
- R.P. Liburdy and R.L. Magin. Microwave-stimulated drug release from liposomes. *Rad. Res.*, 103: 266-275, 1985.
- R.P. Liburdy and A. Penn. Microwaves bioeffects in the erythrocyte are temperature and pO<sub>2</sub> dependent: cation permeability and protein shedding occur at the membrane phase transition. *Bioelectromagnetics*, 5:283-291, 1984.
- N. Ling. *Life at the Cell and Below-Cell Level. The Hidden History of a Fundamental Revolution in Biology*. Pacific Press, New York, 2001.
- R. Lipowsky and E. Sackmann. *Structure and dynamics of membranes: from cells to vesicles*, volume 1A. Elsevier science B.V., 1995.
- O. Lopez, A. de la Maza, L. Coderch, C. Lopez-Iglesias, E. Wehrli, J.L. Parra. Direct formation of mixedmicelles in the solubilization of phospholipid liposomes by Triton X-100. *FEBS Lett.*, 426:314-318, 1998.
- V. Luzzati, H. Mustache, A. Skoulios, F. Husson. La structure des colloides d'association. I. Les phases liquides-cristallines des systemes amphiphile-eau. *Acta Crystallogr.*, 13:660, 1960.
- R.C. MacDonald, R.I. MacDonald, B.Ph.M. Menco, K. Takeshita, N.K. Subbarao, L. Hu. Small-volume extrusion apparatus for preparation of large unilammelar vesicles. *Biochim. Biophys. Acta*, 1061:297-303, 1991.
- H. Madani and E.W. Kaler. Aging and stability of vesicular dispersions. *Langmuir*, 6:125-132, 1990.
- M. Marcus, B. Pattan. Millimeter wave propagation: Spectrum management and implications. *IEEE Microwave Mag.*, 6:54-62, 2005.

- J.C. Mathai, S. Tristram-Nagle, J.F. Nagle and M.L. Zeidel. Structural Determinants of Water Permeability through the Lipid Membrane. *J Gen Physiol.*, 131:69-76, 2008.
- L.D. Mayer, M.J. Hope, P.R. Cullis. Vesicle of various sizes produced by a rapid extrusion procedure. *Biochem Biophys Acta*, 858:161-168, 1986.
- M.K. McGahon, J.M. Dawicki, A. Arora, D.A. Simpson, T.A. Gardiner, A.W. Stitt, C.N. Scholfield, J.G. McGeown, T.M. Curtis. Kv1.5 is a major component underlying the A-type potassium current in retinal arteriolar smooth muscle. *Am. J. Physiol. Heart. Circ. Physiol.*, 292:H1001-H1008, 2007.
- P. Méléard, J.F. Faucon, M.D. Mitov, and P. Bothorel. Pulsed-light microscopy applied to the measurement of the bending elasticity of giant liposomes. *Europhysics Letters*, 19:267-271, 1992.
- L. Miao, U. Seifert, M. Wortis, and H.G. Döbereiner. Budding transitions of fluid-bilayer vesicles: The effect of area-difference elasticity. *Phys. Rev. E*, 49:5389-5407, 1994.
- O.G. Mouritsen and M. Bloom. Mattress model of lipid-protein interactions in membranes. *Biophys. J.*, 46:141-153, 1984.
- J.F. Nagle. Area lipid of bilayers from NMR. *Biophys. J.*, 64:1476-1481, 1993.
- J.F. Nagle, J.C. Mathai, M.L. Zeidel, and S. Tristram-Nagle. Theory of passive permeability through lipid bilayers. *J. Gen. Physiol.*, 131:77-85, 2008.
- J.F. Nagle and H.L. Scott. Lateral compressibility of lipid mono- and bilayers lateral compressibility of lipid mono- and bilayers. theory of membrane permeability. *Biochim. Biophys. Acta*, 513:236-243, 1978.
- J.F. Nagle and S. Tristram-Nagle. Structure of lipid bilayers. *Biochim. Biophys. Acta*, 1469:159-195, 2000.
- H.O. Negrete, R.L. Rivers, A.H. Goughs, M. Colombini, and M.L. Zeidel. Individual leaflets of a membrane bilayer can independently regulate permeability. *J. Biol. Chem.*, 271:11627-11630, 1996.
- K. Olbrich, W. Rawicz, D. Needham and E. Evans. Water permeability and mechanical strength of polyunsaturated lipid bilayers. *Biophys. J.*, 79:321-327, 2000.

- U. Olsson and H. Wennerström, On the ripening of vesicle dispersions. *J. Phys. Chem B*, 106:5135, 2002.
- L. Onsager. Reciprocal relations in irreversible processes. *Phys. Rev.*, 37:405-426, 1931.
- D. Papahadjopoulos, K. Jacobsen, S. Nir, and T. Isac. Phase transition in phospholipid vesicles. Fluorescence polarization and permeability measurements concerning the effect of temperature and cholesterol. *Biochim. Biophys. Acta*, 311:330-348, 1973.
- A.G. Pakhomov, Y. Akyel, O.N. Pakhomova, B.E. Stuck, M.R. Murphy. Current state and implication of research on biological effects of millimeter wave. *Bioelectromagnetics*, 19:393-413, 1998.
- A.G. Pakhomov and M.R. Murphy. Low intensity millimeter waves as a novel therapeutic modality. *IEEE Trans. Plasma Science*, 28:34-40, 2000.
- T. Parasassi, M. DiStefano, M. Loiero, G. Ravagnan, and E. Gratton. Cholesterol modifies water concentration and dynamics in phospholipid bilayers: a fluorescence study using laurdan probe. *Biophysical Journal*, 66:763-768, 1994.
- V.A. Parsegian, R.P. Rand, N. Fueller and D.C. Rau. Osmotic stress for the direct measurement of intermolecular forces. *Methods in Enzymology*, 127:400-416, 1986.
- S. Paula, A.G. Volkov, A.N. Van Hoek, T.H. Haines, and D.W. Deamer. Permeation of protons, potassium ions, and small polar molecules through phospholipid bilayers as a function of membrane thickness. *Biophys. J.*, 70:339-348, 1996.
- J. Pécéréaux, H.G. Döbereiner, J. Prost, J.F. Joanny, and P. Bassereau. Refined contour analysis of giant unilamellar vesicles. *Eur. Phys. J. E*, 13:277-290, 2004.
- M.A. Peterson, H. Strey, and E. Sackmann. Theoretical and phase contrast microscopic eigenmode analysis of erythrocyte flicker: amplitudes. *J. Phys. II France*, 2:1273-1285, 1992.
- N.O. Peterson, S.I. Chan. More on the motional state of lipid bilayer membranes: interpretation of order parameters obtained from nuclear magnetic resonance experiments. *Biochemistry*, 16:2657-2667, 1977.
- J.M. Pope, L. Walker, B.A. Cornell, G.W. Francis GW. NMR study of synthetic lecithin bilayers in the vicinity of the gel-liquid-crystal transition. *Biophys. J.*, 35:509-520, 1981.

- T. Pott and P. Méléard. The dynamics of vesicle thermal fluctuations is controlled by intermonolayer friction. *Europhys. Lett.*, 59:87-93, 2002.
- P.H. Puech, N. Borghi, E. Karatekin, and F. Brochard-Wyart. Line thermodynamics: adsorption at a membrane edge. *Phys. Rev. Lett.*, 90:128304-128307, 2003.
- A.A. Radzievsky, O.V. Gordiienko, I. Szabo, S.I. Alekseev and M.C. Ziskin. Millimeter waveinduced suppression of B16 F10 melanoma growth in mice: Involvement of endogenous opioids. *Bioelectromagnetics*, 25:466-473, 2004.
- R.M. Raphael, R.E. Waugh, S. Svetina, B. Zeks. Fractional occurrence of defects in membranes and mechanically driven interleaflet phospholipid transport. *Physical review. E, Statistical, nonlinear, and soft matter physics.*, 64:051913, 2001.
- A. Ramundo-Orlando, G. Longo, M. Cappelli, M. Girasole, L. Tarricone, A. Beneduci, R. Massa. The response of giant phospholipids vesicles to millimeter wave radiations. *Biochim. Biophys. Acta*, 1788:1497, 2009.
- A. Ramundo-Orlando, G. P. Gallerano, P. Stano, A. Doria, E. Giovenale, G. Messina, M. Cappelli, M. D'Arienzo, I. Spassovsky. Permeability changes induced by 130 GHz pulsed radiation on cationic liposomes loaded with carbonic anhydrase. *Bioelectromagnetics*, 22:303-313, 2007.
- A. Ramundo-Orlando, G. Longo, M. Cappelli, M. Girasole, L. Tarricone, A. Beneduci, R. Massa. The response of giant phospholipid vesicles to millimeter waves radiation. *Biochim Biophys Acta*, 1788:1497-1507, 2009.
- A. Ramundo-Orlando. Effects of Millimeter Waves Radiation on Cell Membrane - A Brief Review. *Journal of Infrared, Millimeter, and Terahertz Waves*, 31:1400-1411, 2010.
- J.P. Reeves and R.M. Dowben. Formation and properties of thin-walled phospholipid vesicles. *J. Cell Physiol.* 73:49-60, 1969.
- F. Richter, L. Finegold and G. Rapp. Sterol sense swelling in lipid bilayers. *Phys. Rev. E*, 59:3483-3491, 1999.
- K.A. Riske and R. Dimova. Electro-deformation and -poration of giant vesicles viewed with high temporal resolution. *Biophys. J.*, 88:1143, 2005.
- M.A. Rojavin, A.A. Radzievsky, A. Cowan and M.C. Ziskin. Pain relief caused by millimeter waves in mice: Results of cold water tail flick tests. *Int. J. Rad. Biol.*, 76:575-580, 2000.

M.A. Rojavin and M.C. Ziskin. Medical applications of millimeter waves. *Q. J. Med.*, 91:57-66 1998.

E. Rommel, F. Noack, P. Meier, G. Kothe. Proton spin relaxation dispersion studies of phospholipid membranes. *J. Phys. Chem.*, 92:2981-2987, 1988.

E. Sackmann. The seventh Datta lecture. Membrane bending energy concept of vesicle- and cell-shapes and shape-transitions. *FEBS Lett.*, 346:3-16, 1994.

M.J. Saxton and K. Jacobson. Single-particle tracking: applications to membrane dynamics. *Annu Rev Biophys Biomol Struct.*, 26:373-399, 1997.

M. Schiewek and A. Blume. Phase transition kinetics of lipid bilayer membranes studied by time-resolved pressure perturbation calorimetry. *Eur. Biophys. J.*, 39:815-824, 2010.

H.P. Schwan. Some tissue determinants of interactions with electric fields. *Neurosciences Res. Prog. Bull.*, 15:88-98, 1977.

T. Shimanouchi, H. Ishii, N. Yoshimoto, H. Umakoshi, K. Ryoichi. Calcein permeation across phosphatidylcholine bilayer membrane: Effects of membrane fluidity, liposome size, and immobilization. *Colloids and Surfaces B: Biointerfaces*, 73:156-160, 2009.

J.M Seddon and R.H. Templer. Polymorphism of lipid-water systems. In: R. Lipowsky and E.Sackmann, (Eds), *Structure and Dynamics of Membranes*, pp:97-160, Elsevier Science B.V., Amsterdam. 1995.

H. Seeger, M. Fidorra, and T. Heimburg. Domain size and fluctuations at domain interfaces in lipid mixtures. *Macromol. Symposia*, 219:85-96, 2005.

M. Seeger, M. L. Gudmundsson, and T. Heimburg. The influence of anesthetics, neurotransmitters and antibiotics on the relaxation processes in lipid membranes. *J. Phys. Chem. B*, 111:13858-13866, 2007.

A. Seelig and J. Seelig. Dynamic structure of fatty acyl chains in a phospholipid bilayer measured by deuterium magnetic resonance. *Biochemistry*, 13:4839-4845, 1974.

A. Seelig, J. Seelig. Bilayers of dipalmitoyl-3-sn-phosphatidylcholine. Conformational differences between the fatty acyl chains. *Biochim. Biophys. Acta*, 406:1, 1975.

A. Seelig, and J. Seelig. Effect of a single cis double bond on the structures of a phospholipid bilayer. *Biochemistry*, 16:45-50, 1977.

A. Seelig and J. Seelig. Lipid conformation in model membranes and biological membranes. *Q. Rev. Biophys.*, 13:19-61, 1980.

J. Seelig. Phospholipid Headgroups as Sensors of Electric Charge. In K.W.A. Wirtz (Eds), *New Developments in Lipid-Protein Interactions and Receptor and Function*, pp:241-248 , Plenum Press, New York, 1993.

J. Seelig, J.L. Browning. General features of phospholipid conformation in membranes. *FEBS Lett.*, 92:41-44, 1978.

J. Seelig, P.M. Macdonald and P.G. Scherer. Phospholipid head groups as sensors of electric charge in membranes. *Biochemistry*, 26:7535-7541, 1987.

J. Seelig and N. Waespe-Sarcevic. Molecular order in cis and trans unsaturated phospholipid bilayers. *Biochemistry*, 17:3310-3315, 1978.

U. Seifert and R. Lipowsky. Adhesion of vesicles. *Phys. Rev. A*, 42:4768-4771, 1990.

U. Seifert. Giant Vesicles: A Theoretical Perspective In: P.L. Luisi, P. Walde (Eds), *Giant Vesicles, Perspectives in Supramolecular Chemistry*, vol. 6, pp:71-92. Wiley, Chichester, 2000.

T. Shimanouchi, P. Walde, J. Gardiner, Y.R. Mahajan, D. Seebach, A. Thomae, S.D. Kramer, M. Voser, R. Kuboi. Permeation of a beta-heptapeptide derivative across phospholipid bilayers. *Biochim. Biophys. Acta*, 1768:2726-2736, 2007.

P.H. Siegel and V. Pikov. THz in Biology and Medicine: Towards Quantifying and understanding the Interaction of Millimeter- and Submillimeter-Waves with Cells and Cell Processes. *SPIE Photonics West, BiOS*, paper 7562-17, San Francisco, CA, 2010

S.J. Singer and G.L. Nicolson. The fluid mosaic model. *Science*, 175:720-731, 1972.

A. Singh, P. E. Schoen and M.A. Guedeau-Boudeville. Temperature dependent membrane phase reorganization in giant vesicles. *Chem. Phys Lip.*, 94:53-61, 1998.

D.M. Small. *The Physical Chemistry of Lipids*, Plenum, New York, 1986.

R.L. Smith and E. Oldfield. Dynamic structure of membranes by deuterium NMR. *Science*, 225:280-288, 1984.

T. Sparmann and P.O. Westlund. An NMR line shape and relaxation analysis of heavy water powder spectra of the  $L_{\alpha}$ ,  $L_{\beta}$  and  $P_{\beta}$  phases in the DPPC/water system. *Phys. Chem. Chem. Phys.*, 5:2114-2121, 2003

A.A. Spector and M.A. Yorek. Membrane lipid composition and cellular function. *J. Lipid Res.*, 26:1015-1035, 1985.

J. Speyer, R. Weber, S. Das Gupta, R. Griffin. Anisotropic h-2 nmr spin-lattice relaxation in l-alpha-phase cerebroside bilayers. *Biochemistry*, 28:9569-9574, 1989.

M.A. Stuchly, S.S. Stuchly. In C. Polk and E. Postow (Eds), *Handbook of Biological Effects of Electromagnetic Fields*, pp:295-336, CRC Press LLC Second Edition, 1996.

T. Sugii, S. Takagi, and Y. Matsumoto. A molecular-dynamics study of lipid bilayers: effects of the hydrocarbon chain length on permeability. *J. Chem. Phys.*, 123:18471-18474, 2005.

I. Szabo, J. Kappelmayer, S.I. Alekseev, and M.C. Ziskin. Millimeter wave induced reversible externalization of phosphatidylserine molecules in cells exposed in vitro. *Bioelectromagnetics*, 27:233-244, 2006.

F.C. Jr. Szoka. The future of liposomal drug delivery. *Biotechnol Appl Biochem.* 12:496-500, 1990.

A. Tardieu, V. Luzzati, F.C. Reman. Structure and polymorphism of hydrocarbon chains of lipids - study of lecithin-water phases. *J. Mol. Biol.*, 75:711, 1973.

K.J. Tielrooij, D. Paparo, L. Piatkowski, H.J. Bakker and M. Bonn. Dielectric relaxation dynamics of water in model membranes probed by Terahertz spectroscopy. *Biophys. J.*, 97:2484-2492, 2009

V.P. Torchilin, V. Weissig. *Liposomes: A Practical Approach*, Second Edition, Oxford University Press, 2003.

T.Y. Tsong and M.I. Kanehisa. Relaxation phenomena in aqueous dispersions of synthetic lecithins. *Biochemistry*, 16:2674-2680, 1977.

W.W. van Osdol, M.L. Johnson, Q. Ye, and R.L. Biltonen. Relaxation dynamics of the gel to liquid crystalline transition of phosphatidylcholine bilayers. Effects of chainlength and vesicle size. *Biophys. J.* 59:775-785. 1991a

W.W. van Osdol, O.L. Mayorga, and E. Freire. Multifrequency calorimetry of the folding/unfolding transition of cytochrome c. *Biophys. J.*, 59:48-54, 1991b.

A.R. Von Hippel. *Dielectris and Waves*, John Wiley & Sons, Inc., London, 1954.

- P. Walde In: H.S. Nalwa (Eds) *Encyclopedia of Nanoscience and Nanotechnology*, Vol. 9, pp:43-79, American Scientific Publishers, Stevenson Ranch, 2004.
- P. Walde, K. Cosentino, H. Engel, P. Stano. Giant Vesicles: Preparations and Applications. *ChemBioChem*, 11:848-865, 2010.
- J.C. Weaver and R.D. Astumian. The response of living cells to very weak electric fields: the thermal noise limit. *Science*, 247:459-462, 1990.
- S.J. Webbs, A.D. Booth. Absorption of Microwaves by microorganisms. *Nature*, 222:1199-1203, 1969.
- S.J. Webbs, D. Dodds. Inhibition of bacterial cell growth by 136 gc microwaves. *Nature*, 218:374-375, 1968.
- J. Wells, C. Kao, E.D. Jansen, P. Konrad, A. Mahadevan-Jansen. Application of infrared light for in vivo neural stimulation. *J. Biomed. Opt.*, 10:64003, 2005a.
- J. Wells, C. Kao, K. Mariappan, J. Albea, E.D. Jansen, P. Konrad, A. Mahadevan-Jansen. Optical stimulation of neural tissue in vivo. *Opt. Lett.*, 30:504-506, 2005b.
- P.O. Westlund. Line Shape Analysis of NMR Powder Spectra of  $^2\text{H}_2\text{O}$  in Lipid Bilayer Systems. *J. Phys. Chem. B*, 104:6059-6064, 2000.
- W. Wintz, H.G. Döbereiner, and U. Seifert. Starfish vesicles. *Europhys. Lett.*, 33:403-408, 1996.
- B. Wunderlich, C. Leirer, A.L. Idzko, U.F. Keyser, A. Wixforth, V.M. Myles, T. Heimburg, and M.F. Schneider. Phase state dependent current fluctuations in pure lipid membranes. *Biophys. J.*, 96:4592-4597, 2009.
- T.X. Xiang and B.D. Anderson. The relationship between permeant size and permeability in lipid bilayer membranes. *J. Membr. Biol.*, 140:111-122, 1994.
- A.Yamaji-Hasegawa, M. Tsujimoto. Asymmetric distribution of phospholipids in biomembranes. *Biol. Pharm. Bull.*, 29:1547-1553, 2006.
- M. Zhadobov, R. Sauleau, V. Viè, M. Himdi, L. LeCoq, D. Thouroude. Interactions between 60-GHz millimeter waves and artificial biological membranes: dependence on radiation parameters. *IEEE Trans. Microwave Theory and Techniques*, 54:2534-2542, 2006.



M. Zhadobov, R. Sauleau, Y. Le Drean, S.I. Alekseev, M.C. Ziskin. Numerical and experimental millimeter-wave dosimetry for in vitro experiments. *IEEE Trans Microwave Theory Tech.*, 56:2998-3007, 2008.

F. Zernike. The wave theory of microscopy image formation. In W.H. Freeman (Eds) *Concepts in Classical Optics*, pp:525-536, San Francisco, 1958.

Y.L. Zhang, J. Frangos, M. Chachisvilis. Laurdan fluorescence senses mechanical strain in the lipid bilayer membrane. *Biochem. Biophys. Res. Commun.*, 347:838-841, 2006.

J.X. Zhao. Numerical dosimetry for cells under millimetre-wave irradiation using Petri dish exposure set-ups. *Phys. Med. Biol.*, 50:3405-3421, 2005.

D.V. Zhelev, D. Needham, and R.M. Hochmuth. A novel micropipette method for measuring the bending modulus of vesicle membranes. *Biophys. J.*, 67:720-727, 1994.

## ACKNOWLEDGEMENTS

Arrivata finalmente al momento di dire “Grazie”, sono tante le persone a cui vorrei rivolgere un pensiero.

*Andando a lavoro...*

I would like to thank my supervisor, Prof. Giuseppe Chidichimo, for believing and trusting in my capability by supporting my enthusiasm for this research field. Thank you for many enlightening discussions... e un sincero grazie per essere stato uno degli esempi più significativi della vivacità intellettuale che contraddistingue chi ama fare scienza.

Many thanks also to Dr. Amerigo Beneduci, who was the person with whom I worked more closely during these three years. He was always available and willing to help during my studies. Thank you for many discussions and useful suggestions related this work. È stato un esempio stimolante, soprattutto per il suo approccio competente e critico ai diversi aspetti che caratterizzano questo campo di ricerca altamente interdisciplinare.

Thanks also to the coordinator of "STM3" doctorate, Prof. Carlo Versace, for being always available and understandable.

I am very thankful to Prof. Peter Walde of the Department of Materials, ETH Zürich, who kindly allowed me to spend part of my PhD in the stimulating environment of ETH. He was always punctual and available in supervising my work, and I have benefited greatly from his extensive expertise in membrane models.

A special thanks to Alfonsina Ramundo-Orlando of the Institute of Neurobiology and Molecular Medicine, CNR Tor Vergata, Rome. She introduced me to the fascinating world of GUVs, and involved in the beautiful experience of the "Cell model system" summer school, which has given me so much not only as a student, but also personally. Grazie in generale per la disponibilità, i consigli e l'affetto dimostrato.

A special thanks to Prof. Marcello Longeri. Al di là della disponibilità dimostrata per il ruolo istituzionale di coordinatore fondi del dottorato per il Dip. di Chimica, ogni firma di autorizzazione si trasformava in un avvincente scambio di battute e divagazioni filosofiche-esistenziali! Grazie per i tanti stimoli e la prospettiva di una visione ampia e critica non solo nel fare scienza, ma come approccio di vita.

Many thanks to Prof. Erich Windhab, Food Process Engineering, ETH Zürich, for giving me the opportunity to work in his lab at the ETH, in an active and collaborative group, to Prof. Attilio Golemme and Dr Roberto Termine of the Dept. of Chemistry, Unical, for the laboratory facilities for the experiments on GUVs, and Prof. Enzo Cazzanelli, Dr. Marco Castriota and Angela Fasanella of the Dept. of Physics, Unical, for the spin coater and for having carried out some measurements on vesicles and introduced me to the use of Raman microscopy.

In particolare ringrazio Roberto per i tanti consigli e il supporto in svariate occasioni.

I would like to give my appreciation to all the people who helped me and shared my working-days: tra queste, a Luigi devo un grazie particolare, a cui si unisce quello per Annaelia, per il sostegno, l'amicizia e la disponibilità in tante circostanze. Grazie inoltre a Maurizio e Sabrina, a Bruna De Simone e Renata De Rose per la stima reciproca, e a Teresa e Vittoria. Ringrazio Renata inoltre per avermi insegnato a coltivare le cellule. Finally, I thank "Upi" Pandey, for his

friendship and for his human value. To all of you I also have many laughs at our coffee breaks, and moments of happiness at work.

In general, thanks to many special people who, for some reason related to this work, I have met, known, and felt respect and affection.

*Tornando a casa....*

Ai miei genitori, perché hanno con pazienza e perseveranza, costantemente e amorevolmente, costruito giorno dopo giorno una splendida famiglia e un rifugio accogliente che ha sempre rappresentato un riferimento stabile e indiscusso nella mia vita...grazie a loro posso dire di sapere quello che si prova tornando a *Casa*.

Ad Erica. E' difficile mettere su carta il bene che ci lega e trovare delle parole capaci di descrivere la riconoscenza che provo nell'averla non solo come sorella, ma anche come migliore amica. A mio fratello Ivan, che con intelligenza e discrezione, fa sentire la sua presenza e la sua disponibilità ad ogni richiesta di aiuto... Da me, soprattutto in questo ultimo periodo, sia tu che Erica ne avete ricevute tante!! Il vostro supporto, materiale e non, è stato indispensabile, e mi ha aiutato a non scoraggiarmi anche nei momenti di maggiore stanchezza. Ringrazio anche Giuseppe, per le battute spensierate e le discussioni (non-politiche!): un cognato simpatico è altamente consigliabile nei momenti di stress!

A zia Elena, zia Rosetta e ai miei cugini, a zio Eugenio e zia Sarina, grazie per il vostro affetto.

Al mio amico Luca. Delle tante persone che si incontrano nel percorso sorprendente e imprevedibile della vita, ce ne sono alcune che, in qualche modo, ricorrono al tuo fianco...tu, invece, ci cammini sempre! Grazie per la tua amicizia. E grazie per l'aiuto indispensabile che mi hai dato nella preparazione finale di questo lavoro di tesi, sacrificando tempo, sonno e alcune puntate dei tuoi programmi preferiti!

Grazie ai miei amici per i tanti momenti "ciurli" e non, che mi avete spesso regalato!

*Infine, un grazie speciale lo devo a te, zio. Che il desiderio di cambiare le cose, e la forza di trasformarle, venga solo da un profondo amore per la vita, propria e degli altri, l'ho capito anche guardando al tuo esempio.*

*In tanti momenti, ho sentito uno sguardo, un aiuto o un intervento inaspettato, e so che provenivano dalla tua posizione privilegiata!*

*Mi dicevi: "Studi troppo, diventerai una scienziata!". L'ho considerato uno dei più begli auguri, e spero proprio di essere sulla giusta strada!*